Large volume multicolor nonlinear microscopy of neural tissues

Lamiae Abdeladim

université PARIS-SACLAY

NNT : 2018SACLX070

Thèse de doctorat

Large volume multicolor nonlinear microscopy of neural tissues

Thèse de doctorat de l'Université Paris-Saclay
préparée à l'Ecole Polytechnique

Ecole doctorale n°573 interfaces : approches interdisciplinaires, fondements, applications et innovation (INTERFACES)
Spécialité de doctorat : Physique

Thèse présentée et soutenue à Palaiseau, le 27/09/2018, par

MME LAMIAE ABDELADIM

Composition du Jury :

Dr. Philippe Vernier Directeur de recherche, CNRS	Président
Dr. Laurent Bourdieu Directeur de recherche, CNRS	Rapporteur
Dr. Martin Oheim Directeur de recherche, CNRS	Rapporteur
Dr. Rosa Cossart Directrice de recherche, Inserm	Examinatrice
Dr. Emmanuel Beaurepaire Directeur de recherche, CNRS	Directeur de thèse
Dr. Willy Supatto Chargé de recherche, CNRS	Co-directeur de thèse
Dr. Jean Livet Directeur de recherche, Inserm	Co-directeur de thèse

Abstract

Multiphoton microscopy has transformed neurobiology during the two last decades by enabling 3D imaging of thick tissues at subcellular resolution. However the depths provided by multiphoton microscopy are limited to few hundreds of micrometers inside scattering tissues such as the brain. In the recent years, several strategies have emerged to overcome this depth limitation and to access larger volumes of tissue. Although these novel approaches are transforming brain imaging, they currently lack efficient multicolor and multicontrast modalities. This work aims to develop large-scale and deep-tissue multiphoton imaging modalities with augmented contrast capabilities. In a first chapter, we present the challenges of high-content large-volume brain imaging, with a particular emphasis on powerful multicolor labeling strategies which have so far been restricted to limited scales. We then introduce chromatic serial multiphoton tomography, a method which combines automated histology with wavelength-mixing to access multiple nonlinear contrasts across large volumes, from several mm^3 to whole brains, with submicron resolution and intrinsic channel registration. In a third chapter, we demonstrate the potential of this novel approach to open novel experimental paradigms in neurobiological studies. In particular, we demonstrate multicolor volumetric histology of several mm^3 of Brainbow-labeled tissues with preserved diffraction-limited resolution and illustrate the strengths of this method through color-based tridimensional analysis of astrocyte morphology, interactions and lineage in the mouse cerebral cortex. We further illustrate the potential of the method through multiplexed whole-brain mapping of axonal projections labeled with distinct tracers. Finally, we develop multimodal three-photon microscopy as a method to access larger depths in live settings.

Key words: Multiphoton microscopy, wavelength-mixing, block-face imaging, three-photon microscopy, Brainbow labeling.

ACKNOWLEDGEMENTS

Au moment où je m'apprête à écrire ces fameux remerciements de thèse, je suis en pleine préparation de mon départ, bientôt imminent, de l'autre côté de l'Atlantique. C'est donc non sans nostalgie, mais surtout avec beaucoup de gratitude que je prend ces quelques lignes pour remercier toutes celles et ceux qui ont contribué à cette aventure.

Je commencerai tout d'abord par remercier les membres de mon jury: Laurent Bourdieu, Martin Oheim, Rosa Cossart et Philippe Vernier. Merci à chacun et chacune d'avoir pris de votre temps pour évaluer mon travail. Merci pour vos retours constructifs et vos encouragements. Par ailleurs, je remercie doublement Laurent et Martin pour leur travail de rapporteurs. Je tiens ensuite à remercier la direction du LOB, tout d'abord Jean-Louis Martin pour m'avoir accueillie au laboratoire puis particulièrement François Hache pour son suivi ces quatre dernières années, et d'avoir toujours été à l'écoute des doctorants.

J'ai eu beaucoup de chance d'être encadrée par trois chercheurs extraordinaires (et non, je n'exagère rien !). Emmanuel, cette thèse a d'abord été pour moi une fabuleuse rencontre scientifique et humaine. Merci infiniment pour ces quatre belles années: you literally changed my life ! Merci pour ta vision, ta générosité, ton soutien sans failles et tout ce que tu m'as transmis. Merci de m'avoir aidée à me construire et à évoluer. Merci pour ton aura positive au quotidien et de réussir à voir le meilleur et à faire ressortir le meilleur en chacun. Merci de m'avoir supportée et soutenue dans les moments difficiles. Je pense qu'on ne peut juste pas rêver d'avoir un meilleur directeur de thèse. Jean, ça a été un énorme plaisir et privilège de travailler avec toi. Merci de m'avoir introduit au merveilleux monde de la neuro (tout en couleurs en plus !). Mais surtout merci de m'avoir très tôt convaincue que je pouvais faire des neurosciences au plus haut niveau malgré mon parcours de physicienne, c'est fondamentalement ce qui m'a donné l'audace de choisir un labo de neurophysiologie pour mon postdoc. Et merci de m'avoir toujours encouragée à voir grand. Willy, merci d'avoir toujours répondu présent quand j'en ai eu besoin. Merci pour toutes les techniques que tu m'as apprises qui ont beaucoup contribué à me construire une culture très large en microscopie et qui me seront certainement précieuses pour la suite. Merci également pour ta précieuse aide Imaris, tes retours toujours pertinents et pour tous tes conseils pour la suite. A tous les trois, je suis fière d'avoir fait ma thèse avec vous, et encore une fois merci pour tout.

J'ai également eu la chance de travailler avec deux jeunes neurobiologistes talentueuses, Katie Matho et Solène Clavreul, que je tiens à remercier pour tout leur travail et les beaux projets qu'on a pu réaliser ensemble. Ca a été un vrai plaisir de travailler avec vous, et j'espère que l'occasion se renouvellera par la suite ! Katie, merci pour tout ce que tu m'as appris et d'être toujours là pour partager ton expérience. On viendra à bout de ce projet titanesque ! Solène, tu m'as inspirée par ta rigueur et ta détermination, j'ai hâte de voir la suite ! J'en profite également pour remercier les autres collaborateurs ayant contribué à ce travail de thèse: Khmaies Guesmi

et Frédéric Druon pour l'aventure OPA, Karine Loulier pour les beaux cerveaux Cytbow, Samuel pour les délicates manips sur tranches vivantes, Nicolas Dray pour les expériences zebrafish, et Sébastien Février et Patrick Cadroas pour les tout premiers essais 3P.

Vient ensuite le tour des Lobsters avec qui j'ai eu l'occasion de travailler. Tout d'abord, un énorme merci à Chiara, pour tous les échanges scientifiques, tes encouragements au quotidien, et tous les bons moments passés au labo et en dehors. I will definitely miss you. Un grand merci également à Pierre d'avoir travaillé avec moi pour upgrader les setups, j'ai énormément appris avec toi ! Merci à Anatole pour ton ouverture d'esprit et tes inputs sur les projets, et merci à Son et à toi d'avoir sublimé le travail MNTB. Merci à Guy, pour avoir été un labmate admirable pendant trois ans, et pour m'avoir fait découvrir la culture israélienne. Un grand merci aussi à Nicolas O. pour toutes les discussions et les précieux conseils, et surtout de m'avoir convaincue de me mettre à LateX pour la rédaction! Je t'en suis éternellement reconnaissante !

Merci également à l'indispensable team technique du LOB. Merci à Laure et Christelle pour votre fantastique efficacité, à Jean-Marc pour ta créativité qui nous aide à réaliser nos designs les plus fous, à Xavier pour les belles conceptions électroniques, et à Isabelle de m'avoir aidée à sécuriser les protocoles que j'ai mis en place. Je n'oublie évidemment pas Emilie et Ernan, pour leur bonne humeur et leur gentillesse !
Je voudrais aussi dire merci à toutes celles et ceux qui m'ont suivie et encouragée ces dernières années, je pense notamment à Laura, Roxane, Adeline, Marie-Claire, Nicolas D., Gaël, Karsten, Hannu, Manuel, et tous les autres que j'aurais oublié.

J'ai biensur une pensée chaleureuse pour mes valeureux compagnons de route, les djeun's du LOB: Helene, Lipsa, Guillaume, Claire, Chao, Joséphine, Julia, Paul, Antoine, Arthur, Margaux, Mayla, Xiujun, Yoann, Clothilde. Un merci particulier à Julia pour son énergie positive et ses encouragements pendant la rédaction et à Joséphine de m'avoir aidée à relativiser par moments. Un petit clin d'oeil aussi à Max et Pascal parce qu'ils sont juste trop cool (et pour les gateaux du vendredi apm).
Enfin un dernier merci aux lunchmates du dernier départ Magnan: Emmanuel, Chiara, Nicolas, Guy : merci pour ces chouettes moments à refaire le monde, les sciences, la politique, en 30 min chrono!

Je prendrai ces dernières lignes pour remercier mes proches qui ont beaucoup contribué à mon équilibre ces dernières années. Merci à mes amis (pardon d'avance à ceux que j'oublie): Chiara P, Hyacinthe et Aude pour avoir pris soin de moi et pour votre soutien continu et tous les autres pour les bons moments passés ensemble Olivier, François, Elodie, Maxime, Louis, Vincent, Pilou, Madeleine, Anne-Laure, Marie, Nico, Matthieu, Jean, Hélène, Fanny, Elena et le club MPSI2 de Saint-Louis. Je vous attends tous en Californie! Merci à toute la famille Dalens de m'avoir 'adoptée' et pour tous les chaleureux moments passés ensemble. Merci à mon papa de m'avoir permis de faire des études longues, en France de surcroît. Merci à ma maman de m'avoir toujours encouragée à me battre et à me dépasser. Merci à Sabrine de croire si fort en moi et de m'encourager à aller toujours plus loin. Enfin merci à Théo pour tout le bonheur que tu m'apportes chaque jour, merci de m'aider à réaliser mes rêves et de me rappeler souvent que rien n'est impossible.

TABLE OF CONTENTS

List of Tables

Table **Page**

List of Figures

Figure **Page**

CHAPTER 1

INTRODUCTION

1.1 Imaging the brain: technologies, scales and challenges

Understanding how the brain develops and how it is organized to drive and support all the diversity and complexity of behavioral phenotypes is a major goal of 21st century modern neuroscience. From the structural perspective, the challenge raises from the outstandingly complex architecture of the brain : if we take the example of the mouse brain, which is already orders of magnitude smaller than a human brain (Fig 1.1), it contains no less than approximately a hundred of millions of neurons, and almost as many glial cells.

Imaging the brain at the cellular and circuit level poses the following challenges:

(i) **Volume**: The mouse brain is approximately 0.6 ×0.9 ×1.1 mm^3 with neurons projecting axons across several millimeters. Brain areas are also largely heterogeneous and functionnally diverse, so mm^3 to cm^3 volumetric imaging is required to capture cellular ensembles within a network/functional areal scale.

(ii) **Resolution**: Neurons usually present thin micron/sub-micron axons and dendritic arbors. Glial cells such as astrocytes also present a highly ramified structure with fine cellular processes. Micron-scale resolution is therefore required.

(iii) **Contrast/Specificity**: Because of the high density and heterogeneity of tightly connected cells in the nervous system, contrast strategies are required to label, visualize and identify individual cells or cell populations of interest within their complex environment.

Fig 1.2 gives an overview of some of the most widely used optical and non optical technologies used for brain imaging. At first glance, one can notice the inevitable trade-off between accessible imaging depth and achievable resolution. Indeed, MRI/fMRI approaches provide whole-organ access, however with a millimetric resolution, not sufficient for cellular/sub-cellular imaging. On the other edge of the spectrum, super-resolution and electron microscopy provide synaptic

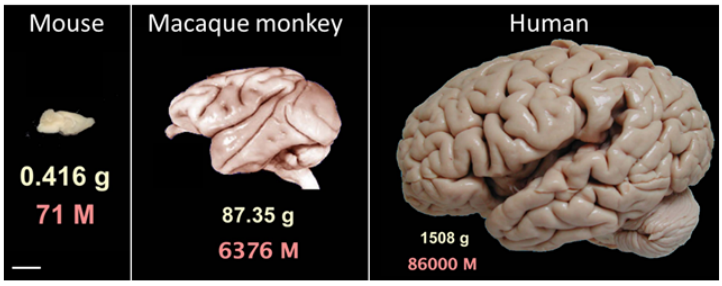

FIGURE 1.1. Comparison of brain anatomical scales across three mammalian species. Yellow: mass. Red: number of neurons. Adapted from [4].

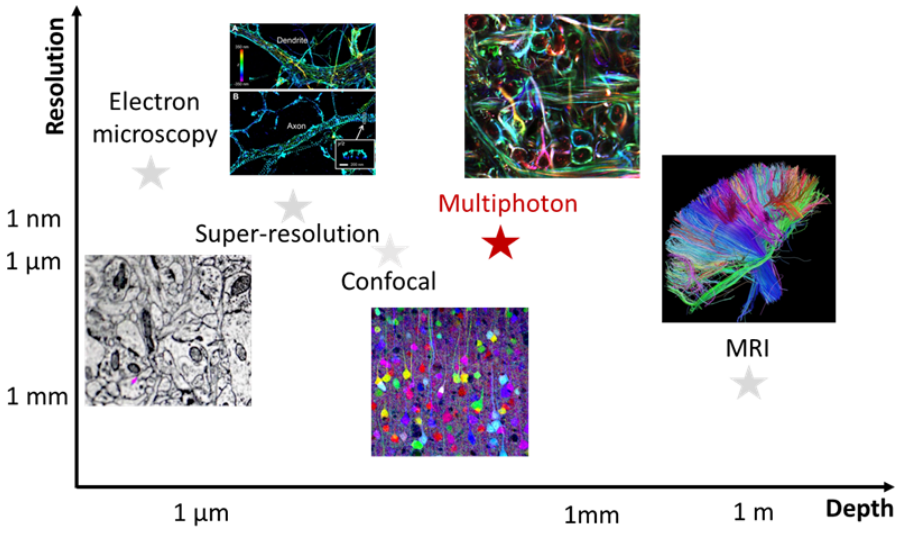

FIGURE 1.2. Comparison depth vs. resolution for different imaging methods. MRI: magnetic resonance imaging.

nanoscale and sub-nanoscale resolution respectively, but within restricted micrometric volumes, although recent outstanding efforts have recently aimed at increasing the accessible volume by harnessing serial tissue sectioning [1][2]. In between these edges, multiphoton microscopy provides cellular to sub-cellular micron-scale resolution upon hundreds of microns of depth within thick tissues, with the additional advantage of providing multiple contrast possibilities [3].

Yet the last five years have witnessed an outburst of technologies aiming to bridge these scales together and overcome the volume/resolution trade-off in light microscopy, both in live (three-photon microscopy using higher wavelengths in the near-infrared [5]) and histological (serial block-face and optical clearing approaches [6][7][8][9]) contexts. Since our starting point in this thesis is multiphoton microscopy, the upcoming section will be devoted to the fundamentals of this technology.

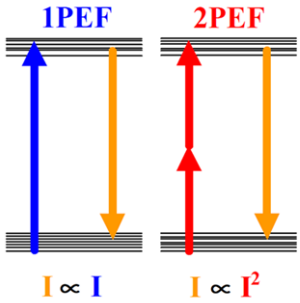

FIGURE 1.3. One-photon excited (1PEF) vs. two-photon excited (2PEF) Jablonski diagrams. Adapted from [16].

1.2 Multiphoton microscopy: principles and applications in neurobiology

The collective absorption of multiple photons following a high temporal and spatial concentration of photons has been theoretically demonstrated in 1931 by Maria Goeppert Mayer in her doctoral dissertation (english translation available at [10]). However, it was not until the development of the first lasers that the effect could be experimentally validated in the 60s. In 1978, Sheppard and Kompfner conceptualized the principle of a multiphoton scanning microscope [11], but again many years have passed before the first effective experimental implementation of a scanning microscope based on two-photon excited fluorescence by W. Denk, J. Strickler and W. Webb in 1990 [12]. In the early 2000's, propelled by the development of turn-key femtosecond laser source, several technological developments have contributed to the maturation of the technology [13][14][15]. In the last ten years, multiphoton microscopy hence became an indispensable tool to study live and intact tissues, both to answer fundamental biological questions and also in more biomedical/clinical contexts. In particular, multiphoton microscopy has had a revolutionary impact in 21st century modern neuroscience. In this section, we will first briefly review some fundamentals of multiphoton microscopy. In the last paragraph, we will give a very short overview of its use in neurobiology.

1.2.1 Principles of non-linear excitation

In a nonlinear excitation process, multiple photons interact almost simultaneously with a single molecule. In linear 'one-photon' fluorescence microscopy, the fluorophore molecule transitions from the ground state to the excited state upon absorption of a single photon which energy corresponds to the energetic gap between the ground and the excited state. Then the subsequent desexcitation of the fluorophore down to the ground state comes along with a fluorescence emitted photon. In 2PEF, two photons of lower energy are simultaneously absorbed to induce the fluorophore excitation (Fig 1.3).

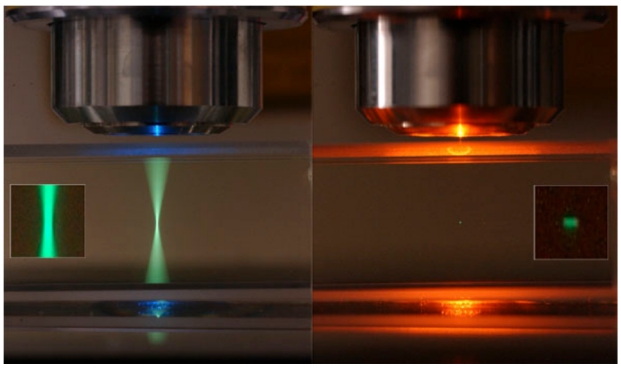

FIGURE 1.4. Optical section in multiphoton microscopy. Left: fluorescein solution excited at 488 nm with a continuous laser. Right: Same solution excited through a 2PEF process with a pused laser in the near IR range. Credit: Steve Ruzin and Holly Aron, UC Berkeley.

One of the hallmarks of multiphoton microscopy is the confinement of the excitation within the focal volume (~μm^3). This phenomenon is termed optical sectioning and is illustrated in Fig 1.4: an n^{th} order nonlinear process in proportional to I^n, with I the excitation intensity, therefore the signal only comes from areas with a very high photon density, i.e restricted to the focal volume [3]. In linear microscopy, fluorescence comes from the whole excitation cone and hence generates significantly more out-of-focus background resulting in a blurred image and more phototoxicity. In order to partially solve the out-of-focus background issue, a pinhole can be implemented in the detection path: that is the principle of confocal microscopy [17], which remains limited to depths inferior to a hundred of microns. On the other hand, 2PEF is 'intrinsically confocal' with a robust excitation confinement within scattering tissues up to hundreds of microns of depth.
The signal S_n of a n^{th} order nonlinear process scales as the average of the n^{th} power of excitation:

$$S_n \propto f.<I(t)^n> \tag{1.1}$$

with f the pulse repetition rate. The intensity of a single Gaussian pulse with a τ pulse width can be expressed as:

$$I(t) = \frac{P_0}{f\tau\sqrt{2\pi}} e^{\frac{-t^2}{2\tau^2}} \tag{1.2}$$

We can therefore derive the dependence of a n^{th} order non linear signal to the excitation power P_0, the repetition rate f and the pulse width τ:

$$S_n \propto \frac{P_0^n}{f^{n-1}\tau^{n-1}} \tag{1.3}$$

This relationship is very important to consider when optimizing multiphoton excitation. It will be central in our work on 3PEF that is presented in the last chapter of this thesis.

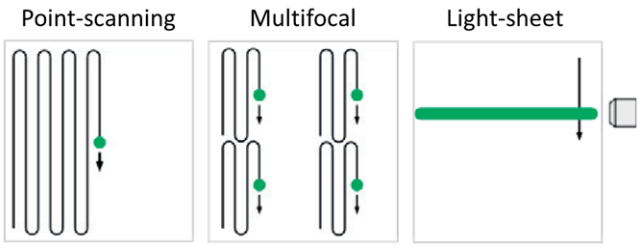

FIGURE 1.5. Scanning strategies in multiphoton microscopy. Adapted from [18].

1.2.2 Experimental multiphoton microscope systems

In a typical multiphoton microscope, images are acquired by point-scanning ([12], Fig 1.5): 2D images are acquired pixel by pixel by scanning the beam in the objective back focal plain which equals translating the focal volume over the field of view. 3D image stacks can then be acquired by moving the objective axial position. Conventionally in multiphoton microscopy, X and Y are used to designate the lateral directions, transverse to the optical axis, while Z is used for axial direction. This is also the convention we will use in this manuscript.

In order to increase the speed of multiphoton microscopy, several multiplexed or parallel scanning approaches have been developed [18] such as multifocal excitation [15] and light-sheet geometries [19]. These methods will not be presented further as all the developments realized in this thesis have been done using point-scanning.

A typical multiphoton microscope is designed as presented in Fig 1.6. We will briefly go through some of its main key elements. For an extensive review of the instrumentation of multiphoton microscopes, the reader is encouraged to refer to the excellent practical guide to multiphoton microscope design by Michael Young and colleagues [20].

Laser source: The laser source is a central element in a multiphoton microscope. Because of their commercial availability and their properties suited for multiphoton microscopy (large wavelength tunability range, ~100-150 fs pulse width, 80 MHz repetition rate, turn-key operation) Titanium:Sapphire lasers have dominated the two-photon and harmonic microscope designs. However, in order to further improve both the performances and the affordability of multiphoton microscopy, more technological laser developements are needed. This will be further discussed in the last chapter of this thesis.

Intensity modulation: This can be done with a half-wave plate and a polarizer or with an electro-optical modulator. Intensity modulation is important in practice in multiphoton experiments, to control the amount of light delivered to the sample and avoid photodamage, saturation and/or photobleaching. Excitation intensity also often need to be increased exponentially with depth to compensate for scattering (cf. section on penetration depth).

Scan system: The scan system is composed of the scanners, the scan lens and the tube lense. The scan and tube lens are positionned in a 4f configuration imaging the scanners onto the back

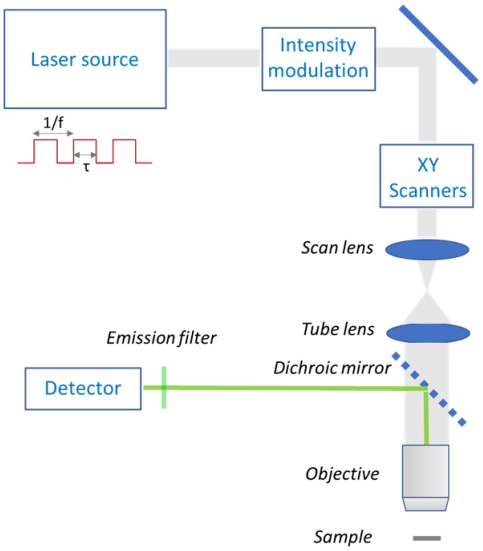

FIGURE 1.6. Point-scanning multiphoton microscope.

aperture of the objective, ensuring that the beam deflection by the scanning device results in a lateral displacement of the focal point. Galvo mirrors are the commonly used as a scanning device, but some other possibilities include acousto-optic deflectors (AODs) [21][22], resonant galvos [23][24], polygonal scanners [25] and digital micro-mirror devices [26] for faster scan rate or MEMs scanners [27][28][29] for miniaturization purposes.

Objective: This is probably the second most important element in a multiphoton setup after the laser source as its design influences drastically the optical performances of the microscope. In multiphoton microscopy, usually high NA low magnification are preferred [13] as they enable high axial resolution (2-3 µm) and a moderate field of view (500-600 µm). For this reason, the Olympus 25X 1.05 NA and the Zeiss 20X 1.0 NA have been one of the most widely used objectives in multiphoton setups. For some applications though (functional imaging for instance), a larger field of view is desired, so lower NA objectives are often used albeit at the expense of a lower axial resolution [30]. Objectif choice is crucial in multiphoton experiment design and the right choice always depends on the application: some guidelines can be found in the litterature to chose the proper multiphoton objective [31][32]. Finally, it is worth mentioning that the recent years have watched the development of several new objectives, both commercial or lab-built, specifically designed for novel applications such as imaging large volumes of clarified tissues [33], deep-tissue three-photon microscopy [5] or mesoscale functional imaging [30][34][35]. Further novel objective designs are expected in the coming years to further enhance the capabilities of multiphoton microscopy.

Detectors: Detectors in multiphoton setups are usually photomultiplier tubes (PMTs), either photon counting or analog, depending on the range of the detected signals. Detection is synchronized to the scan through an external acquisition FPGA card.

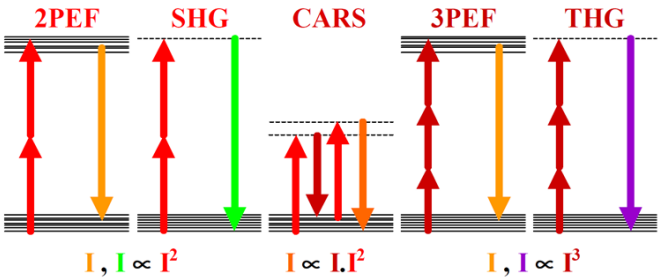

FIGURE 1.7. Sources of contrast in multiphoton microscopy. Incoherent contrasts: 2PEF, 3PEF. Coherent contrasts: SHG, THG, CARS. Adapted from [16].

1.2.3 Sources of contrast

There are two general types of contrast mechanisms in multiphoton microscopy (Fig 1.7): (i) incoherent contrasts i.e fluorescence excited multiphoton absorption, described above through the two-photon excited process, but which can be generalized to three photons (or more in principle!), and (ii) coherent label-free contrasts which originate from the structural and/or chemical properties of tissues. Under the proper conditions, these contrasts can be combined to perform multimodal multiphoton tissue imaging [36][37][38].

1.2.3.1 Two and three photon excited fluorescence

Two-photon excited fluorescence (2PEF) is the most widely used contrast in multiphoton microscopy. It is compatible with almost all the fluorophores and dyes developed for linear fluorescence microscopy, although the quantum selection rules are different [39], and the spectra are slightly blue-shifted [40]. Excitation spectra are also broader than their 1P counterparts, making it 'easier' to achieve 2P excitation albeit with more potential spectral bleedthrough [41].
On the other hand, three-photon excited fluorescence (3PEF) has been more scarcely adopted. However with the recent demonstration of its potential for deep-tissue imaging by the Xu lab at Cornell [5], the technology has gained a larger attention both from technologists and neurobiology users. 3PEF will be more deeply discussed in the last chapter of this thesis. It is however worth mentioning here that the excitability of common fluorophores as well as their excitation spectra in 3PEF are still poorly known.

1.2.3.2 Coherent contrasts

Among the most commonly used coherent contrasts in biomedical sciences are second harmonic generation (SHG), third harmonic generation (THG) and Coherent Anti-Stokes Raman Scattering (CARS).
In SHG, two photons are scattered to produce a photon at half the initial wavelength. Because of the dependence of SHG on the tensioral properties of the tissue, SHG can only happen in

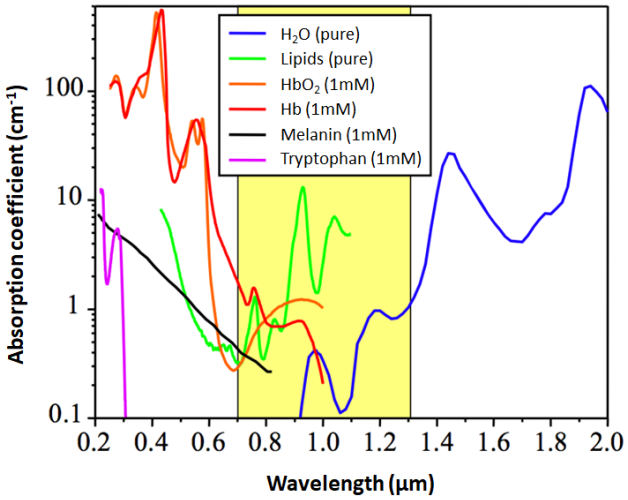

FIGURE 1.8. Absorption coefficients of some of the main biological tissue components. Data retrieved from http://omlc.ogi.edu/. Adapted from [49].

non-centrosymmetric media [42]. In biology, it is mostly used to study fibrillar structures, mainly collagen, but also tubulin or actomyosin [43][44]. Its use in neurobiology has remained limited mostly because of the brain extracellular matrix shortage in collagen. Some SHG contrasts in brain tissues have though been demonstrated: microtubules have been visualized with SHG in both cultured neurons and hippocampal and cortical acute slices [43][45].
In THG, three photons are scattered to produce a photon at a triple frequency. THG signal is strong at the interface between two heterogeneous media and null within a homogeneous medium [46]. On the other hand, CARS is more of a spectroscopic technique where specific chemical vibrational bonds can be probed [47][48]. For instance, CARS can be used to probe CH2 bonds (lipids), CH3 bonds (proteins/lipids) or OH bonds (water). THG and CARS will be presented in more details in the last section of the next chapter of this thesis.

1.2.4 Imaging depth in multiphoton microscopy

1.2.4.1 Tissue properties limiting light penetration in biological tissues

Light penetration in biological tissues is hampered by intrinsic properties of the tissues, namely absorption and scattering, which prevent the incoming photons to reach the focal volume. These properties, although intrinsic to the tissue, are also dependent on the wavelength.
Absorption:
The absorption mean free path l_{abs} is the average distance traveled by a photon before it being absorbed by the tissue. Fig 1.8 presents the absorption coefficients μ_{abs} ($\mu_{abs} = 1/l_{abs}$) of some tissue components. The 700-1300 µm window is called the transparency/therapeutic window as most tissue components absorb less at these wavelengths.

a

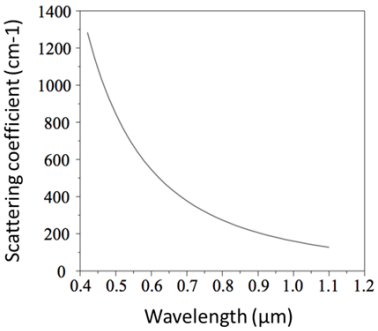

b

	λ (µm)	ls (µm)	g
Mouse brain (grey matter)	400	79	0,85
	800	127	0,87
	1200	181	0,95
Mouse brain (white matter)	400	42	0,91
	800	71	0,95
	1200	91	0,95

FIGURE 1.9. Scattering within biological tissues. (a) Model of Mie scattering for lipid droplets of size between 20 nm and 700 nm in aqueous solution. Adapted from [50]. (b) Mean scattering mean free path and anisotropy coefficient values in brain tissue for different wavelengths. Data from [13]

.

Scattering:

Scattering within a biological tissue can be characterized by the scattering mean free path l_s which corresponds to the average distance traveled by a photon between two scattering events. The scattering direction can be characterized by the anisotropy parameter g=<cosθ>, where θ represents the angle between the incoming direction and the scattered one. g=0 corresponds to an isotropic scattering, while g=1 corresponds to an anisotropic scattering towards a preferential direction. Given than in the 700-1200 nm range, scattering dominates absorption (μ_s » μ_{abs}), the two-photon intensity decays exponentially with depth with a characteristic distance of twice the scattering mean free path:

(1.4) $$I^2(z) = I_0^2.e^{\frac{-2z}{l_s}}$$

Some characteristic scattering mean free path and anisotropy ratios from the literature are presented in Figure 1.9. Scattering coefficients are largely dependents on tissue properties: age, myelin content, live vs. fixed etc. [13].

1.2.4.2 Deep-tissue imaging with two-photon microscopy

Two-photon microscopy is particularly favorable for deep-tissue imaging, for three cumulated reasons:

(i) Higher penetration of infrared light within biological tissues because of both reduced absorption and scattering compared to the visible wavelength range.

(ii) Confinement of the excitation even deep within scattering tissue because of the nonlinear two-photon absorption process. Resolution is therefore preserved even at depth.

(iii) Since photons originate only from the focal volume, detection is more efficient than most other microscopy techniques as even scattered photons contribute to the detected signal.

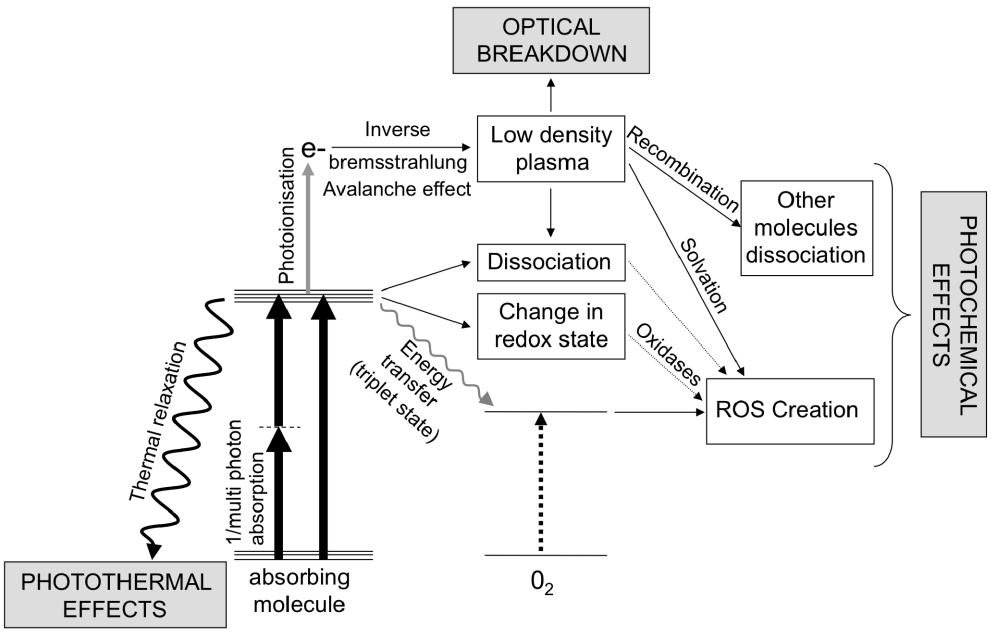

FIGURE 1.10. Light-induced toxicity mechanisms in multiphoton microscopy. Adapted from [51]

.

1.2.5 Photodamage

Another greatest strengths of multiphoton microscopy is its compatibility with long-term *in vivo* imaging because of its reduced photodamage compared to one-photon imaging. First, as photodamage occurs mainly through one or more photon absorption by the tissue, the use of higher wavelengths allows imaging in the so-called therapeutic window, which is 'safer' because of reduced absorption (cf. previous section). Secondly, because of optical sectioning, photon absorption is localised within the femtoliter size focal volume, unlike in confocal microscopy for exemple where the entire excitation cone is exposed (Fig 1.4, [3]). Multiphoton microscopy has successfully been used in the last decade to non invasively monitor live processes and developing organisms (early stage zebrafish [36], drosophila embryos [52][51], early mouse embryos [53]).

Nevertheless, photodamage is usually the main bottleneck in live multiphoton experiments. In point-scanning multiphoton microscopy, short (~100 fs) energetic pulses (nJ) with high peak powers (1-1000 GW/cm²) are delivered at high repetition rate (80-120MHz) and tightly focused using a high NA objective onto a sub-μm^3 volume, which corresponds to relatively high amounts of energy deposited on the tissue. Light-induced toxicity can occur through multiple pathways which are summarized in Figure 1.10. Photothermal damage is a linear effect, while nonlinear damage mechanisms involve photochemical perturbation of several intracellular cascade mechanisms and usually start by the creation of reactive oxidized species (ROS). Careful adjustment of laser properties and acquisition parameters is therefore necessary [51] to ensure safe imaging protocols

for live imaging. Although it has been shown that in typical multiphoton microscopy acquisitions nonlinear photodamage is the main limitation [54], recent investigations highlight that heating can also be a concern [55][56]. Ultimately the balance between these two damage mechanisms will depend on the tissue samples and experimental conditions. This balance might be even more delicate to adjust when moving to higher infrared wavelengths. This will be discussed in more details in the chapter on three-photon microscopy.

1.2.6 Multiphoton microscopy in neurobiology

Multiphoton microscopy, more specifically two-photon excited fluorescence microscopy has been extensively used in neurobiology, almost exclusively for *in vivo* imaging of rodent brains (refer to [57] [58] for reviews). Some notable applications, among several others, include calcium or voltage imaging to measure neural activity *in vivo* [59][60], live dendritic and spine imaging to monitor synaptic plasticity *in situ* [61], live monitoring of oxygen and blood flow [62] and the combination of two-photon imaging and two-photon neurotransmitter photolysis [63] or optogenetic activation [64]. Nevertheless, there has been a recent regain of interest for using multiphoton microscopy in *ex vivo* contexts, in particular for large volume neuroanatomy [6][65].

1.3 Multicolor labeling strategies

The discovery of the green fluorescent protein (GFP) [66] from the jellyfish *Aequorea victoria* and most importantly its capability to be genetically targeted into living organisms and expressed as an internal fluorescence indicator has completely revolutionized the life sciences at the beginning of the century. The breakthrough was recognized by a Nobel prize in 2008 (Shimomura, Chalfie and Tsien), further celebrating and confirming the role of optics and microscopy in the biosciences. In the last two decades, outstanding efforts in site-directed mutagenesis and protein engineering have resulted in a large palette of fluorescent proteins (FPs) available, with variable excitation and emission spectra, and variable brightness and photophysical properties [67][68][69].
Expressing and detecting multiple FPs in biological tissues enables to substantially increase the information throughput from a given sample. In particular, it provides the opportunity to visualize different cell populations or cell compartments and analyse their interactions. A first approach to multicolor labeling is to individually express multiple fluorophores, each one directly adressed to a given cell type or subcellular compartment. Such labeling approaches are particularly powerful to reveal the organization and development of complex biological tissues [70][71]. However, given the very high cellular density in the mammalian brain, such approaches are limited because of the restricted number of independently detectable colors: the overlap of emission and excitation spectra of common fluorophores limits the number of simultaneously and independently detectable labels (<5), especially when imaging with two-photon microscopy as fluorescence excitation spectra are usually broader than their one-photon counterparts. Spectrally-

resolved approaches [72][73] combined with post-processing unmixing strategies [74][75] can extend this palette to few more labels, however still not sufficient for applications such as individual axon tracing or clonal fate mapping in dense cellular networks. The other alternative for multicolor labeling is to use a stochastic and combinatorial FP expression as in Brainbow [76]. The latter approach will be the main focus of this section.

1.3.1 Genetic and molecular tools for fluorescence labeling

Prior to presenting multicolor labeling strategies, we will first briefly introduce the basic principles of some commonly used methods for labeling neural cell populations in the brain, mainly insisting on the pros and cons of each technique relative to the biological and/or practical context. These considerations were central when designing experiments with our neurobiologist collaborators.

1.3.1.1 Transgenic lines

Transgenic lines expressing a fluorescent protein under the control of a given promoter are widely used in systems biology for labeling cell populations of interest. The first useful transgenic mice for neuroscience have been Thy1-XFP lines [77] because of high expression in neurons but also sparsness due to stochastic silencing of the transgene. For stronger and more specific expression, Cre/Lox site-specific recombination [78] or other similar two-component technologies (Flp/Frt, UAS/Gal4, etc.) is extensively used: animals expressing the recombinase under usually a cell-type or region-specific promoter are crossed with animals expressing the FP reporter (usually under a strong ubiquitous reporter). Upon recombinase action, the reporter is expressed in the area or cell type of interest. Furthermore, drug-inducible forms of Cre (CreER) can be used to control the sparsness of the labeling. While this strategy is the method of choice for targeted and specific labeling, *de novo* generation of a transgenic line is a heavy procedure, especially when working on murine models. Transgenic mouse lines typically take months to generate and require substantial breeding effort and cost to maintain.

1.3.1.2 *In utero* electroporation

Historically developed for chick samples, in utero electroporation has been extensively used in the last decade to label and/or to modulate gene expression in mouse brain neural progenitors in neurodevelopmental studies [79][80][81]). The procedure consists in injecting plasmid DNA onto the embryonic mouse brain using electrical pulses which transiently disrupt the plasma membrane and force DNA into the cells. The DNA is then inherited in cells born from the electroporated progenitors, where it is expressed. Hence this approach allows precise temporal "birth-dated" labeling in addition to spatial control. However the labeling with such an approach is both focal (i.e spatially-restricted) and sparse as it is particularly challenging to achieve dense

widespread labeling with this technique. For cortical labeling, a subset of neural progenitors can be targeted in the lateral ventricles. Cell-type specificity can be achieved to a certain extent by targeting progenitor zones giving birth to different neural types and by controlling the electroporation timing based on the neurodevelopmental schedule.

1.3.1.3 Virus-mediated labeling

Viral-mediated labeling is based on using the particularly robust capability of viruses to infect and deliver genetic material onto the cells of interest, by literally hijacking the host cell machinery. Two types of viruses have been used in neurobiology: genome integrative viruses (retro/lentiviral vectors) to study lineage during development and non integrative viruses which have been broadly used in systems neuroscience. One of the most commonly used viruses for circuit mapping, functional imaging and manipulation is the recombinant adeno-associated virus (rAAV, see [82], [83]). The virus family and serotype determines the nature of the transfected cells. Most AAV serotypes efficiently transduce post-mitotic cells such as neurons while some serotypes can transduce glial cells. AAVs are usually delivered via intracranial site-directed injections. The spatial location of the injection can be precisely controlled by using the atlas stereotaxic coordinates. Recently, efficient systemic intravenous delivery has also been demonstrated, overcoming the challenge of crossing the blood brain barrier [84]. Fluorescent labels are robustly expressed few weeks (3-6) after the viral delivery. Viral labeling is therefore a fast and versatile means to label specific cell populations in adult murine and non human primate brains. Sophisticated labeling strategies can be implemented for highly specific cell-type labeling by combining Cre transgenic lines and Cre-dependent AAVs to allow genetic dissection and manipulation of neural circuits [85]. AAV labeling has also been used in high throughput mesoscale connectomic efforts [86]. AAV labels are nevertheless episomal, making them poorly suited for lineage tracing. Another limitation of viral labeling is the restricted size of the deliverable genetic material (few kilobases). Virus-mediated labeling remains nonetheless a flexible way for labeling cells in a spatially restricted manner, within reasonable experimental time frames.

1.3.2 The Brainbow technology

The Brainbow strategy [76] is a labeling technique based on the Cre/Lox recombination system which achieves stochastic and combinatorial multicolor labeling. The technology was developed by Jean Livet and colleagues at Harvard University in 2007. For extensive reviews on the technology, see [87][88][89][90].

The principles of Brainbow are presented in Figure 1.11. A Brainbow transgene contains two or more incompatible pairs of Lox sites, so that upon Cre-mediated recombination stochastic events of DNA excision (or inversion) occur, leading to different possible expression outcomes. In the Brainbow 1.0 construct, two incompatible variants of LoxP sites are used, Lox2272 and LoxN : without exposure to Cre recombinase, the default expression is red but Cre-mediated

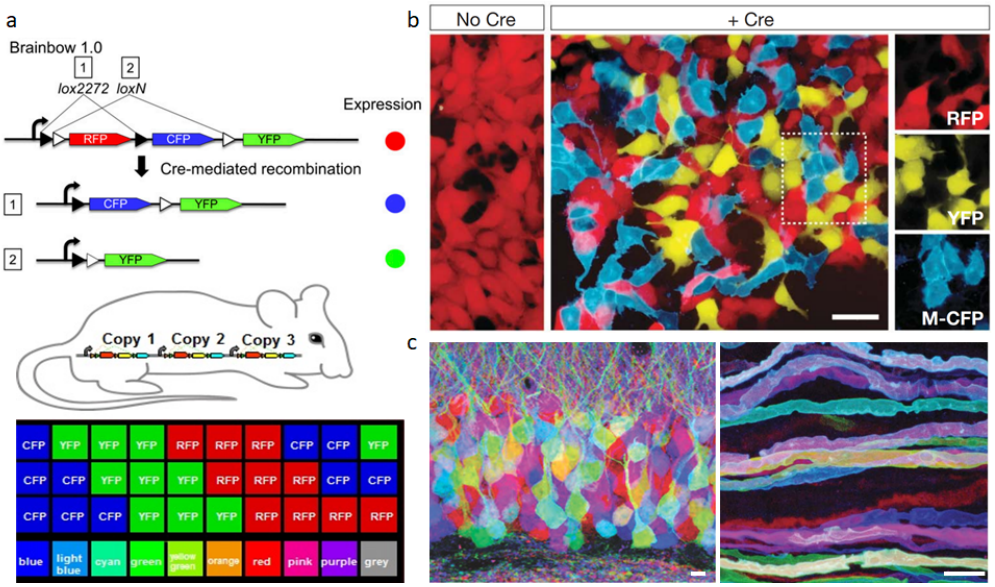

FIGURE 1.11. Brainbow strategy. (a) Top: Original Brainbow 1.0 construct with two incompatible lox sites. Red is expressed by default, and blue and green are stochastically expressed upon recombination. Bottom: Example of combinatorial FP expression with three copies of the Brainbow transgene. (b) HEK cells stably transfected with CMV-Brainbow-1.0 express RFP. On transient transfection with Cre, these cells randomly switch to YFP or M-CFP expression. Scale bar: 50 µm. (c) Combinatorial multi-copy Brainbow labeling of hippocampal neurons in the dentate gyrus (left) and of oculomotor axons (right). Scale bars: 10 µm. Adapted from [76].

excision stochastically generates two novel possible outcomes i.e green or blue expression. Hence, one Brainbow transgene copy leads to mutually exclusive red, green or blue labeling. However, the coexpression of multiple Brainbow copies leads to combinatorial expression of the FPs thus significantly extending the color possibilities. Such situation of multiple copies is a common outcome of the transgenesis process. Since the process is stochastic, each cell expresses a random combination of red, green and blue fluorescent proteins resulting in an individual color tag for each cell. Figure 1.11c shows densely packed neurons from the dentate gyrus in the hippocampus and axons from an oculomotor nerve labeled with Brainbow. The Brainbow approach is a powerful multicolor strategy to study complex tissues such as the brain for the following reasons: (i) it allows to spatially single out individual cells among densely packed ensembles of cells, either of similar or different type, (ii) it significantly increases the number of detectable colors which is no more limited by the number of independent detection channels, and importantly, (iii) it opens the way to ratiometric and quantitative multicolor imaging. Finally, to obtain Brainbow expression in the mouse brain, Brainbow constructs are expressed under a pre-defined promoter (Thy1 for instance for neuronal expression or CAG for ubiquitous expression). These Brainbow lines need then to be crossed with either a Cre- or a CreER-expressing line. In the latter case,

Cre expression is chemically inducible via tamoxifen injection which gives more control both on the timing and degree of recombination.
Brainbow has been originally developped for the mouse brain. However, since its release in 2007, the technology has been adapted to many other tissues (intestinal epithelium homeostasis [91], heart [92], hemapoetic stem cells (HSCs) [93], epithelial wing disk [94]) and species (Flybow [95], Drosophila Brainbow [96], Zebrabow [97] among others). Technical improvements of the original Brainbow designs have also been introduced, to improve the color expression balance [98][99], the ubiquity of expression [91][100], and to make it compatible with more versatile transgenic delivery methods (AAV Brainbow [98], *in utero/in ovo* electroporation [99]). Derived Brainbow labeling strategies are still actively being developed by the team of Jean Livet, and by others. In order to give an overview of the potential of multicolor strategies in neurobiology and beyond, we will present in the following sections developments in multicolor labeling in the light of two of the most promising applications of the technology: lineage tracing and neuroanatomical/connectivity studies.

1.3.3 Multicolor strategies for lineage tracing

1.3.3.1 Why multicolor labeling for lineage tracing ?

Lineage tracing is an approach that aims at reconstructing the cellular ancestry, with different degrees of precision, of a complex tissue, organ or organism. From the neurobiology perspective, unraveling neural lineages is fundamental to understanding the development of complex cellular patterns and arrangements underlying function and behavior. For extensive reviews on lineage tracing technologies, refer to [101][102][103]. In the current landscape of lineage tracing techniques, there are mainly three different approaches: (i) Live-cell tracking in living organisms, (ii) permanent labeling strategies followed by post'hoc *ex vivo* imaging or chronical live-cell tracking, and finally (iii) DNA/RNA barcoding methods which consists in tracking low frequency mutations within a tissue or organism cell population. This last approach is a powerful approach to expand the scope and scale of lineage tracing to entire organisms, taking advantage of the steep technological improvement of single-cell sequencing and genetic manipulation tools [104][105][106]. Another strength of barcoding approaches is that, within the current state of the art, it is the only method compatible with the study of human tissues: rare somatic mutations can be harnessed rather than engineered genetic barcodes to reconstruct lineages in normal and diseased human tissues [107][108]. However, these approaches require tissue disruption, hence do not preserve information on cellular morphologies and relative spatial arrangement. On the other hand, live-cell tracking in living organisms provides the opportunity to follow individual cell fates with high spatio-temporal resolution [36]. These approaches are ultimately limited by the number of cells that can be effectively tracked, although light-sheet microscopy approaches have opened the possibility of in toto imaging of entire organisms during development with single-cell resolution [19][109]. These methods can however not be applied to follow mammalian

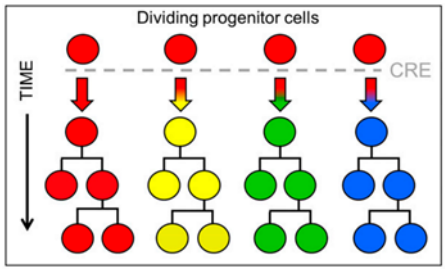

FIGURE 1.12. Principle of multicolor lineage analysis with Brainbow. Adapted from [87].

development *in utero* or at postnatal stages. To study mouse brain development, the last category based on high-content labeling is hence the preferred approach.

Stochastic multicolor labeling is particularly powerful for lineage studies because of three main reasons: (i) it alleviates the need to use very sparse labeling which is indispensable in monochrome lineage analyses. Therefore multiple clones can be traced within the same tissue without compromising the precision of the mapping; consequently, (ii) it provides clonal precision i.e the possibility to trace cell fate at the individual progenitor level and (iii) it allows one to map and characterize intermingled clonal cohorts. In this section, we will go through the main multicolor strategies developed for lineage tracing, with a particular emphasis on the MAGIC markers strategy which was used in our work.

1.3.3.2 The MAGIC markers strategy

The MAGIC (Multi-Adressable Genome-Integrative Color) markers labeling approach is a strategy for multicolor clonal labeling. It has been developed in the team of Jean Livet at Institut de la Vision.

One of a stringent requirements of a labeling strategy for tracing cell lineage is its capacity to robustly be transmitted to the descent. To achieve genome integration of Brainbow labels, Loulier and colleagues [99] framed the Cre/Lox Brainbow transgene by vertebrate transposon sequences (Tol2 or Piggybac) at both 5' and 3' extremities, hence enabling a direct chromosomal insertion (Fig 1.13). Two-photon live time-lapse multicolor imaging on electroporated embryonic chick sample demonstrated color-preservation between a cell and its daughter-cell upon division. The authors further confirmed this property by imaging streams of clonally-related cells in electroporated embryonic chick spinal cord and retina (Fig 1.14). The compatibility of this tool with *in utero* or *in ovo* electroporation allows more spatio-temporal control of the labeling for increased specificity, as well as more versatility for use across multiple species.

Furthermore, Loulier et al demonstrated subcellular compartmented adressing of the color labels. One of the main limitation of multicolor clonal labeling is that the number of discernable clones is limited by the number of color combinations. Hence compartmented adressing is a powerful

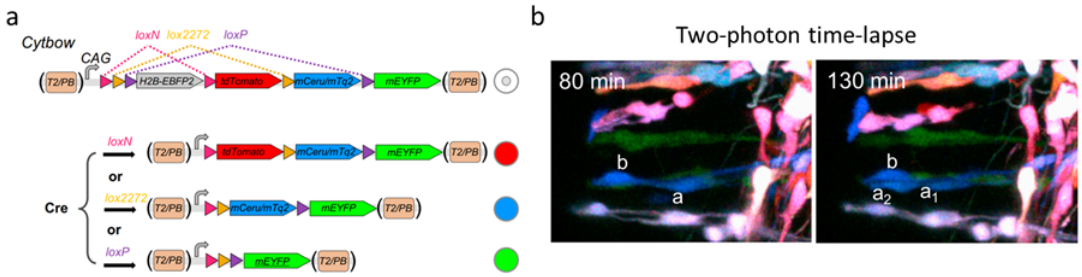

FIGURE 1.13. The MAGIC marker strategy to label individual clones. (a) Cytoplasmic MAGIC marker transgene Cytbow. Default ubiquitous nuclear EBFP2 expression ensures improved color balance upon Cre recombination. Transposons (T2/PB) ensure genome integration.(b) Time-lapse of a E4 chick embryo neural tube section electroporated at E2. Adapted from [99].

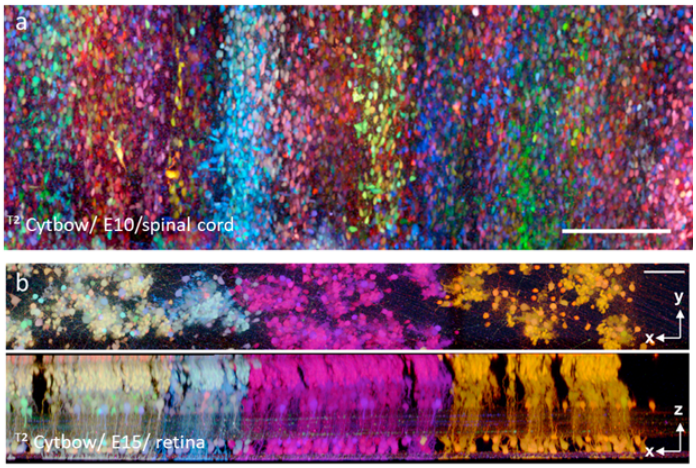

FIGURE 1.14. Radially oriented streams of clonally related cells in chick embryonic tissues: spinal cord (a) and retina (b).Scale bars: 100 µm. Adapted from [99].

approach to push back this limitiation by nonlinearly expanding the number of color codes through a 'double-Brainbow' targeting (example: nuclear + cytoplasmic labeling Nucbow/Cytbow (Fig 1.15).

1.3.3.3 Other multicolor strategies for cell fate mapping

Other strategies derived from Brainbow have been developed for lineage tracing purposes. These strategies are summarized in Table 1.1. Brainbow 1.0, 1.1 and 2.1 transgenes have been knocked into a Rosa26 locus for ubiquitous expression, and further expressed under an ubiquitous promoter for a stronger expression [100][91]: these *Rainbow* and *Confetti* lines have been used in a series of studies characterizing tissue homeostasis and regeneration in epithelial tissues, notably to demonstrate a drift towards monoclonality in the mouse intestinal crypt [91], or to

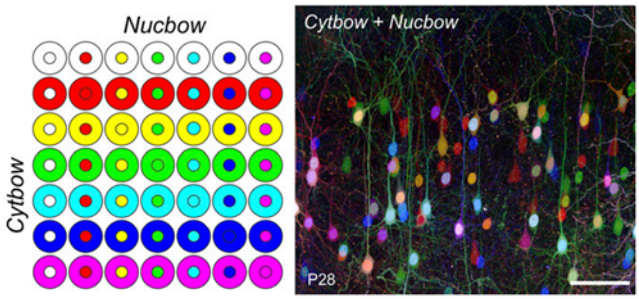

FIGURE 1.15. Dual-compartment Brainbow targeting increases the possible color combinations. Scale bar: 100 µm. Adapted from [99].

characterize clonal patterns during fingertip and tip-toe regeneration after mouse limb injury [110]. For an extensive review of related studies, refer to [117]. Rainbow lines have also been used to study early blastomere cell fates [100]. Recently, a very elegant study crossed a Confetti line with a Cx3cr1CreER line to achieve specific labeling of microglia in the mouse brain, enabling thus analysis of microglia self-renewal and clonal expansion during steady-state and disease [111].

Lentiviral vectors have also been harnessed for individual clonal tracking [93]. This approach relies on the random integration of viral vectors to achieve combinatorial expression of multiple FPs. While this approach presents the advantage of versatility, it however needs to be crossed with RNA barcoding to achieve rigorous clonal identification [118][119]. Lentiviruses can also be combined with the Cre/Lox system, as demonstrated in a recent study (pLenti multicolor) which monitored clonal dynamics of a pancreatic tumor xenograft [113].

Similarly to MAGIC markers, other strategies relying on transposons and *in utero* electroporation have been demonstrated (StarTrack [115], CLoNe [114]). Finally, multicolor cell fate mapping methods have also been adapted to zebrafish ([97] and drosophila [116]).

In this context however, two comments need to be made at this stage: (i) Almost all multicolor-based lineage studies reported so far concern non cerebral/nervous tissues, mostly 2D epithelia and (ii) all these studies have been performed on limited tissue volumes.

1.3.4 Multicolor strategies for connectivity and neuroanatomical studies

1.3.4.1 Why multicolor labeling for neuroanatomy ?

Golgi staining is the first labeling technique that significantly expanded our knowledge of the structure of the brain at the cellular level [120]. It consists in impregnating fixed nervous tissue with potassium dichromate and silver nitrate. The power of the technique stems from the fact that (i) it labels neuronal cells in their entirety (soma, axons and dendrites) and importantly, (ii) it targets only a sparse ensemble of neurons. The latter property is of crucial importance to enable anatomical tracing and morphometry in a highly complex and dense tissue such as the

brain. Within the years, with the advent of fluorescence microscopy and viral tracers, these tools have been extensively used for circuit mapping and neuroanatomy. These approaches however also require highly sparse labeling, therefore identifying multiple single neuronal morphologies in their highly complex environment with current monochrome fluorescent light microscopy approaches has remained outstandingly challenging. This challenge was not restricted to neuronal connectomics : high-throughput glioanatomical maps also remain difficult to produce given the density and complexity of the neural environment. Therefore Brainbow, with its capability of uniquely color tagging individual cells provides an excellent opportunity to reconstruct morphologies in densely-packed cellular environments, to follow unambiguously intermingled axons and to study spatial relationships between neighboring cells. The following section presents a brief overview of the neuroanatomical studies realized so far using Brainbow.

1.3.4.2 Multicolor strategies for connectivity and neuroanatomical studies

Brainbow strategies have been used so far in a couple of neuroanatomical studies in the past decade, both in the central and peripheral central nervous systems. It has been used to characterize glial morphology and innervation of sensory projections: Wang and colleagues used multicolor labeling to analyze the morphology of Müller glial cells in the mouse retina and found that these cells occupy distinct exclusive territories with few overlap ([121], Figure 1.16), Dumas et.al used Brainbow to analyze oligodendrocyte morphology and possible interactions, suggesting that two oligodendrocytes can simultaneously interact at multiple Ranvier nodes [123], and Zaidi et. al color-labeled mouse gustatory ganglion somata to visualize and characterize taste bud innervation by nerve fibers [124]. Brainbow has also been used to study the plasticity of neural projections during development [122]: the lamination of retinal ganglion cells (RGCs) axons and the spatial rearrangements of their arbors have been characterized in the developing zebrafish tectum (Fig 1.16). Another study have elegantly correlated Brainbow imaging in the mouse brain and electron microscopy to study the convergence of RGCs onto relay cells of the dorsal lateral geniculate nucleus (dLGN), a thalamic nucleus of the visual pathway, hence re-evaluating some previous hypotheses on RGC innervations in the dLGN [125]. Last but not least, few studies have attempted partial or complete circuit tracing using Brainbow: in the original Brainbow paper Livet, Lichtman and colleagues demonstrated 3D reconstruction of an ensemble of 341 cerebellar axons and 93 granule cells contained in a 160 $\mu m^2 \times 65$ µm volume. However, despite the growing toolbox of multicolor virus labels increasingly optimized for circuit tracing [98][84][126], mesoscale connectivity using Brainbow has sill not yet been demonstrated in a CNS system. More generally, color-based neuroanatomical studies have until now been restricted to limited tissue volumes.

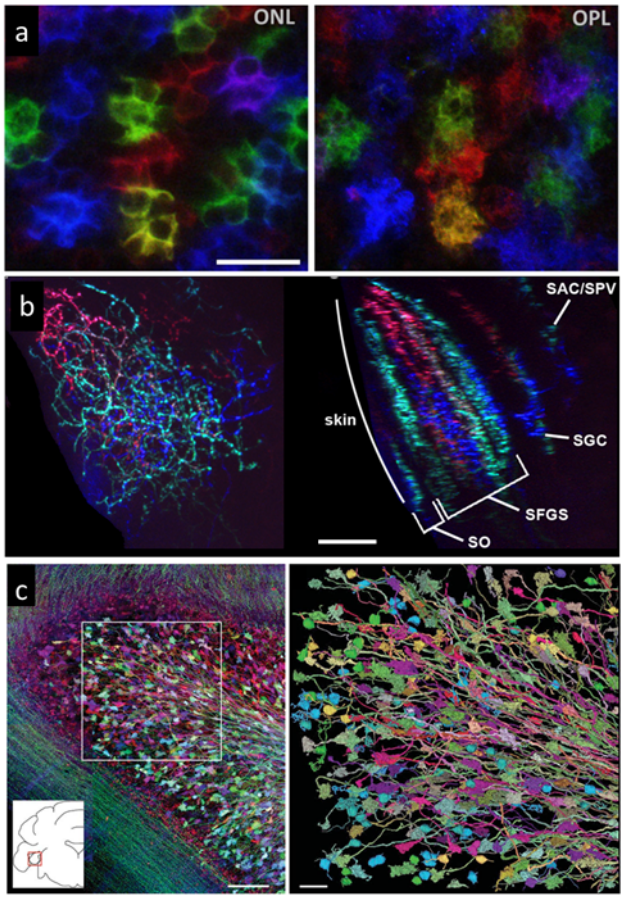

FIGURE 1.16. Examples of Brainbow applications to neuroanatomy. (a) Brainbow-labelled Müller glial cells in the retina in two different retinal layers (ONL: outer nuclear layer, INL: inner nuclear layer) occupy spatially distinct non-overlapping territories. Scale bar: 20 µm. Adapted from [121]. (b) Brainbow labeling of zebrafish tectum. Dorsal view (left) shows axonal arbors while the side view (right) highlights a lamination pattern. Scale bar: 20 µm. Adapted from [122]. (c) Left: Brainbow-labeled cerebellar flocculus. Right: Three-dimensional digital reconstruction of region boxed in the left panel, comprising 341 axons and 93 granule cells within a 160 µm ×160 µm ×65 µm tissue volume. Adapted from [76]. Scale bars: 50 µm.

1.4 Multicolor multiphoton microscopy

Given the robust performances of multiphoton microscopy to obtain single-cell resolution images relatively deep within scattering tissues, microscopists have sought to develop nonlinear optical strategies to target multiple fluorophores within the same sample in order to benefit from the increasingly sophisticated multicolor labeling tools being developed for high-content imaging of complex biological environments. Here we will focus mostly on strategies for multicolor two-photon excitation. Multicolor three-photon imaging will be addressed in the last chapter of this thesis.

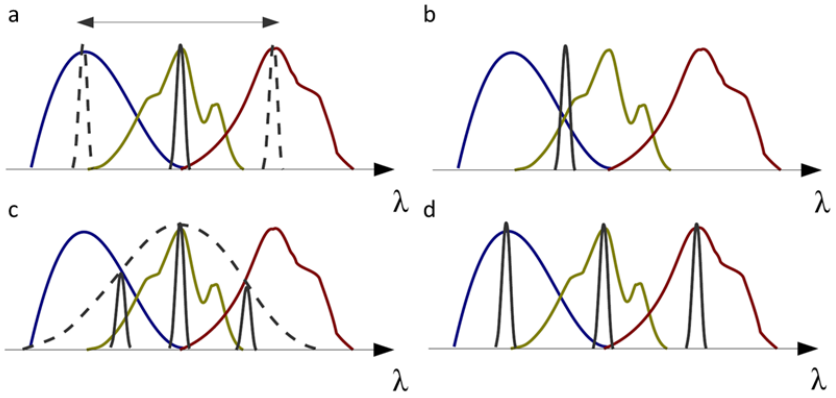

FIGURE 1.17. Multicolor nonlinear strategies. (a) Sequential excitation of different fluorophores using a tunable femtosecond laser. (b) Simultaneous excitation of fluorophores with overlapping spectra at a 'trade-off' wavelength. (c) Simultaneous targeting of multiple fluorophores using a broadband shaped pulse. (d) Simultaneous targeting of three fluorophores using three independent laser outputs. Adapted from [127].

1.4.1 Strategies for multicolor nonlinear microscopy

The first and most straightforward way to achieve multicolor two-photon imaging is to perform sequential excitation at multiple excitation wavelengths (Figure 1.17). Indeed, Ti:Sa lasers, which are the most commonly used laser sources for two-photon microscopy, offer a large spectral range for tunability, typically from ~680 nm to ~1300 nm hence potentially allowing excitation of almost all fluorophores used in light fluorescence microscopy from the UV range up to the far-red, albeit with a reduced available power at the edges of the tunability range. However such an approach is not optimal for live and/or ratiometric imaging as it might be subject to motion blur and channel misalignment in the case of dynamic samples. In the case of large-scale acquisitions with extended acquisition times (1 day to 1 week), sequential acquisition of multiple channel images substantially increases the acquisition time.

A second approach to achieve nonlinear multicolor excitation is to take advantage of the large overlapping 2P excitation spectra of most of the commonly used fluorophores: dual-color excitation can be obtained by selecting an optimal 'trade-off' wavelength intersecting two fluorophore spectra. However, this 'trade-off' wavelength is usually optimal for neither of the targeted fluorophores. Besides, there is no independent control over each beam, making such an approach not adapted to image samples where fluorophores are expressed in different concentrations. Another approach, also taking advantage of the large and overlapping 2P spectra is the use of spectrally broadened pulses [128][129]. However, such pulse-shaping based strategies require high pulse energies to be spread across multiple excitation wavelengths and maintaining robust amplitude and phase patterns at the sample plane can be difficult in practice. Besides, chromatic aberration correction

in such a configuration is particularly challenging.
Finally, trichromatic simultaneous excitation can be achieved using laser outputs at three separate wavelengths (Fig 1.17). Such a strategy has been implemented using self-soliton frequency shift (SSFS) in optical fibers [130]: a first design has been proposed in 2012 by the team led by Chris Xu at Cornell University where SSFS is performed to obtain 1728 nm and 1900 nm pulsed from an upstream 1550 nm pump laser. These three outputs are then frequency-doubled using SHG crystals to obtain 3 outputs tailored for CFP, YFP and RFP excitation [131]. A similar approach has recently been introduced starting instead with a 1030 nm pump laser and both blue-shifting and red-shifting the pump laser pulses to obtain outputs at 0.6 µm-0.8µm and 1.2 µm-1.4 µm [132]. However this design does not provide independent power control over the three beams and yield relatively low energy pulses thus significantly increasing the imaging time (several accumulations necessary). Another SSFS-based design of a multi-wavelength fibered source has been recently proposed, offering more wavelength tunability with the use of a pulse-splitting scheme [133], but yet with no immediate independent power control of each beam. While the design and commercialization of robust turn-key multi-wavelength femtosecond fiber lasers will certainly facilitate wide adoption of multicolor multiphoton microscopy in neuroscience laboratories, more technological developments are still needed to achieve efficient ratiometric two-photon multicolor excitation. The most optimal way to do so in the current state of the art is to use bulk femtosecond laser sources. However using three femtosecond outputs might present a heavy financial cost and require complex setup arrangement. To circumvent this, a strategy based on nonlinear wavelength-mixing [134] and achieving trichromatic excitation through a single Ti:Sa/OPO chain has been developed at the Laboratory of Optics and Biosciences during the PhD of Pierre Mahou [127]. This method will be presented in more details in the next section.

1.4.2 Multicolor two-photon microscopy using wavelength-mixing

The method relies on the temporal and spatial overlap of two synchronous pulse trains, for instance from a Ti:sapphire laser and a downstream OPO. Temporal synchronization of the two pulses is achieved using an optical delay line. The two beams are then recombined using a dichroic mirror and spatially co-aligned onto a two-photon microscope (Fig 1.18). These excitation scheme hence achieves simultaneous 'regular' two-photon excitation from the Ti:S and the OPO beams along with a third 'virtual' excitation at an intermediate wavelength through a two-color two-photon (2c-2P) process. In this process, a photon is absorbed from each if the two initial beams, therefore providing virtual excitation at $\omega = \omega_1 + \omega_2$, corresponding to a wavelength of $\lambda = 2\,\lambda_1\lambda_2 \backslash (\lambda_1+\lambda_2)$. Typically, with a (850 nm, 1100 nm) couple of wavelengths, this strategy can be used to simultaneously excite blue fluorophores (ex: CFP, mTurquoise2), red fluorophores (ex: dTomato, mCherry) and yellow-green fluorophores (EYFP). Fig 1.18c shows an example of trichromatic excitation of HEK cells expressing mutually exclusive labeling of CFP, YFP and RFP. The wavelength-mixing scheme is particularly adapted to image Brainbow samples

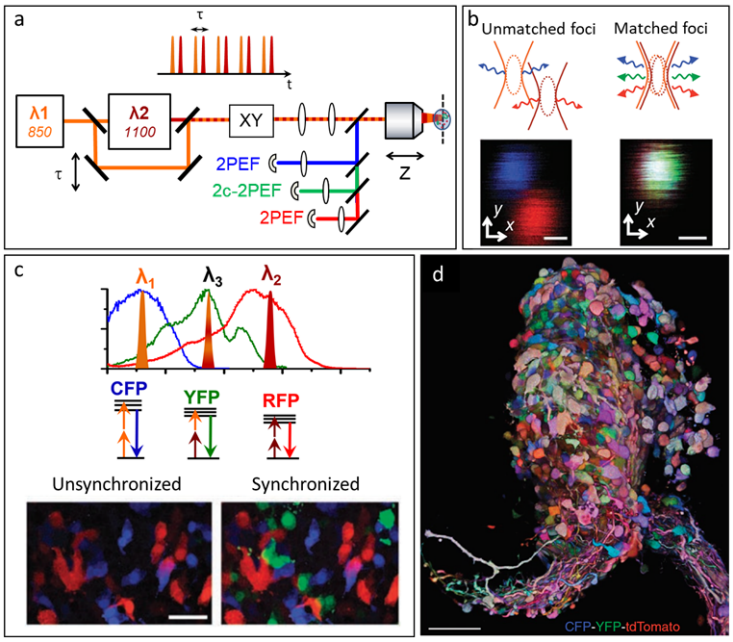

FIGURE 1.18. Multicolor 2P microscopy using wavelength-mixing. (a) Wavelength-mixing optical setup. Synchronous pulse trains from an OPO and its Ti:Sapphire laser pump are temporally synchronized using an optical delay line and spatially coaligned in the microscope. (b) The wavelength-mixing process occurs only if the two foci remain spatially overlapped. Scale bar: 0.5 µm. (c) Top: the wavelength-mixing scheme yields 2P excitation from the Ti:S and the OPO pulses (blue and red respectively) along with a 'virtual' green excitation via 2c-2P. Bottom: CFP, YFP and RFP labeled HEK cells imaged with unsychronized and synchronized pulses. Scale bar: 50 µm. (d) Multicolor 2P imaging of a live Brainbow-labeled embryonic chick spinal tissue (E3.5) using wavelength-mixing. Scale bar: 50 µm. Adapted from [134].

expressing differential ratios of blue, green and red FPs. Notably, wavelength-mixing presents several advantages as a multicolor imaging design:

(i) Fluorophores over an extended spectral range can be targeted efficiently and independently. The design is compatible with multiple FP combinations.

(ii) Independent power control of each spectral channel makes it particularly adapted to imaging samples where fluorophores are expressed in different concentrations [134][135].

(iv) Channel registration at the voxel level is intrinsically provided by the method, making it uniquely suited for fast and/or ratiometric measurement.

(v) It is fundamentally a two-photon imaging scheme scattering, hence particularly adapted for imaging scattering tissues such as the brain.

Furthermore, this technology is decidedly flexible and adaptable in a variety of imaging schemes and multimodal contexts: light-sheet configuration [136], fluorescence lifetime (FLIM) imaging

[135], and it can be combined with simultaneously acquired coherent contrasts [137][135][134]. It can also be used with other laser configurations/wavelengths [138][139], and combined with algorithmic procedures to increase the number of resolvable colors in non combinatorial schemes [74].

1.5 Challenges and aims

In the last decade, powerful genetic and molecular tools have been developed to enable multicolor labeling of cell populations of interest with high specificity and individual cell resolution. These technologies, by enabling specific labeling with individual cell resolution, present an outstanding potential to understand brain development, structure and ultimately function in health and disease. However, because of the lack of suitable imaging methods allowing high-resolution aberration-free multicolor imaging throughout large volumes of tissue, these strategies have not been able yet to reach their full potential. Reciprocally, the last five years have witnessed an outburst of large-scale microscopy techniques allowing to achieve cellular/sub-cellular resolution imaging throughout large volumes of intact tissues or hundreds of microns deeper i*n vivo*, but these have so far been restricted to monochrome or dual-color approaches. Our aim in this PhD work is to augment the contrast capabilities of these latter technologies in order to achieve high-content multicolor/multimodal imaging upon larger scales and depths.

Technique	Description	Delivery	Species	References
Confetti	Brainbow 2.1, locus R26 CAG promoter	Transgenic line	Mouse	[91]
Rainbow	4 color Brainbow, locus R26, CAG promoter ⊗ actin CreER	Transgenic line	Mouse	[110]
Rainbow3	CAGGS promoter upstream Brainbow 1.0	Transgenic line	Mouse	[100]
Microfetti	Confetti ⊗ Cx3cr1CreER	Transgenic line	Mouse	[111]
LeGO	Combinatorial RGB	Virus transfection	Mouse	[93][112]
pLenti multicolor	Cre/Lox lentiviral system	Virus transfection	Mouse (xenograft)	[113]
MAGIC	Tol2/PB + Brainbow	Electroporation	Mouse, Chick	[99]
CLoNe	Tol2/PB + Brainbow	Electroporation		[114]
StarTrack	Combinatorial RGB	Electroporation	Mouse, Chick	[115]
Zebrabow	Gal-4 inducible Brainbow lines	Transgenic line	Zebrafish	[97]
TIE-DYE	Multivector Brainbow + genetic manipulation	Transgenic line	Drosophila	[116]

Table 1.1: Multicolor strategies for lineage and clonal analysis.

CHAPTER 2

CHROM-SMP: PRINCIPLES AND IMPLEMENTATION

Large volume microscopy techniques, either based on tissue clarification or synchronized automated tissue slicing, are emerging as powerful new imaging modalities opening the way to truly system-level neurobiological studies. However, these large-scale techniques lack efficient spectral contrast modalities and are essentially producing monochrome datasets so far. Here, we introduce chromatic serial multiphoton microscopy (Chrom-SMP), a novel imaging method combining microtome-assisted synchronized tissue slicing and wavelength-mixing, enabling to generate datasets of mm^3 to cm^3 volume size with extended color and contrast possibilities, while mitigating chromatic aberration. In this chapter, we first review the state of the art of automated histology approaches and outline how Chrom-SMP integrates in this landscape. Next, we describe the design and implementation of the Chrom-SMP pipeline, covering instrument engineering as well as tissue and data processing. Finally, we demonstrate proof of principle acquisitions of brain-wide multicontrast datasets.

2.1 Block-face and microtome-assisted large volume light microscopy approaches: state of the art

Block-face acquisition schemes have profoundly transformed neuroanatomical imaging in the past decade. These approaches rely on alternating cycles of en-face imaging of a tissue block and removal of superficial tissue, and consequently have the potential to considerably expand the accessible imaged volume of any given microscopy technique that relies on epi-illumination and detection. They inherently require accompanying reconstruction methods for 3D assembly of the imaged volume. Importantly, as we will illustrate throughout this thesis work, these methods generate substantial amounts of data and are therefore bringing new challenges in terms of data

storage, processing and mining/analysis.

The brain is formed by an ensemble of densely connected neurons organized as units and acting in a network fashion to produce complex behaviors. Understanding the structural and functional basis of this network architecture has been a long-standing goal in neuroscience. Connectomics refers to the anatomical connectivity studies aiming to reveal this network architecture [140]. Connectomic descriptions of the brain span multiple scales: at the macro-scale level, fiber tracts are reconstructed and their inter-areal organisation revealed with up to millimetric resolution over cm^3 sized brains, including large primate brains, using non-invasive magnetic resonance imaging (MRI) based techniques such as diffusion tensor imaging (DTI) [141]. On the other hand, micro-scale connectomics reconstructs connectivity with nano-scale resolution at the level of individual synapses using essentially electron microscopy approaches [142][143]. Between these two scales, mesoscale connectomics focuses on circuit-level analyses and inter-areal long-range projections with cellular micron-scale resolution [86][144][145][146][147]. Both micro- and meso-scale connectomics are based upon ex vivo anatomical reconstructions which largely rely on technological developments in automated histological methods [148]. Block-face imaging indeed represents the building block of most electron microscopy based micro-scale connectomics [149]. Similarly, this approach is also becoming central in meso-scale brain mapping efforts [86]. In this section, we will review the current state of the art of slicing-based large volume light microscopy techniques and present our motivations in developing chromatic serial multiphoton microscopy.

2.1.1 Initial efforts

Serial Histology methods are the basis of many neuroanatomical studies and were extensively used to build whole brain atlases in multiple species [150][151]. Traditional histology usually involves tissue slicing, labeling, mounting and imaging of each individual slice. The process is therefore intrinsically slow and labor-intensive. Furthermore, accurate submicron registration of manually acquired serial slices is challenging if not impossible because of inevitable tissue deformation/distorsion. In addition, serial 2D histology does not allow continuous 3D reconstruction of cellular structures over large volumes because of unavoidable tissue loss between sections. In an attempt to further automate histology, block-face histology has first emerged in the form of cryomacrotomes [152], which were used to produce a human brain atlas with self-registered sections and higher resolution than MRI-based atlases. However this early method did not provide micron-scale resolution, was hardly applicable to continuous 3D imaging and necessitated working with frozen samples. The first setup aiming at continuous block-face volumetric imaging of fluorescently-labeled samples was demonstrated in the early 2000's and was based on all-optical sectioning/imaging cycles [153]: 1 to 10 nJ fs pulses at 800 nm were used to ablate series of stacked superficial tissue layers of ~10 µm, then 2P imaging was done using 120 fs Ti:Sa pulses. However, this approach has never been pushed beyond the proof of

concept, probably because of the inevitable tissue damage provoked by laser ablation, preventing reconstruction of intact tissue volumes. In 2007, another approach combining multiphoton microscopy and tissue sectioning was introduced by T. Ragan, P. So and colleagues under the name "two-photon cytometry" with an illustrative demonstration on mouse heart tissue [154]. The setup consisted of a high-speed two-photon setup based either on a fast polygonal scanner or a multifoci configuration combined with a micromilling machine. However their approach required harsh tissue processing not compatible with most fluorophores. Since these first optical block-face implementations were not yet mature for high-resolution fluorescence imaging of neuronal structures, initial neuroanatomical studies over hundreds of microns depth have started using vibratome tissue sections serially imaged with a confocal microscope [155][156][157]. This approach however suffers the same caveats as traditional serial histology methods, i.e partial tissue loss and tissue distorsion often requiring tedious manual registration procedures.
It was not until the early 2010's that game changing technologies allowing high-thoughput high-resolution whole-brain imaging were introduced [158][6], using instruments that combine serial sectioning with wide-field illumination or with two-photon imaging. Implementations of these two strategies will be presented in more details in the following sections.

2.1.2 Wide-field approaches: MOST, fMOST and WVT

These approaches have been pioneered and continue to be actively developed by the laboratory of Qingming Luo at HUST (Wuhan, China). Micro-optical sectioning tomography (MOST) [158] was the first technology to provide whole mouse brain imaging with micrometer-scale resolution. The sample is embedded in a plastic resin and stage-scanned in the X direction while a diamond knife placed on top slices tissue ribbons (450 µm large, 1 µm thick, cf. Fig 2.1a). Bright-field imaging is performed synchronously with slicing to ensure axial optical sectioning. The axial resolution is therefore set by the ribbon thickness. The first version of this approach was demonstrated on Golgi-stained mouse brains [158] and then was adapted to GFP-labelled samples (fMOST)[160]. Given that resin embedding inherently quenches fluorescence, a protocol to recover GFP fluorescence after quenching was implemented to adapt fMOST to fluorescence imaging. The technology further matured and recently evolved into wide-field volumetric tomography (WVT) [159] for high-throughput dual-color whole-brain imaging with 0.3×0.3×2 μm^3 voxel sampling. WVT relies on a dual-channel wide-field scheme combined with structured illumination [161] for optical sectioning. Similarly to MOST/fMOST, the sample is embedded in resin and slicing is performed with a diamond knife. However, in this configuration slicing and imaging are uncoupled: imaging is done in a mosaic manner, then a 2 µm-thick superficial slice is shaved off the embedded sample (Fig 2.1d). This allows significant reduction of imaging duration. Another improvement compared to fMOST is the implementation of real-time nuclei counterstaining with propidium-iodide (PI) (Fig 2.1d) simultaneously excited with GFP, and providing additional morphological landmarks. All in all, WVT is one of the most promising technologies for high-throughput whole-brain circuit

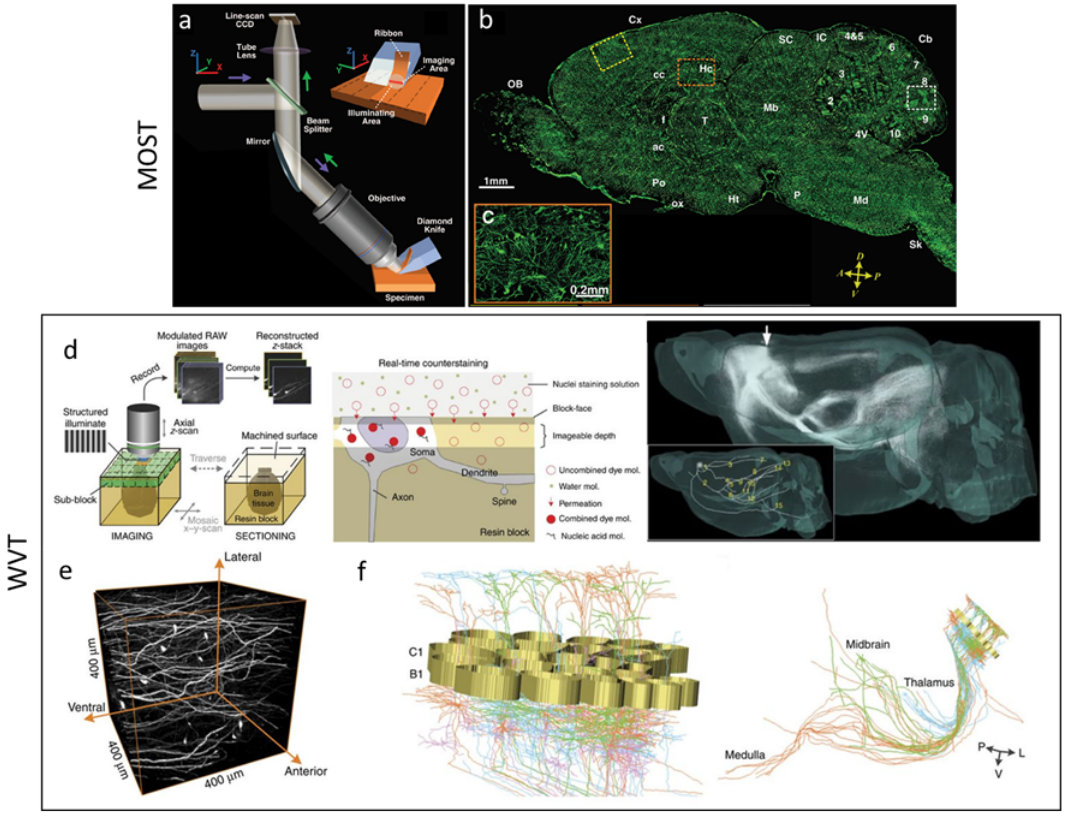

FIGURE 2.1. Wide-field automated sectioning techniques: micro-optical sectioning tomography (MOST) and wield-field volumetric tomography (WVT). (a-c) MOST acquisition scheme consisting of line ribbon slicing and simultaneous imaging (a) and example of a reconstruction of a sagittal brain section from 100 virtual sagittal sections (total thickness 100 µm) from original coronal sections acquired with MOST. Annotations: OB-olfactory bulb, Cx-cerebral cortex, Hc-hippocampus, f-fornix, ac-anterior commissure, T-thalamus, Cb-cerebellum; Mb-midbrain; P-pons, Md-medulla, cc-corpus callosum, SC-superior colliculus, IC-inferior colliculus, Ht-hypothalamus, Po-preoptic area, ox-optic chiasm, 4V-4th ventricle, arabic numerals 2 to 10- nine lobules of the cerebellum, Sk-spinal cord. Adapted from [158]. (d-f) Principles of WVT combining structured illumination, resin embedding for thin tissue sectioning and real-time counterstaining to acquire whole mouse brain datasets (d) with constant high-resolution (e). (f) Tracing of few entire neuronal morphologies of barrel cortical neurons using WVT. Adapted from [159].

mapping because of its high resolution (~0.5 µm lateral, ~2.5 µm axial) and speed (~3 days per brain) provided. This system has been used to trace entire morphlogies of corticofugal neurons in the mouse barrel cortex [159][162], and will certainly be leveraged in the future for brain-wide single-cell morphological studies. However, it presents an important caveat: the harsh resin embedding procedure drastically limits the number of fluorophores compatible with this technique and hence restricts the number of neurons that can be unambiguously analyzed within

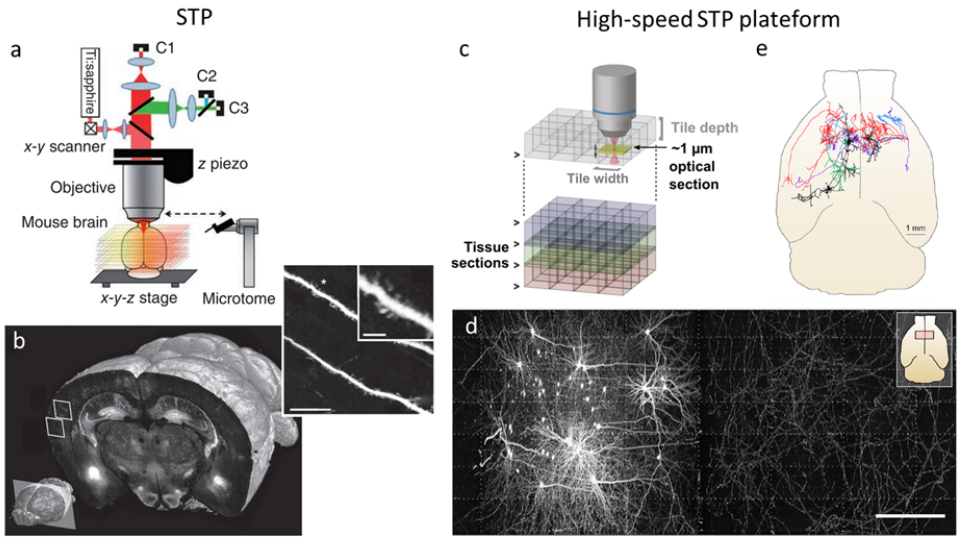

FIGURE 2.2. Serial two-photon tomography (STP). (a-b) Principle of STP (a) and whole mouse brain reconstruction from a series of serial 2D sections sampled at 100 µm acquired at submicron lateral resolution with STP. Scale bars 25 µm and 5 µm (inset). Adapted from [6]. (c-e) Optimization of STP acquisition speed allowed acquisition of continuous whole brain datasets with dendritic resolution and tracing of corticofugal neurons. Scale bar: 250 µm. Adapted from [65].

a single brain.

2.1.3 Serial two-photon tomography (STP) and derived methods

Serial two-photon tomography (STP) is based on the combination of two-photon microscopy and automated microtome-based tissue sectioning. It was introduced in 2012 by Tim Ragan and colleagues [6] and constituted a first important step towards high-throughput whole-organ anatomical studies. STP technically relies on the capability of two-photon microscopy for high-resolution deep-tissue imaging and a microtome with optimised flexures [163] for high-quality slicing compatible with aqueous sample embedding. STP allows to acquire series of mosaic 2D sections throughout the entire brain with discrete Z sampling (50-100 µm) at submicron lateral resolution (Fig 2.2a-b), or continuous mm^3 brain areas with diffraction-limited resolution, in typically ~1 day of acquisition. More details about the acquisition scheme will be presented in the Experimental Setup section of this chapter. Overall, STP presents several advantages for large volume high-resolution imaging:

- Diffraction-limited lateral optical sections can be acquired by imaging 30-40 µm below the surface.
- The serial 2D sections are automatically registered with no distorsion/deformation between sections.

- Continuous diffraction-limited volumes of virtually unlimited size can be acquired with mitigated optical aberrations because of the 2P imaging/slicing cycle scheme.

- The aqueous embedding procedure does not quench fluorescence and is therefore compatible with most fluorophores.

The main limitation of STP would be the acquisition times, as it remains fundamentally a point-scanning based approach. This specific point and ways to adress it will be discussed later.

In recent years, STP has enabled multiple whole-brain anatomical studies, some of which are reviewed in [164]. Examples include the generation of a brain-wide atlas of the mouse cholinergic system [146], the identification of stereotyped sex-based anatomical differences in cell-type distribution throughout the brain [165] and large-scale investigation of local vasculature changes in mouse models of Alzheimer's disease [166]. Importantly, it has served as the workhorse of the large-scale Allen Brain Institute connectivity project (http://connectivity.brain-map.org/) which aims to provide to the community a comprehensive mapping of projections and inter-connections within the mouse brain [86][167]

In 2016, researchers at Janelia Research Campus built a plateform for high-resolution continuous whole-brain imaging, building on STP and significantly improving imaging speed [65]. The main technical improvements consisted in using resonant scanners, strong-expressing AAV viral labeling associated with very high-power imaging (350-400 mW at the objective back aperture, minimizing thus the necessary pixel dwell time), and contour detection to avoid unnecessary background imaging. These improvements allowed for whole mouse brain imaging at full resolution within a week of continuous acquisition (Fig 2.2c).

2.1.4 Emerging trends

Driven by the neuroscience community motivation of tracing circuits across the whole-brain, an important focus has been made on increasing the speed of the above large volume slicing-based approaches. The WVT system and the Janelia plateform have made a significant step towards this goal. Very recent approaches aimed to further decrease the acquisition time by one to two orders of magnitude, i.e few hours per mouse brain [168][169]. They rely either on a spinning-disc scheme or on a light-sheet configuration with V-mounted objectives. While the former comes at the expense of a degraded image quality compared to 2P-based methods, the latter is a promising way for future improvement of the technique.

More generally though, serial two-photon tomography has paved the way for automated slicing-based imaging of intact organs. Automated slicing has recently been combined with other imaging modalities such as OCT [170], photoacoustic imaging [171], spinning-disc [168] and confocal fluorescence microscopy. Beyond neuroanatomy, microtome-assisted microscopy methods are certain to transform histopathological screening.

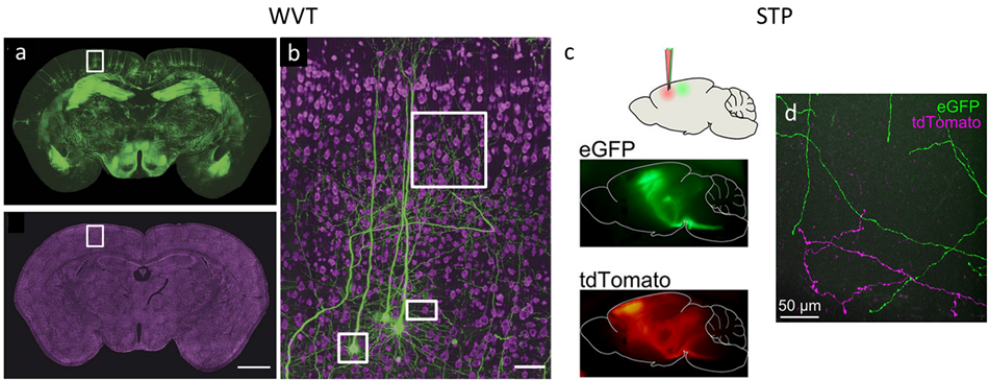

FIGURE 2.3. Color contrast in automated histology methods. (a) Dual-contrast coronal section acquired with WVT of GFP-labelled neurons (Thy1-GFP line) and PI nuclear staining. Scale bar: 1 mm. (b) Inset showing the dual-color local contrast. Scale bar: 50 µm. (a-b) Adapted from [159]. (c) Dual-color red/green serial two-photon tomography achieved with a single 2P excitation and example of local dual-color contrast (d). Adapted from [65].

2.1.5 Chrom-SMP: rationale

Contrast in large-scale automated histology methods has been restricted at best to two-color imaging [159][65][6] (Fig 2.3), thus limiting the quantity of information extractable from a single brain because of the sparsity requirement of single-cell analysis.

Dual-color STP imaging has been demonstrated so far with a single although not optimal two-photon excitation at ~920 nm of red and green fluorophores [65][6][172].

WVT has only been demonstrated so far for GFP together with blue dye staining fluorescence imaging [159]. This limitation is intrinsically due to the sample preparation procedure. Although the protocol was recently optimized for red fluorescence [173] allowing two-color red/green fMOST imaging, this development has been tailored to pHuji, a pH sensitive red FP and has still not been demonstrated with common red FPs used in widely available transgenic lines. Besides, blue excitation in WVT is restricted to dye staining as the protocol is not compatible so far with blue FPs. WVT-based approaches are therefore limited in terms of fluorophore versatility and are hence not well-suited for Brainbow and other multicolor labeling strategies.

Our aim has thus been to develop a large-scale histological method with augmented contrast capabilities. Its aqueous based sample preparation procedure makes STP a more suitable starting point for multicolor imaging. Our strategy was therefore to complement STP with an efficient non linear multicolor excitation strategy to produce high-content large volume datasets.

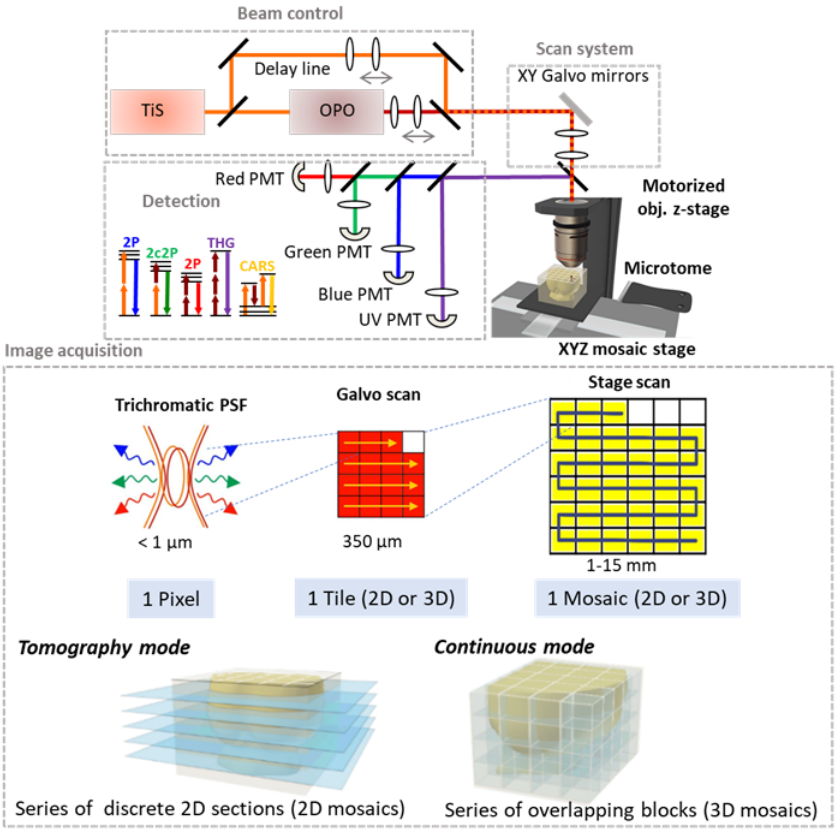

FIGURE 2.4. Chromatic serial multiphoton microscopy (Chrom-SMP): principle and experimental setup overview.

2.2 Chrom-SMP: experimental setup and performances

2.2.1 Experimental setup

The setup was entirely built from scratch by myself and Emmanuel Beaurepaire, with technical help from Jean-Marc Sintes (mechanics), Xavier Solinas (electronics) and Pierre Mahou (scan optics design).

2.2.1.1 Overview

Chrom-SMP microscopy relies on the combination of one-shot multimodal multiphoton excitation with large-range mosaic lateral stage-scanning and sequential microtome tissue slicing to access virtually unlimited tissue volumes (Fig 2.4). Chrom-SMP can be used to perform large volume tricolor or combinatorial imaging based on simultaneous excitation of red, green/yellow and blue fluorescent proteins through wavelength-mixing. Alternately, the wavelength mixing scheme can be used to target specific vibrational bonds and perform CARS imaging, simultaneously with THG signals detected on a separate channel. Upon certain conditions, the setup can also be used

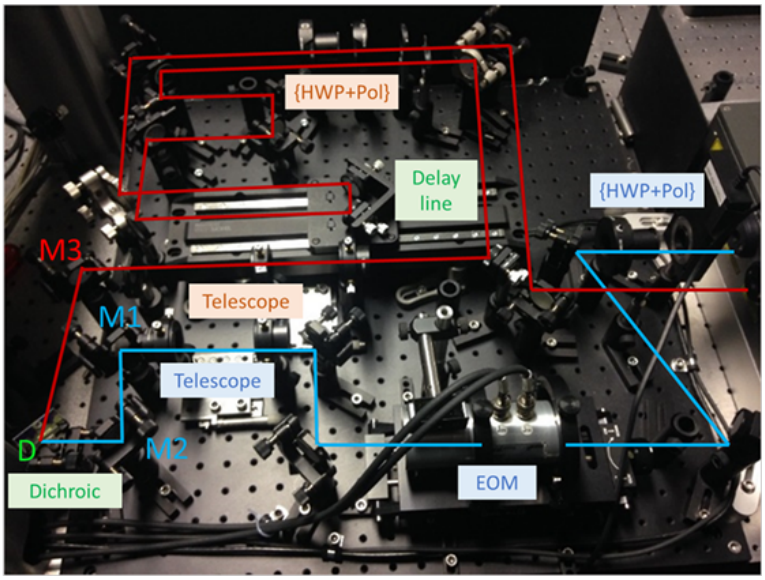

FIGURE 2.5. Chrom-SMP: wavelength-mixing stage. *HWP: half-wave plate; Pol: polarizer; EOM: electro-optical modulator; M1, M2, M3: alignment mirrors; D: recombination dichroic.*

to perform simultaneous multicolor and THG imaging (cf. Chapter 3). In the following section, each microscope module will be presented in further details.

2.2.1.2 Beam shaping/control

We use two synchronized laser outputs from a commercial Ti:Sapphire and OPO chain (Chameleon Ultra2 and MPX, Coherent) at 80 MHz. The two outputs are initially separated 7 ns. 2.1 m are therefore added to the OPO beam optical path to adjust the paths for temporal overlap. A motorized optical delay line is placed on the OPO path to finely tune the temporal matching of the two beams. A telescope is placed on each path to control the size of each beam at the objective rear pupil, i.e the effective numerical aperture (NA) and hence the effective optical resolution. The telescopes are also used to control the beam divergence which can be used to control the relative axial mismatch between the two beams (cf. Optical perfomances section). The Ti:Sa and OPO beam are recombined using a dichroic mirror (DMSP-1000, Thorlabs) and a mechanical shutter synchronized with the image frame rate is placed right after. Moreover, a motorized power control consisting of a rotating half-wave plate and a polarizer is placed on each beam to independently control the blue and red excitation power. Moving the delay line provides an additional degree of freedom to control the green excitation power independently (cf. Optical perfomances section). The rotation of the half-wave plates can be synchronized with the objective z-position to automatically adjust power with depth. Finally, an electro-optical modulator is placed on the Ti:Sa path and was programmed to shut off laser illumination during

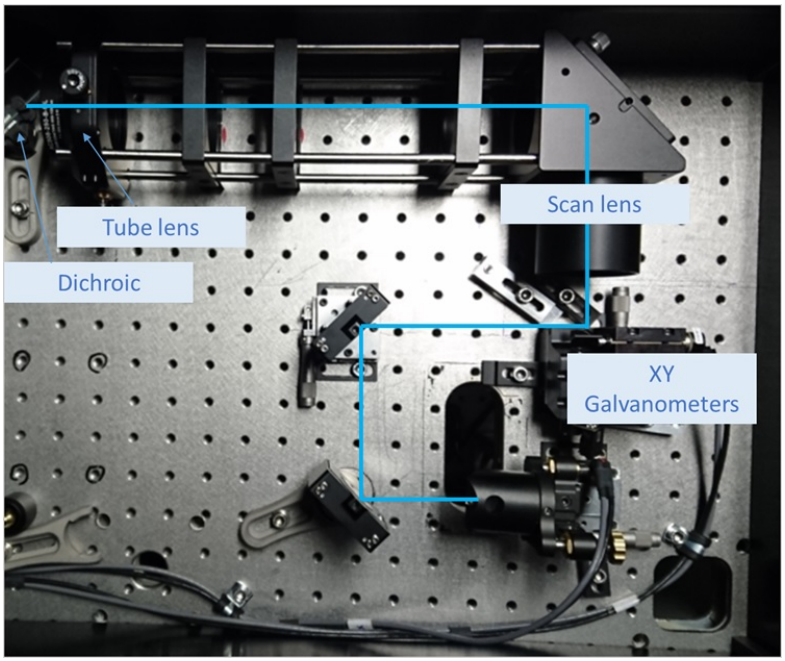

FIGURE 2.6. Chrom-SMP: scan system.

the unidirectional line scanning fly-back to prevent unnecessary tissue exposure and potential Ti:Sa induced photobleaching of red fluorophores [41].

2.2.1.3 Scan system

After recombination, the recombined beams are sent onto galvanometers for X and Y scan in the field of view. The galvanometers are optically conjugated to the objective rear pupil through the scan lens and tube lens ensemble placed in a 4f configuration (Fig 2.4). The commonly used achromatic doublet for the scan lens has here been replaced by a Plössl lens assembly, which significantly improves the system performance [174], by strongly reducing field curvature thus increasing the size of the usable field of view. The tube lens is here a 2" achromatic doublet, which is immediately followed by a dichroic (Semrock 751 nm) separating the excitation from the detection. 2" size optics were preferred in this design to minimize both power loss and off-axis aberrations.

2.2.1.4 Slicing and stage-scanning system

The Chrom-SMP microscope was built around a stripped-down version of the TissueCyte®system commercialized by TissueVision, comprising solely the stacked X, Y and Z sample stages, the vibratome system (vibratome arm and motor) and the plastic bath container (Fig 2.7). The sample stages are commercial stages (PI, Physikinstrumente). X and Y stages provide a high positional accuracy (0.1 µm) across a centimetric range. A custom frame for the microscope with an elevated

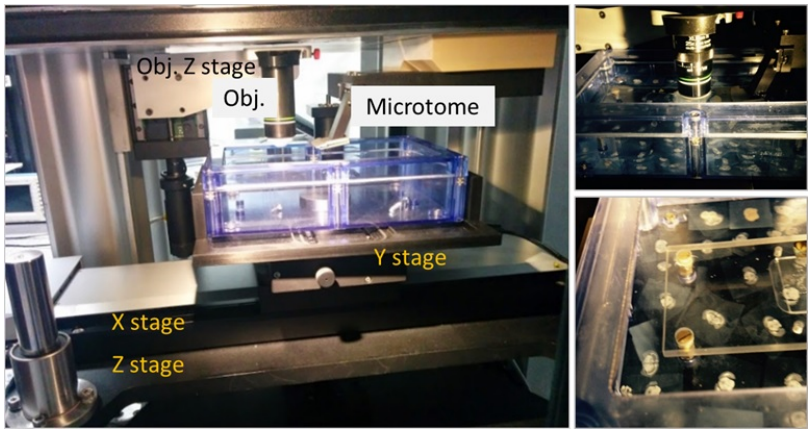

FIGURE 2.7. Chrom-SMP: sample stage. *Obj: objective*. The sample block is placed in the PB-filled plastic bath and the objective is directly immersed in the cuve. Insets on the right show floating tissue sections after repeated imaging/slicing cycles.

optical breadboard has been designed to accomodate for the whole slicing and stage scanning system.

The vibratome design (patented by TissueVision [175]) was optimized for high-quality slicing by being constrained to oscillate solely in the transverse direction to the cut, while being supported and guided with a flexure drive. The system was provided with a custom software (Orchestrator) which controls the stage scanning and the vibratome slicing. We developed a Labview module to interface Orchestrator with our lab-built acquisition software (used in several microscope installations at LOB) in order to synchronize the acquisition with the mosaic scanning and the slicing.

Finally, the plastic bath has also been re-engineered to have a more flexible sample holder within the tank (credit Jean-Marc Sintes).

2.2.1.5 Image acquisition

Excitation and epi-detection is done using an Olympus 25x 1.05 NA water immersion objective. This objective has been specifically selected for its low chromatic aberrations at our typical wavelengths of interest (850 nm/1100 nm), compared to other commercial low magnification high NA objectives (cf. Optical performances section). These objectives are commonly used in multiphoton microscopy because of their relatively large field of view (520 µm ×520 µm), high NA and large working distances [13] (here 2 mm).

In Chrom-SMP experiments, the sample block is placed in a PB or PBS filled plastic bath (Fig 2.7) and en-face imaging is alternated with superficial tissue block removal using a synchronized vibrating blade microtome.

The current setup can be used through two acquisition modes: a discrete tomography mode and a continuous mode (Fig 2.4).

The **tomography mode** consists in the succession of **large-scale 2D mosaics**: prior to each section the microtome blade is placed at the sample surface plane. For each 2D section, a single plane is imaged 30-40 µm below the surface over a large XY area through several XY individual field of views (tiles) then the sample is elevated by a user defined thickness (50-100 µm), brought to the microtome and sliced. This specified slicing thickness corresponds to the axial sampling of the dataset. Within a 2D section, 10% lateral overlap is taken between tiles to ensure a seamless continous lateral reconstruction. The imaging/slicing cycle is repeated iteratively until the entire sample (ex. a whole brain) is imaged.
The **continuous mode** consists in the iteration of **successive 3D mosaics**, with enough X, Y and Z overlap to ensure continuous imaging without information loss. Typically, a 3D stack is acquired for each XY position of the mosaic. At the end of such 3D mosaic acquisition, a superficial portion of the imaged block, smaller than the imaged depth, is sliced. This ensures overlap between the last images of a block n-1 and the first images of the following block n. This acquisition mode is particularly suited for diffraction-limited continuous imaging of large >mm^3 tissue volumes. Typical parameters/orders of magnitude relative to the different modes are given in Table 2.1 below.

Parameters	Tomography mode	Continuous mode
Field of view (µm)	200-400	200-400
Number of tiles per section or block	700-1200	20-60
Lateral tile overlap (%)	10	10
Axial overlap (%)	-	20-40
Lateral sampling (µm)	0.5-1	0.3-0.5
Axial sampling (µm)	50-100	1-2
Acquition time per section or block (h)	0.5-1	2-4

Table 2.1: Acquisition parameters in Chrom-SMP experiments.

The lexicon related to these large-scale acquisitions is presented in Figure 2.4. A **tile** refers to an individual field of view. It can be 2D (one image) in the case of tomography acquisitions, or 3D (z-stack) in the case of continuous acquisitions. A tile is the building unit of **2D or 3D mosaics** since mosaics consist of laterally assembled tiles. In the tomography mode, a 2D mosaic is often called a **2D section**. In the continuous mode, a 3D mosaic is referred to as a **3D block**.

2.2.1.6 Detection stage

In the current Chrom-SMP setup, signals are collected in an epi-configuration through the excitation objective, are reflected by the main excitation/detection dichroic and are directed to photomultiplier tube detectors (PMTs) with a set of dichroics (Semrock FF520 and FF560) /mirror and focusing lenses. Three independent channels were installed in routine, but when necessary

FIGURE 2.8. Detection stage with three independent channels.

a detector could be stacked vertically to the blue PMT, and beams would be separated after the focusing lens by an additional dichroic placed on a filter cube. The initial design consisted of bialkali photomultiplier modules in the blue and green channel (P25PC, Senstech) and a GaAsP module (H7422P-40, Hamamatsu) all used in photon counting modes in order to have the sufficient sensitivity to capture small multiphoton signals. However, for two major experimental situations encountered in my PhD work, photon counting was not adapted. Indeed, photon counting was neither suited for strongly-labelled AAV samples as the detection range was limited because of early saturation, nor for three-photon experiments (Chapter 4) where it heavily slowed down acquisition times due to the low excitation repetition rate. An off-the-shelf solution to this could have been to switch to a basic analog detection. However, we still needed for our applications to be sensitive to low multiphoton signals. Our final implementation therefore consisted in using three GaAsP detectors and replacing their photon counting module by a custom integration-based detection system designed by Xavier Solinas. This system integrates all incoming pulses during a pixel dwell time by storing the signals in an electrical capacitor which discharge rate is synchronized to the acquisition pixel clock (Fig 2.9).

2.2.2 Tissue processing

Tissue processing is a crucial step in a Chrom-SMP experiment. The sample needs to be rigidly maintained to ensure proper sectioning. In this section, I will first present the embedding protocol that I implemented in the laboratory based on the STP tissue processing protocol [6][86](TissueVision inc.), then I will present an optimization of the protocol for very soft tissues.

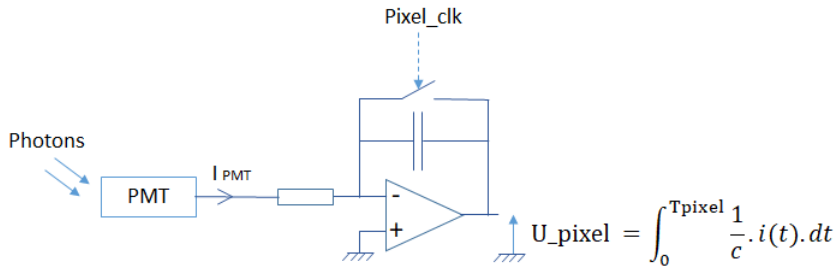

FIGURE 2.9. Scheme of integration-based detection. Courtesy of Xavier Solinas.

2.2.2.1 STP Embedding protocol

This protocol is adapted to prepare adult mouse brains. It was used in routine for almost all the Chrom-SMP experiments presented in this thesis.

Rationale: The concept of this embedding procedure is to covalently attach the mouse brain to an agarose matrix. The first step consists in preparing an oxidized agarose gel. Agarose oxidation creates aldehyde groups in the polysaccharide matrix that covalently attach to amin groups present at the surface of the tissue in the presence of a reducing agent (sodium borohydride).

Steps:

1) **Borate buffer preparation**: Mix 9.5 g of borax $Na_2B_4O_7$ (Sigma, Catalog # 221732) and 1.5 g of boric acid H_3BO_3 (Sigma, Catalog # B6768) in 500 mL of water. Stir until dissolved. The solution can be kept several weeks, at room temperature (RT), protected from light.

Critical steps: The most important parameters of the buffer solution is the solubility and the pH. Make sure, prior to each experiment that the pH of the buffer is around 9-9.5. As for solubility, it takes some time to entirely dissolve the compounds in water. If no buffer solution in stock, it is advised to prepare it 2 days ahead of a planned experiment, so that it is entirely transparent prior to making the cross-linking solution 1 day before the experiment.

2) **Cross-linking solution preparation**: Under the hood, and in a bottle protected from light, add 0.2 g of $NaBH_4$ (Sigma, Catalog # 452882) in priorly heated (40 °C) 100 mL of borate buffer solution. Vigorous effervescence needs to be observed. Place the bottle cap untightened and stir for 15-30 min. Important: leave the cap untightened overnight and tighten cap next morning. It is not recommended to use this solution the same day it was made as this would result in brittle blocs. Also, for covalent chemistry, this solution is best prepared fresh.

3) **Oxidized agarose preparation** (4.5% agarose solution in 10 mM $NaIO_4$): mix 2.25 g agarose (agarose type I, Sigma Catalog # A6013), 0.21g $NaIO_4$ (Sigma, Catalog # S1878) and 100 mL PBS. Immediately protect from light (aluminium foil) and gently stir under the hood, at RT, for 2-3 hours. Filter out the solution using a vacuum pump under the hood and perform 3 rinses with 50 mL PBS for each rinse, to remove all excess sodium periodate from the agarose which could induce mouse brain tissue oxydation. Resuspend the agarose in a 50 mL PBS solution and store

at 4°C, protected from light. Any unused solution can be stored up to one week.
Criticial steps: Use the type I agarose reference specified. Mix the solid powders prior to adding the PBS solution. Do not exceed 3 hours of steering as it will result in poor brittle block formation.
NB: *$NaIO_4$, $NaBH_4$ borax and boric acid are hazardous compound. Wear appropriate individual protection equipment (mask) for weighting and work as much as possible under the hood*.
4) **Sample preparation**: Heat the oxidized agarose gel until ebullition. Homogenize the gel regularly during the heating. Boil the gel ~3 times until the obtention of a limpid solution, then cool down the agarose to ~40°C. Embed the brain using an appropriate mold (preferentially embedded in ice) and wait ~10-15 min until the gel becomes solid. Cut the agarose block to adjust the size and the orientation of the brain sample, then immerse it in the cross-linking solution overnight at 4°C (or alternately at RT for 4-5 hours). After the cross-linking step, rinse in PBS and blot the tissue block, then glue it on a frosted glass slide using a cyanoacrylate glue. Press the glued sample for few seconds and leave it to dry for ~10-15 min. The sample is then ready to be mounted in the PBS-filled waterbath.
Critical steps: We found the use of frosted glass slide critical to keep the sample mounting intact during the long acquisition times, otherwise the tissue block may detach from the slide after several hours and imaging/slicing cycles.
Note: PBS or PB (0.42 g/L monobasic sodium phosphate, 0.92 g/L dibasic sodium phosphate) can be used indifferently as preparation and imaging buffers as long as the same buffer is used throughout the entire sample preparation pipeline. PB is however preferred for long-term preservation of metallic parts of the sample tank and vibratome arm.

2.2.2.2 Embedding protocol for very soft tissues

The protocol described above enables to perform routine adult mouse brain imaging. However, it was not fully optimized for soft and heterogeneous tissues such as embryonic brain tissues. Building on the CLARITY hydrogel mesh concept [176][177] and an improved version of the STP embedding protocol provided by TissueVison, I optimized the embedding protocol for soft tissue materials.

Rationale: The previous protocol relied on covalently attaching primary amins present on the tissue proteins, DNA and RNA to the oxidized agarose. CLARITY is a tissue clearing procedure on fixed tissues featuring multiple steps [176]. The step that is conceptually interesting to us is the first one which aims at creating a tissue-hydrogel hybrid by binding the tissue amins to acrylamide monomers that form a rigid skeleton structure upon polymerization. The initial CLARITY-like matrix can be used in our case to primarily maintain the tissue instead of solely relying on covalent cross-linking to the agarose gel. After polymerization, the mouse brains tissue hydrogels are extracted from the acrylamide gel then embedded in oxidized agarose for Chrom-SMP imaging. However, soft tissues such as embryonic brains do not tolerate this procedure as extraction from the surrounding acrylamide gel often results in the tissue getting

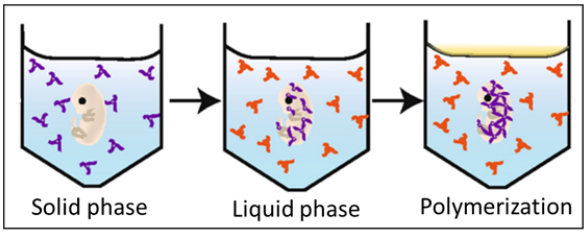

FIGURE 2.10. Biphasic acrylamide embedding. The sample is first soaked for several hours (overnight) in a monomer solution which transforms upon polymerization into a solid phase (purple). The sample is then quickly transferred into a monomer solution (orange) which remains liquid after polymerization. The tissue is then easily extractable after polymerization. Adapted from [177].

damaged and torn apart. To avoid this issue, a solution is to use biphasic acrylamide embedding, as described in [177] and in Fig 2.10: the sample is first soaked overnight in a hydrogel monomer solution (purple, solid phase) to allow for the monomers to diffuse within the tissue. Then prior to thermally-initiated polymerization, the sample is transferred to a monomer solution without the capacity for solid polymer formation (orange, liquid phase). This results on the formation of a solid tissue-hydrogel hybrid within a liquid phase which hence can be extracted easily for subsequent agar embedding.

Steps: Biphasic acrylamide embedding

- Prepare a solution of Surecast (Acrylamide:Bis-acrylamide ratio of 29:1, ThermoFisher Catalog # HC2040) and VA-044 activator diluted in PB with a total concentration of 4% Acrylamide and 0.5 % activator (i.e, for a 40 mL total volume, use 4 mL Surecast and 0.2 g activator). This solution is the solide phase solution (SP). Soak the tissue in SP overnight at 4°C.

Critical notes: All components should be kept cold at all times to avoid spontaneous polymerization. Also acrylamide is a carcinogenic compound, handle with appropriate care.

- After the overnight soak, shake gently at RT, for 1 hour approximately.

- Prepare 40 mL of liquid phase solution (LP) using the same precautions as the solid phase. The LP solution consists in a solution of Surecast and VA-044 activator diluted in PB with a total concentration of 1.6% Acrylamide and 0.5 % activator.

- Transfer the tissue from the SP phase to the LP phase into a closed plastic container. Cover the LP phase solution with vegetal oil to avoid excess oxygen during polymerization, and place the container at 40°C into an oven for 5 hours.

- After the polymerization, extract the tissue from the acrylamid liquid phase and prepare it for imaging as in the previous protocol.

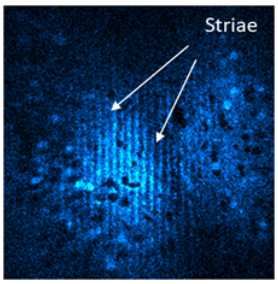

FIGURE 2.11. Vibratome striae.

2.2.3 Tissue sectioning

Tissue sectioning quality is central to the success of Chrom-SMP experiments. It relies essentially on sample preparation (cf. previous section), but also on the mechanical properties and parameters of the microtome during the cut. Table 2.2 presents the microtome parameters that have here been used successfully.

Parameters	Regular tissue	Soft tissue
Vibration frequency (Hz)	60	60
Vibration amplitude (mm)	0.8	0.8
Vibratome speed (mm/s)	0.3-0.5	0.1-0.3
Blade pitch angle (°)	10	10

Table 2.2: Vibratome settings for regular and soft tissue sectioning.

It is also important to use a fresh blade for each experiment. The blade roll angle also needs to be adjusted using the screws on the vibratome arm. Slicing striae, visible on the tissue surface (Fig 2.11) and which result from the blade passage on the tissue surface are used for this purpose. For whole brain experiments, the slicing angle in the Y direction needs to be set to less than 10 µm over ~7 mm in order to obtain sections with homogeneous quality.
We evaluated the slicing quality achieved with regular agarose embedding compared to the borate mediated crosslinking protocol upon similar sectioning parameters (60 Hz, 0.8 mm amplitude, 0.5 mm/s, 10° pitch angle) by comparing XZ resliced views of 3D mosaics. Crosslinking ensured better sectioning quality both at the large mosaic scale and at the local scale (Fig 2.12). Covalent crosslinking prevented mechanical distorsions during the blade passage. Slicing with low parasitic Z-vertical deflection as optimized through the vibratome flexure arm design [175] could be achieved. Insets in Fig 2.12 show that the vertical deflection in the case of a crosslinked sample is less than 2 µm while structures are heterogeneously torn apart in the case of non covalent agarose embedding.

Finally, we also verified that morphological structures (cells, blood vessels) could be recovered

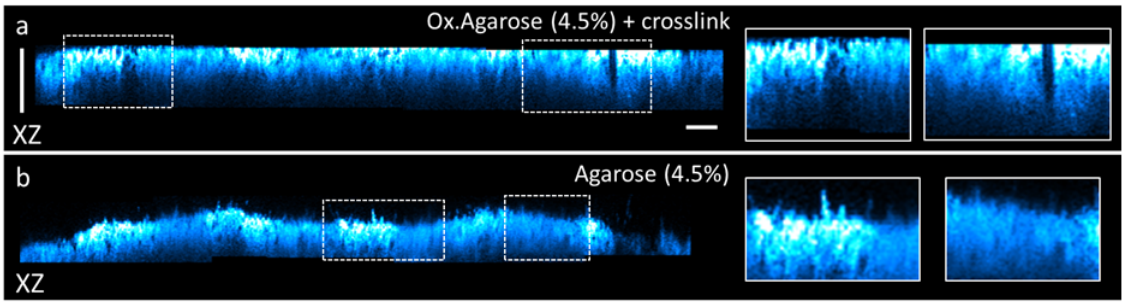

FIGURE 2.12. Influence of cross-linking on slicing quality. Scale bars: vertical: 120 µm, horizontal 100 µm.

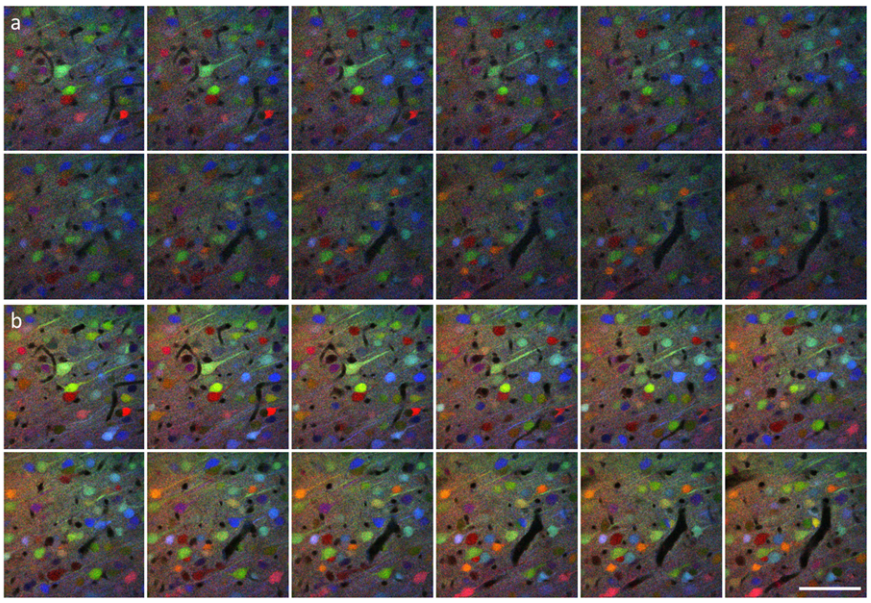

FIGURE 2.13. Lossless imaging with Chrom-SMP. (a) Z-stack sequence from Z = 98 µm to z = 120 µm sampled at 2 µm from the lower part of an acquired block n-1. Scale bar: 100 µm. (b) Z-stack sequence from Z = 6 µm to z = 28 µm sampled at 2 µm from the upper part of the subsequent block n after sectioning. Structures are recovered from one block to another with improved resolution and signal to background ratio. Scale bar: 100 µm.

from one block to the other upon sectioning. This point is indispensable to perform continuous lossless high-resolution imaging. As expected, structures reimaged closer to the sample surface following sectioning are recovered with a better image quality, not affected by depth-induced aberrations. In Chrom-SMP continuous acquisitions, the determination of the optimal slicing thickness is sample-specific since it is a tradeoff between slicing robustness (better with thicker slices) and image degradation with depth, the aim being to obtain continuous volumes with homogeneous image quality (cf. Chapter 3 for examples).

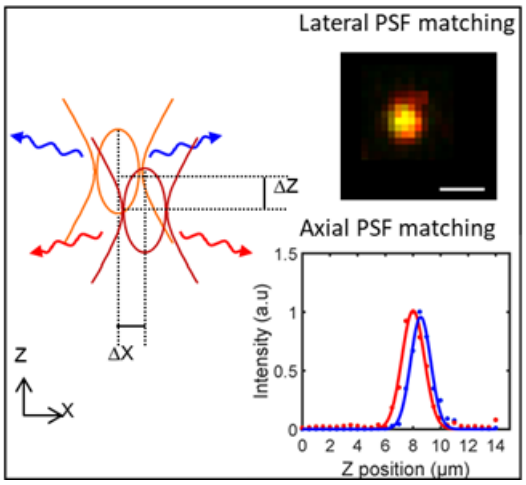

FIGURE 2.14. Lateral and axial point-spread function (PSF) matching. The graph shows Gaussian-fitted PSFs acquired with a 500 nm z-step. Blue: 850 nm beam, red: 1100 nm beam. Scale bar: 1 μm.

2.2.4 Optical performances

2.2.4.1 Resolution and PSF matching

A fundamental requirement for wavelength mixing is the spatial overlap of the two excitation foci in 3D (Fig 2.14). A practical way to perform this calibration is to use SHG nanoprobes such as KTP nanocrystals [31], below the resolution of the system, and can therefore be used to match the two foci at the PSF scale, while at the same time providing a measurement of the resolution for each beam. An advantage of this system for metrology is that the same objects can be probed simultaneously with the two beams and generate two specific, spectrally-narrow SHG signals that can be detected in separate channels. Also, these probes can be used with a large range of excitation wavelengths, although most of the applications of Chrom-SMP in this thesis were done using the 850 nm/ 1100 nm combination.

In practice, lateral coalignment is first done grossly using M1 and M2 to adjust the Ti:Sa beam position and M3 and D to adjust the OPO beam position (Fig 2.5), and two spatial landmarks one right after the recombination dichroic and the second one close to the objective rear pupil. The coalignment adjustment is then refined on a KTP nanoparticle imaged at the center of the field of view (Fig 2.14), using the far-field mirrors only (M3 and D on Fig 2.5).

The relative axial mismatch between the two beams can be adjusted by controling their divergence using the telescopes on the beam paths. For compacity reasons, the telescopes used here are 2-lenses telescopes, which means that beam size and beam divergence cannot be tuned independently. However, the beam size at the objective back aperture is also a fundamental parameter in multiphoton microscopy experiments as it determines the effective NA and hence the resolution of the system, as well as the available power after the objective. A large beam

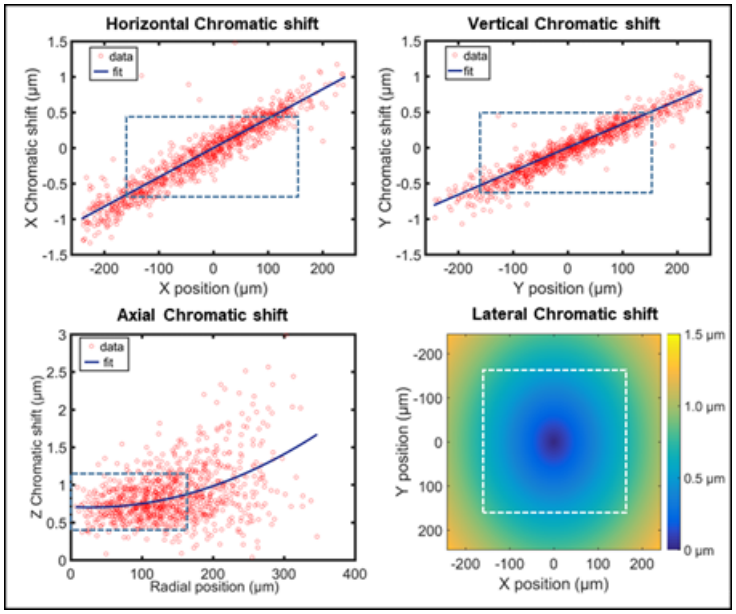

FIGURE 2.15. Chromatic aberration characterization across the field of view (fov) for the 850 nm/1100 nm wavelength combination. Top: Chromatic horizontal (resp. vertical) shift ΔX (resp. ΔY) as a function of the horizontal (resp. vertical) position in the fov. Measurements were performed on n=1012 KTP nanocrystals across the fov and data fitted using an affine model. Bottom left: Chromatic axial shift ΔZ (resp. ΔY) as a function of the radial position in the fov. Measurements were performed on n=1037 KTP nanocrystals across the fov and data fitted using a polynomial model. Bottom right: Lateral chromatic shift mapped across the fov. Lateral chromatic shift is defined as $\sqrt{(\Delta X^2 + \Delta Y^2)}$ with ΔX and ΔY the corresponding fitted horizontal and vertical chromatic shifts. Dashed boxes outline the maximal effective fov used for Chrom-SMP imaging experiments.

at the back aperture (over-filled aperture) will give a higher resolution at the expense of laser power loss, while under-filling the back aperture will result in a lower resolution but higher available power. A strategy to optimize both axial mismatch and axial resolution of both beams is to: (i) precalculate the telescope magnification required for each beam to match the size of the objective back aperture, knowing the initial beam size and the magnification of the scan system; (ii) optimize the resolution for one beam and then use the second telescope to adjust the relative axial mismatch; (iii) if the resolution and/or power for the second beam is not optimal, change the second telescope magnification to increase or decrease the beam size. A typical working configuration obtained using this procedure is presented in (Fig 2.14): 1.8 µm resolution for the 850 nm beam, 2.6 µm resolution for the 1100 nm beam and 0.5 µm axial mismatch.

2.2.4.2 Chromatic aberrations

Definition

Chromatic aberrations are wavelength-dependent artefacts due to optical dispersion. As the refractive index of a lens varies with the wavelength, light beams of different wavelengths are focused onto different spots. There are two types of chromatic aberrations: axial (longitudinal) chromatic aberrations and transverse (lateral) chromatic aberrations. Axial chromatic aberration refers to the foci z-mismatch of light beams of different wavelengths, as described in the previous section. Lateral chromatic aberration is a lateral chromatic mismatch which increases with the distance to the center of the field of view. In other terms, it is a chromatic difference of magnification. Mitigating both axial and longitudinal chromatic aberrations at the PSF scale is fundamental for quantitative and high-resolution anatomical multicolor imaging.

Characterization of chromatic aberration

We characterize chromatic aberrations within the field of view using SHG KTP nanocrystals as described in [31]. Axial chromatic aberrations are minimized by matching the beam foci using telescopes, as described in the previous section. Lateral chromatic aberration are mitigated by selecting a microscope objective appropriate for wavelength-mixing [31] and designing a scan system with corrected chromatic aberrations. The performances of the system for the 850 nm/1100 nm wavelength combination are presented in Figure 2.15. While the lateral chromatic mismatch increases linearly with the distance to the center of the field of view (fov), the axial mismatch is constant over ~350 µm. Overall, a color mismatch of less than 0.6 µm is obtained in all three dimensions over a field of view exceeding 350 µm. These performances determine the maximal usable field of view for a single tile in Chrom-SMP experiments.

Chromatically corrected multicolor large volume imaging

An important feature of Chrom-SMP is the intrinsic 3D channel registration at the submicron scale that stems from the excitation process. Indeed, green fluorescence signals obtained through a wavelength-mixing scheme provide an intrinsic quality check: they are observed only if the excitation point spread functions of the two beams overlap in 3D with submicron precision, in turn ensuring that all signals originate from the same diffraction-limited volume. Another advantage of wavelength-mixing as a multicolor imaging scheme is that chromatic aberrations only need to be mitigated for narrow laser excitation bands instead of the entire 800-1100 nm range. Chrom-SMP further builds on (i) lateral stage mosaicking, (ii) robustness of two-photon processes with depth and (iii) tissue sectioning to provide high resolution large volume imaging with multicolor voxel precision (Fig 2.16). The matching between channels is preserved over mm^3 of imaged volumes and submicron structures such as astrocyte processes and neurites can be visualized with high multicolor resolution (i.e not affected by chromatic aberrations).

2.3 Chrom-SMP: Image processing workflow

In this section, we will present the processing steps from raw images acquired with the microscope to reconstructed multicolor volumes corrected from acquisition artifacts. A general overview of the

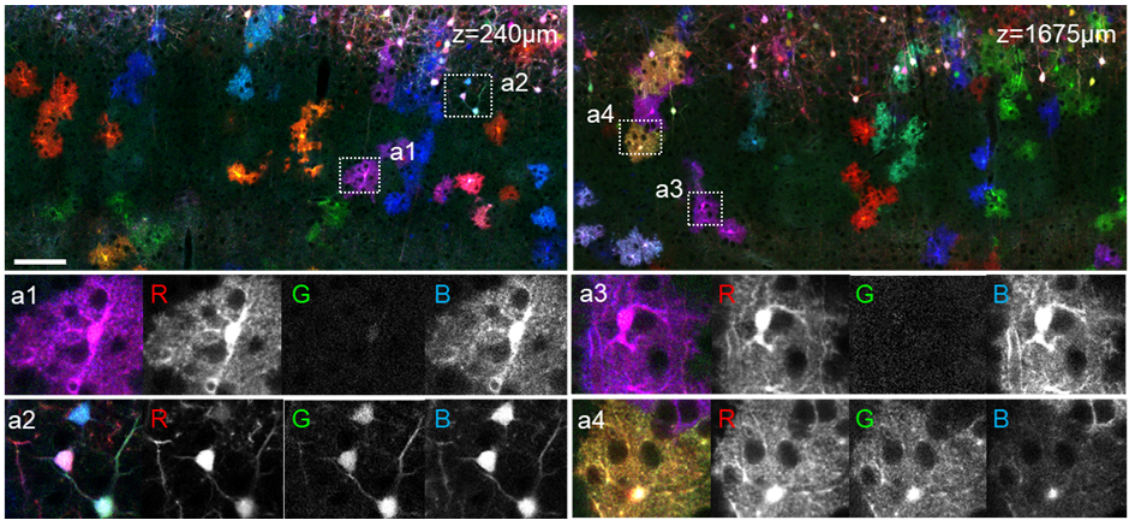

FIGURE 2.16. Registration of multichannel images is maintained at all imaging depths. XY representative multicolor images from a MAGIC marker-labelled dataset acquired with Chrom- SMP with 0.4 µm×0.4 µm ×1.5 µm voxel size. Inserts demonstrate channel co-registration at arbitrary depths within the dataset. Cell structures (astrocyte domains and processes, cell bodies, axons) can be visualized with multicolor precision (i.e not affected by chromatic aberrations) and discriminated with a quantitative color ratio. Scale bar: 100 µm.

pipeline developed is presented in Figure 2.17 and the main steps are presented in further details throughout this section. Our goal when designing this workflow was to derive all the correction parameters directly from the dataset, without the need to proceed to additional measurements before or after the experiment.

2.3.1 Individual tile processing

Two operations are applied to individual tiles at this stage, prior to image stitching: tile crop and flat-field correction.

Individual tiles are cropped in order to remove artifacts due to scanning nonlinearity at a lateral edge of the field of view. The extent of this scanning artifact depends on both the size of the tile and the lateral sampling. Since this artifact is constant across the whole dataset, the size of the crop is determined for each dataset by the user from any non blank image.

Another common artifact on individual tiles is the inhomogeneous illumination profile which results from both uneven excitation and detection patterns. While it is usually inconvenient in mosaic acquisition schemes since its prevents seamless smooth renderings of large volumes, it is particularly problematic for multicolor quantitative imaging since the illumination profiles for each channel are often different, resulting in undesirable color gradients across the field of view (ex: tile more red at the bottom than the top). In order to correct for this, we first generate

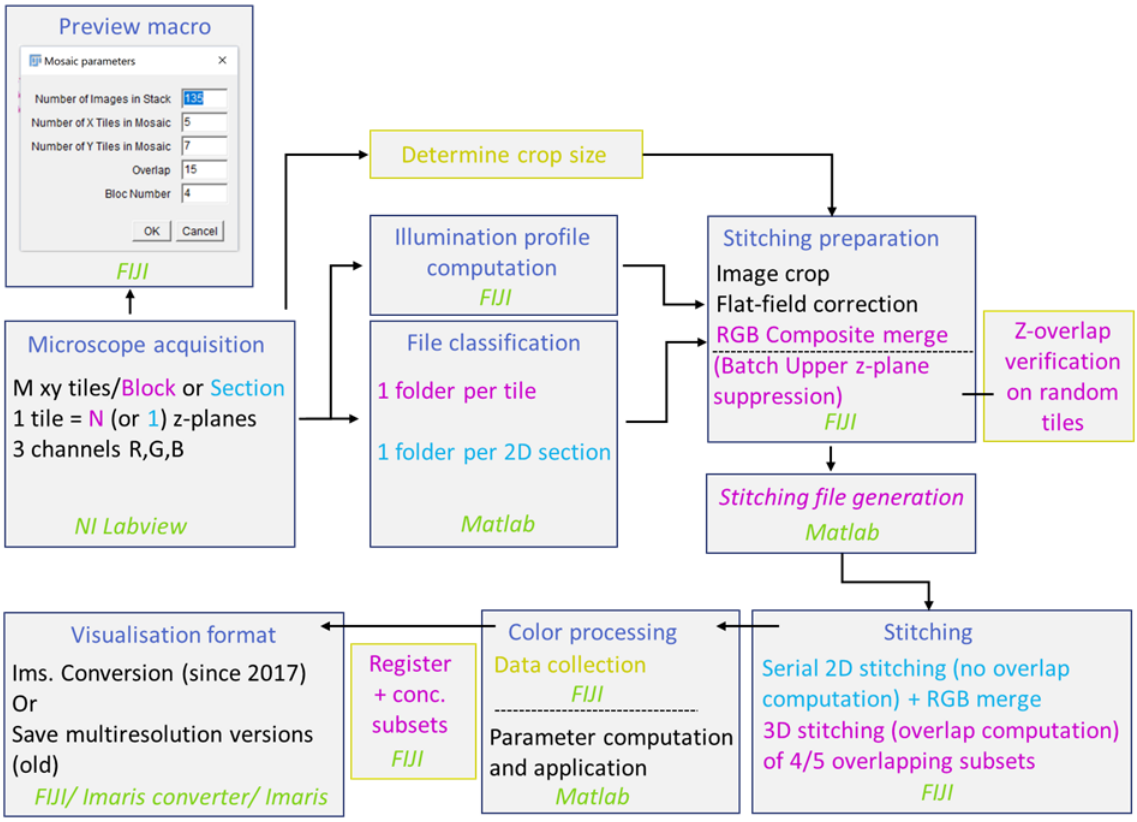

FIGURE 2.17. Overview of the visualization and processing workflow. Magenta: continuous block-face acquisitions; Cyan: serial tomography acquisitions; otherwise common to both. Blue: automated process; Yellow: manual process by user; Green: software plateform.

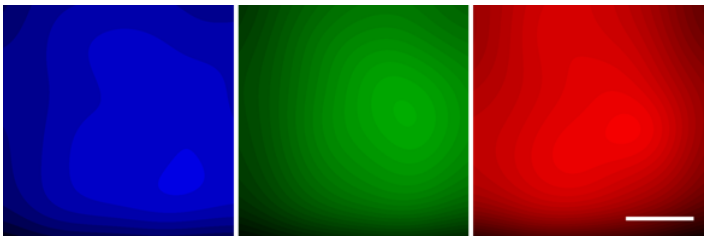

FIGURE 2.18. Flat-field correction profiles for each of the three imaged channels. Scale bar: 100 µm.

illumination profiles from the dataset by averaging all acquired images for each channel. The average profiles are then smoothed using a very coarse grain gaussian blur filter (80 pixels radius) to obtain the flat-field correction profiles (Fig 2.18). These profiles are then each normalized by their maximum intensity value. Individual tiles are then divided by these profiles. Example of a

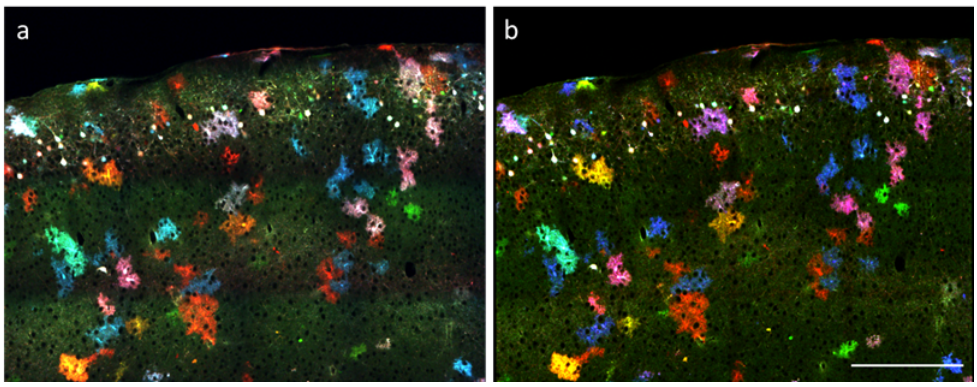

FIGURE 2.19. Mosaic from a MAGIC markers labeled cortex dataset before (a) and after (b) flat-field correction. NB- Image (b) was also color-processed (cf. section 2.3.3). Scale bar: 300 µm.

multicolor mosaic before and after flat-field correction is presented in Figure 2.19.

2.3.2 Dataset stitching

Stitching refers to the operation of assembling all the individual tiles of a dataset into a 3D continous volume (in the single 3D mosaic or continuous block-face mode) or a series of homogeneous 2D mosaics (in the STP tomography mode).

2.3.2.1 Stitching of serial 2D brain sections

For whole-brain tomography datasets, we take advantage of the high precision of the motorized XY stages for fast and accurate 2D mosaic reconstruction. For this, we adjust the automatic closed-loop parameters of the X and Y stages (PID values) to achieve less than 0.2 µm of error positioning. Mosaics are acquired with 10 % spatial overlap between the tiles in a snake-like pattern. We use the precise position of each tile within the mosaic together with the overlap parameter to assemble each 2D mosaic, without the need of further overlap computation. 2D sections are automatically self-registered, so there is usually no need for rigid (translation or rotation of a brain section relatively to the upper or lower section) nor elastic (b-spline deformation) registration between sections. Though, if two successive sections have been acquired with different starting points, a translation is of course required to recover the self-registration. To assemble the tiles, we use the *Grid / Collection Stitching* plugin [178], but this operation can be done using any other software. In this particular case, computing the overlap does not bring any particular advantage. In fact, large-scale brain mosaics can be very heterogeneous with some regions with lower signal to noise ratio. This may leed to some artifacts when computing the overlap. Furthermore, computing the overlap significantly increases the processing time.

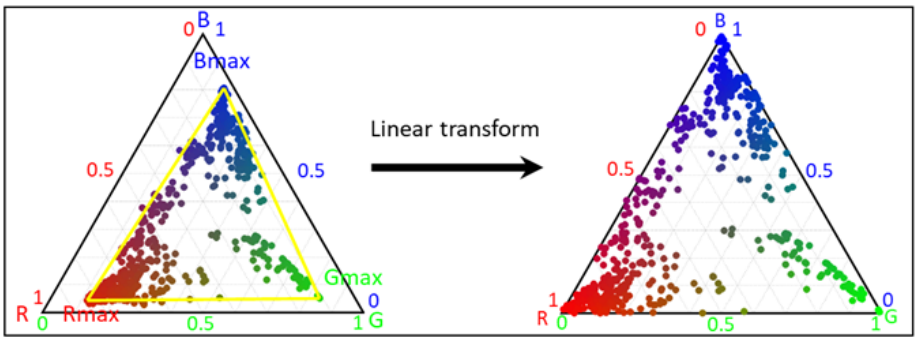

FIGURE 2.20. Ternary color diagrams before (left) and after (right) color processing.

2.3.2.2 Stitching of continous 3D volumes

For stitching 3D volumes from acquisitions in the continuous block-face mode, we use a version of the *Grid/Collection Stitching* plugin [178] which has been modified by Ignacio Arganda-Carreras (University of the Basque Country and Donostia International Physics Center, San Sebastian, Spain). The method relies on calculating cross-correlations in all three directions between adjacent tiles and overlapping blocks in the Fourier space and then select the maximum correlation. Below a certain correlation threshold, tiles are not considered adjacent. For our data, we found that the value of correlation threshold for optimal stitching results should be set to 0.1. Although this stiching algorithm provided unmatched performances, at the time of our implementation, in terms of stitching output and large volume handling, an important caveat of the program is its memory storage handling: by design it required loading in memory the input dataset twice, which added to the poor memory handling inherent to the Java language. Therefore, despite running the algorithm on a high RAM machine, whole continuous datasets of typically 250 Go/300 Go priori to stitching could not be stitched in their entirety. We proceeded by stitching overlapping subsets (4 or 5 subsets per dataset) and then registering and concatenating the subsets onto one dataset. However, a very recent release of a new version of the stitching algorithm [179] allows now to stitch large volumes in their entirety.

2.3.3 Color processing

The goal of this processing step is to remove spectral bleed-through from the multi-channel images and to fill the entire RGB color space. This is the first step towards quantitative multicolor imaging. The particularity of our procedure compared to other classical unmixing procedures ([180]) is that the unmixing parameters here are directly retrieved from the dataset, without the need of prior calibration data acquired from the microscope.

First, to assess the colorimetry of a dataset, we manually select >500 regions of interest (ROIs) in color-labelled areas throughout the stitched raw dataset, and measure raw intensities on these

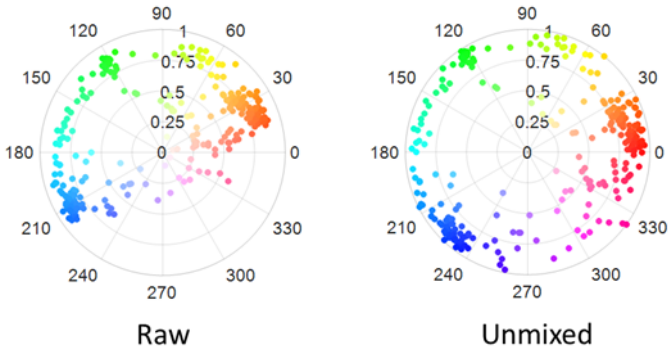

FIGURE 2.21. Hue and saturation polar plots before and after linear unmixing. Value is set to 1 for all points.

ROIs. The measurements correspond to the average signal in each channel over 2-6 pixel diameter area in structures of interest related to the application (cell bodies, axons, nuclei). The ROI pool is selected to include as much as possible the most extreme RGB values of the dataset. The multi-channel intensity measurements are then displayed in a ternary color diagram (Fig 2.20). Each point in the diagram corresponds to an RGB measurement within a single ROI, with the coordinates corresponding to the relative intensities (R,G,B)/(R+G+B).

We model the channel intensities as follow:

$$R_{raw} = R_{corr} + a_{GR}.G_{corr} + a_{BR}.B_{corr}$$

$$G_{raw} = a_{RG}.R_{corr} + G_{corr} + a_{BG}.B_{corr}$$

$$B_{raw} = a_{RB}.R_{corr} + a_{GB}.G_{corr} + B_{corr}$$

The a_{xx} coefficients are determined using maximum red, green and blue ROI intensities and by setting the maximum blue ROI to 'pure blue'. In other terms, our procedure consists in applying a linear transform to uniformly stretch the $R_{max}G_{max}B_{max}$ triangle in the color space (Fig 2.20) so that B_{max} is projected to the 'pure blue' (0,0,1) position while maintaining the RGB color ratio. The unmixing coefficients are then simply obtained by inverting the associated system matrix.

In Figure 2.21, we represented the color ROIs in a hue/saturation color plot to illustrate the effect of color stretching on the dataset colorimetry. This procedure allows to maximize the number of discernable colors, which is particularly useful for neuronal tracing applications. Finally, Figure 2.22 shows an example of the effect of the procedure on the color contrast on a multicolor crop from a dataset labeled with the MAGIC markers strategy.

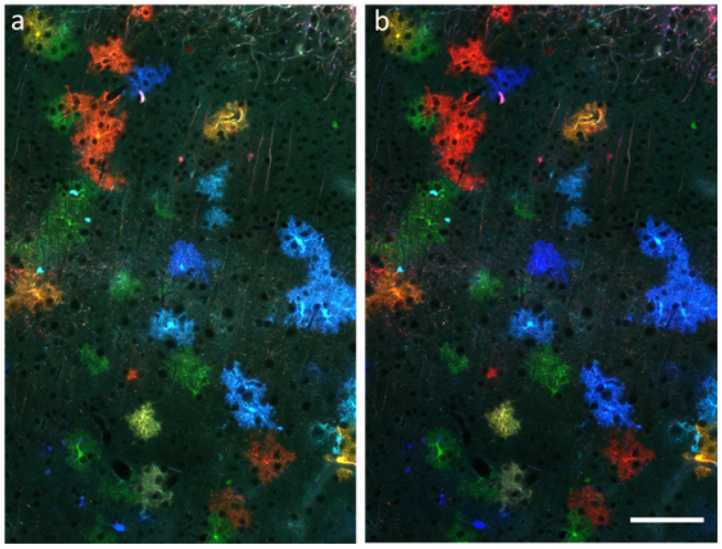

FIGURE 2.22. Color contrast before (a) and after (b) linear unmixing in the cortex of a fixed mouse brain labelled with MAGIC MARKERS. Scale bar: 100 µm.

2.4 Chrom-SMP validation: whole-brain serial multicolor tomography

In order to validate the applicability of our system to deliver brain-wide high resolution multicolor we performed a proof-of-principle tomography experiment on a densely labeled Brainbow mouse brain. We used a novel Brainbow transgenic line developed at Institut de la Vision by Jean Livet and Karine Loulier, termed CAG-Cytbow, driving random expression from based on the crossing of a transgenic CAG-Cytbow line (random expression driven by the ubiquitous promoter CAG of mTurquoise2, EYFP or tdTomato following Cre recombination) [99] with a Nestin-Cre line. Nestin is a gene transiently expressed by neuroepithelial stem cells during development. This strategy labels all nestin positive progenitors descent, therefore creating a dense multicolor labeling throughout the brain of both neurons and glial cells. The FP expression is mostly mutually exclusive in this construct, therefore providing an excellent test of our chromatic imaging scheme. We acquired a 3D multicolor whole-brain dataset consisting of 92 self-registered three-channel coronal planes with a lateral sampling of 0.55 µm and a discrete axial sampling of 100 µm (Fig 2.23). Each coronal section consists in 32 ×21 assembled individual tiles acquired in ~1h each (of note, the size of the mosaic was reduced for the smaller upper and lower brain sections). These multicolor serial 2D sections, ranging from the olfactory bulb to the brainstem, constitute each a comprehensive submicron neuroanatomical map of labeled neurons and glial cells in which color contrast facilitates individual cell distinction. As shown in Figure 2.23, the resolution provided by Chrom-SMP enables to visualize fine neural processes such as Purkinje cell dendrites and axons in the cerebellum. This Chrom-SMP experiment represents (i) the first demonstration of serial

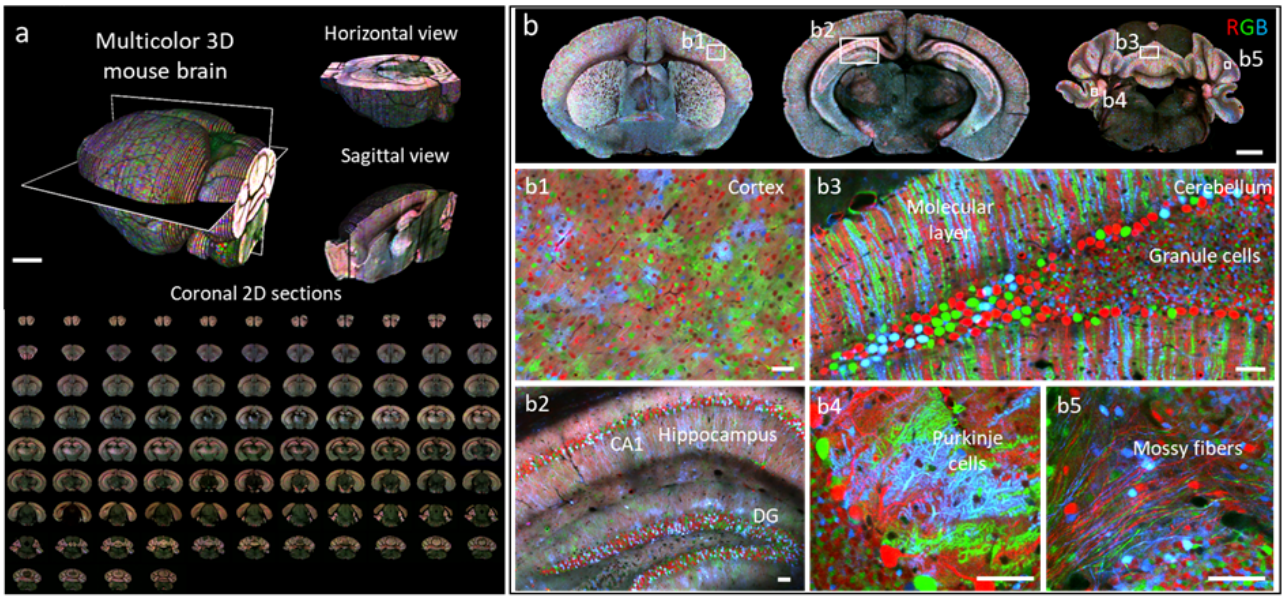

FIGURE 2.23. Whole-brain serial multicolor multiphoton tomography using Chrom-SMP. (a) 3D views from a whole CAG-Cytbow; Nestin-Cre mouse brain (10.5×7.3×9.2 mm3) imaged with Chrom-SMP. Scale bar: 1 mm. (b) 2D sub-cellular multicolor brain-wide anatomical maps from the brain in a. Upper panel displays representative coronal views. Middle and lower panel correspond to magnified crops from boxed regions in the coronal views, demonstrating sub-cellular lateral resolution enabling the visualization of dendritic and axonal processes. Scale bars: 1 mm (upper panel), 50 µm (middle and lower panels). DG: Dentate Gyrus.

multicolor tomography of a whole mouse brain endogenously expressing multiple transgenic fluorescent labels, and also (ii) the first brain-wide atlas-like dataset in which individual cell morphology is accessible in dense labeling conditions (usually serial tomography approaches are limited to sparse labeling, precisely because of the color limitation). In Figure 2.24, we present examples of these brain-wide multiscale densely labeled anatomical maps. This dataset will be publicly available at the Image Data Ressource depository (https://idr.openmicroscopy.org/) along with ontological referencing.

2.5 Multimodal brain-wide imaging using Chrom-SMP

2.5.1 Coherent contrasts

Complementary to incoherent fluorescence imaging, there is a number of coherent processes occurring as a result of the interaction of a tightly focused highly energetic beam with a given medium, therefore providing additional contrasts in the context of biological/biomedical imaging.

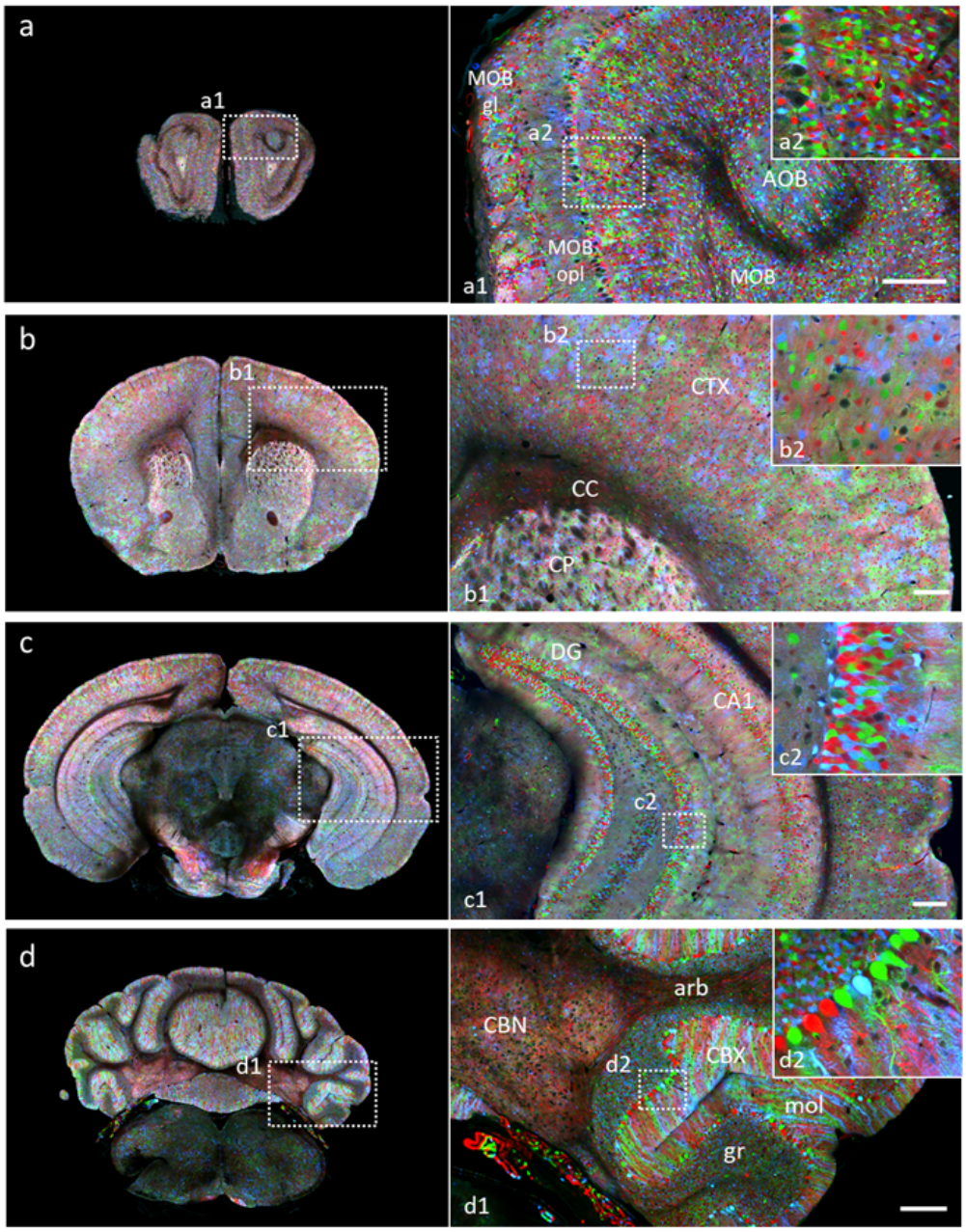

FIGURE 2.24. High-resolution multicolor anatomical views acquired with Chrom-SMP. Multicolor coronal maps in the olfactory bulb (a), forebrain (b) and cerebellum (d). *MOB: main olfactory bulb, AOB: accessory olfactory bulb, gl: glomerular layer, opl: outer plexiform layer , CTX: cortex, CC: corpus callosum, CP: caudate putamen, DG : dentate gyrus, CBN: cerebellar nuclei, CBX: cerebellar cortex, gr: granular layer, mol: molecular layer, arb: arbor vitae*. Scale bars: 200 µm.

Such contrasts include second harmonic generation (SHG) [42], third harmonic generation (THG) [181], coherent anti-Stokes Raman scattering (CARS) [182], and depend only on the

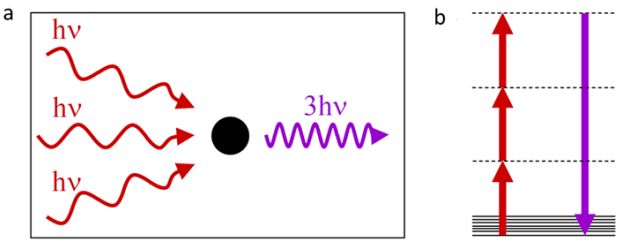

FIGURE 2.25. THG nonlinear process. Third harmonic generation is an elastic scattering process resulting in the scattering of a photon which energy is equal to the sum of the three incoming photons (a). This process being quasi-instantaneous, it involves very short-lived (10^{-15}s) virtual excitation states (b). Adapted from [49]

structural properties of the sample and the characteristics of the excitation beam. In such coherent processes, light-matter interactions are instantaneous, therefore there is a known phase relationship between all points (dipoles) within the focal volume which result in either constructive or destructive interference at the origin of the observed contrast.
A material's response to an incident electrical field $\vec{E}$ can be described by the polarization density $\vec{P} = \epsilon_0 \chi \vec{E}$, where ϵ_0 is the vacuum permittivity and χ the electric susceptibility of the material. In the case of a strong incident electric field, the response material is nonlinear and the polarization density can be written as: $P(t) = \epsilon_0[\chi^{(1)}E(t) + \chi^{(2)}E^2(t) + \chi^{(3)}E^3(t) + ...]$ where $\chi^{(1)}$, $\chi^{(2)}$ and $\chi^{(3)}$ represent respectively the linear, second order nonlinear and third order nonlinear optical susceptibilities. Nonlinear optical susceptibilities, which depend on sample geometrical properties, and/or with their variations within the focal volume drive the observed optical contrast in coherent nonlinear microscopy. For instance, since $\chi^{(2)} = 0$ in centrosymmetric media, SHG is particularly sensitive to molecular symmetry breaking. In our current study, we will focus mostly on third order i.e $\chi^{(3)}$ related processes: THG and coherent anti-Stokes Raman (CARS). These processes are said parametric, in a sense that there is no direct energy transfer to the sample involved.

2.5.1.1 Third harmonic generation (THG)

In third harmonic generation, three photons are scattered to produce a photon at one third of the excitation wavelength. In this process, higher energy levels involved are virtual as they do not correspond to specific quantum states of the molecule (Fig 2.25). Since the third order nonlinear susceptibility is not canceled by the geometrical arrangements of the molecules in the focal volume such as centrosymmetry, $\chi^{(3)}$ does not directly provide THG contrast. In fact, in the focal volume of a tightly focused beam, the beam accumulates a Gouy phase shift in the axial focal direction which produces destructive interferences canceling out the THG contrast in homogeneous media (Fig 2.26a). However, when the beam is focused at the interface between two different media, the destructive interference is not complete and results in THG signal.

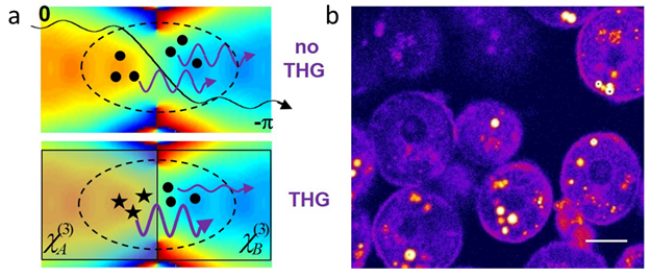

FIGURE 2.26. THG contrast.(a) Origin of THG contrast. Color code for phase ranges from 0 in red to 2π in blue. Adapted from [16]. (b) THG signal from lipid droplets in rat hepatocytes. Scale bar: 10 µm. Adapted from [49].

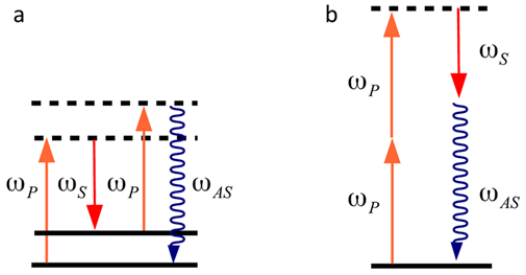

FIGURE 2.27. Nonlinear processes in CARS signal. (a) Resonant CARS (chemically specific signal). (b) Non resonant background. Adapted from [127].

THG signal can therefore be considered as a probe of the local $\chi^{(3)}$ variation. It can be used as a contrast mechanism in biological tissues, to highlight lipids for instance [37] (Fig 2.26b), or more generally to reveal morphological heterogeneities at the scale of the focal volume (blood vessels, vesicles, fibers, etc. For review refer to [183].

2.5.1.2 Coherent anti-raman scattering (CARS)

CARS is another parametric nonlinear process which in contrast to SHG and THG, probes effective vibrational states of molecules [47]. In CARS, the pump beam and the Stokes beam interact in a wave-mixing fashion: when the energy difference between the pump and Stokes beams (ω_P-ω_S) matches the energy gap to reach a particular vibrational of the molecule, resonant oscillators within the focal volume are coherently driven and generate a strong output signal ω_{AS} = $2\omega_P$- ω_S (Fig 2.27). OH and CH vibrational stretches are among the most commonly probed with CARS hence producing a water or lipid specific contrast respectively. Figure 2.28 shows an example of lipid structures in the mouse kidney imaged with CARS. This chemical specificity of the signal is one of the main advantages of CARS microscopy. However, CARS signal does not contain solely the vibrational stretch (Fig 2.28a) and the presence of non-specific contrast

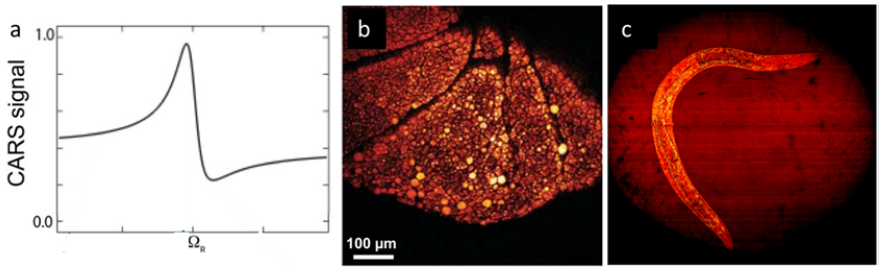

FIGURE 2.28. CARS contrast. (a) Total theoretical CARS signal. (b) Epi-CARS image of the surface of the adipocyte-covered mouse kidney. (c) Epi-CARS image of a live worm, C.elegans. In (b) and (c) the Raman shift is set to the lipid band 2845 cm^{-1}. Adapted from [47][48].

(Fig 2.28c) can sometimes challenge the interpretation of CARS signals.

2.5.2 Multimodal brain-wide imaging using Chrom-SMP

2.5.2.1 THG and CARS contrasts in the brain

THG contrast in the mouse brain have been demonstrated initially in 2011 by two different groups: Farrar et al showed that the main source of THG signal in both fixed and live mouse brain tissue was myelin [184], hypothesizing in passing THG specificity for myelin due to its intrinsic geometrical and optical properties. The study showed, from a horizontal and a sagittal section of fixed mouse brain tissue, strong THG signal in corpus callosum axon bundles and in other white matter brain regions (mossy fibers in the cerebellum, pons, hindbrain). Strong THG was also demonstrated in spinal white matter. Few months later, Witte et al confirmed THG contrast in both live and fixed brain tissue, with strong signal coming from white matter fibers [185]. Additionally, they showed that THG also provides contrast in grey matter areas where neural cell bodies appear negatively contrasted. In 2014, another study used THG to analyse myelination by Shwann cells in the murine sciatic nerve, further confirming the myelin-based THG contrast in the murine nervous system [186].

As for CARS, since the wavelength combination can be set to target the CH2 vibration and because of the high density of CH2 groups in myelin, its contrast sensitivity and specificity to myelin has been demonstrated even earlier: axonal myelin sheaths have been imaged in vivo in murine central and peripheral nervous system, in both healthy [187][188] and pathological conditions [189][190][191]. In the mouse brain, CARS was used to image axon bundles and membranes in white matter regions [192].

In both cases, THG or CARS contrasts in fixed mouse brains were only shown in a single brain section at the largest scale. Also, to the best of our knowledge, simultaneous/correlative THG and CARS in the mouse brain has never been demonstrated so far.

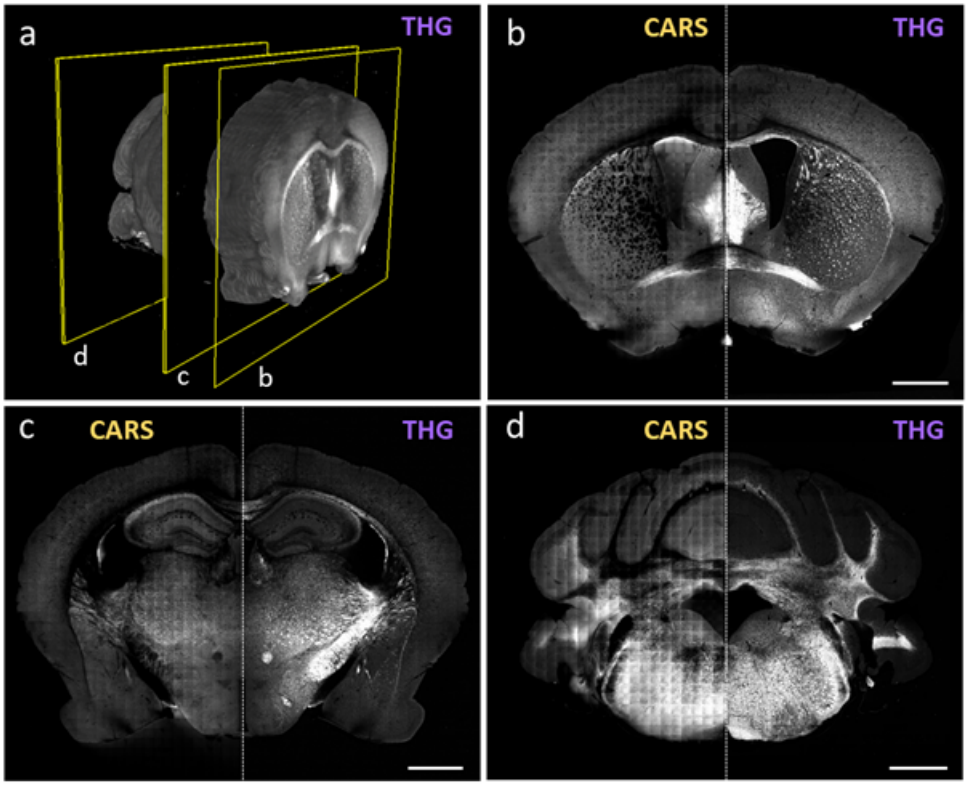

FIGURE 2.29. Brain-wide label-free THG/CARS imaging. (a) Coronal 3D view from the whole-brain THG volume. (b-d) Representative coronal sections showing dual endogenous THG/CARS contrasts acquired with WM-STP. Excitation wavelengths set at 832 nm/1090 nm to match the CH2 stretching vibrational band (Ω = 2845 cm-1) generate a CARS signal detected at 673 nm. THG from the 1090 nm beam is detected at third the excitation wavelength (363 nm). Scale bars: 1 mm.

2.5.2.2 Brain-wide label-free imaging

Here we used the Chrom-SMP system to generate a label-free organ-scale multimodal dataset highlighting cyto- and myelo-architecture in the adult mouse brain (Fig 2.29). The wavelength combination was set to 832 nm/1090 nm, this way targeting the CH2 vibrational band at Ω = 2845 cm-1, while simultaneously permitting third harmonic excitation at 1090 nm. CARS and THG signals were both detected in an epi-configuration, in the red and blue channels respectively. To obtain efficient THG with the ~250 fs OPO beam, the maximum output power was used in this acquisition (P=150 mW). 2D sections were acquired at 30 µm below the surface and the effective CARS field of view restricted the tile size to 200 µm × 200 µm.

Across the brain, both in THG and CARS, contrasts were very diverse and varied across brain areas (Fig 2.29). THG contrast was present in both white and grey matter areas, with strong signal in white matter areas (Fig 2.29, Figure 2.30). Fig 2.30 displays an example of encountered THG contrast: strong signals were observed in the mossy fibers of the cerebellar folia, fasciculated in

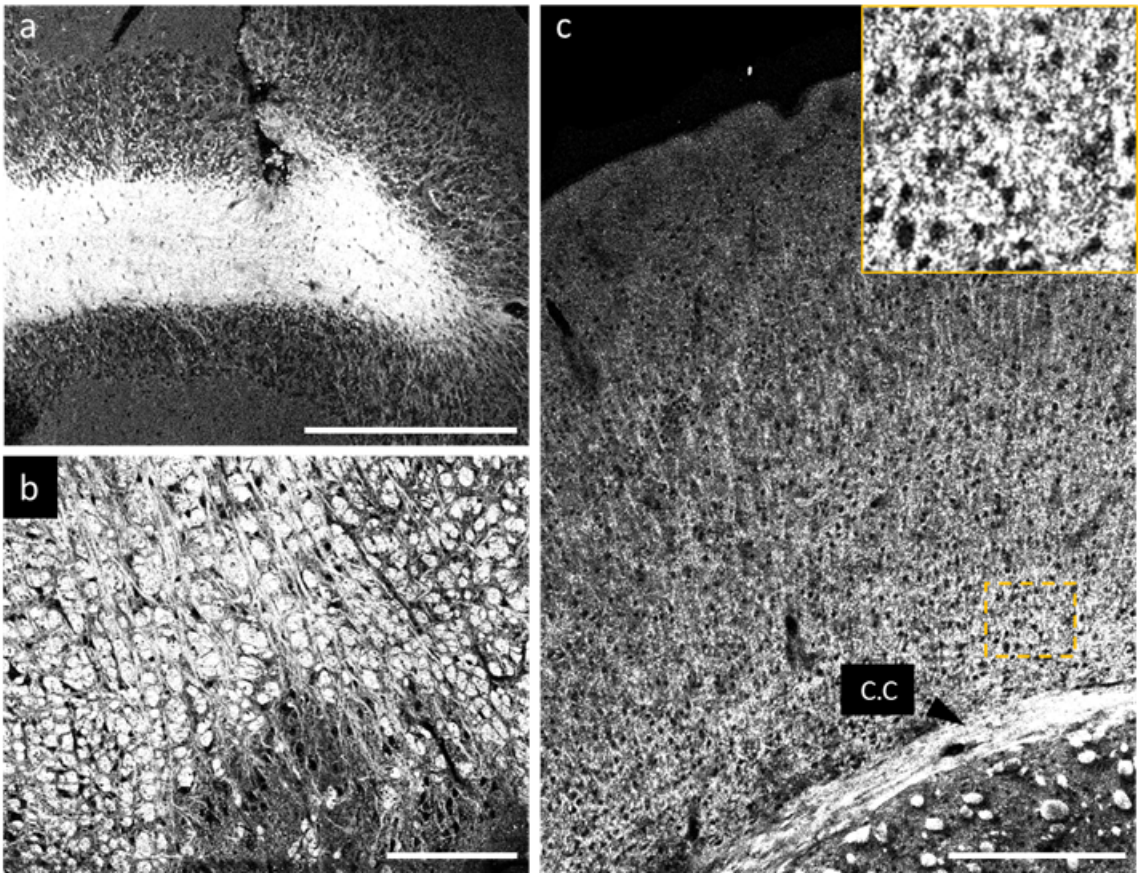

FIGURE 2.30. THG contrast in the mouse brain: (a) cerebellum follium, (b) brainstem and (c) cortex. *C.C: Corpus callosum*. Gamma correction: (a) 0.75, (b) 1.40, (c) 1.25. Scale bars: 300 µm.

the center of the folia and forming a network of surrounding fine ramifications. In the brainstem, radially-oriented fibers could clearly be identified between 'patch-like' structures of different sizes, probably corresponding to myelinated tracts orthogonal to the imaging plane. Expectedly in the forebrain, callosal and commissural large fiber bundles connecting both hemispheres were also visible with THG. In the cortex, neural cell somata were highlighted by inverted contrast (Fig 2.30c). Interestingly, a myelin gradient was observed from deeper to more superficial cortical layers.

In CARS images, fiber-like structures could be identified in several brainstem areas, despite a strong presence of non-specific background throughout the dataset (Fig 2.31). Some large fiber tracts, such as the commissures also exhibited a strong CARS signal. However, quite surprisingly, correlative THG/CARS imaging presented strong differences, despite both contrasts probing myelin in principle. In particular, in some myelin-rich areas such as callosal, striatal fibers (Fig 2.32a-b) and cerebellar mossy fibers (Fig 2.32c-d), THG displayed strong signals, while CARS

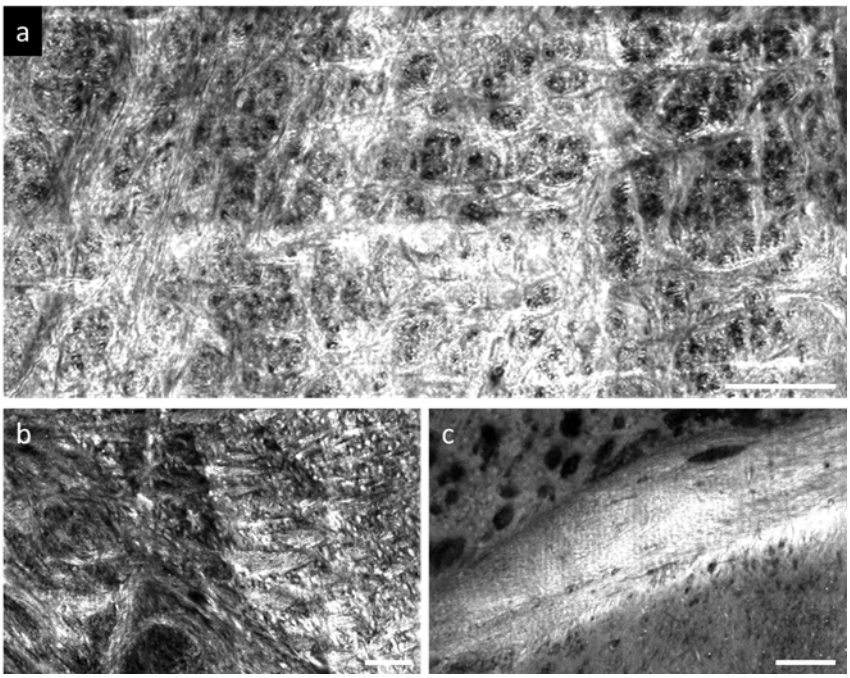

FIGURE 2.31. CARS contrast across the mouse brain: (a-b) brainstem, (c) anterior commissure. Gamma correction: (a-b) 1.20, (c) 1. Scale bar: 100 µm.

contrast appears completely canceled out. An hypothesis would be that due to strong aberrations in these zones, phase matching and/or beam overlap is strongly altered, yielding to very low CARS signals. These data hence suggest that THG might be more robust for investigating myelin organization deep within tissue. THG/CARS image comparisons also revealed strong non-specific background in CARS images (for instance, the ventricle in Fig 2.32b appears 'filled') which makes the images difficult to interpret in terms of myelin content. Nevertheless, non-specific CARS background also provided morphological contrasts complementary to THG, particularly in molecular neuronal layers (cerebellum, hippocampus) and neuropil regions. It is also worth mentioning that since we are using 150-200 fs pulses, the resonant CARS to non-resonant background ratio is not optimal. Strategies such as using chirped pulses [193] or extracting the CARS resonant contribution [194] can be implemented to improve this ratio, although at the cost of increasing the complexity of the system.

Work on these large-scale label-free multimodal datasets is still ongoing to further understand the origin of contrast differences and document contrast heterogeneities across the central nervous system. An appealing perspective is to extend the work to other species (ex: primates). Similarly to the multicolor Brainbow dataset, these datasets will also be publicly to available as a resource upon completion.

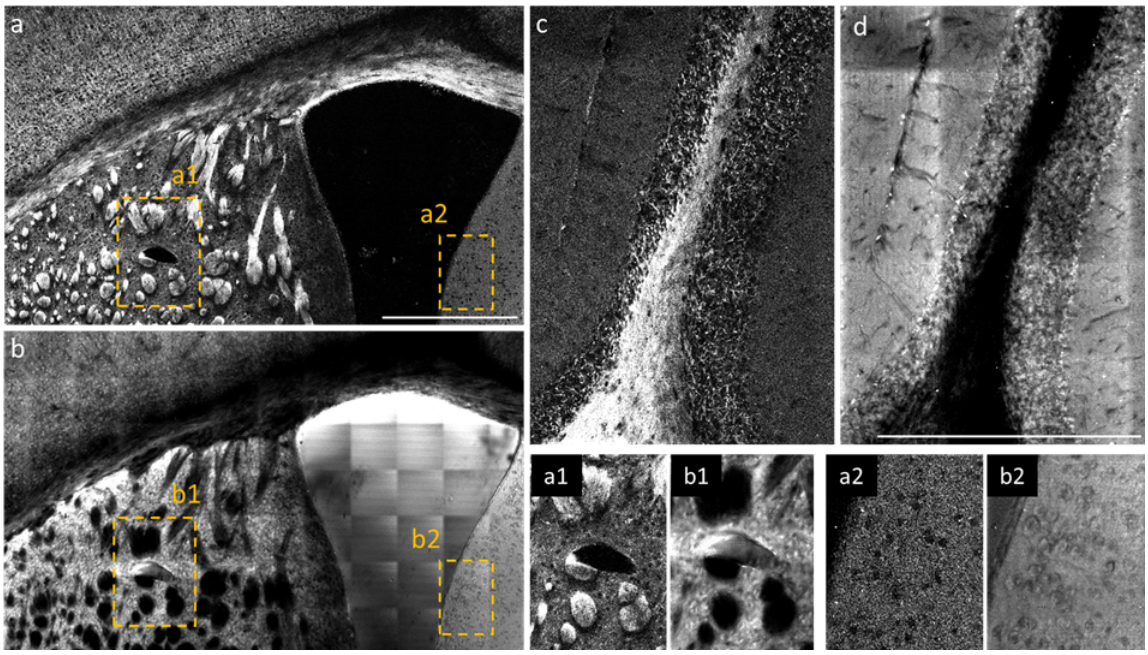

FIGURE 2.32. THG vs. CARS contrasts in the fixed mouse brain. THG (a) and CARS (b) contrasts in the dorsal striatum and lateral ventricle. THG (c) and CARS (d) contrasts in a cerebellar follium. Scale bar: 500 µm.

2.6 Conclusion and perspectives

In this chapter, we have introduced chromatic serial multiphoton microscopy (Chrom-SMP) as an effective strategy to generate large volume multicolor and multicontrast datasets with intrinsic channel registration and controlled chromatic aberrations. We have presented all the aspects of the experimental pipeline we implemented (optics, tissue preparation, image processing) to obtain multimodal large-scale datasets with optimal image quality. In particular, we have demonstrated the first multicolor mouse brain atlas-type dataset imaged at the whole-brain scale with submicron lateral resolution. A variation of the excitation wavelength combination also allowed us to record simultaneous CARS and THG contrasts on the same brain, at the scale of the whole organ, which is also the first time that these contrasts are acquired at such scale. In our demonstrations, the emphasis was made on brain-wide datasets acquired in the tomography mode. Demonstrations of Chrom-SMP operating in the continuous block-face mode will be presented in the next chapter. Meanwhile, we shall discuss in the coming lines the perspectives of bridging these two scales.

A current limitation of the actual Chrom-SMP setup is the imaging speed since typical large-scale acquisitions last ~2 to 4 days. This limitation is however far from being unbreakable since multiple solutions can be envisioned depending on the applications required. In the case of

serial tomography experiments (serial 2D sections), the main speed limitation is the mechanical lateral displacement of the stage. Indeed since the displacement time between adjacent tiles is currently ~1s to prevent motion blur, this scales up to more than 20h for the whole acquisition. An attractive solution to this limitation would be to implement strip-mosaicking scanning as it has been successfully implemented in confocal microscopes for fast 2D histopathological screenings [195]. Strip-mosaicking consists in synchronizing the galvanometers with the lateral movement of one of the stages (the one with the longest range, for instance the stage corresponding to displacement along the medio-lateral axis in case of imaging in a coronal geometry), in order to achieve continuous lateral stage scanning in one direction which would result in a mosaic acquired with rectangular tiles (strips) to be stitched only in one direction. The synchronization needs however to be carefully adjusted to ensure smooth and artifact-free transition between the units of field of view. Also, for quantitative multicolor imaging flat-field correction needs to be readjusted to accommodate such an acquisition scheme.

Further improving the speed of the block-face continuous imaging mode, even up to the organ scale would require a different strategy, based on several cumulated improvements [65] that could be harnessed:

(i) Faster lateral scanning by using resonant galvanometers or a polygonal scanner. The latter would be preferable since it should allow a more flexible adjustment of the scanning speed. It is important to mention that using the scanning system at its full speed capacity will ultimately depend on the strength of FP expression in the sample (cf. (iv)).

(ii) Faster axial scanning by implementing a piezo stage for the objective z-stage, or even a remote focusing module [196] to eliminate the impact of mechanical inertia of the massive objective. This improvement however would only be significant for whole-brain scale acquisitions.

(iii) 'Smart' acquisition schemes such as automated contour detection in order to avoid imaging blank tiles and/or to image only the areas of interest.

(iv) Using very bright labeling and strong excitation power to reduce the pixel dwell time to the minimum necessary to have enough signal to noise ratio. For instance, authors in [65] used strong AAV labeling together with 350-400 mW at the objective output. It is however important to note that such an option is not always implementable since in transgenic lines or electroporated samples, FP expression levels are generally lower than what that can be obtained with AAV vectors. High expression in transgenic lines have recently been demonstrated based on an amplification scheme relying on a positive transactivation feedback loop [197] and could be an effective tool to be harnessed in large scale acquisitions. As regards laser powers, while 350-400 mW at the objective output can be obtained from a Ti:Sa laser, it is more challenging to obtain such power a Ti:Sa/OPO chain since part of the Ti:Sa power is used to pump the OPO.

(v) Increasing the accessible field of view, especially in the case of wavelength-mixing where chromatic aberrations ultimately limit the accessible field of view. This can be achieved by designing a custom objective with a larger field of view and chromatically corrected for the

spectral bands of interest over the large field of view. It is still however challenging to design objectives with both a large field of view and a high numerical aperture. Complementarily or alternately dynamic chromatic aberration synchronized with the beam scanning can be introduced.

Pushed to the maximum, such cumulative approaches can enable the generation of whole-brain datasets with diffraction limited resolution within approx. 7 to 10 days of continuous acquisition (as reported in [65]). Further improving the acquisition speeds would still not be above reach although it would imply a complete redesign of the system since it would require the use of parallel excitation and/or detection strategies (multifocal point-scanning [15] or upright light-sheet geometry [169]).

Yet as the speed of acquisition increases, so too does the amount of potential data generated, and the latter is certainly the most limiting bottleneck of large volume acquisitions. Multi-channel whole mouse brain datasets at full resolution would generate tens of Tb of data for a single brain, which would require a large amount of computational work and infrastructure to be able to store, transfer, visualize and let alone analyze the acquired datasets. But the field is progressing towards handling these issues, with an increasing number of computational scientists involved in large-scale anatomical studies and a general effort to upgrade both open source and commercial analysis and visualization software for a better compatibility with Tb size datasets (for instance improved stitching software [179], improved Imaris versions to visualize large volumes etc.). More developments in hierarchical and/or loss compression image formats are indeed indispensable in order to lighten the informatics pipelines. Computational tools developed for large-scale electron microscopy datasets could be harnessed and adapted for processing, visualizing and annotating large light microscopy datasets. However, in the current state of the art, these developments require custom designed informatics platforms [198] with large GPU clusters for parallel computing and predictive multi-resolution display.

Finally, another potential axis of improvement that would be also facilitated by higher acquisition speeds and better large data handling would be to complement the multicolor fluorescence contrasts with orthogonal biologically relevant stains. For instance live nuclear labeling with DAPI, propidium iodide (PI) or Hoechst stains to be detected on the fourth UV channel could be implemented. The staining agents would be incorporated in the bath and would stain the upper part of the tissue block at each round of acquisition [159]. An important challenge for efficient implementation of such a strategy would be to design an appropriate tissue processing protocol to permeate the tissue to the staining agents over a sufficient depth, while preserving the tissue rigidity for high quality slicing. Similarly live immunological staining can be envisioned although it would substantially increase the complexity of the system. Indeed, it is would require another degree of automation since regulated fluid circulation would need to be implemented in the water tank to allow multiple rounds of washing and/or incubation. This would however be a powerful improvement of the system since it would enable complementary molecular characterization of

the tissues.
Nevertheless, despite these exciting perspectives to further develop the technology, Chrom-SMP in its current form already unlocks a vast number of possibilities and applications in neuroanatomy and way beyond. Examples of such applications will be presented at length in the upcoming chapter.

CHAPTER 3

CHROM-SMP: APPLICATIONS IN NEUROBIOLOGY

Chromatic serial multiphoton microscopy as introduced in the precedent chapter enables the generation of multi-contrast datasets with submicron resolution at unprecedented scales. Hence, combining this technology with genetic or viral multicolor fluorescence labeling enables neuroanatomical and neurodevelopmental studies that rely on these approaches to be performed across extended brain areas. In this chapter we will specifically highlight the capabilities of Chrom-SMP in opening such new experimental paradigms.

We will start by demonstrating the continuous Chrom-SMP acquisition scheme which has only been briefly evoked in the previous chapter. In particular, we will demonstrate the capacity of Chrom-SMP to generate multi-channel datasets of several cubic millimeters acquired with diffraction-limited resolution and multicolor voxel precision. We illustrate how such datasets can be harnessed first for large-scale cortical neuroanatomy, through color-based tridimensional analysis of astrocyte morphology and interactions in the mouse cerebral cortex. Next, in a second part of this chapter, we show how Chrom-SMP opens the way to tridimensional and large areal clonal analysis in the context of cortical astroglial network development. Finally, we also establish the potential of Chrom-SMP outside the combinatorial Brainbow labeling paradigm by demonstrating multiplexed whole-brain mapping of axonal projections labeled with tracers of distinct colors.

3.1 Multicolor volumetric histology

In this section, we demonstrate high-resolution imaging of several millimeter cube-size portions of mouse cerebral cortex encompassing thousands of multicolor-labeled cells captured within their intact environment, in essence large-scale multicolor 3D histology. Our focus here is on

cortical astrocytes which have been shown to form an uninterrupted cellular network throughout the neuropil [199]. Multicolor labeling of astrocytes combined with continuous 3D Chrom-SMP acquisitions provides a unique opportunity to study both their morphology in a high-throughput manner as well as their interactions without biases introduced by tissue sectioning. To this end, we (i) performed a partial anatomical reconstruction of the astrocyte network over a volume of ~1.2 mm × 2 mm × 1 mm with 3D positioning of labeled astrocytes together with the cell bodies of neurons engulfed within their domains, (ii) analyzed astrocyte individual volume variation across cortical layers of more than 130 astrocytes within the same brain and finally (iii) developed an analytical workflow for quantitative characterization of the contact surface between color-segregated neighboring astrocytes.
In the work presented below, electroporated mouse brain samples labeled with the MAGIC markers strategy were provided by Solène Clavreul, a PhD student working on the development of cortical astrocytes with Karine Loulier and Jean Livet at Institut de la Vision.

3.1.1 Multicolor semi-sparse cortical astrocytes labeling

3.1.1.1 Astroglial cells

Astrocytes or astroglial cells are the most numerous glial cells in the central nervous system. These cells have long been thought to merely serve as 'brain glue', providing mechanical support to neurons. This theory has been reconsidered during the last decade as many novel functions have been discovered for astrocytes [200]. In particular, they play a major role in regulating the cerebral blood flow, maintaining the blood brain barrier [201], providing nutrients and metabolic support to neurons [202], buffering potassium and regulating neurotransmitter uptake. Astrocytes have also been demonstrated to play a major role in synapse development, maturation and pruning [203][204] which make them indispensable to the development of neural circuits. Notably, astrocytes can regulate synaptic transmission [205] by releasing gliotransmitters (glutamate, ATP). Recent studies also specifically highlight the role of astrocytes in high order cognitive functions such as memory and learning [206][207]. Finally, changes in astrocytes functions have been also been associated to aging and decline of cognitive functions [208] as well as to pathologies linked to neurodevelopmental and psychiatric diseases [209][210].
Historically, astrocytes have long been considered as a homogenous cell population but there is growing evidence for morphological, molecular and functional heterogeneity in astrocyte populations [211], [212]. Astrocytes can be broadly classified in three main types, although diverse molecular and functional profiles can be found within these large categories: protoplasmic (grey matter) astrocytes, fibrous (white matter) astrocytes and radial glia. In this study, we will focus mostly on protoplasmic astrocytes, the most abundant type in the cerebral cortex.
Protoplasmic astrocytes are distributed in all cortical layers, forming an uninterrupted network of contacting cells (cf. section below on astrocyte tiling) and can be recognized by their characteristic star-shaped and bushy structure (Fig 3.1a). They present several main processes originating from

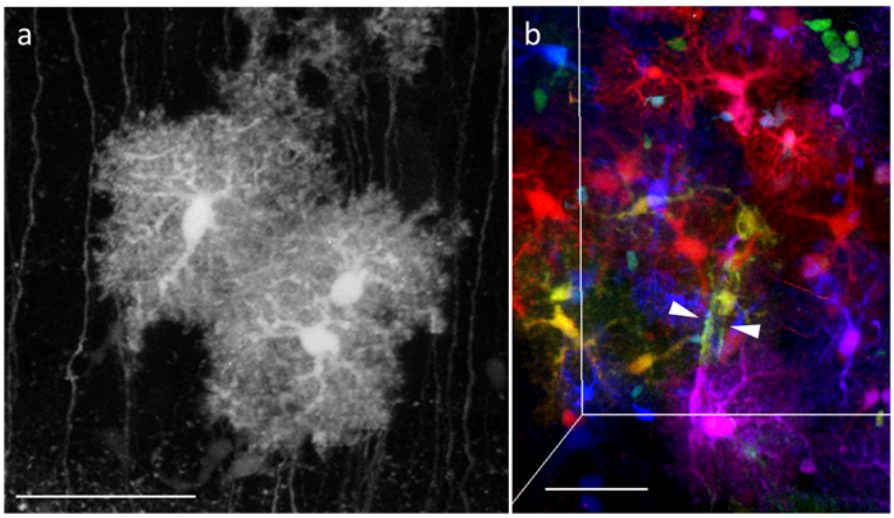

FIGURE 3.1. Protoplasmic astrocyte morphology. (a) Maximum intensity projection over 150 µm shows the "bushy" morphology of astrocytes with their main and secondary processes. (b) 3D rendering of color-labeled astrocytes with arrows showing astrocyte endfeet wrapped up around a blood vessel. Scale bars: 50 µm.

the soma as well as an elaborate arborescence of fine ramifications. These processes cover an extended 3D "domain" that can control thousands of synapses [199]. Astrocytes also contact blood vessels and capillaries through processes wrapping around them called 'perivascular end-feet' (Fig 3.1b). These particular morphological properties confer to protoplasmic astrocytes the unique capability of sensing and integrating multiple cues and signals in their local environment.
Studying astrocytes in intact cerebral tissue faces two major difficulties: (i) **imaging astrocytes** at **high resolution**, **in their entirety**, both at the **local and regional scales**, and (ii) **achieving high-thoughput** characterisation of individual astrocytes within the same region in the same animal. Indeed, most anatomical studies of astrocytes have relied on dozens of micron thick histological sections combined with very sparse targeted labeling, yielding to low throughput measurements within one same brain biased by sectioning artifacts. In this work, we use multicolor astrocyte labeling combined with chromatic serial multiphoton microscopy to characterise astroglial morphological properties with high throughput within a large >mm^3 size volume of mouse cerebral cortex.

3.1.1.2 Multicolor astrocyte labeling in the mouse cerebral cortex

Astrocytes were labeled by targeting their progenitors using the MAGIC marker strategy [99]. *In utero* electroporation was performed in the dorsal telencephalon, at embryonic day 15 (E15). The timing of electroporation was chosen to obtain semi-sparse labeling of a large number of astrocytes, with limited neuronal targeting. Indeed, the generation of neural cell types occurs sequentially during development. In mice, neurons are generated first with a peak of neurogenesis

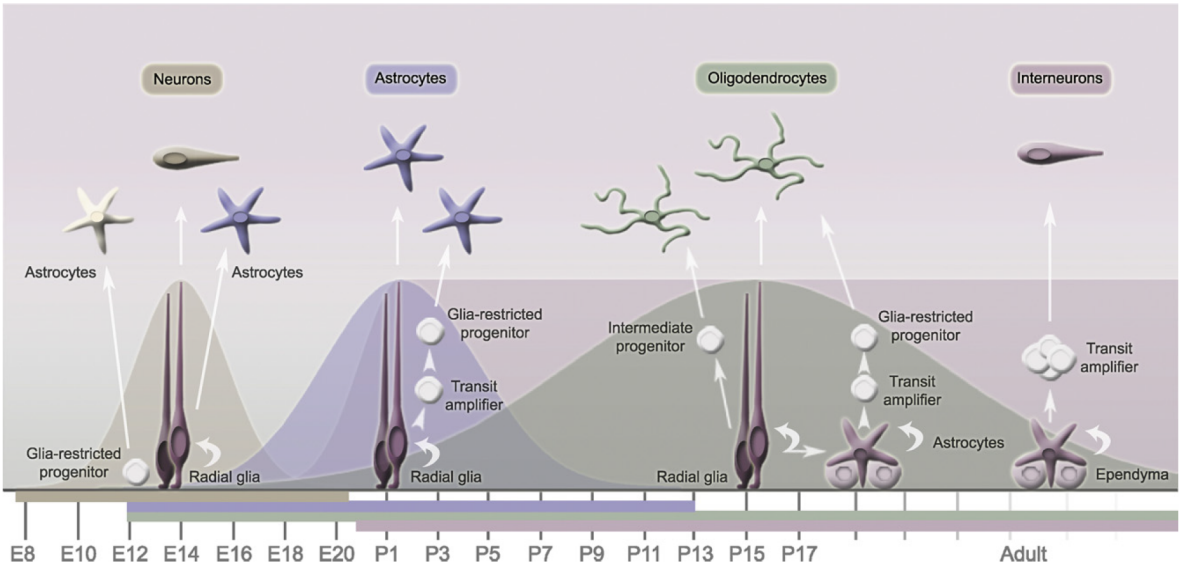

FIGURE 3.2. Sequence of development of neurons and glial cell in the mouse brain. Adapted from [200].

at E14, while most astrocytes and oligodendrocytes are generated at post-natal stages (Fig 3.2). Our reasoning here was to aim for E15, i.e at the end of neurogenesis and prior to the beginning of astrogenesis, so that a majority of astrocyte progenitors would be labeled with few neuronal labeling. Since upper layer cortical neurons are the last ones generated during corticogenesis [213], this strategy resulted in a semi-sparse labeling of astrocytes in all cortical layers, together with neuronal labeling in the upper cortical layers (L2/3).

3.1.2 Continuous high-resolution multicolor imaging over several mm^3 volumes of mouse cerebral cortex

We used Chrom-SMP in the continuous block-face acquisition mode to image a large cortical portion (~5 mm^3) of an adult P65 mouse brain labeled as described above. We were able to image the entire volume with diffraction-limited resolution, at a 0.4 µm ×0.4 µm ×1.5 µm voxel size (Fig 3.3). Of note, the sample was fixed and processed as described in the precedent chapter but no clarification procedure was applied. The dataset consisted in 34 blocks, each block consisting of 4 ×8 tiles. Each tile was a 3D stacks of 68 z-planes (i.e 102 µm imaging depth). Slicing was performed every 60 µm. Typically, each block (i.e 3D mosaic) took 2 hours and 50 minutes of acquisition time. Overall, the dataset captured thousands of color-labelled astrocytes with high-resolution in an extended somato-sensory area.

The following features need to be particularly highlighted to comment on this demonstrative dataset:

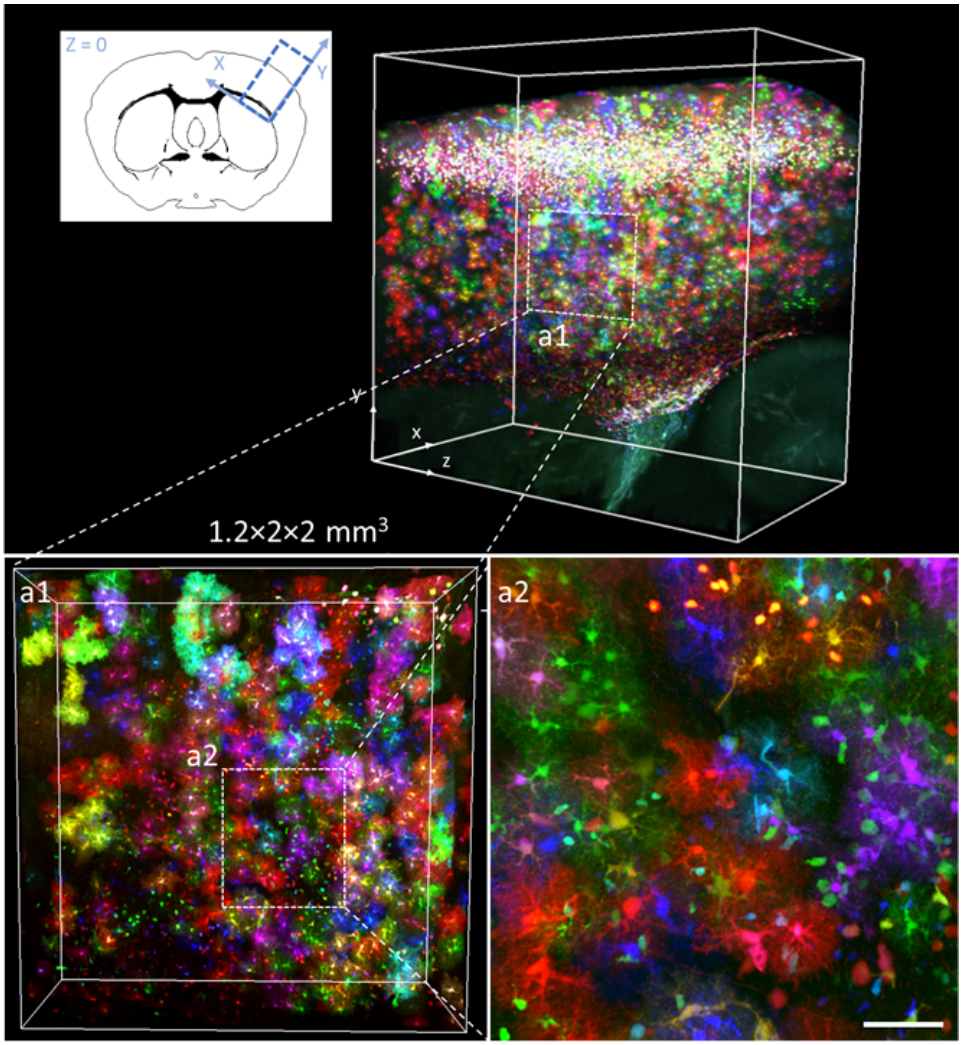

FIGURE 3.3. Multicolor 3D micrometric imaging of a 1.2×2×2 mm^3 volume of a P65 mouse cerebral cortex with Chrom-SMP, showing semi-sparse multicolor labeling with MAGIC markers. Scale bar: 50 µm.

(i) After 3D stitching, the **reconstruction is completely continuous** i.e there is no tissue-loss due to slicing (Fig 3.4).

(ii) Structures of interest could be visualised with **high-resolution** and **multicolor precision** (i.e not affected by chromatic aberrations) within the entire volume. In particular, the cell bodies and main cytoplasmic processes of astrocytes as well as the tridimensional domain of neural tissue occupied by their fine processes were resolved throughout the entire volume. This dataset also demonstrates multicolor axon-level resolution imaging of the densely labeled neurons located in the upper cortical layers (Fig 3.5).

As a result, this dataset is particularly state-of-the art as it sets a new quality standard for micron-scale multicolor large volume imaging over >mm^3 volumes. It is important to recall

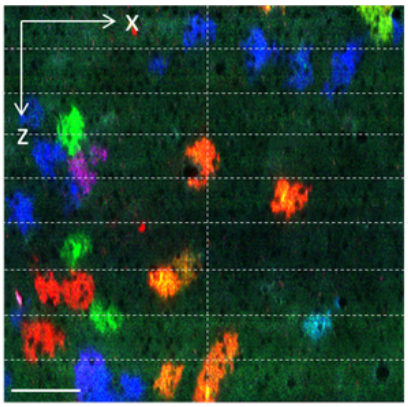

FIGURE 3.4. Continuous 3D stitching. XZ view of 9 successively imaged blocks stitched in 3D, showing the continuity of the dataset in depth. Cellular structures are recovered from one block to another with no tissue loss. Scale bar: 100 µm.

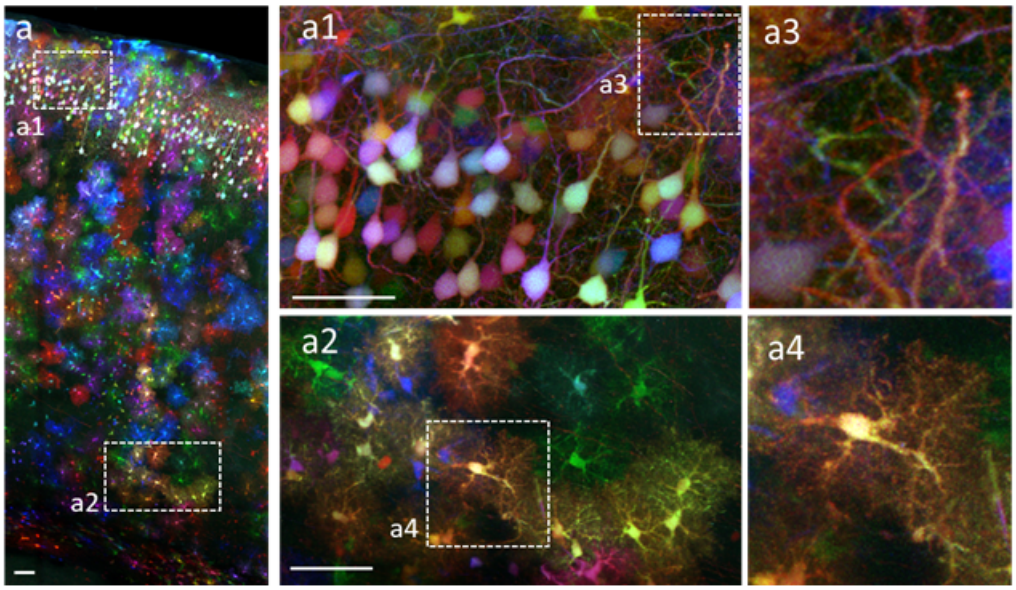

FIGURE 3.5. Maximum intensity projection over 500 µm and XY crops showing high resolution imaging of axons and astrocyte processes with multicolor precision. Scale bars: 200 µm (a) and 50 µm (a1-a2).

here that high-resolution Brainbow imaging has been restricted so far to very shallow volumes, precisely due to technological limitations of microscopy techniques. More generally, despite the outburst of micrometric large volume imaging methods in the recent years, continuous diffraction-limited multicolor datasets of few mm^3 have not been demonstrated so far. This work is, as will be illustrated in the next sections, a first step towards cellular-level quantitative color analyses at the scale of large volumes of cerebral tissue.

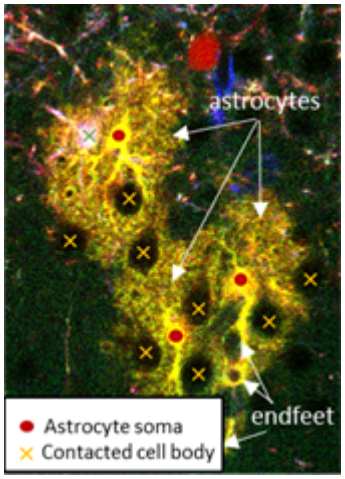

FIGURE 3.6. Astrocyte domains. 2D crop showing a cluster of three astrocytes together with the contacted cell bodies within their territories.

3.1.3 Dense astroglial network reconstruction

As described above, astrocytes are characterized by the territorial domains they form on the neuropil, this way encompassing hundreds of thousands of synapses ('synaptic islands' as termed in [199]) and several neuronal cell bodies. The ratio of neurons to astrocytes within different brain regions has been debated. In our datasets, these domains can be clearly visualized, particularly in 2D z-planes (Fig 3.6). Notably, we can identify the negatively contrasted cell bodies encompassed by the astrocytes territories. These 'hole-like' structures correspond mostly to neurons, as verified by several studies [199][214].

First, we derived a reconstruction of the astroglial network over a depth of 1 mm, from a volume containing 1055 labeled astrocytes which we all positioned in 3D (Fig 3.7). These astrocytes often formed clusters of juxtaposed cells expressing an identical color (n=261), as expected from clonally-related cells generated by local proliferation [215][99]. In this analysis, a 3D color-cluster was defined as an ensemble of astrocytes expressing a same color combination and whose domains are continuously in contact with each other. Individual astrocytes were considered as size 1 color-clusters. For each cluster, the associated relative red, green and blue detected intensities measured within a cytoplasmic ROI were reported onto a ternary color plot (Fig 3.7b), after a linear unmixing procedure performed as described in the previous chapter. On another note, within the set of color clusters present in the dataset, more than 20 different color combinations could readily be discriminated (Fig 3.8).

In each clusters, as the dataset resolution and contrast permitted to unambiguously identify the encompassed cell bodies within astrocyte domains, we pointed the position in 3D of all these contacting negatively contrasted structures. In total, 12265 contacted cell bodies related to the 1055 analyzed astrocytes were positioned. The positioning was done entirely manually as classical

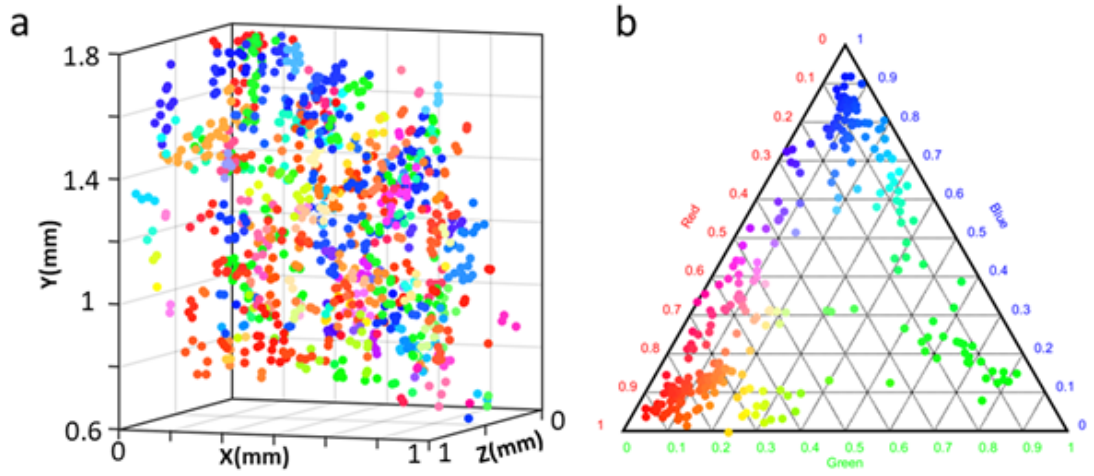

FIGURE 3.7. 3D detection of astrocyte color clusters. (a) 3D positions of the 1055 analyzed astrocytes arranged within 261 clusters. Each dot corresponds to an astrocyte somata and its display color is representative of the relative RGB detected intensities of the associated cluster. (b) Colorimetric positions in the RGB ternary plot of the 261 astrocytes clusters detected in the imaged volume.

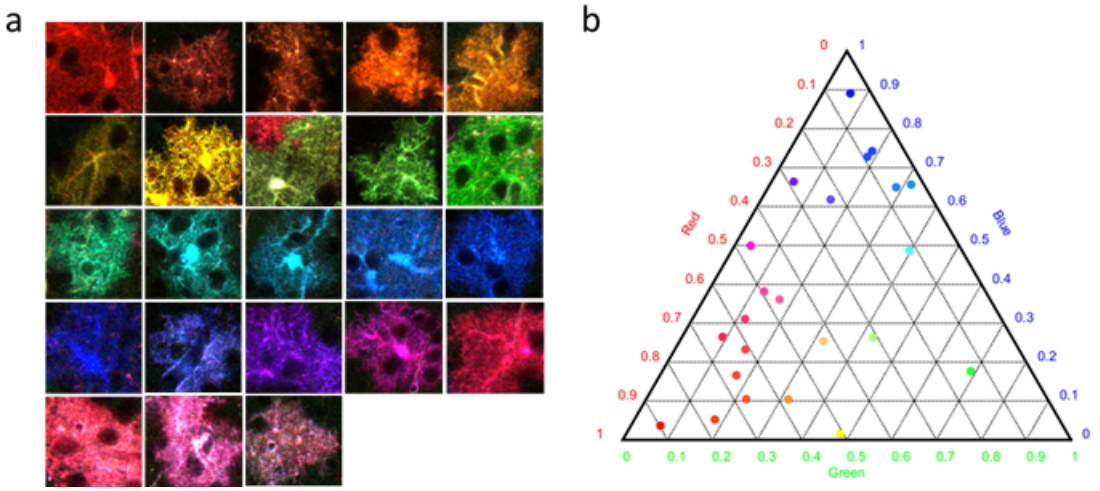

FIGURE 3.8. Example of detected color combinations. (a) Examples of 23 detected astrocytes from distinct color clusters, i.e labeled with distinct color combinations. Shown are crops from the original dataset after linear unmixing (cf. Chapter 2). (b) Positions of the associated relative RGB intensities represented in a ternary color plot.

image processing tools were not adapted to this task, mainly because blood vessels would also appear as 'hole-like' structures and could only be robustly separated from cell bodies by a trained annotator. More specifically, cell bodies were discriminated from transverse blood vessel sections

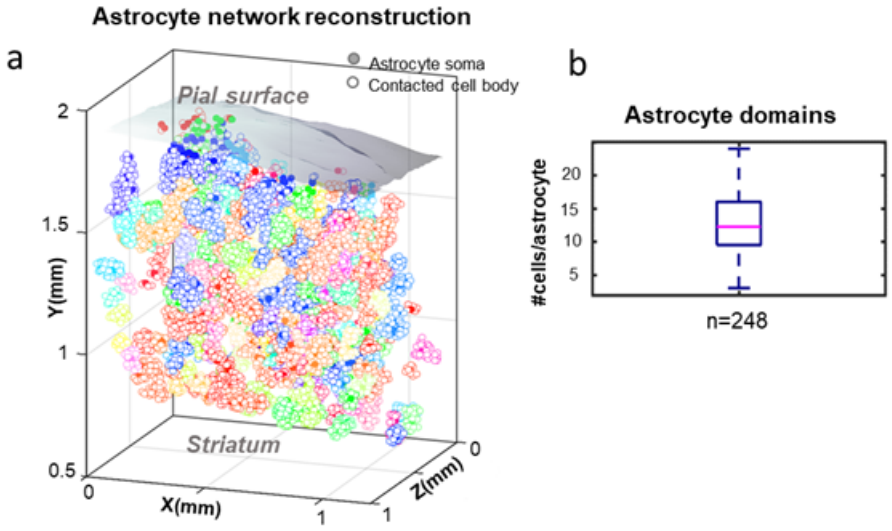

FIGURE 3.9. (a) Reconstruction of labeled astrocytes and their environment in a 1.2×2×1 mm^3 subvolume of the multicolor dataset presented above. The 3D positions of 1055 glial cells forming 261 color clusters and 12265 contacting neurons have been extracted. Color-filled markers correspond to labeled glial cells and white-filled markers to cell bodies visible in the images as negatively contrasted. (b) Mean number of cell bodies in contact with individual astrocytes. Data is presented here as box-and-whisker plots, central magenta mark representing the median value, bottom and top blue box edges indicating the 25th and 75th percentiles, whiskers extending to min and max values of non-outlier data points.

by scrolling upon adjacent upper and lower slices within the z-stack. Cell somata were considered in contact when they were either completely embedded inside the domain or if the edge of the astrocyte border accommodates the shape of the cell. Cell somata were 4 to 6 µm diameter size. Holes with twice this size in the axial direction were considered as stacked cells.

Ultimately, we obtained the reconstruction of astrocyte clusters and their environment presented in Figure 3.9. The pial surface was automatically segmented using intensity thresholding and morphometric boundaries detection. The segmented surface was then downscaled and fitted with linear interpolation for 3D visualization. From this reconstruction, we computed the average soma-to-astrocyte ratio in each cluster and we infered that each mouse cortical astrocyte is in contact with an average of 12 ± 4 (mean ± s.d, n=248) cells.

3.1.4 Individual astrocyte volumes across cortical layers

Next, we sought to characterize the volumes of neuropil occupied by astrocyte domains. The multicolor large volume scheme provides here the opportunity to perform this measurement over an extended cortical area with a large number of analyzed cells within the same brain. Taking advantage of the morphological background, we furthermore describe the variation of astrocyte

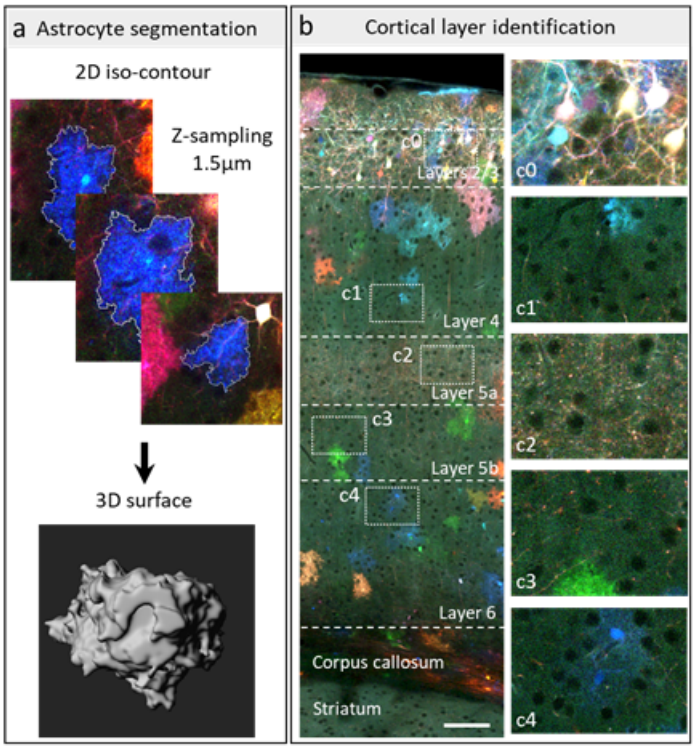

FIGURE 3.10. Methodology for 3D astrocyte volume analysis. (a) Individual astrocyte segmentation. 2D cell contours are traced in each plane of the corresponding z-stack and a 3D surface is generated by interpolating all the successive 2D contours. (b) Morphological criteria used for cortical layer identification. Layers 2/3 are identified by the presence of labeled neurons from in utero electroporation at E15 (c0). Layer 5a, is identified by the presence of visible projections from upper layers pyramidal neurons (c2). Layer 4 astrocytes included in cortical layer analysis were mostly located in the lower layer 4 region, with smaller and densely packed cell bodies (c1). Layers 5b and 6 were discriminated based on cell size and density (c3-c4) and distance to corpus callosum. Scale bar : 100 µm.

volume across cortical layers.

3.1.4.1 Segmentation and cortical layer identification

We segmented in 3D the domain of all isolated astrocytes (single-cell clusters) as well as color-segregated astrocytes i.e astrocytes which could be singled out by color contrast. This resulted in a total of 130 segmented individual astrocytes. The segmentation was performed on Imaris (Bitplane). For each astrocyte, semi-automatic iso-intensity contours were drawn in all planes of the z-stack containing the cell (Fig 3.10). When the iso-intensity contour tool did not provide accurate segmentation (low color SNR), contours were defined manually. Segmented astrocytes were then classified into cortical layers based on morphological landmarks (cf. Fig): layer 2/3

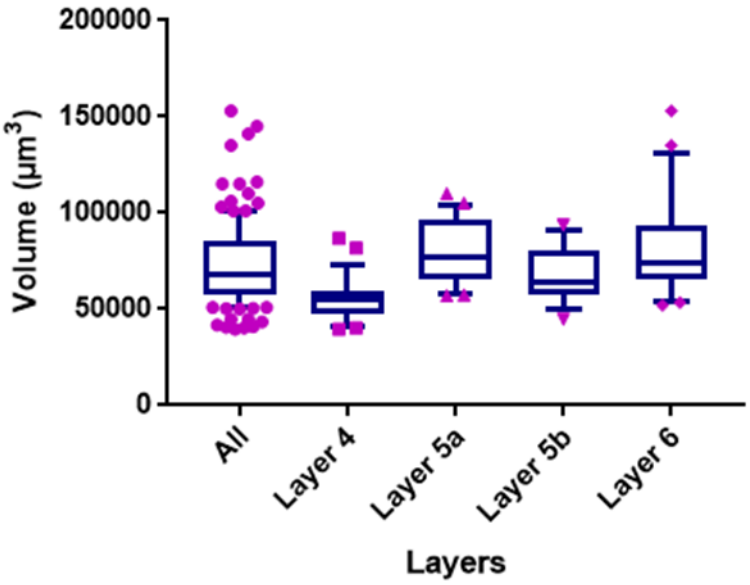

FIGURE 3.11. Volume of the 130 segmented astrocyte domains and volume distributions across cortical layers (layer 4: n=30, layer 5a: n=22, layer 5b: n=19, layer 6: n=43). Data are presented as box-and-whisker plots, central mark representing the median value, bottom and top blue box edges indicating the 25th and 75th percentiles, whiskers extending to 10th and 90th percentiles. Data outside the 10th to 90th percentile range is scatter plotted (magenta dots). Non-parametric one-way statistical test (Kruskal-Wallis) followed by post hoc multiple comparison tests (Dunn) indicates strong significant difference between layer 4 and layer 5a distributions (adjusted p-value< 0.0001) and between layer 4 and layer 6 distributions (adjusted p-value< 0.0001).

was identified by the neuronal labeling resulting from E15 electroporation [216]; layer 5a was discriminated using visible projections from layer 2/3 pyramidal neurons [216]; and layers 5b and 6 were discriminated based on cell density, size and distance to the corpus callosum. Only astrocytes that could be unambiguously attributed to a specific cortical layer (as defined above) were considered for analyses.

3.1.4.2 Astrocyte volumes

We derived from the 3D segmentation an average astrocyte volume of 7.3×10^4 µm^3 ± 2.2×10^4 (mean ± s.d, n=130) with a median value at 6.8×10^4 µm^3. The average value found in our study is close to the one measured for single cortical astrocyte territories measured *in vivo* (6.4×10^4 µm^3 ± 4314 in [217]). Interestingly, our measured value was less coincident with two previously reported studies on cortical astrocyte volumes performed on fixed tissue slices: Halassa et al. reported a volume of 2.4×10^4 µm^3 for a single cortical astrocyte [199], while a very recent anatomical study on cortical astrocytes reported a mean astrocyte volume larger than 9×10^4 µm^3 [211]. Such

discrepancies could be explained by a difference in the tissue processing protocol employed: in the former study, 300 µm tissue sections were mounted in sucrose, a mildly clearing dehydrating agent while in the latter 400 µm tissue sections were mounted in a Cubic hyperhydrating clearing medium [9]. Indeed, in order to capture a sufficient number of complete 3D astrocytes thick tissue sections are required, therefore to image such preparations with a standard confocal microscope, tissue clarification is indispensable. This approach inevitably induces a bias since dehydration-based clearing methods are associated with tissue shrinkage while hyperhydration-based methods tend to enlarge the tissue size. This further confirms the interest of Chrom-SMP for anatomical studies with minimal biases, since Chrom-SMP datasets are acquired on intact uncleared tissues. Besides, it is worth mentioning here that in each of the cited above studies, 5 animals were required to obtain about a hundred of cells that can be entirely segmented in 3D. In our study, 130 cells were analyzed within a single mouse brain. This number could be further increased by refining the labeling strategy, for example by postnatal electroporation of MAGIC markers at P0 which should lead to more individualized clusters.
We then investigated the variation of astrocyte territorial volumes across cortical layers. Since the acquired dataset did not contain enough singled-out astrocytes in upper cortical layers (layers 1 and 2/3), the analysis focused on deep cortical layers (layer 4 to 6). Notably, this analysis revealed a significant volume difference (adjusted p-value<0.0001) between layer 4 astrocytes (5.8×10^4 μm^3 ± 1.9×10^4, n=30, median=5.5×10^4 μm^3) and astrocytes located in projection layer 5a (8.1×10^4 μm^3 ± 1.7×10^4, n=22, median=7.7×10^4 μm^3), as well as a significant volume difference between layer 4 astrocytes and deep layer 6 astrocytes (8×10^4 μm^3 ± 2.2×10^4, n=43, median=7.4×10^4 μm^3). This finding goes in line with the growing evidence for morphological, molecular and functional heterogeneity of astrocytes ([212], [211]).

3.1.5 3D reconstructions of astrocyte-astrocyte contact

Finally, we present a method to quantitatively characterize in 3D the tiling of the astroglial network from our large-volume multicolor data.

3.1.5.1 Astrocyte tiling

In the mouse brain, protoplasmic astrocytes have been demonstrated to occupy exclusively non-overlapping territories of the neuropil, first in the hippocampus [218] and then similarly in the cortex [199]. In other terms, astrocytes form an uninterrupted cellular network tiling the the cortical grey matter. This 'patchwork'-like arrangement can be visualized with very dense multicolor astroglial labeling (Fig 3.12). This structural arrangement has been demonstrated to underly a functional organization related to astrocyte-neuron interactions: astrocyte territorial domains can be considered as functional 'synaptic islands', where all synapses encompassed within a given volume are regulated by a single astrocyte [199]. In this work, we take advantage of the multicolor labeling to analyse the spatial relationships between neighboring astrocytes

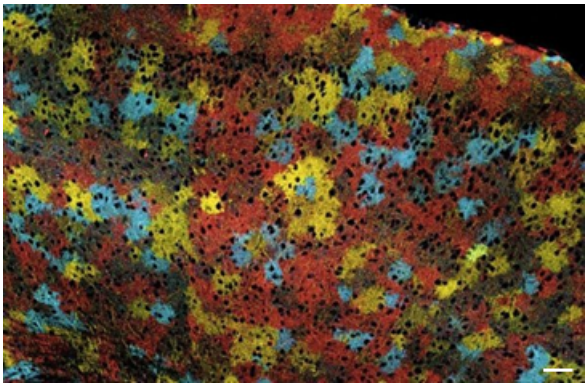

FIGURE 3.12. Dense Brainbow astrocyte labeling. Adapted from Livet et al ([76]). Scale bar: 50 µm.

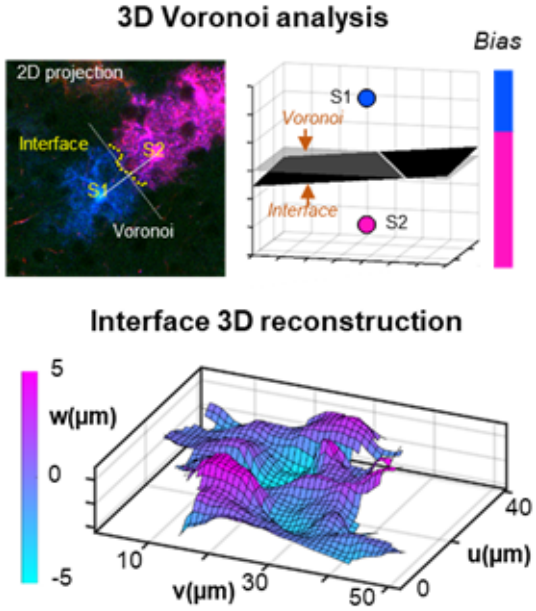

FIGURE 3.13. Morphological analysis of astrocyte-astrocyte contacts. The interface is compared to the median position given by a Voronoi tessellation then reconstructed in 3D within the interface framework. The bias parameter corresponds to the proportion of interface above or below the Voronoi plane.

labeled with distinct FP combinations within our 5 mm^3 imaged cortical volume. To this end, we developed an analytical workflow to reconstruct contact interfaces in 3D and to characterize astrocyte tiling as compared to an equi-parted Voronoi arrangement (Fig 3.13).

3.1.5.2 3D interface reconstruction

The workflow to analyse the contact interface between neighboring astrocytes is summarized in Fig 3.14.
(i) First, taking advantage of the color contrast between two neighboring astrocytes A_1 and A_2 , the contact frontier is segmented using a discrete set of coordinates (x_i, y_i, z_i) in the acquisition frame XYZ.
(ii) The 3D positions xA_1,yA_1,zA_1 and xA_2,yA_2,zA_2 of A_1 and A_2 somatas define the Voronoi axis, with $\mathbf{A_1A_2}$ being set as the axis orientation vector. We define the Voronoi plane as the plane perpendicular to the Voronoi axis and passing through the astrocyte pair midpoint M defined as the center of the [A1A2] segment.
(iii) Interface 3D coordinates are then expressed in the Voronoi frame and fitted with a 2D polynomial function. The resulting fitting plane define the interface plane. We compute the angle between the Voronoi plane and the interface plane that we term orientation parameter. This parameter indicates how much the interface deviates from the equi-distal Voronoi plane. We also compute the ratio of interface points above the Voronoi plane in the Voronoi frame, which we call the bias parameter. This parameter characterizes wether astrocyte territories are leaning more towards one cell or if the interface is equiparted.
(iv) We use the interface plane and a corresponding normal vector to define the local interface frame.
(v) 3D interface coordinates are in turn expressed in the local interface frame and fitted with a biharmonic surface model. This step provides a 3D reconstruction of the interface in the local framework.
(vi) Interfaces are then semi-automatically detoured and amplitude and gradient maps are generated. Gradient maps are calculated as:

$$\frac{\partial w}{\partial u}.\frac{\partial w}{\partial u}+\frac{\partial w}{\partial v}.\frac{\partial w}{\partial v} \tag{3.1}$$

Quantitative mesoscale characterisation of the interface in 3D can therefore be obtained.

3.1.5.3 Results

We analyzed n=9 dual-color astrocyte pair. For each pair, we reconstructed in 3D the surface of contact and analyzed its position and orientation relative to the cell-cell median plane given by a Voronoi tessellation based on astrocyte soma positions (Fig 3.15). This analysis revealed frequent imbalance in the positioning of the limits of astrocyte cytoplasmic domains with respect to the median plane (mean bias parameter 75.2% ± 15.2 (s.d)), and showed that the tiling of the cerebral cortex by astroglial cells deviates from an equiparted Voronoi geometry. However, these are preliminary results and more measurements are required to fully characterize the tessellation of the astroglial network. Here again, a postnatal electroporation strategy could increase the number of interfaces to be analyzed.

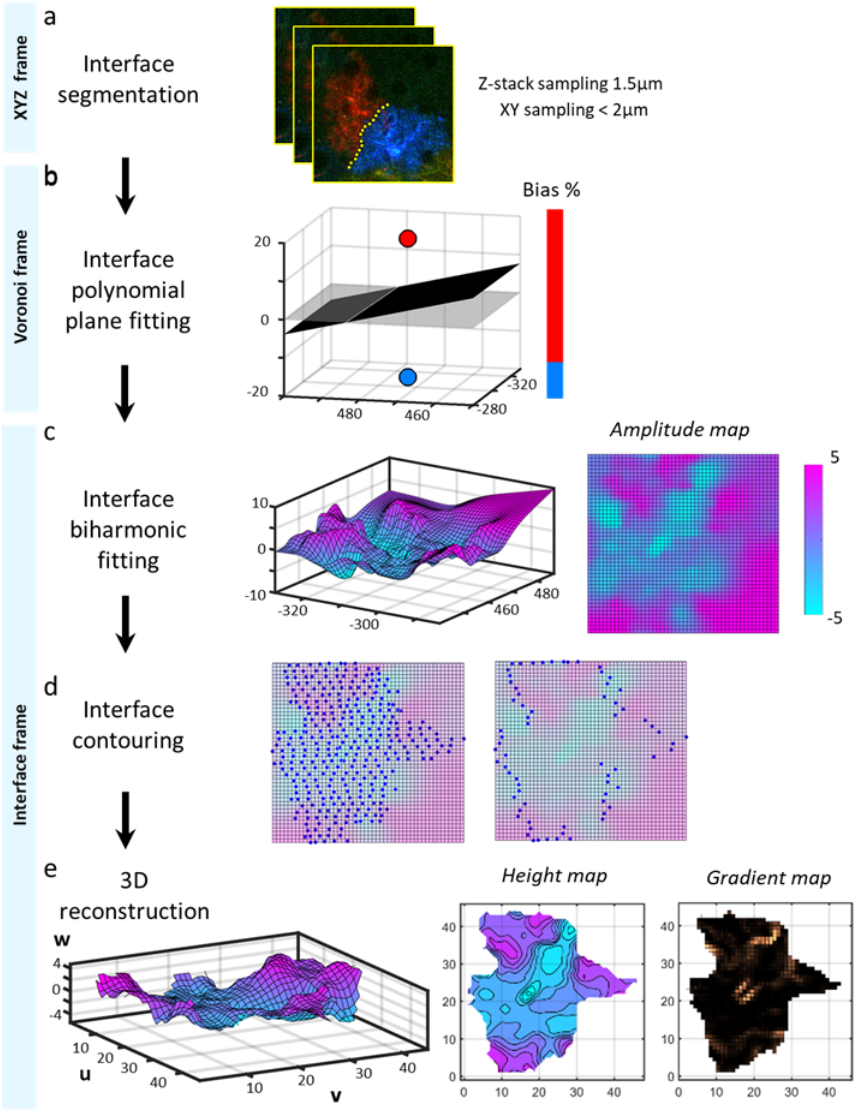

FIGURE 3.14. Astrocyte-astrocyte contact processing workflow. (a) Interface segmentation of color-segregated astrocyte pair. (b) Interface representation in the Voronoi frame. In grey : Voronoi plane. In black: interface plane. Binary color bar represents the bias parameter (ratio of interface points above the Voronoi plane). (c) 3D Surface fitting in the interface frame Sampling : 1 µm x 1 µm. (d) Projection of interface points onto the interface plane (left). Contour points are defined as the most distant points on each interface z-stack plane (right). (e) 3D interface reconstruction and derived height and gradient maps. 3 × 3 median filtering is applied on the 1 µm × 1 µm surface fit to generate the height map. Black lines on the height map represent altitude isolines referenced to the interface plane. Axis units: µm.

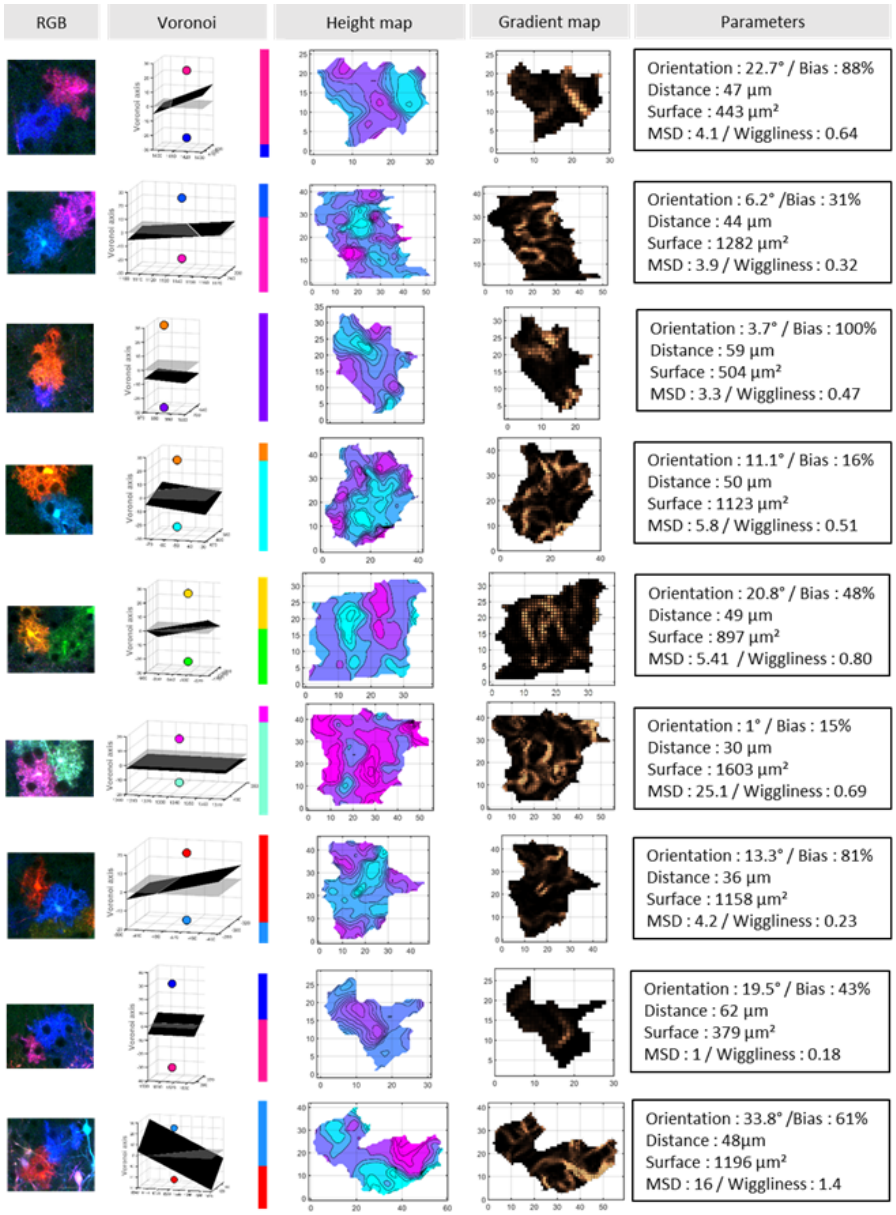

FIGURE 3.15. Inventory of analysed astrocyte color pairs. Orientation: angle between the Voronoi plane and the intereface plane in the Voronoi frame. Bias: Ratio of interface points above the Voronoi plane. Distance: distance between the two astrocyte somata. Surface: interface area. MSD: mean square distance parameter computed as the total sum of square amplitudes divided by the interface area. Wiggliness: total sum of the gradient parameter (as defined in equation (3.1)) divided by the restricted interface area. Restricted interface area is defined as the interface area with a finite gradient parameter value i.e borders of the interface area are excluded.

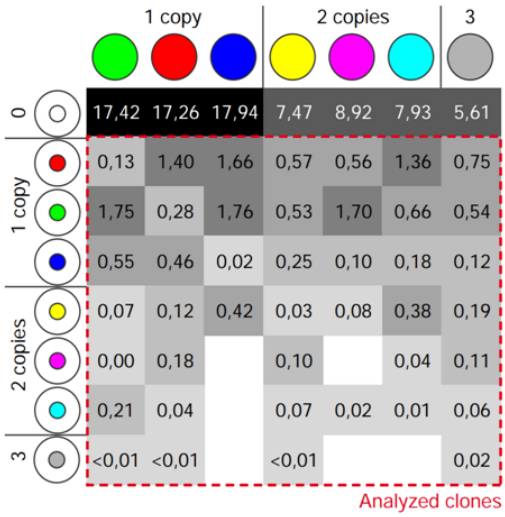

FIGURE 3.16. Relative frequency of observed color combinations in mouse cortical samples labeled with a dual-compartment Nucbow/Cytbow MAGIC marker strategy (*Courtesy of Solène Clavreul*).

3.2 Large volume clonal analysis

In this section, the combination of a dual-compartmented MAGIC marker labeling strategy and continuous 3D Chrom-SMP acquisitions is used to characterize the development of the astroglial network in the mouse cerebral cortex. The work presented below is part of a collaborative project led by Solène Clavreul, Karine Loulier and Jean Livet at Institut de la Vision. My contribution to this project was to acquire and process the 3D continuous volumes. Analyses were then performed by Solène Clavreul.

3.2.1 Multicolor astrocyte clonal labeling

Mouse brains are electroporated with MAGIC markers [99] at E15 as described above. Electroporation is performed in embryonic ventricles to target SVZ progenitors prior to the onset of astrogenesis. This strategy results, as described above, primarily in the labeling of cortical astrocytes, together with L2/3 neurons and SVZ progenitors, identified from astrocytes by their morphology. However, in order to achieve lineage analysis with single-progenitor precision, a compartmented MAGIC marker strategy was employed. The Nucbow and Cytbow constructs [99] were used simultaneously to achieve independent stochastic combinations in both nuclei and cytoplasms of labeled cells. For clonal analysis, only rare color combinations corresponding to cells displaying at least 1 copy of both Nucbow and Cybow were selected. Figure 3.16 presents the relative frequency of observed color combinations, calculated from a set of 57535 astrocytes from serial confocal datasets (n=12 animals).

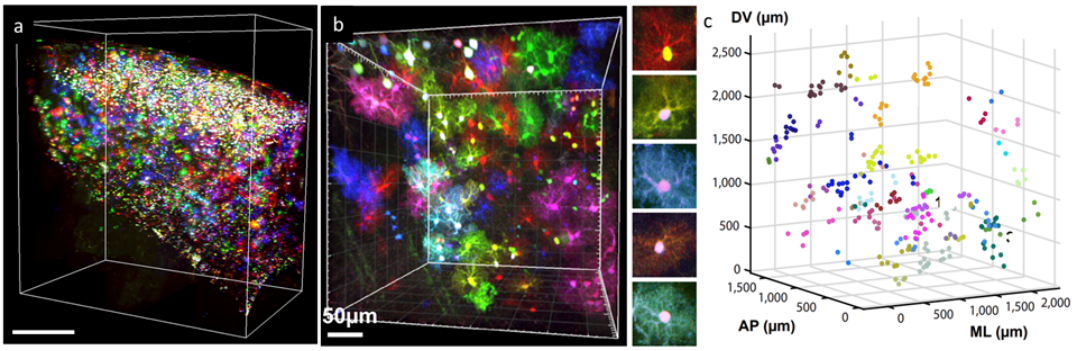

FIGURE 3.17. Large volume multicolor clonal analysis with Chrom-SMP. (a) >mm^3 volume of electroporated mouse cerebral cortex labeled with the dual-compartment Nucbow/Cytbow MAGIC marker strategy. Scale bar: 500 µm. (b) 3D crop within an acquired cortical volume at P21 showing the tridimensional arrangement of astrocyte clones. (c) Astrocyte clones spatial distribution.

In the study presented below, brains were analyzed at two different postnatal developmental stages: P7 and P21.

3.2.2 3D large volume clonal datasets

We acquired n=2 Chrom-SMP continuous 3D datasets for each developmental timepoint. Multicolor mm^3 volumes were imaged with similar conditions as the ones described in the first section of this chapter. A main difference was that here, sagittal sections were performed, instead of coronal sections. Figure 3.17 shows a representative cortical volume, with the dual-labeled astrocyte clones arranged in 3D. The 3D positions of these clones were retrieved to analyze the spatial arrangement of the clones. Clones were identified as cells displaying the same rare color labels and within a maximum 300 µm distance between each other. Following these criteria, few dozens of clones could be entirely captured within each of the four continuous large volume datasets. This further enhances the relevance of Chrom-SMP in clonal analysis of the highly extended cortical astroglial networks since several mm^3 of cortical volume is required to capture few dozens of clones.

We present in Figure 3.18 2D crops maximum intensity projections from the acquired clonal datasets, at P7 and at P21. These images are representative of the acquired datasets, and morphological differences between astrocytes at both stages can be observed. Notably, one can observe from the high-resolution insets a complexification of the astrocyte bushy structure between the two stages. 3D domains of individual astrocytes were segmented as described in the previous section and a significant volume increase was reported between P7 and P21.

Beyond these morphological analyses, analysis of the clonal 3D spatial arrangements were performed by S.Clavreul and colleagues from the Chrom-SMP datasets. Figure 3.20 briefly presents some of these results: large clonal dispersion, superior to 100 µm, was reported in all

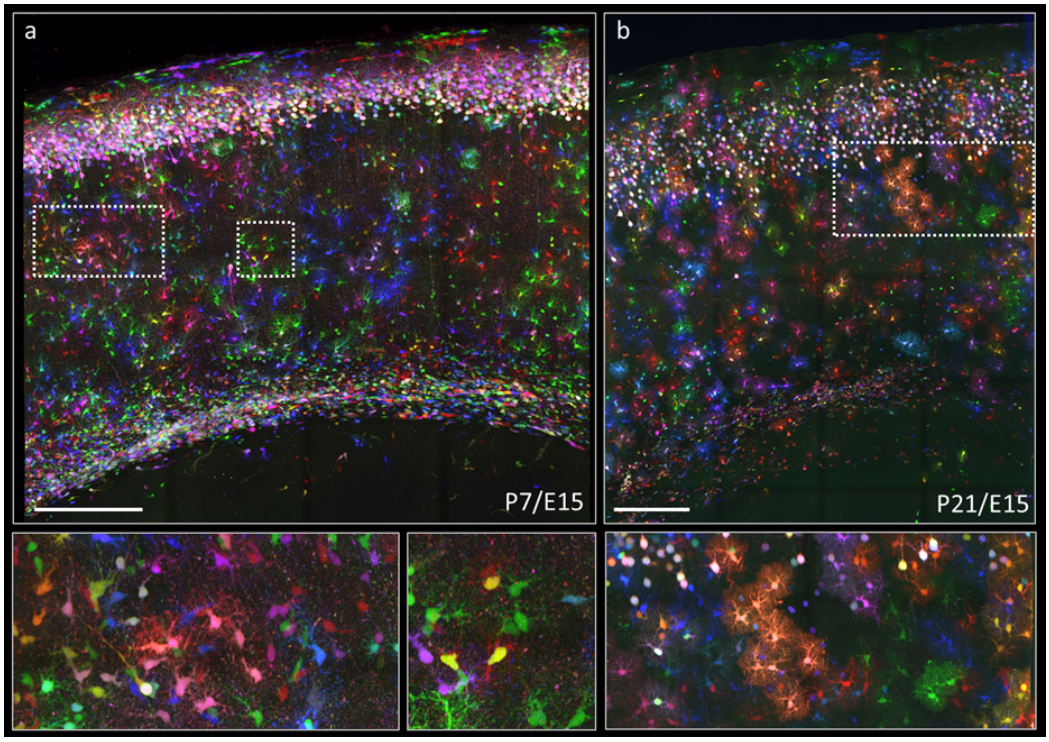

FIGURE 3.18. Cortical astrocyte clones at different developmental stages: (a) P7 and (b) P21. Maximum intensity projections over 500 µm. Scale bars: 200 µm.

three directions and at both developmental stages, contrarily to what was found using serial section analyses [115], and with a particularly prominent dispersion in the dorso-ventral direction. Interestingly, the 3D dispersion was found constant between the two stages. This result, combined with the morphological analyses suggest a two-step astroglial network development process with first a dispersion phase, followed by a maturation phase with no significant spatial dispersion. Spatial analyses within clones were also performed, and revealed that clones are topologically organized into separated ensembles of cohesive clusters. This result further confirms clonal dispersion during development, and suggests the spatial intermixing of clones from distinct progenitors within the astroglial network.

3.3 Whole-brain multiplexed projection mapping

In this section, the experimental paradigm is shifted compared to the studies presented above. The main focus here is to illustrate how the combination of whole-brain Chrom-SMP tomography and non combinatorial multicolor AAV labeling can be leveraged for mesoscale connectomics to image multiple long-range projections within the same brain.

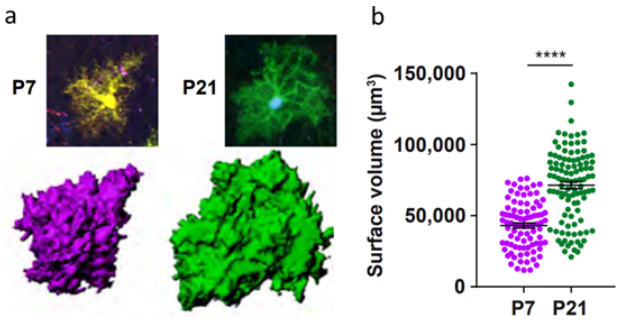

FIGURE 3.19. Volume of cortical astrocytes at two developmental stages: (a) 3D domain segmentation and (b) volume analysis results.

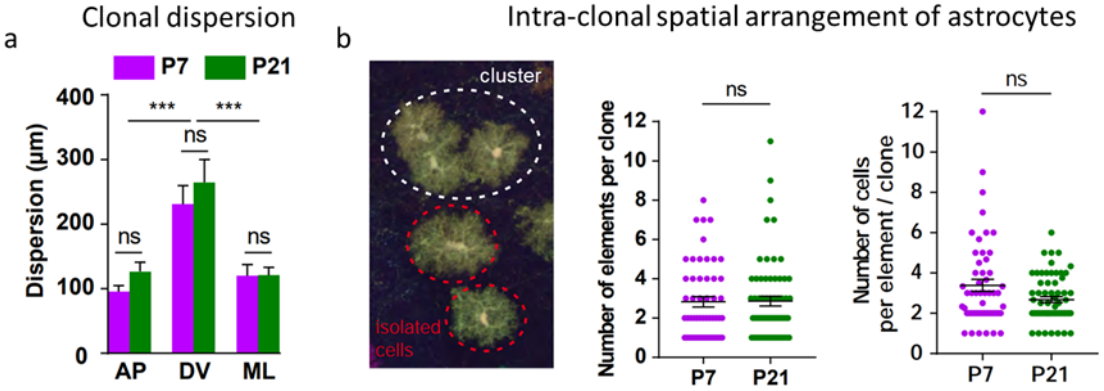

FIGURE 3.20. Analysis of the 3D spatial arrangements of astrocyte clones. (a) 3D Clonal dispersion at P7 and P21. (b) Arrangement of astrocytes within the analyzed clones at P7 and P21.

3.3.1 STP tomography-based mesoscale connectomics

As mentioned in the previous chapters, mapping the brain connectivity at the cellular-scale is a long-standing and important challenge in neuroscience. The STP technology combined with the strong initiative from the Allen Brain Institute in Seattle has permitted to make a giant step forward towards this aim.

In the Allen Brain mouse brain connectivity atlas project [86], 469 whole-brain tomography datasets have been sytematically acquired with the TissueCyte®1000, the commercial STP system developed by TissueVision (Cambride, MA). For each of the 469 brains, viral EGFP-AAV labeling was delivered in a stereotaxically defined injection site and long-range axonal projections imaged throughout the brain. In total, the injection site targeting resulted in an almost complete coverage of the brain surface. 2D sections were performed every 100 µm with 0.35 µm lateral sampling. Figure 3.21 shows examples of projection patterns obtained from the STP datasets in several subcortical and brainstem structures (striatum, thalamus, zona incerta,

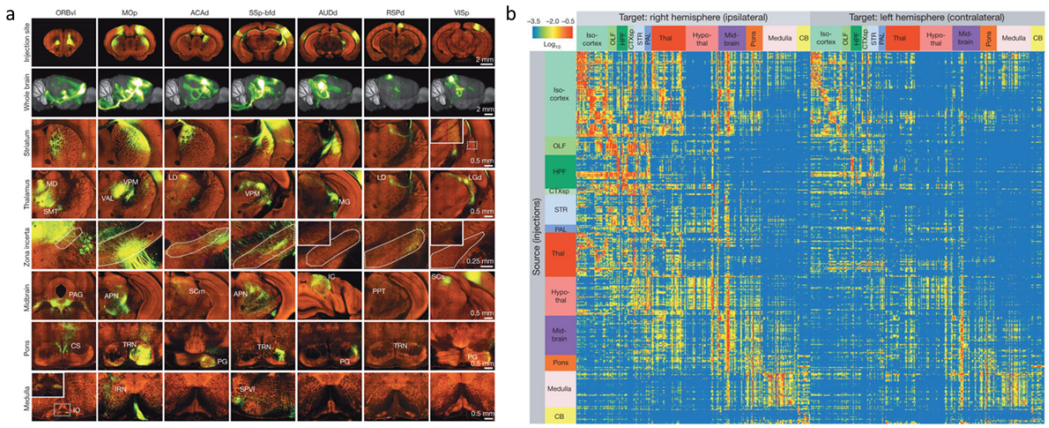

FIGURE 3.21. An example of mesoscale connectomics: The Allen mouse brain connectivity atlas project. (a) Projection patterns from seven representative cortical regions. (b) Brain-wide connectivity matrix. Each row displays the quantitative projection signals from one of the 469 injected brains to each of the 295 non-overlapping target regions (in columns). The color map indicates $\log_{10}$- transformed projection strength. The projection signal strength between each source and target is defined here as the total volume of segmented pixels in the target (summed across all voxels within each target), normalized by the injection site volume (total segmented pixels within the manually drawn injection area).

midbrain, pons and medulla) and from 7 different cortical injection areas. For each brain, 2D sections were segmented and registered to a template brain obtained by averaging 1231 mouse brains. Fluorescence signals were segmented from the brain datasets and associated to the atlas registration to produce a quantitative mesoscale connectivity matrix as presented in Figure 3.21 where the color is coding for the inter-areal connectivity strength.

Besides the Allen Brain gigantic effort, lab-scale quantitative connectivity studies are increasingly emerging thanks to the diffusion of the STP technology in several microscopy plateforms [219][220][165].

3.3.2 Multiplexed projection mapping with Chrom-SMP

In this part of the Chrom-SMP project, the goal was to demonstrate how Chrom-SMP microscopy can enhance the possibilities offered by monochrome STP for mesoscale connectomics. The experiment that will be presented here was designed by myself together with Katie Matho who performed the stereotaxic injections on the mouse brains. AAV plasmids were provided by the team of Alexis Bemelmans at CEA, Fontenay-aux-Roses.

3.3.2.1 Brain-wide multiplexed projection mapping

Interrogating the anatomical convergence and segregation of axonal projections from different sets of neurons across large distances is essential to understand how information is relayed across the distinct functional areas of the nervous system. Until now, structural and functional studies of interacting projections have mostly relied on registration of different tract-tracing datasets to a common framework, usually obtained by averaging multiple datasets to generate a reference brain template [86][221]. Yet, using distinct color labels can more precisely inform on the anatomical relationships between different tracts in the same brain volume [222][223][172], but a convenient approach to map these labels in 3 dimensions has been lacking. Here, using Chrom-SMP microscopy, we achieved **one-shot whole-brain tricolor projection tract imaging** on mouse brains injected with three distinct anterograde AAV tracers (AAV-dTomato, AAV-EYFP and AAV-mTurquoise2) emitting respectively in the red, yellow and cyan spectral ranges, and delivered in three discrete locations of the sensorimotor cortex. Figure 3.22a shows representative 3D and 2D views of the dataset after stitching.

As presented in the introduction chapter, AAV-based labeling is widely used in neuroanatomical and circuit studies as it enables fast, efficient and versatile labeling of neurons and their long-range projections. In this demonstration, the AAVs were delivered by 3 distinct intracranial injections, spatially localized by pre-defined stereotaxic coordinates, onto 11 week old C57Bl6 female mice. Recombinant AAVs were based on a single-stranded (ss) AAV plasmid backbone with a CMV early enhancer/chicken β actin (CBA) promoter driving ubiquitous FP expression. Injections were performed using the following AAVs and coordinates along the medio-lateral (ML), antero-posterior (AP) and dorso-ventral (DV) axis (defined relative to Bregma for ML and AP coordinates, and with reference to the surface of the brain for DV): AAV2/9-CBA-tdTomato-2A-WPRE (ML 2.4 mm, right; AP +2.7 mm; DV 1 mm, α = -30 º), AAV2/9-CBA-mTurq2-2A-WPRE (ML 2.4 mm, right; AP +2.2 mm; DV 1 mm, α = 0 º) and AAV2/9-CBA-EYFP-2A-WPRE (ML 2.4 mm, right; AP +1.9 mm; DV 1 mm, α = -30 º). **In particular, the RGB injections display a topographic order along the rostro-caudal axis : red, blue and green in this order from the rostral to the caudal end**(Fig 3.23). The td-Tomato injection was located in the anterior motor cortex, and the EYFP injection was predominantly in the somatosensory (SSP) cortex. While the mTurquoise2 injection was mostly located in the motor cortex, it also extended to the SSP region.

To generate this multiplex projection dataset, we used Chrom-SMP in the **serial 2D tomography mode** acquiring 82 2D sections every 100 µm from the anterior cortex to the midbrain. Each 2D section consisted of 37×24 tiles of 330 µm × 330 µm stitched together. The lateral sampling was set to 0.55 µm in order to capture fine axonal processes. Figure 3.22 particularly highlights the multiscale mapping of axonal projections in this dataset from the long-range brain-wide scale to the local circuit scale. Such multiplex long-range projection datasets can also be complemented by local continuous 3D high-resolution of a priorly defined projection target, through the use of

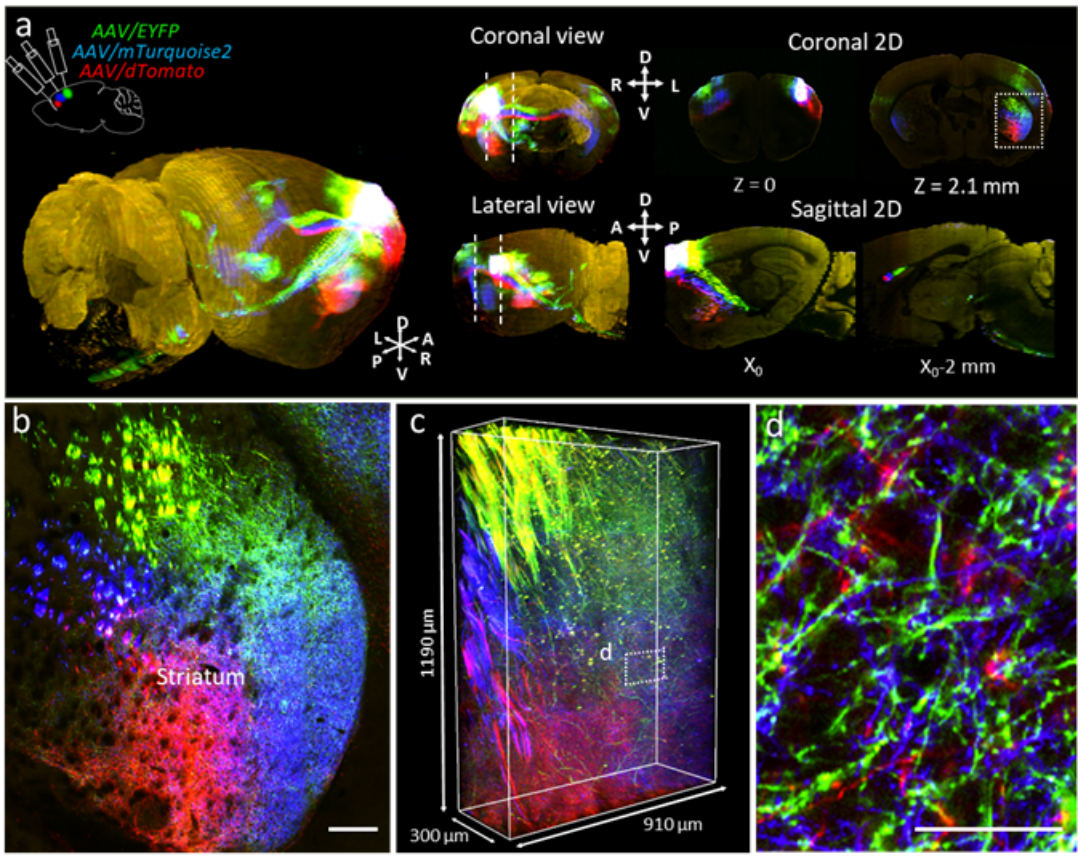

FIGURE 3.22. Brain-wide multiplexed projection mapping with Chrom-SMP. (a) Brain-wide mapping of neural projections using tricolor AAV anterograde labeling and Chrom-SMP. 3D, coronal and sagittal views of the 3 labeled projections. (b) Magnification of the region boxed in (a) showing topographic arrangement of labeled projections in the striatum. Scale bar: 200 µm. (c) Continuous high-resolution 910×1190×300 μm^3 volume acquired with 0.4×0.4×1.5 μm^3 voxel size in the striatum, within the brain-wide dataset. (d) Magnification of the boxed region in (c) showing intermingled axonal processes. Scale bar: 30 µm.

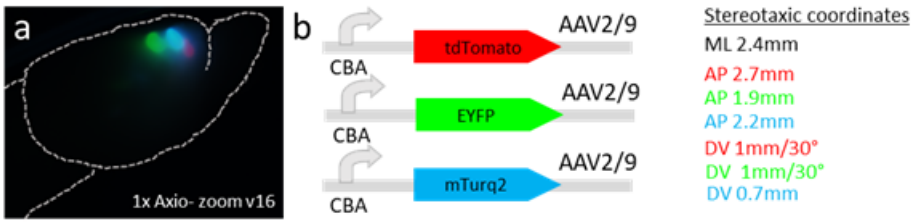

FIGURE 3.23. Triple AAV injection. (a) Epifluorescence whole-brain snapshot of tricolor injection areas. Image acquired on commercial Zeiss Axio-zoom microscope. (b) Viral constructs and injection coordinates used in tricolor multiplex AAV labeling.

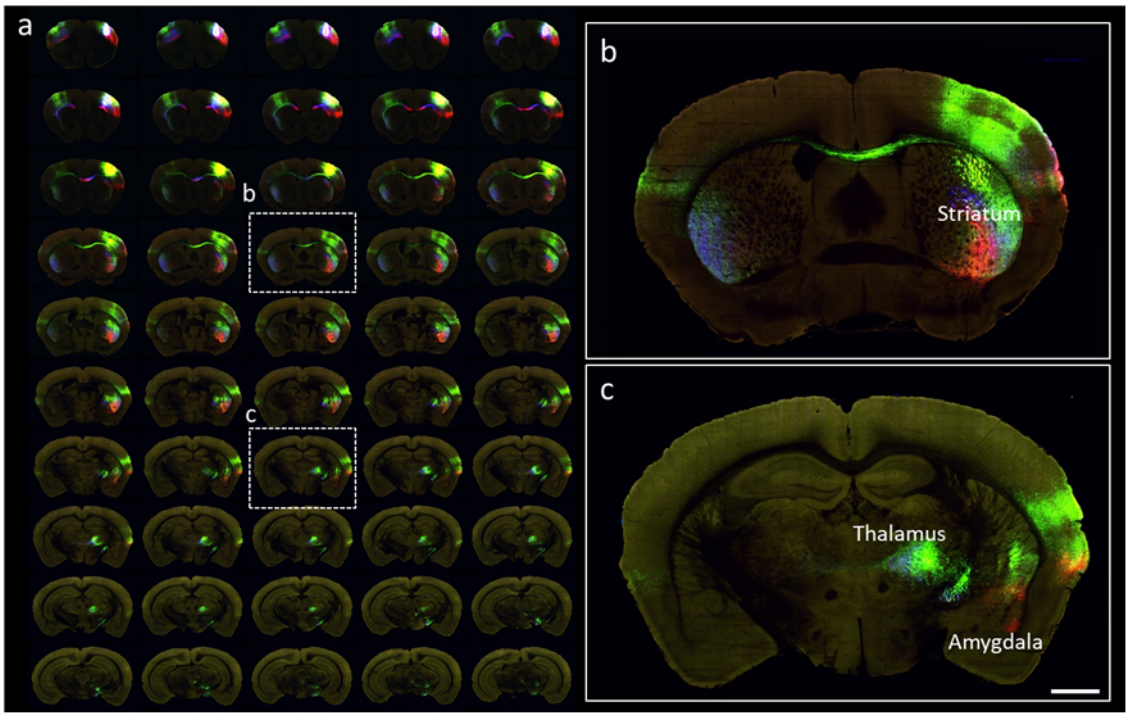

FIGURE 3.24. Triple AAV projection mapping across the forebrain. (a) Coronal sections extracted from the triple AAV projection labelled whole-brain dataset. Consecutive sections are spaced by 100 µm. (b-c) Magnification of the maps boxed in (a). Images downscaled 10×. Scale bar: 1 mm.

a hybrid tomography/continuous acquisition mode. In the presented dataset, we demonstrated this hybrid acquisition scheme by capturing a 910 × 1190 × 300 μm^3 volume of fascicled yet entangled striatal projections (Fig 3.22c-d).

Several projections can be identified in this dataset (Fig 3.24): cortico-striatal projections from the three injection zones, cortico-thalamic projections passing through the globus pallidus from the green- and blue-labeled injection zones, callosal projections from all three injections, projections in the contralateral cortex and striatum mostly for green- and blue-labeled axon tracts, and also cortico-cortical projections in the main hemisphere. While both blue- and green-labeled projections feed the thalamus, a major relay of sensory and motor information, the red-labeled projections stops at a more rostral target, the amygdala, which is a structure known to be involved in memory, decision-making processes and emotional responses, fear in particular [224][225]. Finally, for this particular set of injections, corticospinal projections have been observed mostly for the green-labeled sensory tract.

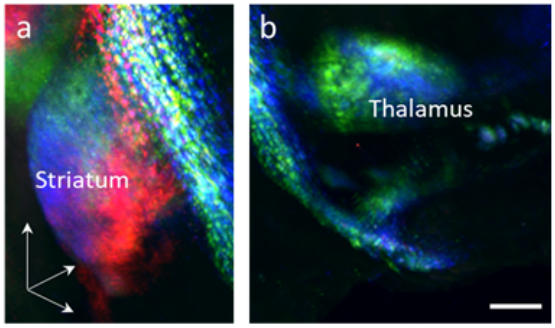

FIGURE 3.25. 3D views extracted from the multicolor volume showing tridimensional topography patterns in target regions (striatum, thalamus). Scale bar: 500 µm.

3.3.2.2 Multiscale topography and projection arrangement

Multicolor imaging of the three distinctly-labeled neuronal populations within the same brain provided immediate access to the relative arrangement of their projections, enabling to directly assess their topographic arrangement and spatial overlap. The dataset presented here displayed some expected large-scale topography patterns, such as conserved relative order arrangement within the callosal tract and the striatum, as well as a core-shell topography in the thalamus (Fig 3.22 and Fig 3.25, [223][172]). Furthermore, a unique feature of simultaneous multicolor projection mapping is that it enables direct access to the local fine scale interdigitation of axonal projections from remote source sites. For instance while initially segregated axons originating from the three labeled cortical areas followed global distinct trajectories, a fine degree of entanglement of color-labeled projections could be observed within dominantly monochrome areas (Fig 3.26). Figure 3.26 also displays a coarse comparison between a multiplexed Chrom-SMP section and an equivalent monochrome STP section from the Allen Connectivity database (http://connectivity.brain-map.org/). Such a dyptich display strongly confirms the interest of a multiplexed approach to spatially dissect large-scale brain-wide projections.

3.3.2.3 Quantitative projection analysis

To further demonstrate how such multicolor projection mapping experiments using Chom-SMP can be used in quantitative connectomics, we devised an analytical workflow to extract quantitative measurements of interdigitation from these large-scale multiprojection datasets. The general scheme of the workflow is presented in Fig 3.27: after preliminary processing steps, fluorescence is separated from background using a high-resolution segmentation algorithm. From these masks and for each channel, projection strength maps are generated by averaging these masks over super-pixels of a pre-defined size. The red, green and blue projection strength maps are then merged to produce a direct measurement and visualization of interdigitation at the scale of the pre-defined super-pixel size. All these steps will be presented in further details in the next

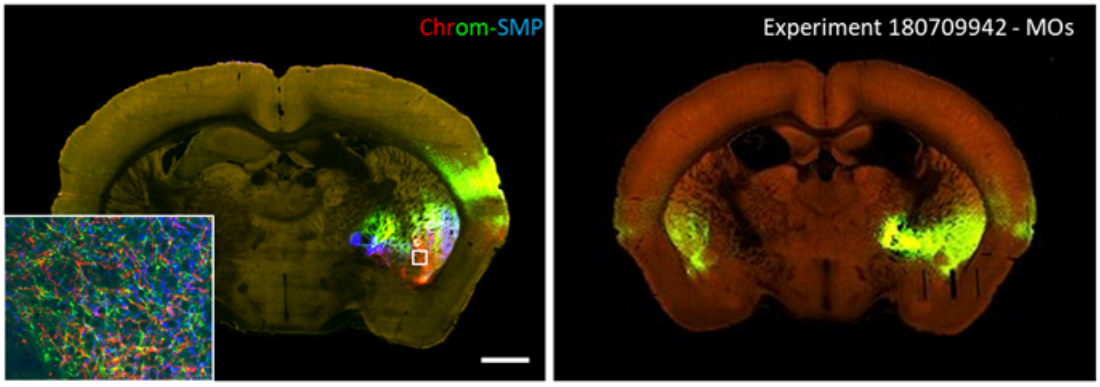

FIGURE 3.26. Neural projection dissection with Chrom-SMP. Multicolor 2D coronal section acquired with Chrom-SMP (left) and equivalent monocolor 2D coronal section (right) from the Allen Connectivity database (http://connectivity.brain-map.org/) shows the capability of Chrom-SMP to segregate neural projections for a given viral tracer injected volume and to visualize fine axonal interdigitation in target zone areas. Scale bar : 1mm.

FIGURE 3.27. Quantitative projection analysis workflow.

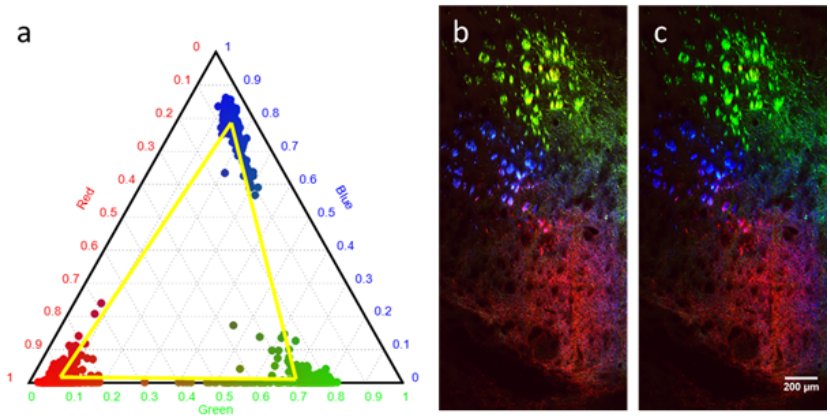

FIGURE 3.28. Linear unmixing procedure. (a) Ternary plot displaying the colorimetry of the multiplex AAV dataset. The yellow triangle indicates the reference triangle used to compute the unmixing parameters. (b-c) XY crops before (b) and after (c) linear unmixing. Scale bar: 200 µm.

paragraphs.

(i) Pre-processing:

Individual tiles are processed and stitched as described in the precedent chapter. A spectral

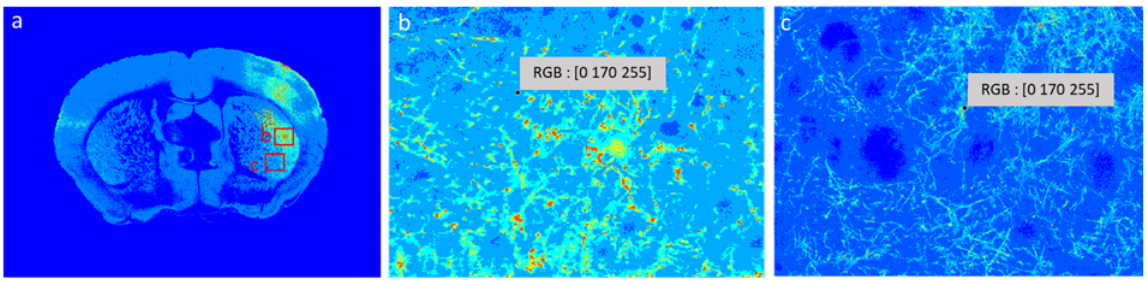

FIGURE 3.29. Multithreshold clustering. (a) Segmentation of a coronal brain section according to 8 intensity bins, indicated by the color code. While upper and lower bins can unambiguously be classified into signal and background respectively, intermediate bins are more challenging to classify since same intensity levels can either correspond to background areas (b) or to signal (c).

unmixing procedure is then applied to the whole assembled dataset to eliminate spectral bleed-through between channels. The same color processing routine as described in Chapter 2 is applied, with a notable difference though, taking into account the exclusively trichromatic labeling and mitigating the intensity-dependent colorimetric variations: the linear stretching in the color space is based not on the $R_{max}G_{max}B_{max}$ triangle but on the $R_GG_GB_G$ triangle, where R_G, G_G, B_G represente respectively the barycenters of the red, green and blue distributions in the ternary color diagram (Fig 3.28).

(ii) High-resolution color-exclusive binary mask generation:

The first step to extract quantitative information from the 2D brain sections is to segment the fluorescence (labeled projections) from the background. Because of the heterogeneity of the projection strengths in the different brain areas, a simple intensity threshold is not optimal to retain all the labeled projections without having a large number of false positive pixels (Fig 3.29).

We therefore implemented a segmentation procedure more optimized for our heterogeneous datasets comprising three main steps: first square root transform followed by histogram matching was applied to intensity images for contrast enhancement and standardization prior to segmentation (Fig 3.30). Then the fluorescence signal is separated from background using an intensity-based clustering algorithm [226]). This multi-threshold segmentation is further complemented by connected-component labeling applied on the intermediate intensity classes (Fig 3.31). The criteria selected for connected-component labeling is the size of the structure (small size objects considered as signal, large size objects as background). This procedure allows to obtain high-resolution segmented binary masks capturing both strong and weak projections, with a limited number of false positives (Fig 3.32). At this stage, for each channel image, each pixel is labeled as signal or background.

Since our aim here is to quantify the far-range interdigitation between three remote separate sites in the cortex, each pixel ought to be considered exclusively as either red, green or blue.

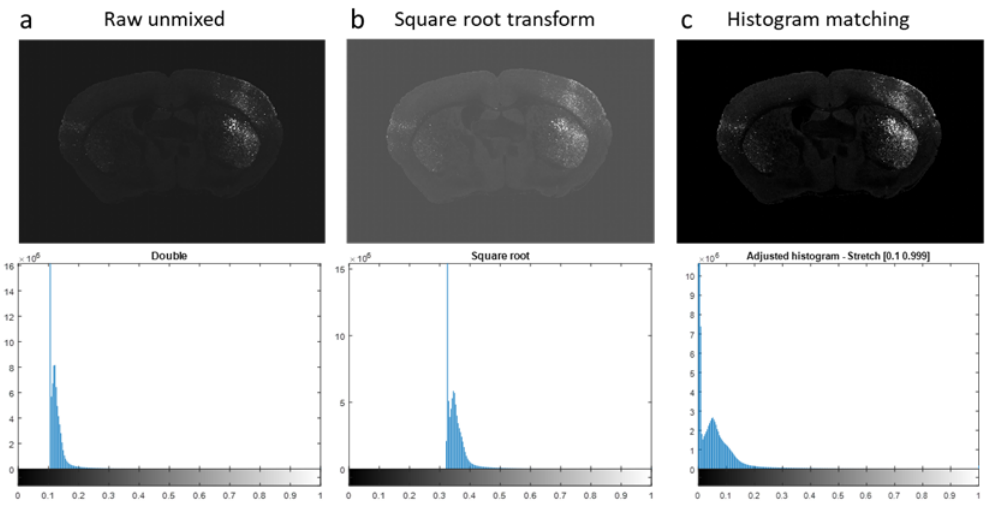

FIGURE 3.30. Automated contrast enhancement steps.

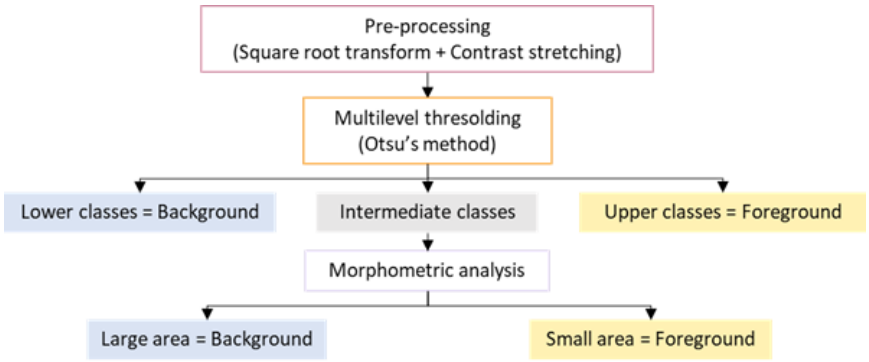

FIGURE 3.31. Segmentation algorithm layout. Fluorescence is separated from background using intensity-based clustering combined with morphometric analysis.

Therefore all pixels which are quantified as signal in 2 or more channels are excluded (i.e set to background). The uncertainty associated with this procedure is quantified (cf. confidence maps introduced in the next paragraph). Therefore at this stage, a color-exclusive binary mask is associated to each channel image.

(iii) Color-exclusive projection strength map generation:

Color-exclusive projection strength maps are generated by computing the ratio of signal pixels over background in non-overlapping adjacent super-pixels of predefined size (here 30x30 pixels). Projection strength maps are generated together with confidence maps to account for quantification errors due to multi-channel pixel exclusion. Confidence maps are computed as the ratio of exclusive signal pixels over the total number of signal pixels on each super-pixel. An example of projection strength maps and corresponding confidence maps is presented in Figure 3.33.

(iv) Interdigitation map generation:

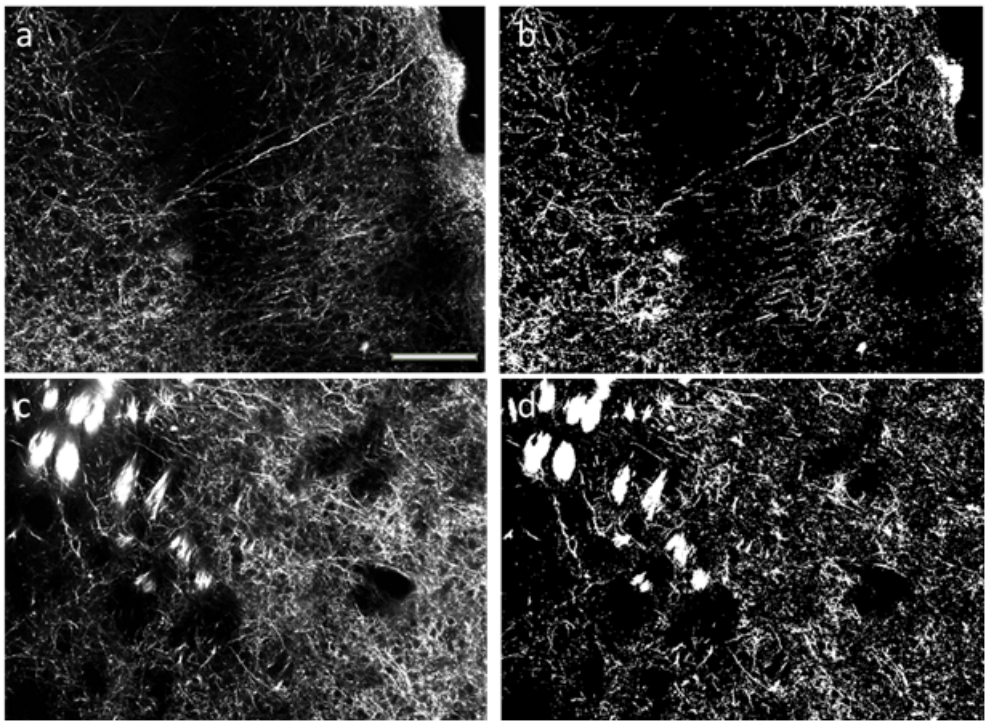

FIGURE 3.32. Signal segmentation. Single-channel images from multiplexed projection dataset (a-c) and corresponding fluorescence binary masks after segmentation (b-d). Scale bar: 200 µm.

Finally, red, green and blue color-exclusive projection strength maps are combined onto RGB interdigitation maps. These maps hence quantify the respective contribution of the labeled projections in each super-pixel. It is also a tool to visualize through the color contrast the interdigitation and projection strengths in different brain areas: the regular contrast display highlights the interdigitation originating from strong projection areas while the heptachromic 'color-saturated' contrast enhances the interdigitation from weaker axonal projections (Fig 3.34).

3.3.2.4 Brain-wide multimodal THG/AAV imaging

Finally, we report on trichromatic fluorescence imaging of viral-labeled axonal projections recorded simultaneously with label-free THG signals channel using 850/1100 nm excitation. Three AAV anterograde tracers (DsRed Express, YFP, mCerulean) were injected in motor and somato-sensory cortex at the following coordinates: AAV2/9-CMV-BI-DsRed-Express-2A-WPRE (ML 2.4 mm, right; AP +2.7 mm; DV 1 mm, α -30º); AAV2/9-CAG(CB7)-CI-mCerulean-WPRE-rBG (ML 2.5 mm, right; AP +2.3 mm; DV 0.7 mm, α 0º) and AAV2/9-CBA-EYFP-2A-WPRE (ML 2.7 mm, right; AP +2.0 mm; DV 1 mm, α -30º). The THG channel complements the color-based projections with a rich morphological background, highlighting myelinated axons, fiber tracts and negatively-contrasting cell bodies. In the context of such sparse projection labeling, it can be

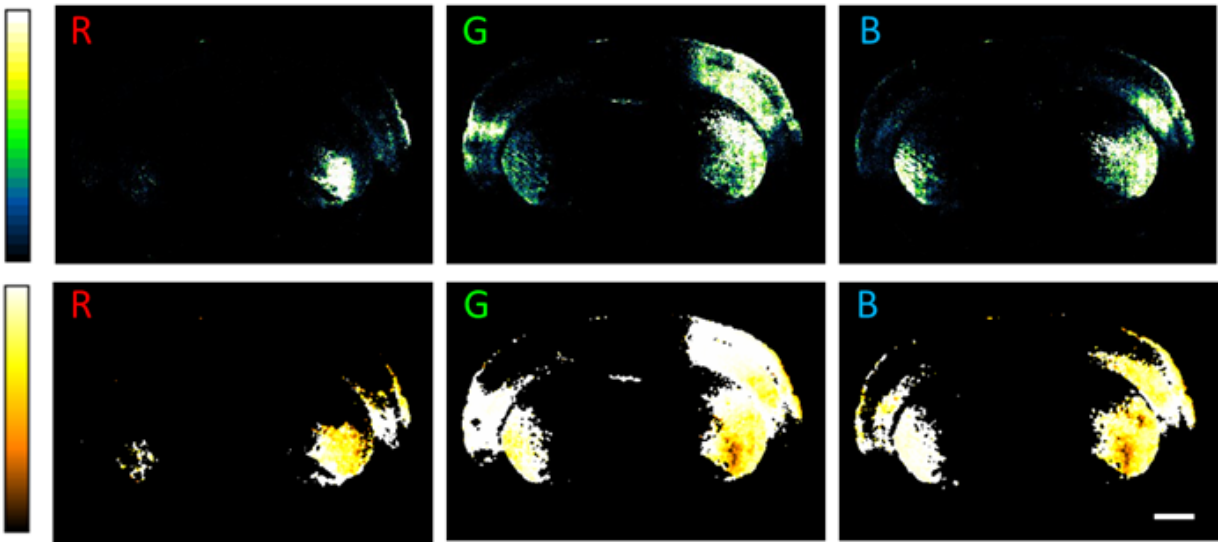

FIGURE 3.33. Top : Red, green, and blue exclusive projection strength maps. Signal intensity is represented in arbitrary units from weak (dark blue) to strong (white) projections. Bottom : Red, green and blue exclusive projection confidence maps. Signal intensity scales range from 0% (dark) to 80% (light). Pixel size : 24 µm x 24 µm. Scale bar: 1 mm

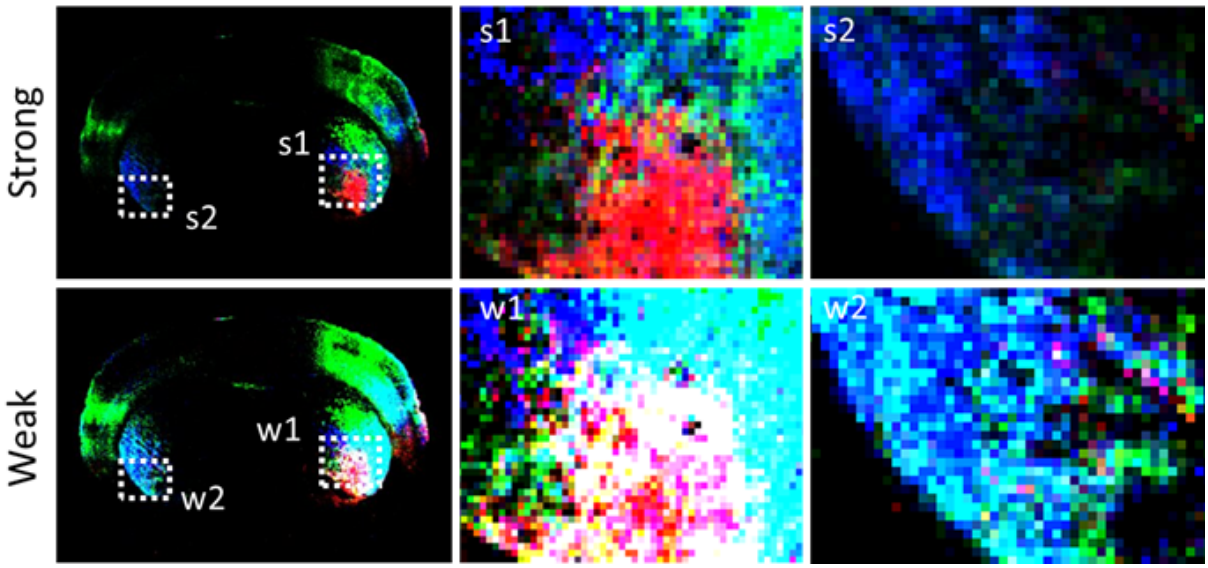

FIGURE 3.34. Interdigitation maps. Color maps displayed in regular contrast (top) allows for direct visualization of interdigitation from high projection strength areas. Heptachromic (bottom) contrast reveals general topography of strong projections and highlights axonal interdigitation originating from weak projections.

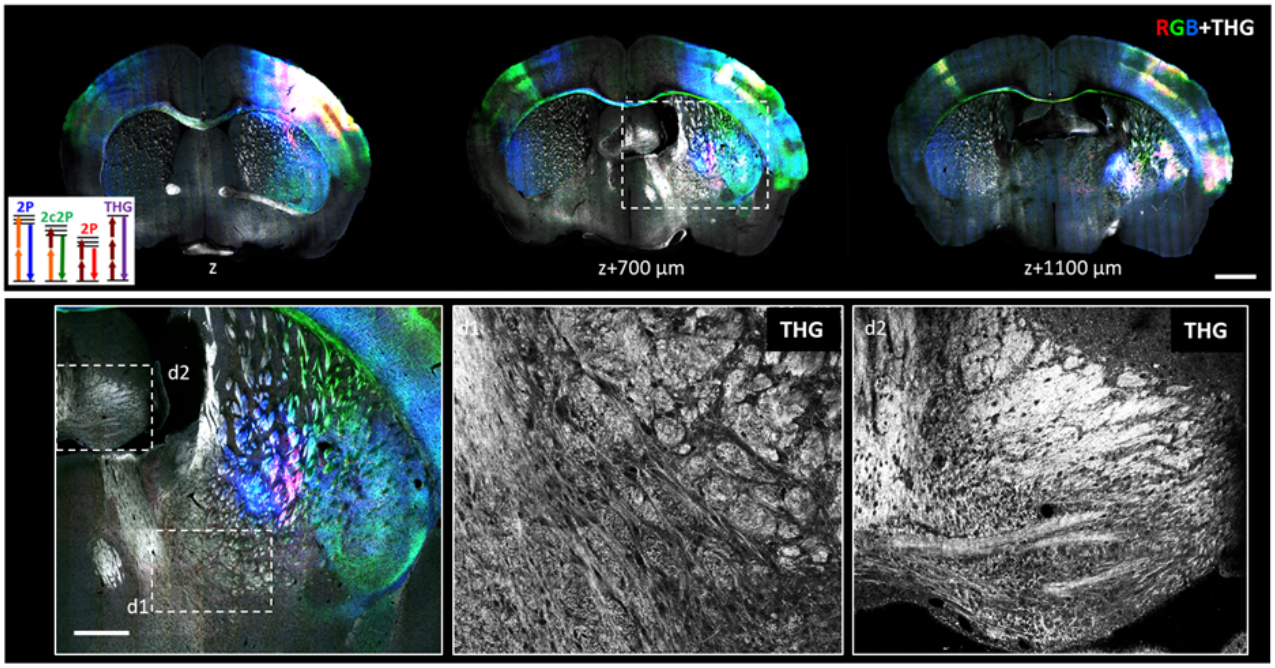

FIGURE 3.35. Multicolor+THG coronal sections extracted from a 8×11×5 mm^3 volume using 850/1100 nm excitation. Top: Overlay of multicolor (RGB) and THG (grays) 2D coronal images acquired simultaneously. Scale bar: 1mm. Bottom: Magnification of the boxed area on upper panel shows multicolor-labeled neural projections along with morphological landmarks. THG signals highlight cytoarchitecture and lipid-rich structures (d1-d2). Scale bar: 500 µm.

harnessed as an additional registration channel. It is worth mentioning though that strong laser power is required to obtain the third harmonic image. Therefore, this should be compensated by an under-expression of the red AAV vector to allow simultaneous THG/multicolor AAV imaging. With the regular red AAV expression levels, the power required for THG induces photobleaching in the red channel hence hampering simultaneous THG and multicolor imaging.

3.4 Conclusion and perspectives

In this chapter, we first demonstrated multiphoton multicolor imaging at diffraction-limited resolution across several mm^3 of MAGIC marker-labeled mouse cerebral cortex. The intrinsic channel registration provided by wavelength-mixing combined with the continuous 3D acquisition scheme allowed to visualize biological structures of interest such as axons, dendrites and astrocyte main processes with multicolor voxel precision throughout the volume over 2mm depth. In principle, the maximal atteignable depth with Chrom-SMP is arbitrary and solely limited by the trade-off over the acquisition time. In our demonstrations though, the cortical electroporation

provided a focal labeling and the volume size was chosen to capture almost the entire labeled volume.

From a technical perspective, an interesting comparison would be with continuous large volume imaging provided by clearing approaches. The concept underlying these approaches is to chemically process the tissue in order to remove optical scatterers such as lipids and minimize refractive index inhomogeneities. In other terms, optical clearing techniques aim at rendering biological tissues transparent to light. A plethora of such chemical protocols have been published in the recent years [7][227][8], with cleared tissues usually imaged in light-sheet platforms providing fast volumetric acquisitions of organ-scale volumes [228][229]. As a rule of thumb, such approaches are ~100 times faster than optimized STP platforms [65], which represents a solid advantage for large-volume continuous 3D imaging. Nevertheless, high-resolution multicolor imaging of large cleared samples over several mm depth has still not been demonstrated mainly because of the challenge of maintaining consistent image quality and channel registration across large depths, particularly in the case of low NA Gaussian light-sheet excitation. Moreover, a majority of the most efficient clearing methods are only compatible with few specific fluorescent proteins. Besides, as evoked in the morphological analysis above, clearing procedures are susceptible to introduce biases such as tissue shrinkage or tissue expansion. Ultimately, by combining channel co-registration through wavelength-mixing, high-resolution imaging through point-scanning and mitigating optical aberrations through serial slicing, Chrom-SMP is up to date the most a robust for multicolor imaging of large volumes of scattering tissue such as the brain, with consistent subcellular resolution. Nonetheless, optical clearing is not fully incompatible with Chrom-SMP. In fact, clearing can be used to enhance Chrom-SMP capabilities, particularly when imaging highly myelinated scattering regions, provided that the clearing procedure is well crafted to (i) allow the preservation of the fluorescence signal of the FPs of interest, and (ii) to not compromise the rigidity and mechanical consistency of the sample, hence the quality of the cut.

Secondly in this chapter, we have leveraged the mm^3 MAGIC marker-labeled cortical volumes acquired with Chrom-SMP to characterize the astroglial network in the mouse cerebral cortex. We derived an approximation of the numbers of cell bodies (mostly neurons) within astrocyte domains as well as the distribution of astrocyte volumes across deep cortical layers (layers 4 to 6), with a large statistical sample size within the same brain. Notably, our analysis highlighted a significant increase of astrocyte volumes between layer 4 astrocytes and layer 5a astrocytes, and between layer 4 and layer 6 astrocytes, in line with the growing reported evidence of astrocyte heterogeneity [211][203][230]. Additionally, we developed a workflow to characterize the astroglial tiling of the grey cortical matter through 3D the reconstruction of the contact interface between color-segregated astrocyte neighbors. Last, we acquired large volume datasets of dual-compartmented MAGIC labeled samples at two developmental postnatal stages (P7 and P21) which highlighted several patterns of astrocyte development in the mouse cerebral cortex. More generally, Chrom-SMP is opening several novel perspectives in Brainbow-based

neurodevelopmental studies with single-progenitor precision. For instance, some of our ongoing work consists of leveraging the previously described methodological developments to reveal the clonal architecture of excitatory neurons in whole mouse brain embryo cortices, with single-progenitor precision. However a bottleneck of these studies remains the data analysis which still requires massive manual annotation. A solution to lift this limitation would be to harness the manually analyzed datasets to train deep-learning neural networks. This will permit to make the most of the Chrom-SMP datasets by enabling extensive morphological and spatial analyses at different stages to be performed within reasonable time frames.

Finally, in this chapter we demonstrated multicolor brain-wide imaging of long-range axonal projections, labeled with three different tracers, from three distinct source locations within the same brain. We specifically highlighted how such a multiplexed experimental design provides a unique opportunity to study relative projection organization and topography at multiple scales. In passing, we also demonstrated that a hybrid tomography/continuous Chrom-SMP acquisition mode can be used to complement such multiplex and multiscale projection datasets by enabling to locally reconstruct projections with 3D diffraction-limited resolution in a continuous volume within a pre-defined target area. Last, we designed an image processing workflow for quantitative assessment of projection strengths and interdigitation patterns. Overall, our work in this section lies in the context of an increasing number of STP-enabled whole-brain projection mapping studies, usually acquired with diffraction-limited lateral resolution and 50-100 µm axial sampling, and which have already started to reveal large-scale foundational principles of brain organization ([86][167][165][172] among many others). Multiplexing these experiments within a single brain through a multicolor tomography scheme presents important advantages. First, multiplexing is obviously a faster approach when acquiring multiple long-range projection data. In large-scale connectomic projects, this can spare a considerable amount of experimental time, especially given the relatively long STP acquisition times. As importantly, it would also reduce the number of animals required to complete given sets of data. Above all, multiplexing allows to obtain the topographical arrangement of projections with a high level of precision because since the projections are mapped within the same animal, (i) all potential inter-individual biases are removed and importantly, (ii) high-resolution interdigitation information, which would usually be lost when averaging onto a common averaged framework, can be obtained and quantitatively assessed. This for instance can be directly applied to compare at different scales arrangement patterns between healthy and diseased brains or to precisely analyze at multiple scale the convergence and/or segregation of axonal projections from distinct cell populations.

On the whole, we have presented in this chapter examples of how Chrom-SMP can be leveraged for large-scale high-content anatomical studies which has so far been technically inaccessible or how it can be used to considerably enrich existing experimental schemes. Further combining Chrom-SMP with the continuously growing genetic labeling toolbox (cell-type/sub-type specific labeling [85], mosaic perturbations [231] etc.) should open a vast range of possibilities and provide

the opportunity to study the brain structure and development with unprecedented precision and scope.

CHAPTER 4

MULTI-CONTRAST DEEP-TISSUE THREE-PHOTON MICROSCOPY

In this final chapter, we explore multi-contrast large volume imaging through a shifted experimental paradigm. Our aim was to push the fundamental depth limitation of two-photon microscopy while maintaining multiple contrast possibilities, in order to access multiple signals simultaneously at larger depths. This approach is particularly relevant in the context of live tissue studies, where destructive imaging methods such as the ones presented earlier, are not an option.

The intrinsic 3D confinement of two-photon excitation together with the higher penetration depths permitted with near-infrared excitation wavelengths established two-photon excited fluorescence microscopy (2PEF) as the reference method for deep imaging within biological tissues with cellular or subcellular resolution. The wide adoption of this technology was largely favorised by the technological development of modern turn-key Titanium:Sapphire (Ti:Sa) laser systems that provide typically ~ nJ femtosecond laser pulses (100-200 fs) at 80 MHz repetition rate. In addition, the tunability of the Ti:Sa system made it particularly suited to target a large number of fluorophores. Nevertheless, routine Ti:Sa based two-photon imaging is limited in terms of accessible depths to typically 200-600 micrometers, depending on tissue type. Accessing larger depths with multiphoton microscopy requires the exploration of novel strategies, including the development of novel laser sources with optimized pulse characteristics for deep-tissue imaging.

In this chapter, we will first present some important directions explored so far to extend the imaging depth of multiphoton microscopy, then we will discuss more specifically the advantages of three-photon microscopy for deep-tissue imaging. We will then review the current technological landscape of pulsed lasers for three-photon microscopy and evaluate the performances for deep-tissue microscopy of two of such sources. Finally, we will present our work on developing dual-color three-photon microscopy relying on a novel multiband MHz source.

4.1 Strategies for deep-tissue multiphoton imaging

4.1.1 Strategies for deep-tissue imaging

Despite the unequaled performances of two-photon microscopy in imaging deep within scattering tissues with single-cell resolution, the imaging depth allowed by 2PEF remains limited to few hundreds of microns, the absolute accessible depth largely depending on the absorption and scattering properties of the tissue sample.
To discuss the parameters that limit imaging depth in multiphoton imaging, we should first remember that the nth order non linear signal depends on the laser parameters (average power P, repetition rate f, pulse width τ) as follows:

$$< S_{\mathrm{n}} > \propto \frac{P^n}{(f \cdot \tau)^{n-1}} \tag{4.1}$$

As the excitation beam is focused deeper in a scattering sample, it experiences losses due to scattering and absorption. Unscattered light obeys a Beer-Lambert law, i.e it decreases exponentially with depth:

$$I(z) = I_0 exp(-\frac{z}{l_s}) \tag{4.2}$$

where l_s is the scattering length, I the laser intensity at the focus, and I_0 the laser intensity at the surface. In 2PEF, the fluorescence generated in the focal plane scales therefore as ${P_0}^2 exp(-2z/l_s)$, with P_0 the laser power at the surface. The usual strategy for in-depth two-photon imaging is therefore to compensate for this attenuation by increasing exponentially the laser power at the tissue surface, so as to maintain a constant intensity at focus.
In a first approximation, if we can consider that (i) excitation remains confined whatever the focusing depth is, (ii) phototoxicity and heating can be neglected, and (iii) imaging depth is limited solely by the available laser power and by the microscope detection noise floor, the maximum imaging depth for two-photon imaging scales as:

$$z_{max} \approx l_s \ln(\alpha P_0 \frac{1}{f.\tau} \sqrt{\Phi(z_{max})}) \tag{4.3}$$

where Φ is the collection efficiency and α is a parameter dependent on the detector shot noise and the fluorophore properties [13]. In practice however, when imaging live samples, the maximum amount of energy that can be deposited at the sample surface is limited by thermal damage [10]. Moreover, even when imaging fixed samples, available power can be a limiting factor with typical Ti:Sa sources.
An interesting approach to attempt to reach larger depths is to redistribute the excitation energy into more energetic pulses compared to the usual 80 MHz/nJ range of the Ti:sapphire oscillators. The idea is to modify the f.τ parameter so as to have more 'extra energy' available in the excitation pulses and enable power increase at larger depths. Of note, the increased depth comes

at the expense of a lower fluorescence flux, since this flux is proportional to the laser repetition rate, which is decreased in this strategy. This approach has been proposed by Beaurepaire and colleagues in 2001 [232] and demonstrated for mouse brain imaging by Theer et al. [233] in 2003, using a regeneratively amplified Ti:Sa providing ~ µJ pulses with a 200 kHz repetition rate at 925 nm. Indeed this approach enabled imaging up to 1mm deep in the *in vivo* mouse brain, which certainly constituted a depth record (considering the *in vivo* mouse cortex system) at the time. However and most importantly, this experiment demonstrated that a fundamental imaging depth limitation in two-photon microscopy in a scattering medium stems from a progressive loss of confinement of the excitation with depth, resulting in a drastic degradation of the signal-to-background ratio (SBR) at large depths (Fig 4.1). This limitation becomes predominant in conditions where laser power is not a limiting parameter. Indeed at large depths, out-of-focus fluorescence, mostly generated from the tissue superficial regions [234], eventually exceeds the fluorescence produced near the beam focus, resulting in a dramatic loss of contrast [233]. We will further discuss this limitation in a later section while comparing 2P and 3P contrasts with depth.

A second and complementary approach for deeper imaging would be to minimize tissue scattering by increasing the excitation wavelength. Several studies reported improved imaging depths in two-photon microscopy using 1100 nm -1300 nm excitation provided by a Ti:Sa pumped optical parametric oscillator (OPO) [235][236]. The ongoing development of new far-red fluorescent probes [237][238] is promising for deep-tissue two-photon imaging using such red-shifted excitation wavelengths. This strategy presents the additional advantage of reduced light scattering in the detection path. To reach its full potential, this approach will require further advances in fluorescent probe engineering and technological developments in detectors with improved sensitivity in the short-infrared range. Ultimately though, and in particular in the case of densely labeled samples, two-photon microscopy will be limited at large depths by the signal to background ratio degradation discussed above.

Recently, C.Xu et al. demonstrated that this limit can be circumvented by implementing three-photon excitation microscopy with short wavelength infrared (SWIR) excitation near 1300 nm [239] or 1700 nm [5]. This approach in principle outperforms two-photon microscopy for deep imaging, as it results in (i) better excitation confinement and (ii) reduced scattering.

To close this introductory section, we shall insist here that there is no absolute value for the maximal reachable depth since this limit is very tissue- and labeling-dependent. Young tissues are usually more transparent than older tissues and it has been shown that fixed tissues are usually more opaque than living tissues in the case of mouse brains [13]. Furthermore, as we will expose in the next section, the signal-to-background ratio at large depths depends on the volumetric labeling density of the sample. Therefore, 3P vs. 2P comparisons on the same samples need to be done to conclude on the potential benefits of 3P imaging, especially in the case of novel or non-standard sample preparations.

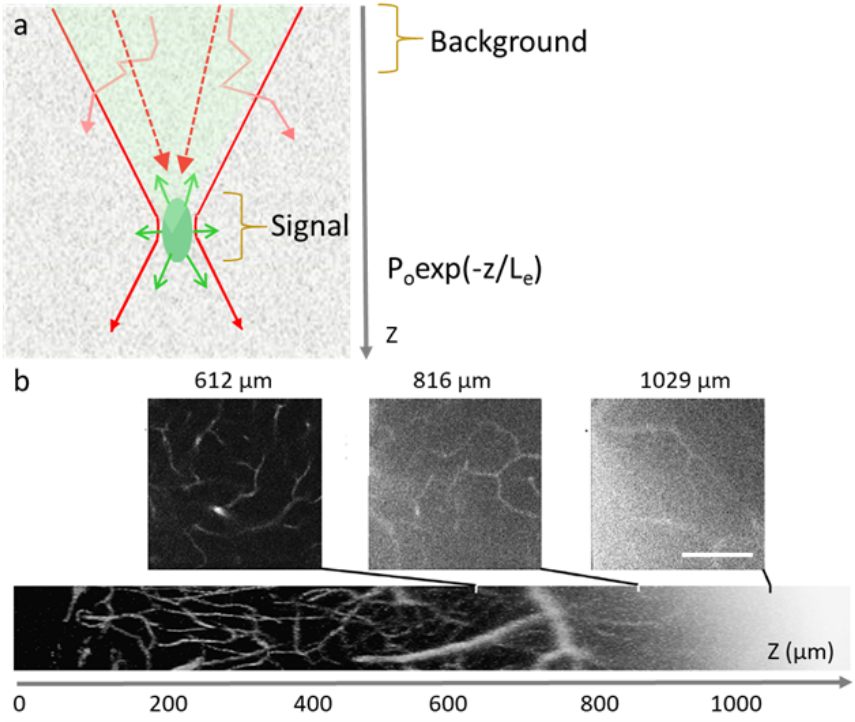

FIGURE 4.1. Depth limitation in two-photon microscopy. (a) Two-photon beam focalized at depth in a fluorescently labeled scattering medium. With increased depth, fewer photons reach the focus and laser power is usually increased to compensate the exponential power decrease with depth. This power increase within a fluorescently labeled medium however starts to produce out-of-focus fluorescence photons from the tissue surface which degrades the signal-to background ratio in depth. (b) *In vivo* two-photon imaging in the mouse cortex where blood vessels have been labeled by a circulatory injected dye (Fluorescein Isothio-Cyanate-Dextran).A XZ projection is shown, together with three corresponding XY planes at large depths. Scale bar: 100 µm. Adapted from [233].

4.1.2 Three-photon microscopy for deep-tissue imaging

Three-photon laser-scanning microscopy has historically been introduced in the early nineties [240][241][242], soon after the first two-photon laser-scanning microscopes [12]. Initially, three-photon excitation was used to further expand the wavelength range of Ti:Sa lasers, mainly to access ultraviolet fluorophores (tryptophan, serotonin, DAPI nuclear staining, etc. [243][244][240]) with 900 nm - 1050 nm excitation. Recently, the use of 3P in the SWIR excitation range was demonstrated to be an interesting strategy for deep-tissue imaging for the reasons briefly outlined above. In this section, we will discuss more precisely some arguments in favor of three-photon microscopy as an approach for deeper tissue imaging. The potential limitations of the method will be discussed in the perspectives/discussion section of this chapter.

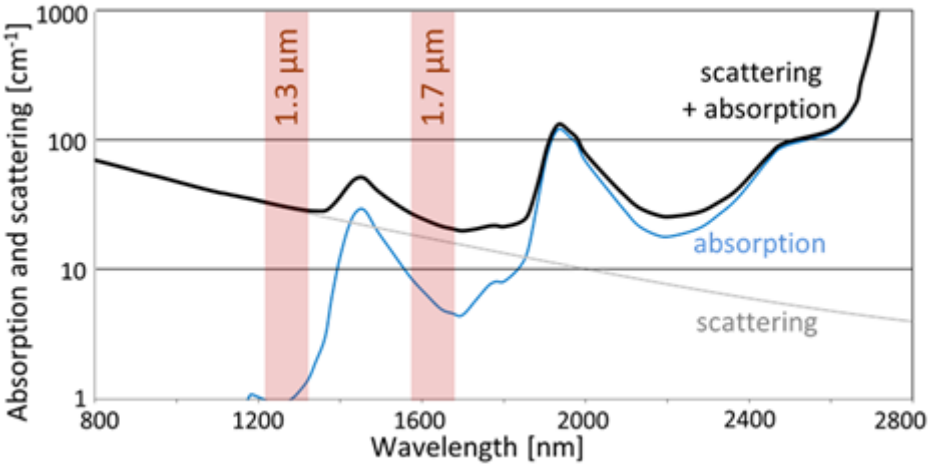

FIGURE 4.2. Absorption and scattering in the near-infrared. When taking into account both scattering and absorption, two windows emerge as particularly optimal for deep-tissue imaging: the 1.3 µm and the 1.7 µm windows.

4.1.2.1 Optical tissue transparency

Shifting the excitation wavelength further in the mid-infrared range compared to the classical Ti:Sa/OPO range is certainly beneficial in terms of reduced light scattering (Fig 4.2). This wavelength range is however characterized by increased water absorption, which brings two main problems for tissue imaging : (i) increased absorption, similarly to scattering, induces light attenuation which reduces the excitation intensity near focus and, most importantly, (ii) water absorption induces tissue heating and therefore photodamage in living biological specimens. Nevertheless, two spectral bands in the short-wavelength infrared (SWIR) range, have been identified as promising for deep-tissue multiphoton imaging : the 1300 nm window and the 1700 nm window [5][239][245]. These spectral regions correspond to local minimas of the water absorption curve (Fig 4.2), hence providing optimas with strongly reduced scattering and limited water absorption. In addition, efficient three-photon excitation of commonly used red or green fluorescent proteins in these spectral ranges have been demonstrated recently, implying great potential for biological imaging. However, while optical tissue transparency at these SWIR wavelengths does improve light penetration inside biological tissues, it is not the only parameter accounting for the superior capabilities of SWIR 3P microscopy for deep-tissue imaging. An important advantage of 3PEF microscopy compared to 2PEF is its improved contrast at large depths.

4.1.2.2 Excitation confinement and signal-to-background (SBR) improvement

As we will derive in this section, superior confinement of the excitation is the most fundamental advantage provided by three-photon microscopy over two-photon excitation.

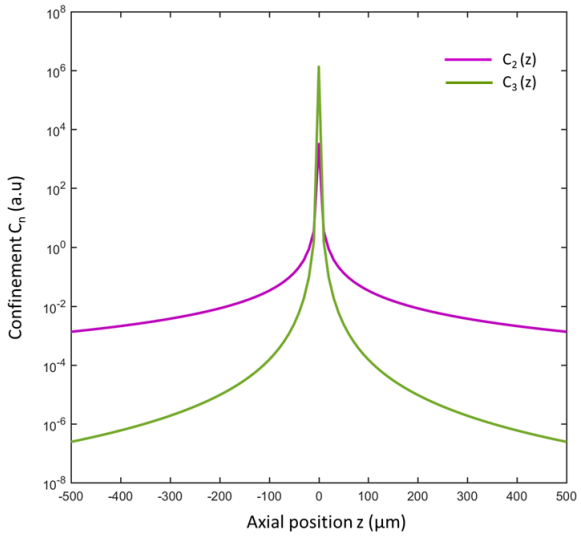

FIGURE 4.3. Excitation confinement in 2PEF and 3PEF.

Let us first calculate the optical confinement in the case of 3PEF in a non-scattering sample. For a non linear signal, the optical confinement C_n is defined as the integral of the non linear intensity within a radial plane at a given depth z:

$$C_n(z) = 2\pi \int_0^\infty I^n(r,z)dr \tag{4.4}$$

For a focalized gaussian beam, the intensity of the excitation profile can be expressed as:

$$I(r,z) = \frac{2P}{\pi\omega(z)^2} \exp(-2\frac{r^2}{\omega(z)^2}) \tag{4.5}$$

where P is the average power, and $\pi\omega(z)^2$ is the transverse beam area at the axial position z. The radial distance to the propagation axis $\omega(z)$ is defined by Gaussian optics as:

$$\omega(z) = \omega_0 \sqrt{1 + (\frac{z}{z_0})^2} \tag{4.6}$$

with ω_0 the lateral extension of the beam at the focus and z_0 defined as: $z_0 = n_0 \pi \omega_0 \backslash \lambda$, where n_0 is the refractive index of the medium of propagation and λ the wavelength. From (6.2) and (6.3), the expression of the non linear confinement can be derived as a function of geometrical parameters of the focusing beam:

$$C_n(z) = \frac{P}{n}(\frac{2P}{\pi\omega(z)^2})^{n-1} \tag{4.7}$$

$C_2(z)$ and $C_3(z)$ are plotted as a function of the axial z position in Figure 4.3 with the following numerical values, corresponding to a typical multiphoton experiment: λ=1.3 µm, n_0=1.35 (approximative refractive index of brain tissue as measured in [246], P=10 mW and ω_0=0.1 µm. The graphs illustrate the increase of optical with non linear order and show that at 500

µm depth with typical experimental parameters, up to 6 orders of magnitude improvement in signal-to-background ratio can be achieved with 3PEF.

In [5], Xu and colleagues proposed a model to calculate the signal to background ratio as a function of imaging depth. In the thick sample limit, i.e when the sample thickness is greater than the focal depth, the 2P fluorescence signal can be approximated as follows [247]:

$$< S_{2P}(t) > \approx 1/2 g_2 \phi \eta C \sigma_2 \frac{8n < P(t) >^2}{\pi \lambda} \tag{4.8}$$

where ϕ is the collection efficiency, η the fluorophore quantum efficiency, C the fluorophore concentration, σ_2 the two-photon absorption cross-section, n the sample refractive index, g_2 a parameter describing the temporal properties of the laser source, λ the laser wavelength and <P(t)> the average power at the focus. In a scattering sample, the average power at a depth z can be expressed as a function of the average power on the sample surface P_0 and the tissue attenuation length l_e:

$$< P(t) > \ = < P_0(t) > e^{\frac{-z}{le}} \tag{4.9}$$

Therefore:

$$< S_{2P}(t) > \approx 1/2 g_2 \phi \eta C \sigma_2 \frac{8n < P_0(t) >^2 e^{\frac{-2z}{le}}}{\pi \lambda} \tag{4.10}$$

The 3P fluorescence signal for a diffraction-limited focus can be approximated as follows [10]:

$$< S_{3P}(t) > \approx 1/3 g_3 \phi \eta C \sigma_3 \frac{3.5 n NA^2 < P_0(t) >^3 e^{\frac{-3z}{le}}}{\pi \lambda^3} \tag{4.11}$$

where NA is the effective numerical aperture and g_3 a parameter describing the temporal properties of the laser source.

Let us estimate now the background for each configuration. We define the attenuation length as the length over which the signal is divided by e^n for a nth order process, and which accounts for both absorption and scattering events:

$$l_e = (\frac{1}{l_s} + \frac{1}{l_a})^{-1} \tag{4.12}$$

where l_s and l_a represent respectively the scattering and the absorption lengths as previously defined (cf. Chapter 1). Under the simple approximation that the background is generated mainly within the first attenuation[53], the n^{th} order background B_n can be approximated by the n^{th} order intensity calculated over the excitation cone from the surface [5]:

$$B_n \ \propto < I >^n \cdot A l_e = \frac{< P_0 >^n}{A^{n-1}} l_e \tag{4.13}$$

with A the area of the laser beam at the tissue surface and <I> the time-averaged intensity of the laser beam. The 2P background is therefore:

$$B_2 \ \propto \ \frac{< P_0 >^2}{A} l_e \tag{4.14}$$

When considering the geometry of the excitation cone, the 2P background can be written as:

$$B_2 \propto \frac{<P_0>^2 n^2}{\pi z^2 NA^2} l_e \tag{4.15}$$

The 2P signal to background ratio scales therefore as:

$$SBR_{2P} \propto \frac{NA^2 z^2}{\lambda l_e} e^{\frac{-2z}{l_e}} \tag{4.16}$$

Similarly, we compute the 3P signal to background ratio:

$$B_3 \propto \frac{<P_0>^3 n^4}{\pi z^4 NA^4} l_e \tag{4.17}$$

$$SBR_{3P} \propto \frac{NA^6 z^4}{\lambda^3 l_e} e^{\frac{-3z}{l_e}} \tag{4.18}$$

Hence with the significant improvement of signal-to-background ratio conferred by three-photon excitation, the fundamental depth limitation of two-photon microscopy can be pushed back to larger depths.

4.1.3 Three-photon microscopy: state of the art

Deep imaging in the living mouse brain three-photon microscopy in both the two SWIR spectral windows of interest (1300 nm and 1700 nm) have been demonstrated in C.Xu's lab at Cornell University. The first demonstration consisted in red fluorescence imaging at 1700 nm in deep subcortical structures *in vivo*, in the intact mouse brain [5]. Vasculature labeled with Dextran-coupled Texas Red and RFP labeled-neurons from a Thy1-Brainbow mouse were visualized more than 1 mm deep within cortical tissue, together with third harmonic generation (THG) contrasts highlighting lipid and myelin structures (Fig 4.4). In particular, THG contrasts revealed that 3P imaging was possible beyond the opaque and highly-scattering corpus callosum, which was reported by the same group to be unreachable using 2P excitation at 1280 nm in the same cortical region on similarly aged animals [236]. The laser used here was a custom fiber laser providing 65 fs pulses at 1MHz centered around 1700 nm (more details on the laser sources will be discussed in the next section). A second important step in the field was the subsequent demonstration of three-photon excitation of the green fluorescent calcium reporter GCaMP6s in deep cortical and subcortical layers in the living mouse brain [239], at 1300 nm using a recently released commercial OPA source (800 kHz, 55 fs). The work demonstrated improved in-depth contrast compared to 2P imaging of green fluorescent proteins, together with neural activity imaging in the hippocampal stratum pyramidale (Fig 4.4). It should be noted however that in this study, imaging was done with a chronic cranial window implantation i.e not through the skull. One should bear in mind that the accessible depth is dependent on the window preparation.

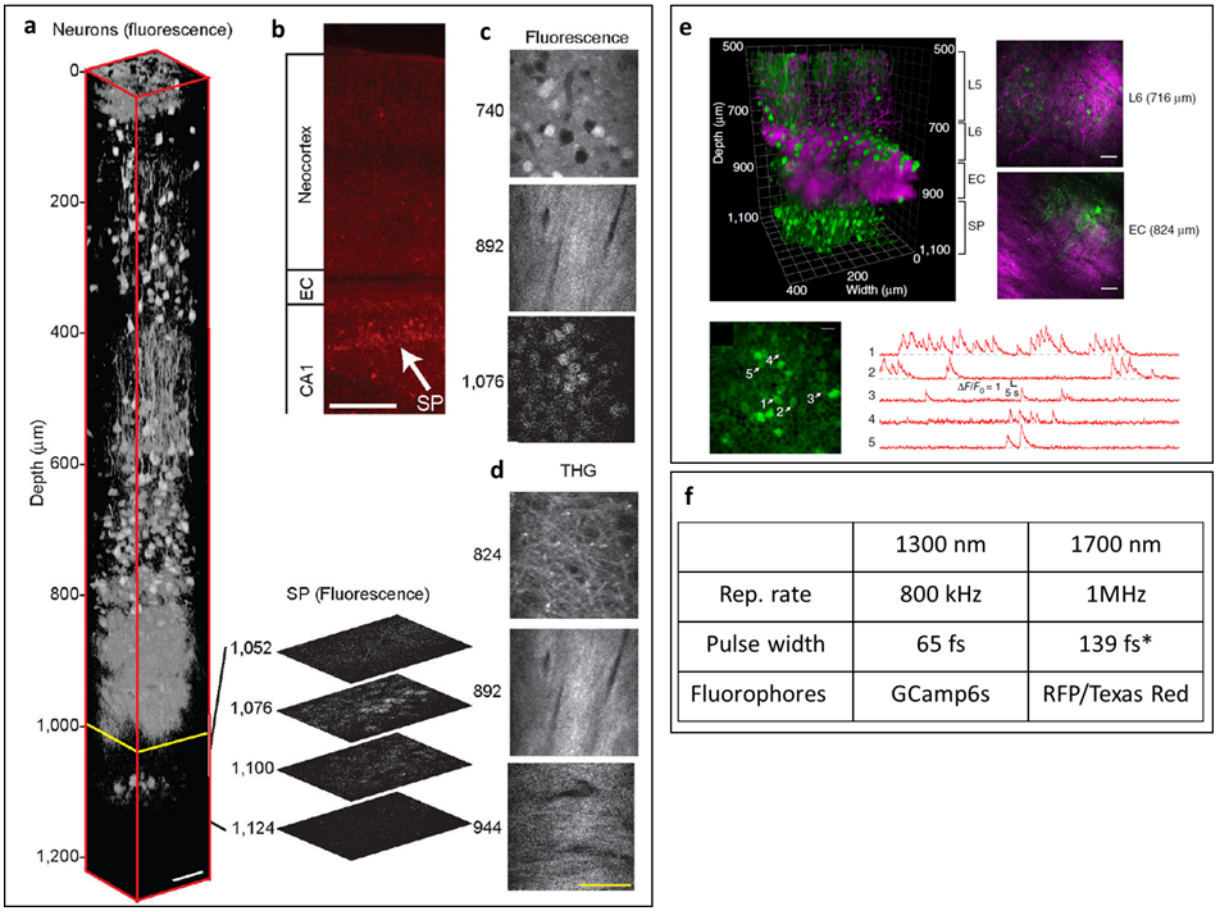

	1300 nm	1700 nm
Rep. rate	800 kHz	1MHz
Pulse width	65 fs	139 fs*
Fluorophores	GCamp6s	RFP/Texas Red

FIGURE 4.4. Three-photon microscopy in the SWIR range: state of the art. (a-d) 3PEF imaging at 1700 nm in the brain of a Thy1-Brainbow1.0, which contains RFP-labelled pyramidal neurons. Epi-fluorescence image from a section of the imaged brain (b) shows that 3PEF imaging crossed the callosal layer to enable hippocampal neuron imaging. Representative XY images at depth are presented in (c-d). Scale bar: 50 µm. Adapted from [5].(e) 3PEF imaging a 1300 nm of spontaneous activity in neuronal population labeled with GCaMP6s in the mouse hippocampus. XY images on the right show the contrast at large depths. Spontaneous activity can be recorded from individual neurons (bottom). Green: 3PEF signal. Magenta: THG signal. Scale bars: 50 µm. Adapted from [239]. (f) Imaging characteristics used in the two [5] and [239] studies. * Value estimated from a subsequent publication [248].

Besides these two pioneering three-photon studies from the C.Xu lab, some early three-photon studies have been enabled by the development of high-frequency commercial OPAs (see next section): wide-field three-photon excitation at 1300 nm has been demonstrated together with a first proof-of-principle experiment of three-photon optogenetic photostimulation of cultured neurons

expressing channelrhodopsin [249]. Three-photon Bessel beam excitation has also recently been demonstrated [250][251]. Finally, 3PEF has already started to open new experimental paradigms, particularly in the context of functional fluorescence microscopy: *in vivo* functional imaging in the adult fly brain without the need of surgically removing the opaque cuticle on top of the brain have recently been demonstrated [252].

4.2 SWIR laser sources for three-photon microscopy

The development of deep-tissue multiphoton excitation strategies crucially depends on the development of optimized laser sources. In this section, we will first discuss the requirements for optimal sources for SWIR 3PEF. Then, we will briefly review some of the main laser designs developed so far for three-photon microscopy in the SWIR range. Finally, we will present our work on performing 3PEF on both fixed and live tissues using two different laser source designs.

4.2.1 Requirements for a laser source optimal for 3P microscopy

Spectral range:

An immediate requirement for a 3P laser source to perform three-photon microscopy using commonly used fluorophores is to emit in the SWIR window, specifically in the water low absorption windows, around 1300 nm and 1700 nm. Deep-tissue THG imaging has also been reported at 1550 nm [253]. However, while deep-tissue 3P imaging may be possible in the SWIR range outside these windows, the very high water absorption at these wavelengths precludes the use of water immersion objectives with a long working distance, and additionally requires thorough management of the imaging frame rate to control water-mediated tissue heating resulting in very slow imaging rates (30 s interval time between two successive frames reported in [253].

3P efficiency:

When designing or choosing a suitable laser source for 3P microscopy a crucial parameter to take into account is the fluorophores three-photon action cross sections. The action cross-section $\eta\sigma_n$ characterizes the fluorophore's contribution to the n^{th} order nonlinear signal, with η the fluorescence quantum efficiency and σ_n the n-photon absorption cross-section. Action cross-sections therefore guide the determination of the required pulse energy for a nPEF process. Table 4.1 presents the order of magnitude of n^{th} order fluorescence action cross sections as measured in the literature from most commonly used fluorophores [247][254].

$\eta\sigma_2$	$\eta\sigma_3$	$\eta\sigma_4$
10^{-49} cm^4s/photon	10^{-83} cm^6(s/photon)^2	10^{-115} cm^8(s/photon)^3

Table 4.1: Orders of magnitude of nPEF action cross sections.

Although exact values of action cross sections depend on the fluorophores and the wavelength used, the general rule is that **n-photon excited fluorescence is weaker with increased**

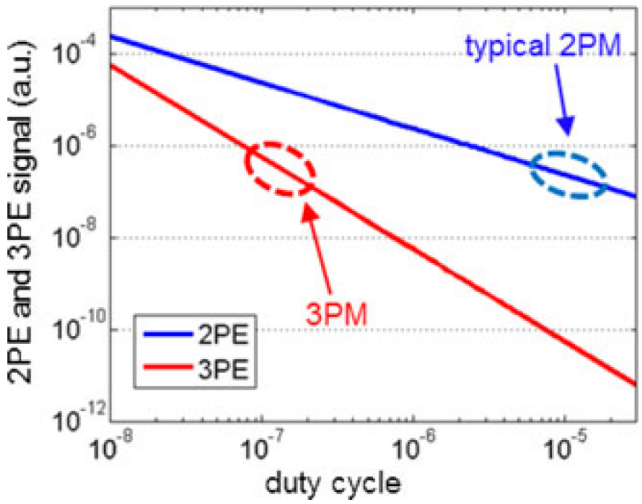

FIGURE 4.5. Multiphoton signal as a function of laser duty cycle. Adapted from [255]

process order. In order to compensate for this, pulses with higher energies are required for efficient fluorescence imaging through higher order processes.

On the upper bound, action cross sections also set a limitation on the maximum pulse energy, above which saturation occurs. The limit for saturation under ultrashort pulse excitation is one transition per pulse per fluorophore. The corresponding maximum pulse energy before saturation at the focus was calculated to be ~1nJ for 2PEF and ~5nJ for 3PEF at 1700 nm [254].

Pulse energy:

In order to compensate for the weaker 3PEF efficiency compared to 2PEF, **higher excitation intensities are required for three-photon microscopy**. However, since the amount of average power deposited on the sample is limited by thermal photodamage, **a strategy is to increase the pulse energy by lowering the laser duty cycle, while keeping the average power constant**. The laser duty D is defined as D=fτ with f the repetition rate and τ the pulse width. Fig 4.5 presents the 2P and 3P fluorescence signals as a function of duty cycle, assuming NA=1, λ=1300 nm and a 5 mW average power. Typical 2P conditions (100fs,100 MHz) correspond to a 10^{-5} duty cycle. The graphs in Fig 4.5 show that a two order of magnitude decrease of the laser duty cycle can counterbalance the weaker efficiency of 3P fluorescence. An efficient strategy for 3P imaging is therefore to use laser sources with ~100 times lower repetition rate, i.e **in the MHz range**. Using **short pulses (<100 fs)** is certainly beneficial for the 3P signal, although in practice it can not be decreased by more than a factor 2.

The first demonstration of deep-tissue 3P microscopy in 2013 has driven the development of both lab-built and industrial laser sources operating in the SWIR range and with increasingly optimized properties for three-photon microscopy. We will briefly review these technologies in the

next section.

4.2.2 SWIR laser sources for 3P microscopy : state of the art

Two types of schemes have been demonstrated so far for SWIR laser sources with performances potentially matching the requirements for three-photon microscopy: fiber-based architectures and parametric amplification schemes. The characteristics of these recent SWIR sources developments are summarized in Table 4.2.

Reference	Design	E (μJ)	f (MHz)	τ (fs)	λ (nm)
Horton et al.	Fiber-based (SSFS)	0.5	1	65	1675
OperA (Coherent)	OPA	1	1	50-100	1140-1600
NOPA (Spectra Physics)	OPA	1	up to 0.4	40-100 fs	1200-2500
AVUS (A.P.E)	OPA	1	1.2	70 fs	1200-2500
Rishoj et al	Fiber-based (HOM)	0.03	-	50 fs	1030-1300
Chung et al	Fiber-based (SPM)	0.01	31	50 fs	1300-1700
Cadroas, Abdeladim et al.	Fiber-based (SSFS)	0.009	50	70 fs	1650
Guesmi*, Abdeladim* et al.	OPA	3-5	1.2	65-69 fs	1300 + 1700

Table 4.2: SWIR laser sources for 3P microscopy.

4.2.2.1 Fiber laser designs

Fiber-based systems provide an attractive alternative to commonly used bulk lasers for multi-photon microscopy as they are more intrinsically stable regarding to environmental parameters while also usually being more compact and cost-effective. The most mature fiber laser systems designed so far are based on rare earth dopants as gain media, mainly ytterbium (Yb) fiber lasers emitting in the 1020-1060 nm range or erbium (Er) fiber lasers emitting in the 1520-1570 nm range. These spectral ranges are however not adapted for SWIR deep-tissue three-photon microscopy. Some recent developments focused on generating direct 1700 nm pulsed emission using alternative rare earth dopants such as bismuth and thulium [256][257][258], but these strategies so far fail to provide sufficient peak powers required for multiphoton imaging.
Another strategy harnessed recently to reach SWIR windows of interest is the use of soliton self-frequency shift (SSFS) which enables wavelength red-shifting [255]. The effect have been demonstrated in 1986 [259] in optical fibers with anomalous dispersion: soliton pulses can continuously transfer energy to higher wavelengths via intrapulse stimulated Raman scattering (SRS). The soliton pulse can therefore be shifted to higher wavelengths by adjusting the input power. Soliton pulses generated from SSFS are particularly suited for multiphoton microscopy as they typically have good pulse quality and femtosecond duration. SSFS has essentially been used to reach the 1700 nm window from a 1550 nm pump laser. An important challenge though

was to reach the high pulse energies required for three-photon imaging. In order to circumvent this difficulty, C.Xu and colleagues used a large effective area PC rod and achieved 1700 nm pulse generation at hundreds of nanoJoules [5]. This laser source was the first laser developed for 3P microscopy at 1700 nm. The second alternative SSFS-based fiber laser design proposed at this wavelength was developed by Sébastien Février and colleagues and relied on the use of a home-made LMA fiber within a master oscillator power amplifier (MOPA) scheme [260]. While this solution presented the advantage of being more integrated, the pulse energies achieved remained lower (~9nJ) than the levels reached by the rod design.
In the 1300 nm spectral window, SSFS-based fiber laser designs with the appropriate pulse energies are still lacking, because of high non-linearities in this regime which constrain the maximum pulse energies to few nanoJoules [261]. To circumvent this limitation, a solution using higher order modes has been implemented although it required a spatial light modulator at the output of the laser to convert the output to a Gaussian output [262]. Recently, self-phase modulation-based spectral broadening has been introduced as an alternative to SSFS generating both blue-shifting and red-shifting from the typical 1550 nm central Erbium wavelength, hence allowing a 1300 nm-1700 nm wavelength tunability [263]. In addition this scheme has the potential for power scalability making it a promising technology for the future of compact 3P-compatible SWIR laser sources.

4.2.2.2 Optical parametric amplifiers

Fiber-based laser designs for SWIR three-photon sources have the potential to substantially decrease the cost, footprint and the laser output variability, and can therefore potentially enable a broader dissemination and use three-photon microscopy. However, these designs are limited in the current state-of-the art to low pulse energies. The laser industry has therefore turned to another technology to design robust sources suited for three-photon microscopy with the necessary pulse energy required: optical parametric amplifiers (OPAs). Parametric amplification is a non linear process where a pump beam of frequency ωp gives rise to a signal and idler beam of frequency ωs and ωi respectively such that ωp = ωs + ωi. In an OPA, the input is both the pump beam and the signal beam so that the signal beam is amplified while the pump beam is weakened. Commercial OPAs developed for three-photon microscopy usually consist of two OPA stages pumped by a high power Yb fiber laser. Some of these developments are listed in Table 4.2 along with their performances. These systems operate at MHz repetition rate (400 kHz to 2MHz) and usually provide a tunable output covering the SWIR range of interest (1300 nm- 1700nm) along with a fixed or tunable output in the visible/near infrared (below 1050 nm). These sources have played a significant role in the emerging interest for three-photon microscopy amongst microscopy and neurobiology laboratories.

Before closing on this brief overview of the laser sources developed in the recent years for three-photon microscopy, it is much worth noting that all these lasers, fiber-based or OPAs, including

those with tunable and/or dual outputs, have been designed to target only one SWIR window at the same time. The immediate consequence is that so far, deep-tissue three-photon microscopy has remained essentially monochromatic.

4.2.3 Comparison of two custom-built SWIR sources for red 3PEF

During my PhD, I had the opportunity to work in collaboration with two laser groups, the team of Sébastien Février from the XLIM institute in Limoges and the team of Frédéric Druon in Laboratoire Charles Fabry (LCF, IOGS), in order to test and optimize some of the first SWIR laser designs suitable for 3P microscopy. Regarding the context of this work, it is worth mentioning that when we started the collaboration with the XLIM team in the fall of 2015, the only published work in the field was the reference Horton paper from C.Xu's laboratory both from the laser design and microscopy perspective. Industrial OPAs operating in the MHz range and suitable for 3P microscopy started to be commercialized in the mid-2016. In this section, we will present our work on three-photon microscopy in the 1700 nm range with the two different lab-built SWIR sources: a fiber SSFS-based source (XLIM) and an optical parametric amplifier (LCF).

4.2.3.1 Experimental setup

For test experiments, either the fiber laser or the OPA laser was routed into the two-photon point-scanning microscope presented earlier, after adapting the setup's optical transmission (more details in the next section) at 1700 nm. In the fiber-laser experiments, the objective used was an Olympus 25X 1.05 NA W specifically coated for improved transmission up to 1700 nm range ('Horton' objective). A similar objective but with an MP2 near-IR coating was used in the OPA experiments, with textasciitilde 60% transmission in the SWIR range. Red fluorescence and third harmonic generation (THG) were detected in two separate epi-detection channels. The characteristics of the two lasers are recapitulated in Table 4.2. Figure 4.6 presents a schematic of the 3P setup with the fiber laser source.

4.2.3.2 3PEF/THG imaging of fixed mouse brain tissue

3PEF/THG imaging with the fiber laser:

We recorded simultaneous red 3PEF/THG stacks from a Rainbow-3 transgenic line [**?**] exhibiting ubiquitous dTomato labeling with a particularly strong expression in blood vessels. Figure 4.7 presents representative images acquired in the cortex and the brainstem. Cortical images were acquired directly from the mouse brain surface (brain horizontally oriented), while the brainstem images were acquired from a coronal orientation. Samples were maintained within an agar gel and immersed in a PBS-filled waterbath for imaging. We observed 3PEF fluorescence from red-labeled blood vessels as well as THG signal emanating from submicron-thin myelinated axons, blood vessels, large fiber tracts and strongly myelinated brainstem nuclei. Figure 4.7

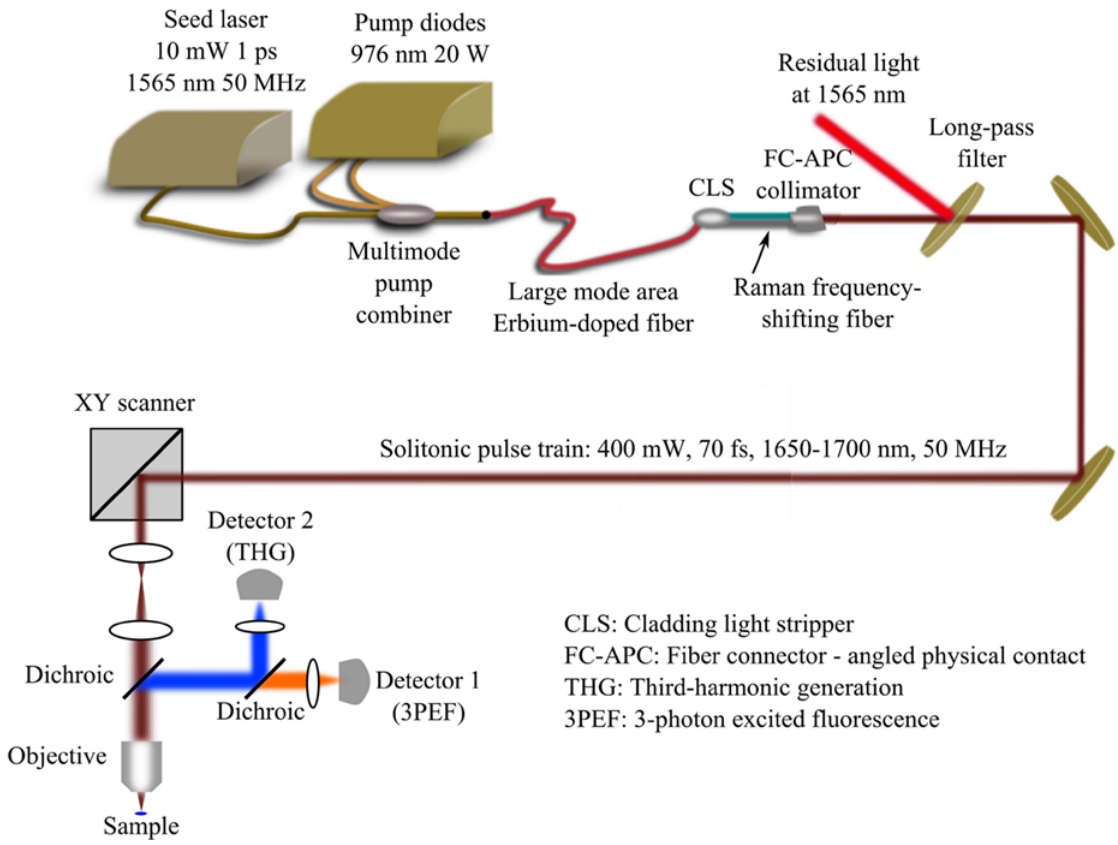

FIGURE 4.6. Experimental setup for 3P microscopy at 1700 nm with a fiber-based laser scheme. Chirped pulses from the seed laser at 1565 nm are amplified directly in a diode-pumped large mode area Er-doped fiber and frequency-shifted in a second large-mode area fiber. A long-pass filter filters out residual light at wavelengths below 1600 nm prior to the three-photon microscope.

presents representative images displaying such contrast from acquired z-stacks, however the presented images correspond to shallow depths only: 30 µm below the surface for cortex images and 100 µm below the surface for brainstem images. With the pulse characteristics provided by this fibered source, due to limited power, we could not reach depths comparable to the ones routinely accessed in two-photon microscopy, despite long pixel dwell times (20-200 µs), due to limited power. Indeed, in three-photon microscopy, the signal is divided by $e^3 \approx 20$ when the beam is focused at an attenuation length distance deeper within the sample. From the acquired z-stacks, we derived attenuation length measurements from the acquired z-stacks and found values of ~250 µm in cortical tissue and ~150 µm in the brainstem. Therefore a large amount of power "supply" is required to enable deep-tissue imaging beyond these depths while we already needed to use the maximum available power (P=130 mW) at superficial depths. We concluded that this fiber source design needed further power scalability to benefit from the advantages of

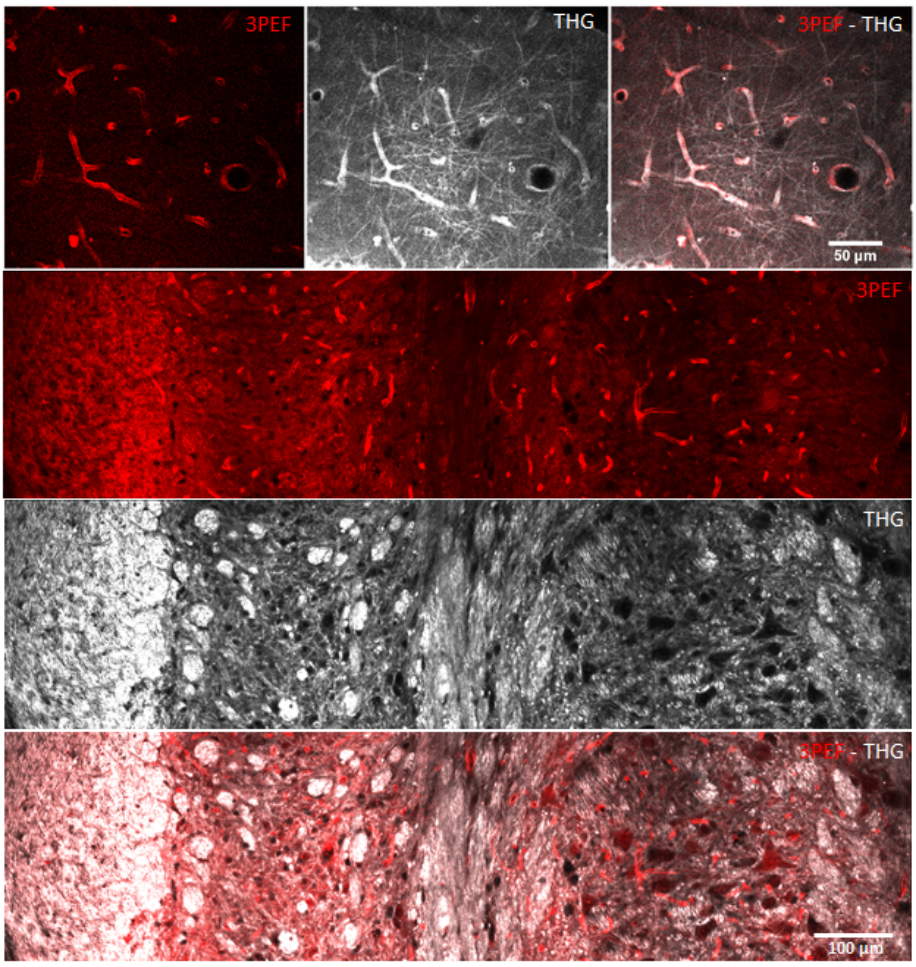

FIGURE 4.7. Simultaneous THG (grays) and 3PEF (red) imaging of fixed *Rainbow*3 mouse cortex (upper panel) and brainstem tissue (middle and lower panels) exhibiting dTomato labeling, acquired with the 1650 nm 50 MHz fiber laser. Pixel size: 0.8 µm/pixel (cortex) and 0.55 µm/pixel (brainstem).

three-photon microscopy for deep-tissue imaging. Nevertheless, this study helped us in better understanding the key parameters enabling deep-tissue three-photon imaging. In addition, we found that dTomato can be excited in this spectral window which had not been shown so far. This result is of particular interest since three-photon excitation spectra and three-photon photophysics properties of commonly used fluorophores are not yet systematically characterized and published.

3PEF/THG imaging with the optical parametric amplifier:

In this section, we discuss deep-tissue imaging in fixed mouse brain using the OPA MHz source at 1.7 µm. Figure 4.8 presents image z-stacks recorded from a fixed mouse brain cortical area, where neural cells were densely labeled with the red FP tdTomato. The exact same zone was imaged at depths ranging from 200 µm to 800 µm sequentially with both the MHz source at 1700

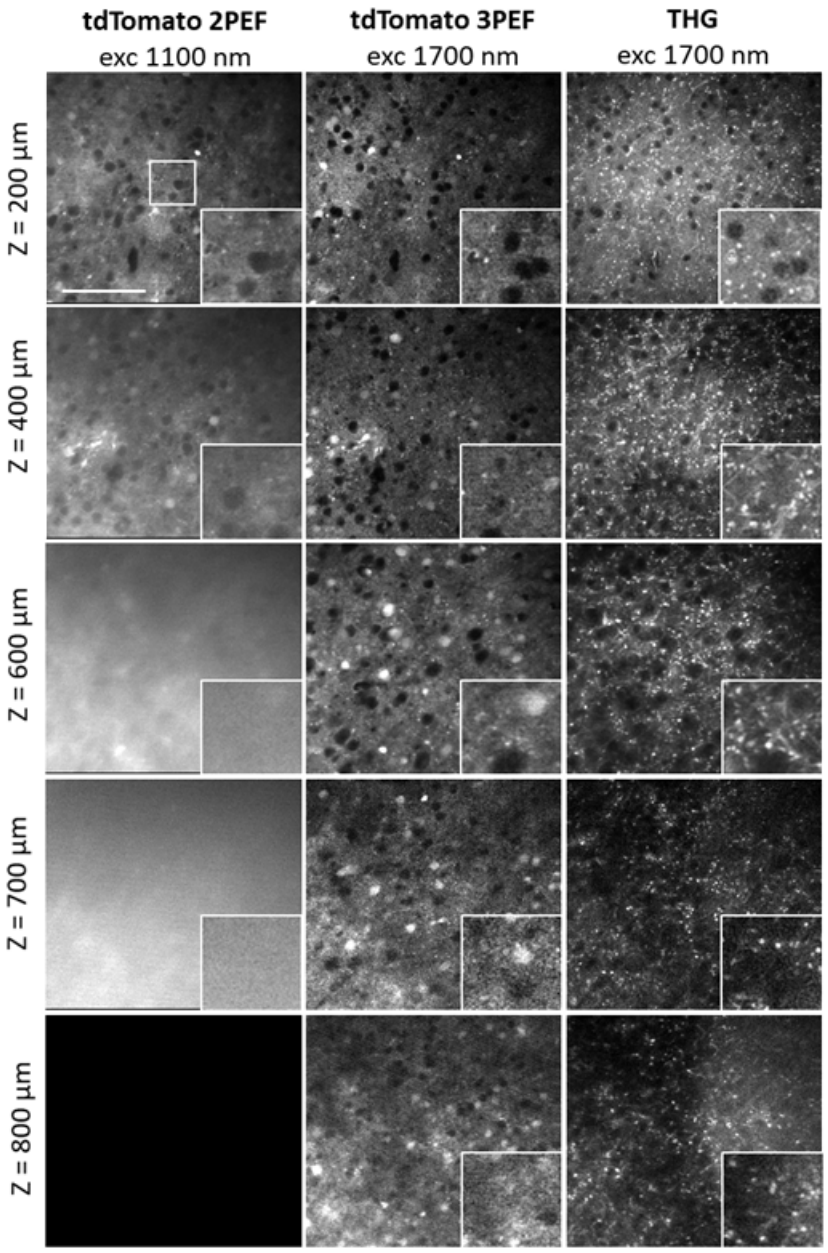

FIGURE 4.8. 2PEF, 3PEF and THG imaging of tdTomato-labeled fixed mouse brain cortex. Image stacks were recorded sequentially with 1100 nm excitation (2PEF) and with 1700 nm excitation (3PEF and THG). Images are intensity-normalized in each plane for contrast comparison. Conditions for 2P imaging: 1100 nm, 80 MHz, 40 to 150 mW on the sample and 1 to 16 accumulations depending on imaging depth. Conditions for 3P imaging: 1700nm,1.2MHz,2 to 100 mW at the sample surface depending on imaging depth, 1 accumulations. Time per pixel, 10 µs. Scale bar, 100 µm.

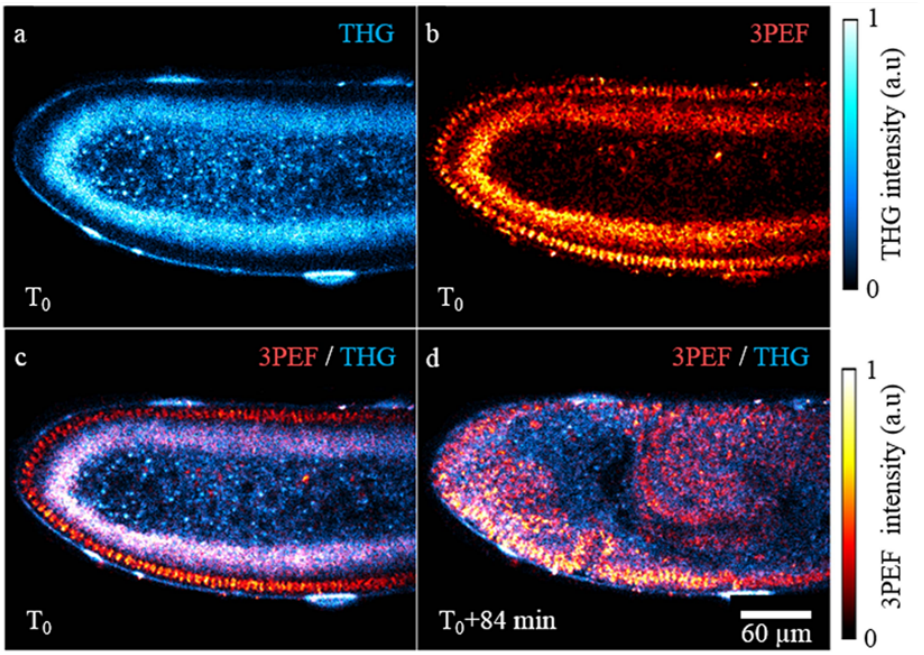

FIGURE 4.9. Simultaneous 3PEF and THG imaging of a developing Drosophila embryo with RFP labeling of cell nuclei with the fibered 50 MHz laser source. (a) THG, (b) 3PEF and (c) overlay images of the embryo before the onset of gastrulation. (d) Same embryo 84 min later. Anterior pole to the left, dorsal side up. Pixel dwell time: 27 µs. Scale bar: 60 µm.

nm (providing simultaneous red 3PEF and THG images) and a 80 MHz OPO source at 1100 nm (providing red 2PEF). Of note, 1100 nm is a particularly favorable wavelength for deep-tissue two-photon microscopy. The acquired stacks demonstrate that, in this densely labeled sample, 3PEF provides superior performances compared to 2PEF in terms of signal-to-background ratio. At depths larger than 600 µm, the benefit of 3PEF is obvious compared to 2PEF. This experiment is the first direct experimental demonstration at 1700 nm of three-photon microscopy as an effective solution to the limiting out-of-focus surface generated fluorescence in two-photon microscopy, as hypothesized by C.Xu and colleagues in the first SWIR three photon paper [5].

4.2.3.3 Live 3PEF/THG imaging in developing Drosophila embryos

Next, we verified that 3PEF sustained *in vivo* imaging could be achieved with both lasers. We chose here as a model system developing *Drosophila melanogaster* embryos since they develop relatively fast and present very stereotyped developmental patterns that can serve as landmarks for normal tissue development [264].

We used the His2AvmRFP1 fly strain (Bloomington Drosophila Stock Center, # 23651) expressing RFP labeling of cell nuclei. Embryo were prepared for live imaging as described in details in [52]. Briefly, the flies were put to lay the day before the experiment into a collection bottle with

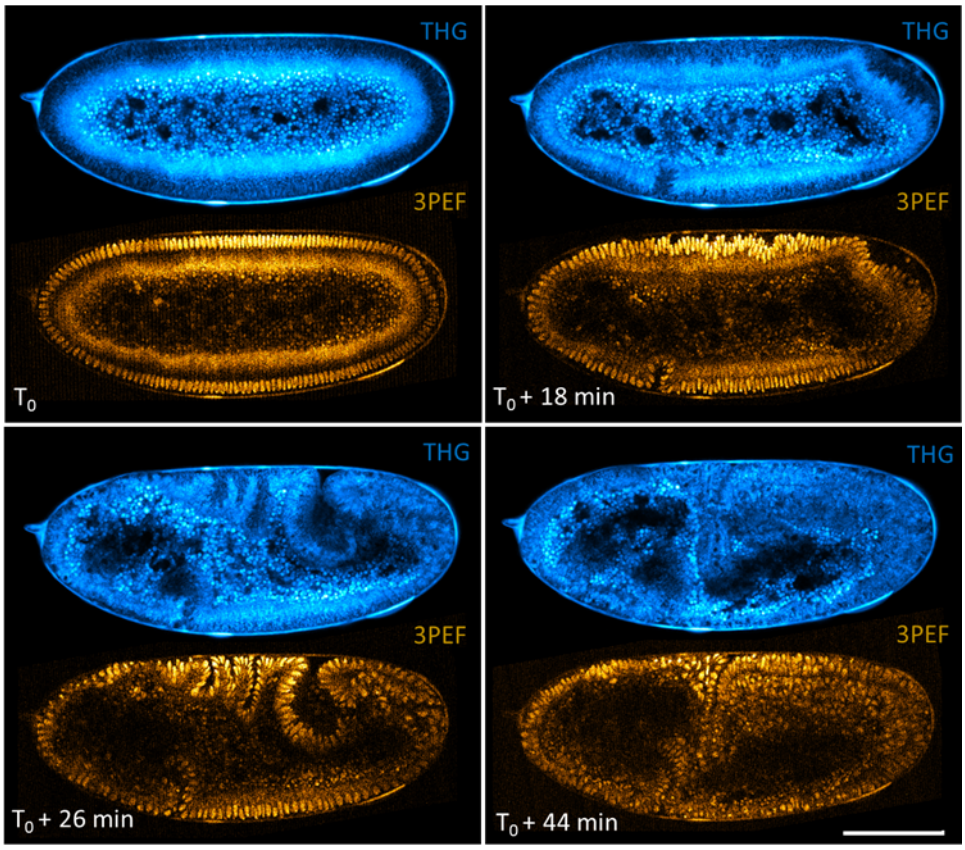

FIGURE 4.10. 3PEF/THG time-lapse imaging of a developing Drosophila embryo with the MHz OPA source. Scale bar: 100 µm.

an agar grapes fruit plate. The plate was changed next morning and embryos were collected ~2-3 hours after laying at 25°C. Embryos were then dechorionated with a freshly prepared 50% bleach solution, gently collected with a paintbrush onto an agar plate and then directly glued on a glass coverslip and covered with a drop of water. Embryos were therefore directly accessible for imaging, the objective directly immersed onto the drop of water, without the requirement of an imaging coverslip.

With both laser sources, we were able to record time-lapse images of developing Drosophila embryos from late cellularization stages (T_0 as indicated in Fig 4.9 and Fig 4.10) onto gastrulation. With the fibered source, the power was set to the maximum available (130 mW), which imposed working with a particularly reduced N.A (5.5 µm axial resolution). To obtain sufficient signal to noise ratio, the pixel dwell time was set to 27 µs and an image was acquired every minute. With the OPA MHz source, the power was set to 30 mW corresponding to an axial resolution of 4.2 µm, the pixel dwell time to 10 µs and images were acquired every 2 min. The image lateral sampling was set to 0.5 µm per pixel. Of note, the time-lapse experiment presented on Figure 4.10 was extracted from a 3D time-lapse were 10 µm axially sampled 3D stacks were

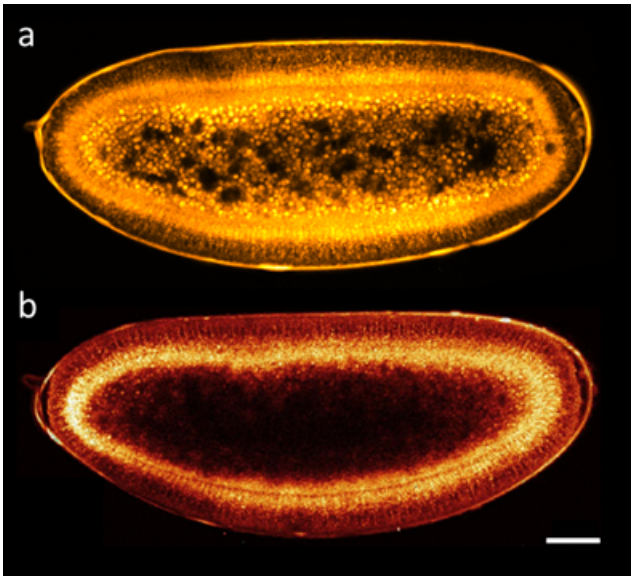

FIGURE 4.11. THG imaging of a Drosophila embryo during cellularization using (a) OPA 1.2 MHz, 1700 nm excitation and (b) OPO 80 MHz, 1200 nm excitation. (b) was adapted from [51]. Scale bar: 50 µm.

acquired every 2 min. In both cases, we could observe unperturbed invagination movement (Fig 4.9d, Fig 4.10), characteristic of gastrulation, suggesting that SWIR three photon microscopy, under the appropriate illumination conditions, is compatible with continuous time-lapse imaging. Finally, one can compare the THG signal obtained at 1700 nm with the MHz OPA source to previously published THG data of developing Drosophila embryos acquired at 1200 nm with an 80 MHz OPO system [51]. Figure 4.11 presents such a comparison. The upper image (OPA acquired) corresponds to a depth of 90 µm below the surface of the embryo, meaning that it is at least at the equatorial plane. It was also selected based on morphological criteria to be at a similar developmental stage to the image acquired at 1200 nm. Interestingly, lipid droplets and vesicles at the center of the highly scattering yolk are clearly visible at 1700 nm and 1.2 MHz while the same region was difficult to reach with the 1200nm/80 MHz configuration, despite the fact that the 1200 nm wavelength is favorable for deep-tissue imaging. SWIR MHz sources seem therefore to be open interesting perspectives for deep-tissue third harmonic generation.

4.3 Dual-color three-photon microscopy

To expand the potential applications of three-photon microscopy, multicolor configurations need to be developed. Indeed, this would enable in situ study of live interactions and relative distributions of different cell types or subcellular components at depths complementing those reached by two-photon microscopy. In particular, the combination of GFP/EGFP and a red fluorophore (RFP/mCherry/dTomato) is widely used in systems biology, mainly because of the fluorophores

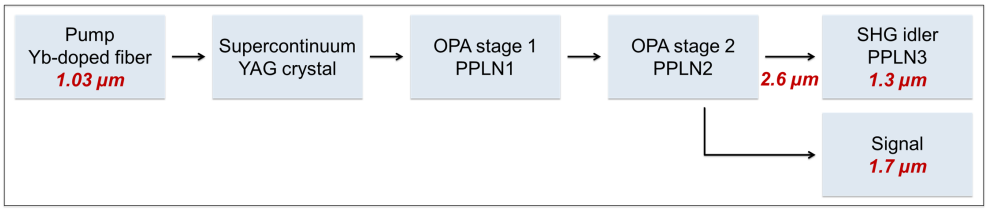

FIGURE 4.12. Multiband MHz OPA source general architecture.

optimized photophysical properties (photostability, brightness) and efficient expression in a wide variety of systems. For instance, the vast majority of commercially available dual-color transgenic lines or plasmids express such a combination. While in two-photon microscopy red and green fluorophores can be simultaneously targeted using a single excitation wavelength (typically 960 nm), this proves to be more challenging in three-photon microscopy because of the wide separation of the relevant spectral bands. Therefore an important step towards multicolor three-photon microscopy is to develop working schemes for red/green 3PEF.

Using a novel original MHz OPA source emitting concomitantly at 1300 nm and 1700 nm ultrashort pulses optimized for three-photon microscopy, we implemented multicontrast three-photon imaging : dual-color red/green 3PEF together with simultaneously generated third harmonic generation. This project was done in collaboration with the team of Frédric Druon at Laboratory Charles Fabry (LCF/IOGS). Khmaies Guesmi built the OPA source during his postdoc at LCF, then the source was moved to LOB for three-photon microscopy implementation.

4.3.1 OPCPA source design

The multiband source is based on the optical parametric chirped-pulse amplification (OPCPA) technology. OPCPA is an attractive approach for developing a MHz source for 3P microscopy since it is, in principle, compatible with energetic short pulses and can enable access to long wavelengths in the near mid-IR range [265][266]. The overall architecture of the multiband source is presented in Figure 4.12. The general strategy here is to perform **parametric amplification with a 1700 nm signal beam and a 1030 nm pump beam**, in order to obtain an amplified 1700 nm beam and an **idler beam of approximately 2600 nm which is then frequency doubled to obtain a 1300 nm synchronous beam**.

The detailed experimental setup and beam paths are presented in Figure 4.13 and Figure 4.14. The design relies on a commercially available Ytterbium-doped fiber amplifier (YDFA) pump source delivering 1.25 MHz highly energetic pulse trains (50W average power, 310 fs) at 1030 nm. In order to reach the 1700 nm spectral band, supercontinuum generation was used by focusing the pump beam into a YAG crystal. In order to reach the µJ pulse energy range necessary for 3P excitation, the 1700 nm supercontinuum output was seeded into two stages of parametric amplification. Two stages of amplification were necessary to achieve sufficient

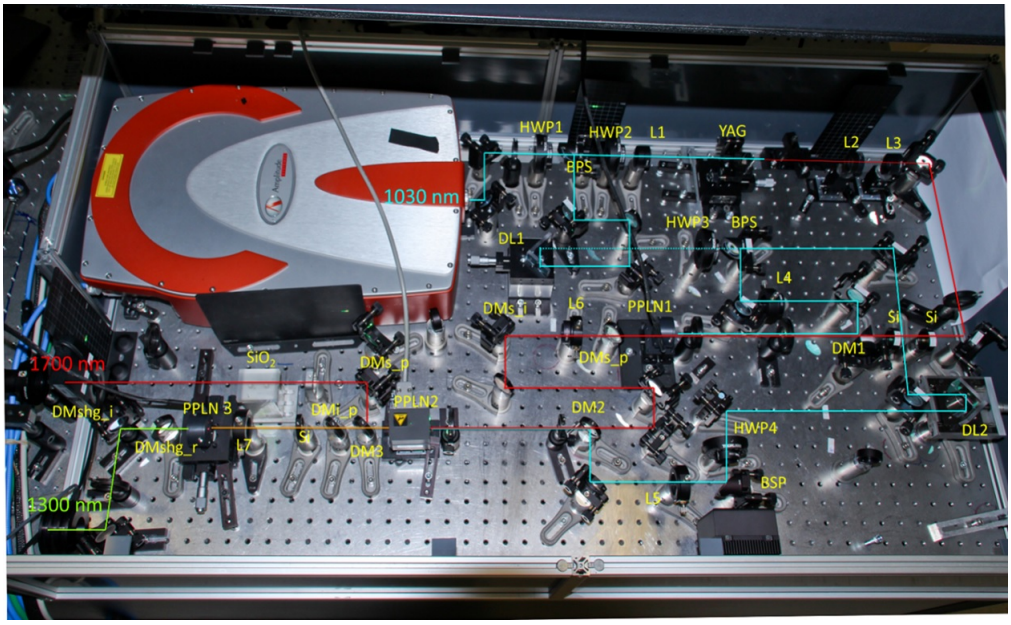

FIGURE 4.13. Multiband MHz OPA source experimental setup.

gain. The amplification process relied on chirped pulse amplification : the 1700 nm signal beam was first temporally stretched prior to entering the first OPA stage using a 3 mm Si plate, then recompressed at the output of the second OPA stage using a 50 mm fused silica slab. This strategy is one of the most efficient way to generate highly energetic pulses (actually, chirped pulse amplification is the technique used to generate petawatt laser pulses in the field of ultrafast high intensity lasers [267]) as the chirped pulse can be safely amplified by several order of magnitude factors in the gain medium due to its lower intensity. In our setup, PPLN crystals are used as gain media for parametric amplification. The 2600 nm idler beam is further focused into a third PPLN crystal for second harmonic generation. Overall, the OPCPA source provides two concomitant 1300 nm and 1700 nm sub-70 fs pulses (Figure 4.14b), at 1.25 Mhz which makes it particularly suited for three-photon microscopy.

4.3.2 Experimental setup and validation

We combined the two mid-IR output beams using a dichroic mirror and then the beams were injected onto the custom-built point-scanning multiphoton microscope described in Chapter 2 of which we adapted the optical transmission to the mid-IR range. We primarily adapted the scan system (scan lens and tube lens) and the main excitation/detection dichroic. The objective used in these experiments was the Olympus 25X 1.05 NA MP2 (infrared enhanced) transmitting above 60% in the two windows of interest. A telescope was placed on each beam path to adjust the beam size at the objective rear pupil and the relative axial mismatch between the two beams. Three independent channel were used for signal detection : the blue channel for 1300 nm THG detection

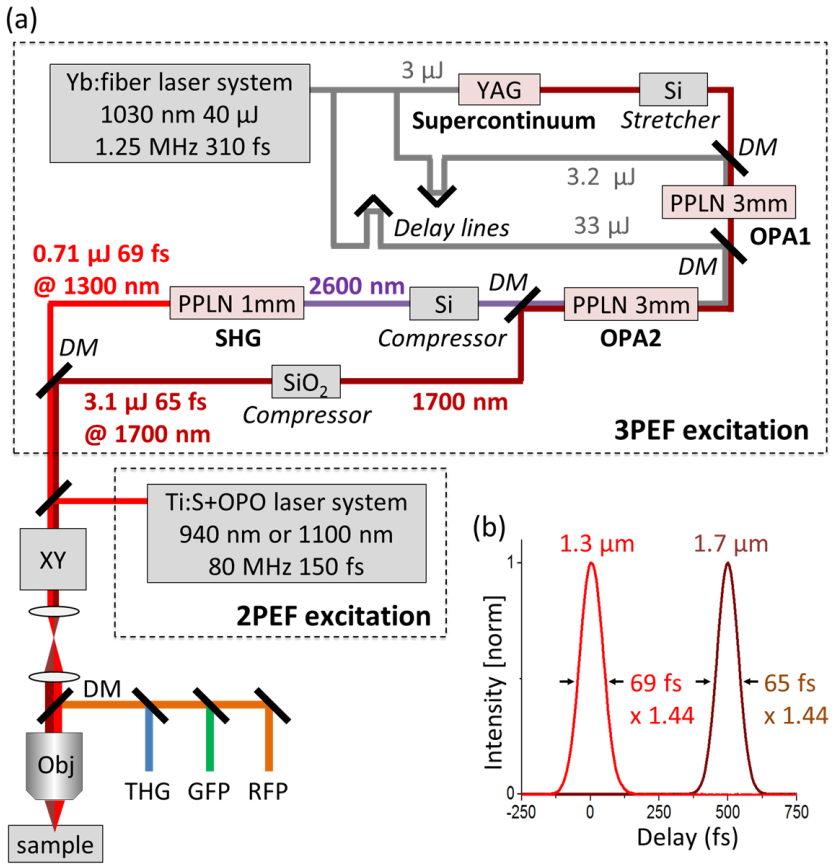

FIGURE 4.14. Dual-color three-photon microscopy setup. (a) Multimodal three-photon microscope. DM dichroic mirrors, OPA optical parametric amplification stages, XY beam scanning, Obj microscope objective. (b) Measured temporal profiles for the two SWIR beams.

occurring at approx. 433 nm, and the green and red channels for green and red fluorescence. 1700 nm THG was rejected from the green channel using a GFP-centered bandpass filter. The experimental setup also offered the possibility to switch to a 80Mhz TiS+OPO excitation for 3P and 2P comparisons. Unless stated otherwise, two-photon excitation was performed at 920 nm and 1100 nm respectively for green and red excitations.

We characterized the optical performances of the microscope by measuring THG stacks across a glass-water interface. In order to co-align the two beams in the microscope, we used THG signal emanating from 1.1 µm size latex beads. We found this approach more practical for daily-basis calibrations than the use of standard sub-micron fluorescent beads. After optimization of the telescopes, we measured point-spread functions with FWHM of 2.8 ± 0.1 µm and 3.8 ± 0.1 µm for the 1300 nm and 1700 nm beams respectively, with an axial mismatch below 0.5 µm between the two foci (Fig 4.15). In these conditions, up to 110 and 100mW of excitation power was available after the objective for the 1300 nm and 1700 nm beams, respectively. It is worth mentioning here

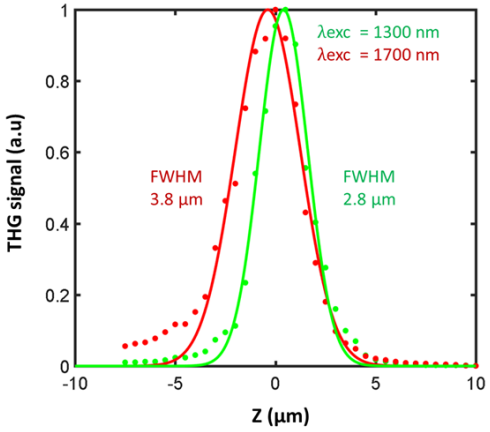

FIGURE 4.15. Axial resolution during two-color 3PEF imaging. Axial resolutions and axial foci mismatch estimated from THG z-stacks through a water-glass interface with the 1300 nm beam (green) and the 1700 nm beam (red). Z-stacks sampled at 0.5 µm and Gaussian-fitted.

that despite the robust design of the laser source (power and spectral performances recovered from one day to another), the output of the source constantly varied from one day to another (beam direction, divergence) hence requiring alignment and telescope adjustment before each experiment.

Finally, we explored the performance of the OPA source for dual-color imaging. We found that combined 1.3 µm and 1.7 µm enables dual-color excitation of three red/green FP combinations expressed in HEK cells or mouse brain tissue (cortex): **GFP/tdTomato**, **GFP/mCherry** and **EGFP/mRFP**. Notably here, we demonstrate the three-photon excitability of mCherry at 1700 nm.

4.3.3 Multimodal three-photon imaging in scattering tissues

Next, we sought to test the capabilities of the dual-output OPA source for multimodal deep-tissue imaging. For this demonstration, we chose to use **fixed embryonic chick spinal tissue** as a model system. Spinal cord samples were coelectroporated at equal concentration (1µg/mL) with plasmids encoding for **EGFP (CAG-EGFP)** and **mRFP (CAG-mRFP)** in Jean Livet's lab. At embryonic day 9, spinal cords were dissected, fixed (4% PFA) and pinned on a silicon substrate longitudinally, with the dorsal horn on top for imaging (Fig 4.17). This configuration is particularly challenging for deep imaging as the light beam needs to cross scattering/aberrating tissue layers before reaching the labeled cells.

We recorded two-color image stacks over a depth of 600 µm using sequential two-photon and three-photon excitation. THG signal was detected simultaneously with the 1300 nm beam. In 3P stacks, the laser power was adjusted from 15 mW to 100 mW, according to the imaging

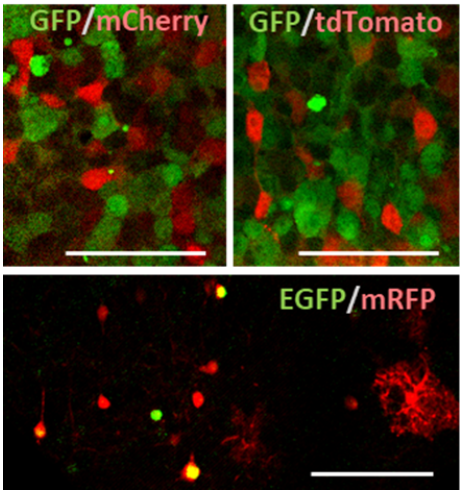

FIGURE 4.16. Dual-color 3PEF imaging for several combinations of green-red fluorescent proteins expressed in HEK cells (top) and mouse brain tissue (bottom) at a depth of 500 µm. Scale bars: 100 µm.

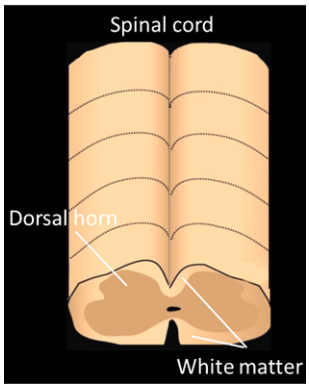

FIGURE 4.17. Spinal cord geometry.

depth. In 2P stacks, the power was adjusted from 10mW to 50 mW for EGFP imaging, and from 10mW to 100 mW for mRFP imaging, together with up to 4 accumulations at large depths. Figure **??** shows examples of in-depth XZ views of the acquired stacks. These views demonstrate the capacity of three-photon microscopy to preserve contrast and SBR at depths surpassing the depths accessible by two-photon microscopy also at 1300 nm, similarly to what we demonstrated in the previous section at 1700 nm. To characterize this gain in performance, we estimated the signal-to-background ratio at 500 µm in three and two-photon images for both EFGP and mRFP signals (Fig 4.19). When using 3P excitation, we observe in this type of sample a two-fold and a four-fold increase of the signal-to-backgound ratio for red and green imaging respectively, compared to equivalent 2P excitation.

Finally, few comments on the acquired THG contrast are worth mentioning, although harmonic

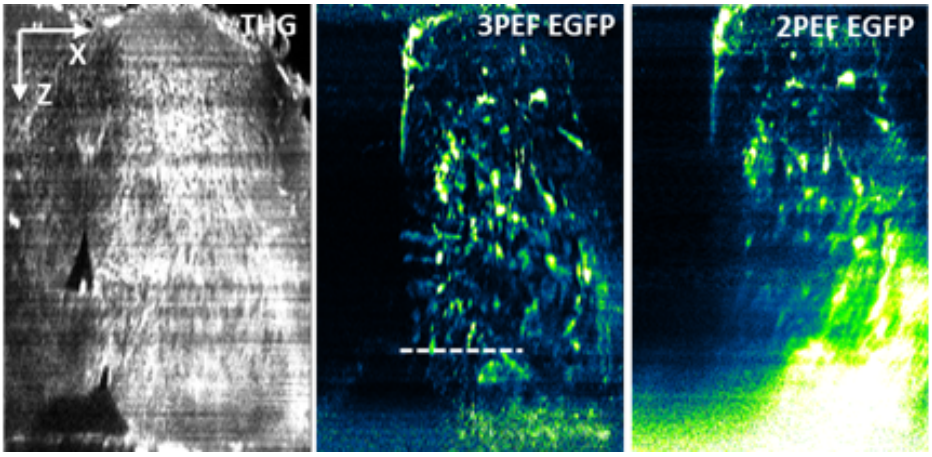

FIGURE 4.18. Deep-tissue imaging of fixed chick spinal tissue (E9).XZ projections of the THG, 3PEF EGFP, and 2PEF EGFP image stacks show the general morphology of the sample and the loss of 2PEF contrast with depth. Dotted line indicates the corresponding XY section presented in Fig 4.19 at 500 µm depth.

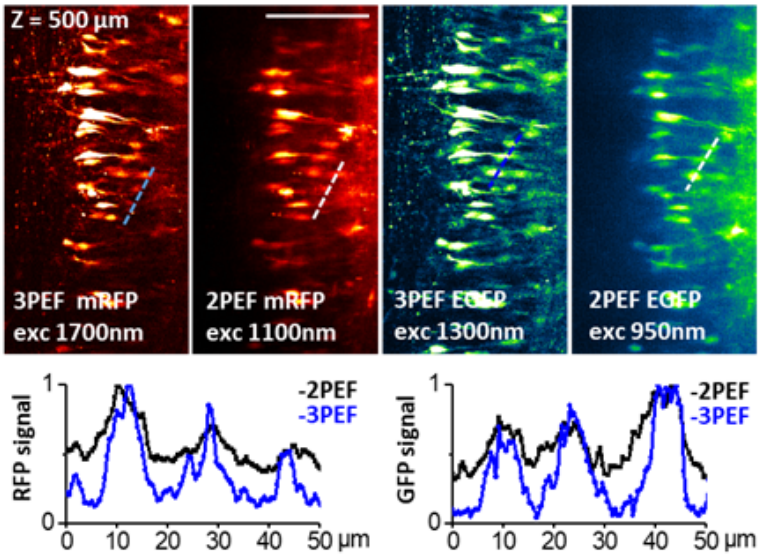

FIGURE 4.19. Red and green 3PEF vs. 2PEF contrasts. 3P and 2P mRFP and EGFP images recorded at a depth of 500 µm in fixed chick spinal tissue (E9). Intensity profiles measured along the dashed lines illustrate the superior contrast provided in both channels by 3PEF excitation. Scale bar: 100 µm.

imaging was not the primary goal of these experiments. THG contrast is basically obtained here 'for free' provided an additional detection channel. This feature is quite advantageous as it provides useful anatomical landmarks which are in general not detected in the fluorescence images. For instance here, the THG XZ projection provided an anatomical image of the neural tube with a clear view of the central canal section, and hence showed that we have captured

the entire depth of the tube. In fact, this excitation configuration based on high-peak power low repetition-rate pulses appears to be once again particularly suited for deep-tissue third harmonic generation. Because of the third-order nature of THG, signal level is very sensitive to scattering and aberrations. Therefore, extra power is needed during deep imaging in order to maintain a constant intensity at focus. Using typical 80 MHz OPOs, THG imaging within scattering tissues such as mouse cerebral tissue or human brain tumors, the maximum reachable depth have been reported to be few tens of microns [184][268]. In our study, we reported THG imaging over 700µm in highly scattering fixed mouse brain tissue. THG imaging beyond 1mm deep in the *in vivo* mouse brain has also been reported by the Xu lab [5][239], despite the fact that in both C.Xu's experimental scheme and ours, the detection configuration is not-optimal for THG imaging (here signals epi-detected while a forward detection would have been more optimal). Therefore MHz SWIR sources are expected to be particularly enabling for THG imaging deep within scattering tissues.

4.3.4 Live dual-color 3P microscopy

Imaging fixed tissues with three-photon microscopy was a well-adapted experimental framework to test our laser source, determine and optimize imaging parameters and compare nonlinear contrasts. However, although some applications can be envisioned *ex vivo*, ultimately the main motivation behind the development of 3P microscopy is the possibility to image deeper inside live tissues. In this last section, we present initial attempts at developing dual-color red/green 3P live imaging in two different vertebrate neural systems : embryonic chick spinal cord explant and intact adult zebrafish brain.

4.3.4.1 Embryonic chick spinal cord explant

For this set of live experiments, samples were prepared by Samuel Tozer (Institut de la Vision, Paris). Electroporation was performed in the chick neural tube at embryonic day 2 (E2), as described in [269]. A plasmid encoding the proneural gene Neurog2 (CAG-Neurog2, 1 µg/µL) was used to induce neural differentiation. This plasmid was co-transfected with CAG-EGFP (1 µg/µL) and CAG-H2B-mRFP (0.5 µg/µL) for dual-color dual-compartment labeling : cytoplasmic green and nuclear red. Embryos were harvested at E3, transferred to F12 medium and slit along their midline from the hindbrain to the caudal end (Fig 4.20a). The electroporated side of the neural tube was peeled off and mounted in a glass-bottom culture dish within a thin layer of 1% low-melting agarose dissolved in F12 medium, covered with 3 mL of culture medium (F12/Penicillin Streptomycin/Sodium pyruvate). Samples were then immediately transferred to a heating plate (37°C) positioned under the microscope objective for live imaging.

We recorded simultaneous dual-color 3PEF and THG time-lapse images of the developing spinal tissue. Images were recorded every 10 minutes, and the pixel sampling was set to 0.55 µm/pixel, with a 5µs pixel dwell time. Approximately 30 mW of laser power was available on each beam.

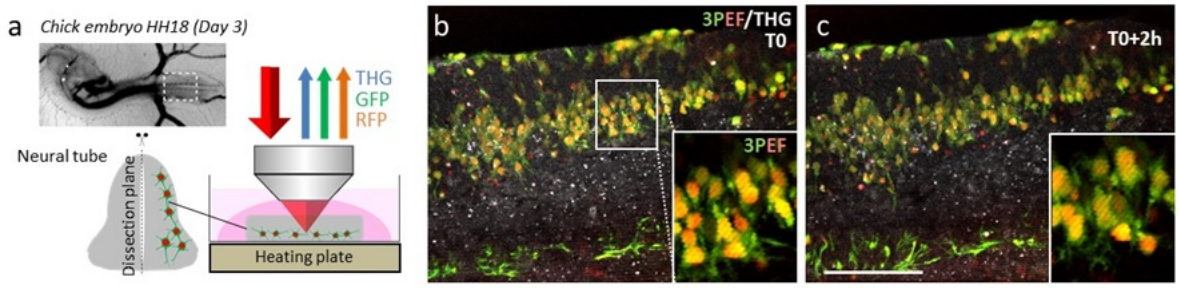

FIGURE 4.20. Simultaneous dual-color 3PEF and THG imaging of developing chick embryo spinal cord tissue (stage E3) expressing cytoplasmic GFP labeling and nuclear RFP labeling. (a) Experimental design. (b) 2h time-lapse imaging. Scale bar: 100 µm.

Figure 4.20 shows two snapshots at the beginning and the end of a 2h time-lapse. We could observe patterns of cell migration and process formation. THG imaging provided a morphological background of the surrounding tissue, useful to determine tissue explant integrity and to spot eventual tissue disruption. We used the morphological THG signal to optimize the imaging parameters for long-term imaging. Under these illumination conditions, we did not see signs of visible photodamage. We repeated a similar time-lapse experiment, here with a dual-color cytoplasmic labeling. In this second essay, images were taken every 15 min, with a 0,54 µm/pixel sampling and 5 µs pixel dwell time, and with 25mW and 15mW power at the sample surface respectively for the red and green beams. Tissue development was monitored for up to 4 hours, with no sign of evident photodamage. We note however that signs of photodamage were visible at subsequent time points. Therefore, although this data demonstrate the possibility of live dual-color 3P imaging, a systematic study of damage thresholds during imaging with MHz laser sources needs to be undertaken.

4.3.4.2 Through-skull adult zebrafish brain imaging

Finally, we developed an assay involving live dual-color 3P imaging in an intravital setting, specifically in a three-month-old zebrafish (*Danio rerio*). *Danio rerio* is increasingly used as vertebrate model in systems biology and neurobiology. This is mainly due to its ex utero rapid development, the availability of large genetic libraries, the ease and rapidity to generate new lines and a general lower maintenance cost. It is most extensively used in larval stages (up to 5 days post fertilization) due to its high optical transparency at these stages, which represents an additional benefit of the model. It is however interesting to develop deep-tissue imaging *in vivo* in the adult zebrafish brain as it is a particularly well-adapted model to study neurogenic niches [137][270][271].

We recorded multimodal 3PEF red/green and THG image stacks in the dorsal telencephalon

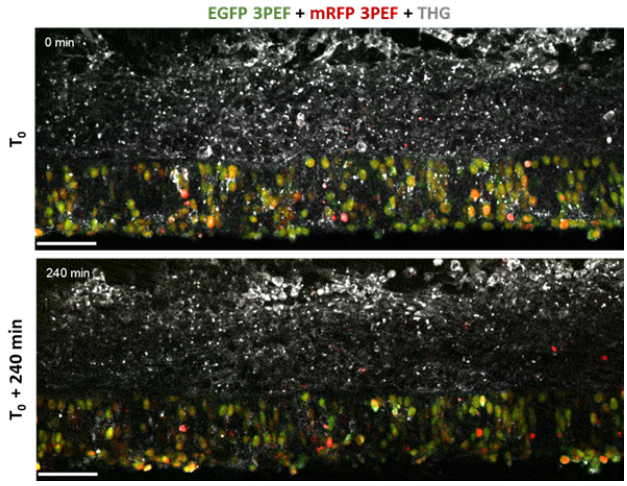

FIGURE 4.21. Simultaneous dual-color 3PEF and THG time-lapse imaging of developing chick embryo spinal cord tissue expressing GFP and RFP cytoplasmic labeling (4 hours experiment). Scale bars: 50 µm.

(pallium) of an adult three-month aged zebrafish *in vivo*. The transgenic line *gfap:dTomato; deltaA:GFP* was obtained from Institut Pasteur (Nicolas Dray and colleagues) by crossing a Tg(gfap: dTomato) line [272] with a Tg(deltaA:GFP) [273] in a *casper* double-mutant background [274]. This transgenic line hence exhibited dual-color dTomato and GFP cytoplasmic labeling targeting two different cell types: radial glia (red) and neural progenitors (green). These cells are located just below the cranial surface beneath the skull. With dual-color three-photon microscopy we imaged these cell populations in their endogeneous niche in the intact living brain, through the skin and skull. The simultaneously acquired THG stack provided a rich anatomical background highlighting skin cells,red blood cells in vessels, lipid accumulations, and skull boundaries in the intact fish head.

Together the two live multimodal three-photon experiments presented in this section present two examples of experimental paradigms that can benefit from live dual-color imaging, in two different physiological contexts: dual-color addressing of different cellular compartments or multiplex targeting of different cell types.

4.4 Conclusion and perspectives

In this chapter, we presented our contribution to the emerging field of deep-tissue three-photon microscopy in the short wavelength infrared (SWIR) range. We have tested two novel SWIR sources and evaluated their potential for three-photon microscopy. We have experimentally confirmed for the first time the signal-to-background improvement of three-photon microscopy at 1700 nm compared to two-photon excited fluorescence of a densely red-labelled scattering

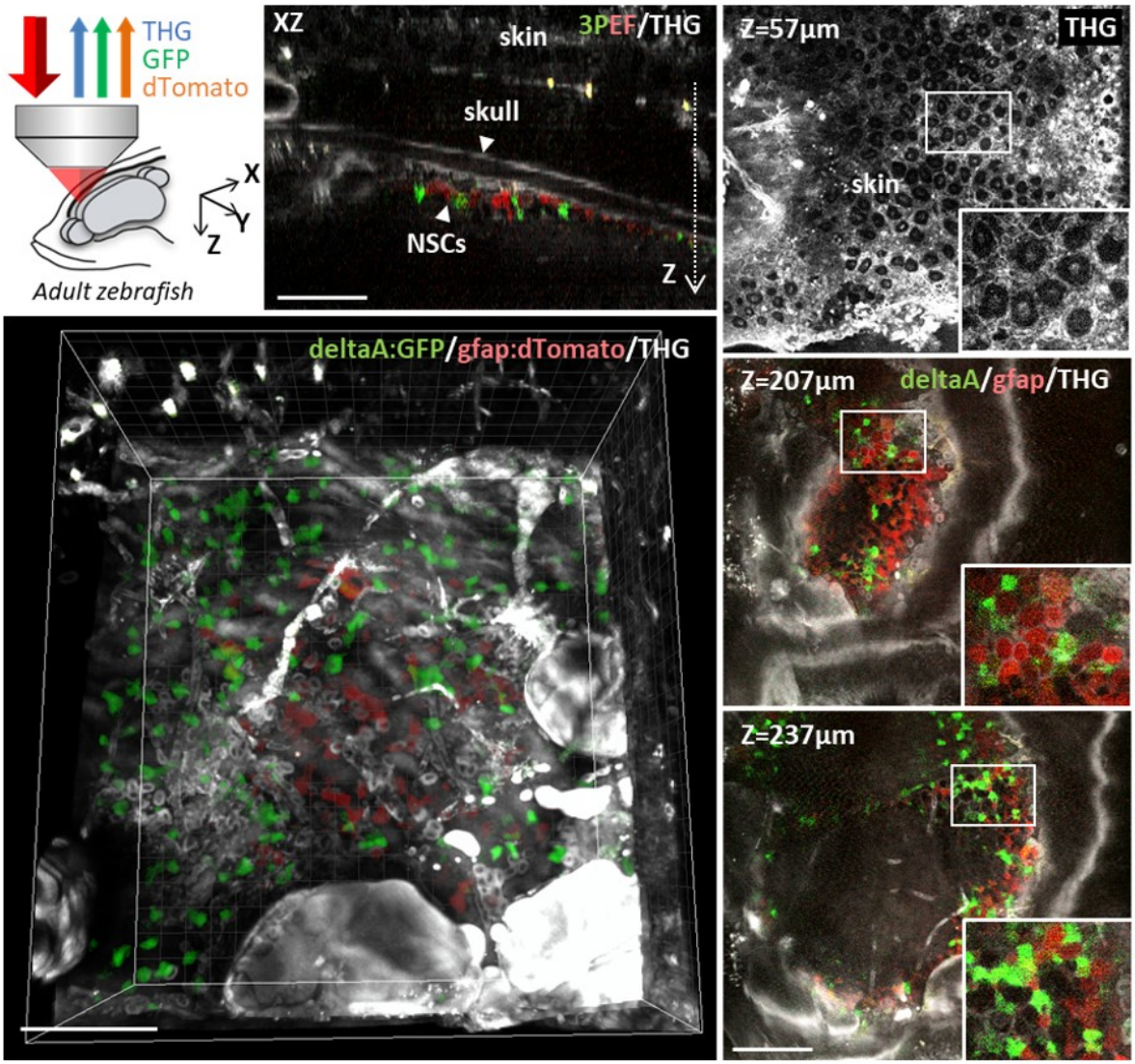

FIGURE 4.22. In vivo through-skull imaging in adult zebrafish telencephalon. The figures show representative XY, XZ and 3D views for a volume encompassing two labelled cell populations : red dTomato-labelled radial glia and green GFP-labelled neural stem cells expressing the deltaA neurogenic gene. Simultaneously acquired THG signals provide additional label-free contextual information (skin and skull morphology, blood vessels, lipid accumulations).Scale bars : 100 µm.

sample. In parallel, we also demonstrated three-photon excitability in the 1700 nm range of some widely used red fluorophores: dTomato, tdTomato and mCherry. We also demonstrated that 3P microscopy with MHz sources is compatible with dynamic live imaging of developing tissues, under the proper illumination conditions. Notably, we provided the first demonstration of simultaneous red and green three-photon excitation along with third harmonic generation in

various biological contexts, hence expanding the contrast possibilities of deep-tissue three-photon microscopy. Nevertheless, SWIR three-photon microscopy is still a burgeoning field and much work is needed beyond these proof of principle experiments in order for this technology to be used at its full potential in neurobiological studies.

In particular, photodamage is a particular concern in three-photon acquisitions as it will limit the spatial and temporal resolution but also the reachable imaging depth which is limited by how much power can the sample tolerate at the surface. In the case of SWIR 3PEF, the balance between nonlinear damage mechanisms and heating needs to be quantitatively assessed in various physiological conditions. Higher water absorption levels in the SWIR range, especially in the 1700 nm window, lowers the threshold of heating-mediated photodamage. The local temperature rise at the focus due to water absorption can be estimated by solving the time-dependent heat transport equation [275]. A recent study applied this model to assess the local temperature rise at the objective focus in the 1700 nm window: the calculated temperature rise for 20ms of irradiation at 20 mW at 1700 nm was 12.4 K assuming a 1.05 NA [276]. Using the same model, the expected temperature rise at 850 nm under 1s of illumination at 100mW was calculated to be only 0.23 K [275], highlighting an almost two order of magnitude increase in local temperature increase at 1700 nm compared to 850 nm. Although the pixel dwell time is typically in the range of ~µs up to tens of µs, cumulative effects due to the heating of adjacent pixels/voxels can be a concern. Laser-induced heating can be mitigated by keeping average power levels low while using high peak powers and by implementing acquisition and/or experimental routines to enable heat dissipation [55][253]. However, increasing the peak powers is limited on the other hand by non linear photodamage effects, which can trigger the formation of reactive oxygen species up to plasma formation and tissue disruption [51][277][278]. Balancing these two damage mechanisms will require optimization of laser repetition rate, pulse duration and elaborate illumination strategies specifically for each sample/experiment type.

Another perspective of this work is the improvement of deep-tissue three-photon microscopy performances through the combination with wavefront correcting strategies such as adaptive optics. The combination of adaptive optics and two-photon microscopy has been demonstrated to significantly improve the signal and resolution within scattering tissues [279][280][281][282] to the extent that it has been used as a strategy for deep-tissue imaging [283]. It is even more relevant to combine adaptive optics and three-photon microscopy since it has been shown by multiple groups that wavefront correction is more efficient in the case of high order non linear processes [284][285][286]. More efforts are however needed for the method to be adapted to large field of views while minimizing computational iterations to avoid sample damage. Another direction to improve the performances of three-photon microscopy in term of imaging speed is to use axially elongated Bessel beams [251][250]. In the context of sparsely Gcamp-labeled brain tissue, this approach can enable high-speed volumetric calcium imaging in the living brain [287] at larger depths.

Finally, while a dual color scheme is certainly a first milestone towards multicolor three-photon microscopy, strategies need to be implemented to further increase the content and obtain more colors. In particular, with the multiple output MHz source described earlier wavelength-mixing approaches can be leveraged to excite simultaneously multiple fluorophores. This is however not straightforward because since commonly used fluorophores do not behave as potentially expected from their 2P or 1P behavior, more studies on 3P fluorophore photophysics are needed. Designing novel probes specifically optimized for three-photon fluorescence microscopy shall even be an interesting approach to further expand its capabilities.

CHAPTER 5

GENERAL CONCLUSION

In this work, we have explored ways to expand the contrast of large volume and deep-tissue nonlinear microscopy techniques.

In the first chapter, after presenting the general challenges of high-resolution large volume imaging and some fundamentals of point-scanning multiphoton microscopy, we reviewed the state-of-the art of multicolor labeling strategies developed for high-content imaging of biological tissues, with a particular emphasis on the Brainbow strategy and derived methods. These strategies rely on the stochastic and combinatorial expression of multiple fluorescent proteins hence allowing to distinctively tag individual cells within a dense environment. Our review of the current state-of-the art of these techniques highlighted that while these strategies present a tremendous potential to reveal the structural development and organization of complex tissues such as the brain, this potential has so far been largely under-utilized due to the lack of suitable large volume multicolor microscopy techniques. We then presented wavelength-mixing-based multicolor two-photon microscopy as an efficient way to image color-labeled samples with intrinsic submicron channel registration. Since this method is however limited by the depth limitation inherent to two-photon microscopy, there was a need to upscale this approach to access larger volumes of tissue.

In the second chapter, we introduced chromatic serial multiphoton microscopy (Chrom-SMP), a novel microscopy method developed during the PhD, which combines wavelength-mixing and large-scale automated histology. This method lies in the context of recent large-scale histological methods which are currently transforming neuroanatomical studies, but which lack efficient contrast possibilities since they have been so far restricted to monochrome or two-color imaging modalities. We presented the various aspects concerning the implementation and development of Chrom-SMP microscopy: design and construction of the optical setup, implementation and optimization of tissue processing protocols, development of an image processing pipeline. We then presented the first multicolor atlas-like whole-brain dataset, with submicron lateral resolution and a discrete axial sampling of 100 µm, as a proof-of-principle experiment acquired with Chrom-SMP. We further demonstrated the ability of Chrom-SMP for large-scale multimodal imaging

by tuning the wavelength combination to target the CH2 vibrational band and performing brain-wide simultaneous THG and CARS imaging. Since these two contrasts are sensitive to the myelin content in the brain, this dyptical large-scale acquisition first presented these contrasts at a brain-wide scale and revealed their rich diversity across brain areas. It also allowed to initiate a comparative analysis between THG and CARS and raised important questions in this direction. This label-free coherent variation of Chrom-SMP hence opens many perspectives, both fundamental and applicative, for future work. We finally closed the chapter by extensively discussing the technological limitations and possible axes of improvement of the current Chrom-SMP system.

Next, in the third chapter, we focused on presenting some applications of Chrom-SMP to neuroanatomical and neurodevelopmental studies. As a preamble, we demonstrated 3D continuous diffraction-limited color-labeled over several mm^3 of mouse cerebral cortex where fine biological structures of interest such as neuronal axons, dendrites and astrocyte processes where visualized with multicolor voxel precision. We have then harnessed such Chrom-SMP acquired multicolor mm^3 datasets to characterize astrocytes morphology, interactions and clonal distribution in the mouse cerebral cortex. More specifically, we derived an approximation of the neuron to astrocyte ratio in the cortical neuropil, as well as the distribution of the volumes of astrocyte domains across deep cortical layers (layers 4 to 6), with a large statistical sample size within the same brain. Notably, our analysis highlighted a significant variation of volume between layer 4 astrocytes and layer 5a astrocytes, and between layer 4 and layer 6 astrocytes. This last finding is an additional argument in favor of astrocyte heterogeneity in the brain. Additionally, we developed a workflow to characterize the astroglial tiling of the grey cortical matter through the 3D reconstruction of the contact interface between color-segregated astrocyte neighbors. Last, we acquired large volume datasets of dual-compartmented color-labeled samples to perform large-scale clonal imaging with single-progenitor precision. The combination of the rare color labels provided by the labeling scheme with large volume Chrom-SMP acquisitions enabled to acquire several clonal datasets, at different postnatal developmental stages (P7 and P21), where dozens of astrocyte clones would be captured in their entirety throughout the mouse cerebral cortex. These datasets enabled to characterize in 3D multiple aspects of the morphological development and the clonal spatial arrangement of the mouse cortical astroglial network.
In the second part of this chapter, we presented a different possible application of trichromatic Chrom-SMP, outside the combinatorial Brainbow context. We demonstrated multiplexed long-range imaging of axonal projections labeled with three distinct color tracers. Our work specifically showed how Chrom-SMP can be used to augment whole-brain projectomic experiments. In particular, multicolor projection datasets provide a unique opportunity to analyze topography and relative projection arrangement at multiple scales and with no biases due to inter-individual variability, and hence open the way to direct visualization of the convergence or segregation of projections from distinct cell populations within the same brain. We further developed an image processing workflow for quantitative assessment of interdigitation patterns. These methods can also be used to spatially dissect the origin of connectopathies in the diseased brain, with unprecedented precision. Overall, combining Chrom-SMP acquisitions with all the palette of increasingly sophisticated genetic labeling strategies should open a vast horizon of possibilities, in neurobiology and beyond.

Finally, in the last chapter. we explore multi-contrast large volume imaging in the context of deep-tissue live imaging, in the case when invasive histological methods are ruled out. In this chapter,

we went back to the fundamental depth limitations in two-photon microscopy and aimed to push these limitations forward, while maintaining multiple contrast possibilities, in order to access multiple signals simultaneously at larger depths. More specifically, we discussed the relevance of short infrared wavelength range (SWIR) three-photon microscopy as an efficient solution for imaging with high contrasts at large depths. We tested two sources for SWIR three-photon microscopy, in fixed and live tissues, to better understand the important parameters necessary for efficient deep-tissue imaging. Last but not least, we achieved the first demonstration of dual-color red/green three-photon microscopy, based on a novel dual-output MHz source, emitting specifically in the two most interesting spectral regions for SWIR three-photon: the 1300 nm and the 1700 nm windows. We ended the chapter by discussing the next steps to be undertaken in this emerging field, which primarily need to provide a better understanding of both three-photon photophysics of commonly used dyes and most importantly the photodamage mechanisms induced by three-photon imaging in the MHz and SWIR regime.

Au cours de ce travail de thèse, nous avons exploré plusieurs approches permettant d'étendre les modes de contrastes accessibles à l'imagerie non linéaire de grands volumes et à l'imagerie multiphoton à grande profondeur de tissus épais.

Dans un premier chapitre, nous présentons les problématiques générales de l'imagerie de grand volume à haute résolution, suivies de quelques généralités sur la microscopie multiphoton à balayage. Nous passons ensuite en revue l'état de l'art des nouvelles stratégies de marquages multicouleur, avec une emphase particulière sur les marquages de type Brainbow. Ces stratégies reposent sur l'expression stochastique et combinatoire de 3 ou 4 protéines fluorescentes permettant de marquer de manière individuelle des cellules dans un environement dense. Notre revue de l'état de l'art de ces techniques met particulièrement en évidence d'une part le grand potentiel de ces méthodes pour analyser l'organisation et le développement de tissus complexes tels que le tissu cérébral, et d'autre part le manque de techniques d'imagerie multicouleur de grands volumes indispensables à la pleine exploration de leur potentiel. Nous présentons ensuite la technique de mélange de fréquence à deux photons comme moyen efficace d'imagerie à deux-photons multicouleur avec un alignement intrinsèque des canaux spectraux. Cette technique étant néanmoins limitée à quelques centaines de microns de profondeur, une approche permettant de repousser cette limitation est donc nécessaire et indispensable à l'analyse à grande échelle d'échantillons Brainbow.

Dans un second chapitre, nous introduisons la technique Chrom-SMP (chromatic serial multiphoton microscopy), une nouvelle technique de microscopie développée au cours de cette thèse combinant le mélange de fréquence à deux photons à un système de découpe sériée automatisé. Cette méthode s'inscrit dans le contexte des récents développements en méthodes d'imagerie à grande échelle de type 'block-face' qui transforment en profondeur le domaine de la neuroanatomie, mais qui jusqu'à présent ont été réduites à des approches souvent monochromes ou plus rarement, bicouleur. Dans ce chapitre, nous décrivons l'ensemble des aspects concernant l'implémentation et le développement de la microscopie Chrom-SMP, à savoir la conception et construction du système optique, l'implémentation et l'optimisation des protocoles de traitement des tissus, ainsi que le développement des routines de traitement et analyse d'images. Nous présentons en guise d'expérience de preuve de principe de la technique Chrom-SMP, le premier dataset de cerveau entier de type atlas, imagé en multicouleur avec une résolution latérale submicrométrique et un échantillonnage axial de 100 µm. Nous démontrons par ailleurs la capacité de Chrom-SMP pour l'imagerie multimodale sans marquage de grande échelle en modifiant les longueurs d'onde d'excitation pour correspondre aux transitions vibrationnelles des liaisons CH2 et démontrons de l'imagerie THG (génération de troisième harmonique) et CARS (microscopie Raman stimulée) simultanées sur cerveau entier. Ces deux contrastes étant sensibles à la présence de fibres myélinisées dans le cerveau, ce premier dataset dyptique a permis de révéler la richesse et la diversité de ces contrastes dans le cerveau murin et d'ouvrir plusieurs perspectives quant à la comparaison de ces deux modalités d'imagerie. Enfin, nous concluons ce chapitre en discutant les principaux axes technologiques d'amélioration de la méthode Chrom-SMP.

Dans un troisième chapitre, nous présentons quelques applications de Chrom-SMP à des études de neuroanatomie et de neurodéveloppement. En préambule, nous démontrons de l'imagerie multicolore 3D continue avec une résolution limitée par la diffraction (i.e résolution latérale submicrométrique, et résolution axiale d'environ 2 micromètres) sur plusieurs mm^3 de cortex cérébral murin, où plusieurs structures anatomiques d'intérêt (axones, dendrites, process astrocytaires)

ont pu être visualisés avec une précision multicouleur sub-voxel. Nous avons ensuite utilisé les datasets générés pour caractériser la morphologie des astrocytes dans le cortex cérébral murin. Plus précisément, nous avons obtenu une estimation du ratio de neurones par astrocyte dans le neuropile cortical, ainsi qu'une charactérisation de la distribution des volumes des domaines astrocytaires en fonction des couches corticales (couches profondes 4 à 6), avec une statistique jusqu'à présent inédite pour ce type d'analyses (130 astrocytes individuels segmentés en 3D, plus d'un millier d'astrocytes analysés pour la mesure du ratio neurone/astrocyte, dans le même cerveau). Notre étude a souligné une variation significative de volume entre les astrocytes de la couche 4 et ceux de la couche 5a, ainsi qu'entre les astrocytes de la couche 4 et ceux de la couche 6. Ces résultats constituent un argument supplémentaire en faveur de l'hétérogénéité de la population astrocytaire dans le cortex murin. Par ailleurs, nous avons également développé une routine d'analyse permettant de charactériser le pavage du cortex par les astrocytes à travers la reconstruction en 3D de l'interface de contact entre deux astrocytes voisins identifiables individuellement par leur couleur. Enfin, nous avons acquis plusieurs datasets corticaux multicouleur avec marquage Brainbow dual (noyau et cytoplasme) pour une étude d'analyse clonale de grands volume avec une précision à l'échelle du progéniteur individuel. La combinaison des configurations de couleur rares obtenues grâce au marquage dual avec la technique multicouleur grand volume Chrom-SMP a permis l'acquisition de plusieurs datasets clonaux, à différents stades postnataux (P7 et P21), où des dizaines de clones ont pu être analysés en entier dans toute leur étendue à travers le cortex cérébral murin. Ces datasets ont permis de charactériser en 3D plusieurs aspects de l'agencement des clones corticaux et du développement du réseau astrocytaire au cours du développement.
Dans une deuxième partie de ce chapitre, nous ouvrons sur une nouvelle application de la technologie Chrom-SMP, complémentaire aux applications Brainbow. Nous démontrons le suivi multiplexé de plusieurs projections axonales marquées à l'aide de trois marqueurs fluorescents distincts, à travers un cerveau murin entier. Plus spécifiquement, notre travail démontre comment la technique Chrom-SMP peut être utilisée pour augmenter le contenu des expériences de connectomique à l'échelle méso- sur cerveau entier. En particulier, ce type de datasets permet d'analyser la topographie et l'arrangement relatif des projections sur plusieurs échelles (du mm au sub-micron) et permet d'éviter les biais dus à la variabilité inter-individus en imageant plusieurs projections axonales dans le même animal. Ces expériences ouvrent donc la possibilité de charactériser la convergence ou la ségregation de projections issues de populations neuronales distinctes au sein du cerveau d'un même animal. Pour aller au delà de la preuve de principe, nous avons ensuite développé une routine d'analyse d'image permettant de quantifier ces patterns d'interdigitation de projections. Ces méthodes seront particulièrement pertinentes pour la dissection spatiale de l'origine des connectopathies et de diverses pathologies cérébrales. De façon générale, la combinaison des acquisitions Chrom-SMP avec l'ensemble des nouvelles stratégies de marquages multicouleur spécifiques devrait ouvrir de nombreuses perspectives et applications en neurobiologie, et plus généralement dans les sciences biomédicales.

Enfin, dans le dernier et quatrième chapitre, nous explorons l'imagerie multimodale dans le contexte de l'imagerie en profondeur de tissus vivants où les méthodes histologiques exposée ci-dessus ne sont plus applicables. Dans ce chapitre, nous avons recentré la réflexion autour des limites optiques fondamentales de l'imagerie à deux photons puis nous avons cherché à repousser ces limites tout en maintenant l'accès à plusieurs contrastes simultanément à grande profondeur. Ansi, nous avons d'abord discuté l'intérêt de la microscopie à trois photons utilisant des longueurs d'ondes dans le proche infrarouge (fenêtre SWIR) pour l'imagerie à grande profondeur avec un

rapport signal sur bruit amélioré. Nous avons ensuite testé deux sources laser émettant dans le proche infrarouge, sur tissus fixés et vivants, pour mieux comprendre les principaux paramètres nécessaire à une imagerie efficace à grande profondeur. Enfin, nous démontrons de l'imagerie à trois photons bicouleur rouge/vert, basée sur une nouvelle source MHz à deux sorties, émettant specifiquement dans les fenêtres spectrales d'intérêt: autour de 1300 nm et autour de 1700 nm. Nous concluons ce chapitre en discutant les prochaines étapes et perspectives à entreprendre dans ce domaine émergent de la microscopie à trois photons, à savoir étudier plus précisément la photophysique des protéines fluorescentes à trois photons ainsi que les différents méchanismes de dommage et de phototoxicité associés à ces nouveaux régimes d'excitation.

BIBLIOGRAPHY

[1] Z. Zheng, J. S. Lauritzen, E. Perlman, C. G. Robinson, M. Nichols, D. Milkie, O. Torrens, J. Price, C. B. Fisher, N. Sharifi, *et al.*, "A complete electron microscopy volume of the brain of adult drosophila melanogaster," *BioRxiv*, p. 140905, 2017.

[2] D. G. C. Hildebrand, M. Cicconet, R. M. Torres, W. Choi, T. M. Quan, J. Moon, A. W. Wetzel, A. S. Champion, B. J. Graham, O. Randlett, *et al.*, "Whole-brain serial-section electron microscopy in larval zebrafish," *Nature*, vol. 545, no. 7654, p. 345, 2017.

[3] W. R. Zipfel, R. M. Williams, and W. W. Webb, "Nonlinear magic: multiphoton microscopy in the biosciences," *Nature biotechnology*, vol. 21, no. 11, p. 1369, 2003.

[4] S. Herculano-Houzel, "The human brain in numbers: a linearly scaled-up primate brain," *Frontiers in human neuroscience*, vol. 3, p. 31, 2009.

[5] N. G. Horton, K. Wang, D. Kobat, C. G. Clark, F. W. Wise, C. B. Schaffer, and C. Xu, "In vivo three-photon microscopy of subcortical structures within an intact mouse brain," *Nature photonics*, vol. 7, no. 3, p. 205, 2013.

[6] T. Ragan, L. R. Kadiri, K. U. Venkataraju, K. Bahlmann, J. Sutin, J. Taranda, I. Arganda-Carreras, Y. Kim, H. S. Seung, and P. Osten, "Serial two-photon tomography for automated ex vivo mouse brain imaging," *Nature methods*, vol. 9, no. 3, p. 255, 2012.

[7] D. S. Richardson and J. W. Lichtman, "Clarifying tissue clearing," *Cell*, vol. 162, no. 2, pp. 246–257, 2015.

[8] R. J. Vigouroux, M. Belle, and A. Chédotal, "Neuroscience in the third dimension: shedding new light on the brain with tissue clearing," *Molecular brain*, vol. 10, no. 1, p. 33, 2017.

[9] E. A. Susaki, K. Tainaka, D. Perrin, H. Yukinaga, A. Kuno, and H. R. Ueda, "Advanced cubic protocols for whole-brain and whole-body clearing and imaging," *Nature protocols*, vol. 10, no. 11, p. 1709, 2015.

[10] E. Potma and X. Xie, "Handbook of biological nonlinear optical microscopy, edited by p. so and br masters," 2008.

[11] C. Sheppard and R. Kompfner, "Resonant scanning optical microscope," *Applied optics*, vol. 17, no. 18, pp. 2879–2882, 1978.

[12] W. Denk, J. H. Strickler, and W. W. Webb, "Two-photon laser scanning fluorescence microscopy," *Science*, vol. 248, no. 4951, pp. 73–76, 1990.

[13] M. Oheim, E. Beaurepaire, E. Chaigneau, J. Mertz, and S. Charpak, "Two-photon microscopy in brain tissue: parameters influencing the imaging depth," *Journal of neuroscience methods*, vol. 111, no. 1, pp. 29–37, 2001.

[14] D. Oron, E. Tal, and Y. Silberberg, "Scanningless depth-resolved microscopy," *Optics express*, vol. 13, no. 5, pp. 1468–1476, 2005.

[15] K. Bahlmann, P. T. So, M. Kirber, R. Reich, B. Kosicki, W. McGonagle, and K. Bellve, "Multifocal multiphoton microscopy (mmm) at a frame rate beyond 600 hz," *Optics express*, vol. 15, no. 17, pp. 10991–10998, 2007.

[16] N. Olivier, *Contrast mechanism and wavefront control in coherent nonlinear microscopy*. PhD thesis, PhD thesis, Ecole Polytechnique, 2009.

[17] J. Pawley, *Handbook of biological confocal microscopy*. Springer Science & Business Media, 2010.

[18] W. Supatto, T. V. Truong, D. Débarre, and E. Beaurepaire, "Advances in multiphoton microscopy for imaging embryos," *Current opinion in genetics & development*, vol. 21, no. 5, pp. 538–548, 2011.

[19] T. V. Truong, W. Supatto, D. S. Koos, J. M. Choi, and S. E. Fraser, "Deep and fast live imaging with two-photon scanned light-sheet microscopy," *Nature methods*, vol. 8, no. 9, p. 757, 2011.

[20] M. D. Young, J. J. Field, K. E. Sheetz, R. A. Bartels, and J. Squier, "A pragmatic guide to multiphoton microscope design," *Advances in optics and photonics*, vol. 7, no. 2, pp. 276–378, 2015.

[21] J. D. Lechleiter, D.-T. Lin, and I. Sieneart, "Multi-photon laser scanning microscopy using an acoustic optical deflector," *Biophysical Journal*, vol. 83, no. 4, pp. 2292–2299, 2002.

[22] R. Salome, Y. Kremer, S. Dieudonne, J.-F. Léger, O. Krichevsky, C. Wyart, D. Chatenay, and L. Bourdieu, "Ultrafast random-access scanning in two-photon microscopy using acousto-optic deflectors," *Journal of neuroscience methods*, vol. 154, no. 1-2, pp. 161–174, 2006.

[23] Q. Nguyen, N. Callamaras, C. Hsieh, and I. Parker, "Construction of a two-photon microscope for video-rate ca2+ imaging," *Cell calcium*, vol. 30, no. 6, pp. 383–393, 2001.

[24] G. Fan, H. Fujisaki, A. Miyawaki, R.-K. Tsay, R. Y. Tsien, and M. H. Ellisman, "Video-rate scanning two-photon excitation fluorescence microscopy and ratio imaging with cameleons," *Biophysical journal*, vol. 76, no. 5, pp. 2412–2420, 1999.

[25] K. H. Kim, C. Buehler, and P. T. So, "High-speed, two-photon scanning microscope," *Applied Optics*, vol. 38, no. 28, pp. 6004–6009, 1999.

[26] J. Cheng, C. Gu, D. Zhang, D. Wang, and S.-C. Chen, "Ultrafast axial scanning for two-photon microscopy via a digital micromirror device and binary holography," *Optics letters*, vol. 41, no. 7, pp. 1451–1454, 2016.

[27] H. Miyajima, N. Asaoka, T. Isokawa, M. Ogata, Y. Aoki, M. Imai, O. Fujimori, M. Katashiro, and K. Matsumoto, "A mems electromagnetic optical scanner for a commercial confocal laser scanning microscope," *Journal of microelectromechanical systems*, vol. 12, no. 3, pp. 243–251, 2003.

[28] W. Piyawattanametha, R. P. Barretto, T. H. Ko, B. A. Flusberg, E. D. Cocker, H. Ra, D. Lee, O. Solgaard, and M. J. Schnitzer, "Fast-scanning two-photon fluorescence imaging based on a microelectromechanical systems two-dimensional scanning mirror," *Optics letters*, vol. 31, no. 13, pp. 2018–2020, 2006.

[29] W. Piyawattanametha, E. D. Cocker, L. D. Burns, R. P. Barretto, J. C. Jung, H. Ra, O. Solgaard, and M. J. Schnitzer, "In vivo brain imaging using a portable 2.9 g two-photon microscope based on a microelectromechanical systems scanning mirror," *Optics letters*, vol. 34, no. 15, pp. 2309–2311, 2009.

[30] J. N. Stirman, I. T. Smith, M. W. Kudenov, and S. L. Smith, "Wide field-of-view, multi-region, two-photon imaging of neuronal activity in the mammalian brain," *Nature biotechnology*, vol. 34, no. 8, p. 857, 2016.

[31] P. Mahou, G. Malkinson, É. Chaudan, T. Gacoin, E. Beaurepaire, and W. Supatto, "Metrology of multiphoton microscopes using second harmonic generation nanoprobes," *Small*, vol. 13, no. 42, p. 1701442, 2017.

[32] A. Singh, J. D. McMullen, E. A. Doris, and W. R. Zipfel, "Comparison of objective lenses for multiphoton microscopy in turbid samples," *Biomedical optics express*, vol. 6, no. 8, pp. 3113–3127, 2015.

[33] V. Marx, "Microscopy: seeing through tissue," 2014.

[34] N. J. Sofroniew, D. Flickinger, J. King, and K. Svoboda, "A large field of view two-photon mesoscope with subcellular resolution for in vivo imaging," *Elife*, vol. 5, p. e14472, 2016.

[35] G. McConnell, J. Trägårdh, R. Amor, J. Dempster, E. Reid, and W. B. Amos, "A novel optical microscope for imaging large embryos and tissue volumes with sub-cellular resolution throughout," *Elife*, vol. 5, p. e18659, 2016.

[36] N. Olivier, M. A. Luengo-Oroz, L. Duloquin, E. Faure, T. Savy, I. Veilleux, X. Solinas, D. Débarre, P. Bourgine, A. Santos, *et al.*, "Cell lineage reconstruction of early zebrafish embryos using label-free nonlinear microscopy," *Science*, vol. 329, no. 5994, pp. 967–971, 2010.

[37] D. Débarre, W. Supatto, A.-M. Pena, A. Fabre, T. Tordjmann, L. Combettes, M.-C. Schanne-Klein, and E. Beaurepaire, "Imaging lipid bodies in cells and tissues using third-harmonic generation microscopy," *Nature methods*, vol. 3, no. 1, p. 47, 2006.

[38] M. Strupler, A.-M. Pena, M. Hernest, P.-L. Tharaux, J.-L. Martin, E. Beaurepaire, and M.-C. Schanne-Klein, "Second harmonic imaging and scoring of collagen in fibrotic tissues," *Optics express*, vol. 15, no. 7, pp. 4054–4065, 2007.

[39] A. Rebane, N. S. Makarov, M. Drobizhev, B. Spangler, E. S. Tarter, B. D. Reeves, C. W. Spangler, F. Meng, and Z. Suo, "Quantitative prediction of two-photon absorption cross section based on linear spectroscopic properties," *The Journal of Physical Chemistry C*, vol. 112, no. 21, pp. 7997–8004, 2008.

[40] M. Drobizhev, S. Tillo, N. Makarov, T. Hughes, and A. Rebane, "Absolute two-photon absorption spectra and two-photon brightness of orange and red fluorescent proteins," *The Journal of Physical Chemistry B*, vol. 113, no. 4, pp. 855–859, 2009.

[41] M. Drobizhev, N. S. Makarov, S. E. Tillo, T. E. Hughes, and A. Rebane, "Two-photon absorption properties of fluorescent proteins," *Nature methods*, vol. 8, no. 5, p. 393, 2011.

[42] C. Sheppard, J. Gannaway, R. Kompfner, and D. Walsh, "The scanning harmonic optical microscope," *IEEE Journal of Quantum electronics*, vol. 13, no. 9, pp. 912–912, 1977.

[43] D. Dombeck, K. Kasischke, H. Vishwasrao, M. Ingelsson, B. Hyman, and W. Webb, "Second harmonic generation microscopy of uniformly oriented microtubules in native brain tissue," *PNAS*, vol. 100, no. 12, pp. 7081–7086, 2003.

[44] V. Nucciotti, C. Stringari, L. Sacconi, F. Vanzi, L. Fusi, M. Linari, G. Piazzesi, V. Lombardi, and F. Pavone, "Probing myosin structural conformation in vivo by second-harmonic generation microscopy," *Proceedings of the National Academy of Sciences*, vol. 107, no. 17, pp. 7763–7768, 2010.

[45] A. C. Kwan, D. A. Dombeck, and W. W. Webb, "Polarized microtubule arrays in apical dendrites and axons," *Proceedings of the National Academy of Sciences*, vol. 105, no. 32, pp. 11370–11375, 2008.

[46] N. Olivier, D. Débarre, and E. Beaurepaire, "Thg microscopy of cells and tissues: contrast mechanisms and applications," 2013.

[47] C. L. Evans and X. S. Xie, "Coherent anti-stokes raman scattering microscopy: chemical imaging for biology and medicine," *Annu. Rev. Anal. Chem.*, vol. 1, pp. 883–909, 2008.

[48] W. Min, C. W. Freudiger, S. Lu, and X. S. Xie, "Coherent nonlinear optical imaging: beyond fluorescence microscopy," *Annual review of physical chemistry*, vol. 62, pp. 507–530, 2011.

[49] D. Débarre, *Microscopie par génération de troisième harmonique appliquée à la biologie.* PhD thesis, Ecole Polytechnique X, 2006.

[50] H. J. Van Staveren, C. J. Moes, J. van Marie, S. A. Prahl, and M. J. Van Gemert, "Light scattering in lntralipid-10% in the wavelength range of 400–1100 nm," *Applied optics*, vol. 30, no. 31, pp. 4507–4514, 1991.

[51] D. Debarre, N. Olivier, W. Supatto, and E. Beaurepaire, "Mitigating phototoxicity during multiphoton microscopy of live drosophila embryos in the 1.0–1.2 μm wavelength range," *PLoS One*, vol. 9, no. 8, p. e104250, 2014.

[52] W. Supatto, A. McMahon, S. E. Fraser, and A. Stathopoulos, "Quantitative imaging of collective cell migration during drosophila gastrulation: multiphoton microscopy and computational analysis," *Nature protocols*, vol. 4, no. 10, p. 1397, 2009.

[53] X. Liu, P. Wang, J. Fu, D. Lv, D. Chen, Y. Li, and W. Ma, "Two-photon fluorescence real-time imaging on the development of early mouse embryo by stages," *Journal of microscopy*, vol. 241, no. 2, pp. 212–218, 2011.

[54] A. Hopt and E. Neher, "Highly nonlinear photodamage in two-photon fluorescence microscopy," *Biophysical journal*, vol. 80, no. 4, pp. 2029–2036, 2001.

[55] K. Podgorski and G. Ranganathan, "Brain heating induced by near-infrared lasers during multiphoton microscopy," *Journal of neurophysiology*, vol. 116, no. 3, pp. 1012–1023, 2016.

[56] E. M. Schmidt and M. Oheim, "Two-photon imaging induces brain heating and calcium microdomain hyper-activity in cortical astrocytes," *bioRxiv*, p. 321091, 2018.

[57] K. Svoboda and R. Yasuda, "Principles of two-photon excitation microscopy and its applications to neuroscience," *Neuron*, vol. 50, no. 6, pp. 823–839, 2006.

[58] R. Mostany, A. Miquelajauregui, M. Shtrahman, and C. Portera-Cailliau, "Two-photon excitation microscopy and its applications in neuroscience," in *Advanced Fluorescence Microscopy*, pp. 25–42, Springer, 2015.

[59] C. Grienberger and A. Konnerth, "Imaging calcium in neurons," *Neuron*, vol. 73, no. 5, pp. 862–885, 2012.

[60] K. F. Ahrens, B. Heider, H. Lee, E. Y. Isacoff, and R. M. Siegel, "Two-photon scanning microscopy of in vivo sensory responses of cortical neurons genetically encoded with a fluorescent voltage sensor in rat," *Frontiers in neural circuits*, vol. 6, p. 15, 2012.

[61] F. Pan and W.-B. Gan, "Two-photon imaging of dendritic spine development in the mouse cortex," *Developmental neurobiology*, vol. 68, no. 6, pp. 771–778, 2008.

[62] J. Lecoq, A. Parpaleix, E. Roussakis, M. Ducros, Y. G. Houssen, S. A. Vinogradov, and S. Charpak, "Simultaneous two-photon imaging of oxygen and blood flow in deep cerebral vessels," *Nature medicine*, vol. 17, no. 7, p. 893, 2011.

[63] D. L. Pettit, S. S.-H. Wang, K. R. Gee, and G. J. Augustine, "Chemical two-photon uncaging: a novel approach to mapping glutamate receptors," *Neuron*, vol. 19, no. 3, pp. 465–471, 1997.

[64] L. Fenno, O. Yizhar, and K. Deisseroth, "The development and application of optogenetics," *Annual review of neuroscience*, vol. 34, 2011.

[65] M. N. Economo, N. G. Clack, L. D. Lavis, C. R. Gerfen, K. Svoboda, E. W. Myers, and J. Chandrashekar, "A platform for brain-wide imaging and reconstruction of individual neurons," *Elife*, vol. 5, p. e10566, 2016.

[66] R. Y. Tsien, "The green fluorescent protein," 1998.

[67] D. M. Chudakov, M. V. Matz, S. Lukyanov, and K. A. Lukyanov, "Fluorescent proteins and their applications in imaging living cells and tissues," *Physiological reviews*, vol. 90, no. 3, pp. 1103–1163, 2010.

[68] R. N. Day and M. W. Davidson, "The fluorescent protein palette: tools for cellular imaging," *Chemical Society Reviews*, vol. 38, no. 10, pp. 2887–2921, 2009.

[69] A. S. Mishin, V. V. Belousov, K. M. Solntsev, and K. A. Lukyanov, "Novel uses of fluorescent proteins," *Current opinion in chemical biology*, vol. 27, pp. 1–9, 2015.

[70] A. D. Almeida, H. Boije, R. W. Chow, J. He, J. Tham, S. C. Suzuki, and W. A. Harris, "Spectrum of fates: a new approach to the study of the developing zebrafish retina," *Development*, vol. 141, no. 9, pp. 1971–1980, 2014.

[71] D. L. Coutu, K. D. Kokkaliaris, L. Kunz, and T. Schroeder, "Multicolor quantitative confocal imaging cytometry," *Nature methods*, vol. 15, no. 1, p. 39, 2018.

[72] M. Dickinson, G. Bearman, S. Tille, R. Lansford, and S. Fraser, "Multi-spectral imaging and linear unmixing add a whole new dimension to laser scanning fluorescence microscopy," *Biotechniques*, vol. 31, no. 6, pp. 1272–1279, 2001.

[73] W. Jahr, B. Schmid, C. Schmied, F. O. Fahrbach, and J. Huisken, "Hyperspectral light sheet microscopy," *Nature communications*, vol. 6, p. 7990, 2015.

[74] A. Rakhymzhan, R. Leben, H. Zimmermann, R. Günther, P. Mex, D. Reismann, C. Ulbricht, A. Acs, A. U. Brandt, R. L. Lindquist, *et al.*, "Synergistic strategy for multicolor two-photon microscopy: Application to the analysis of germinal center reactions in vivo," *Scientific reports*, vol. 7, no. 1, p. 7101, 2017.

[75] F. Cutrale, V. Trivedi, L. A. Trinh, C.-L. Chiu, J. M. Choi, M. S. Artiga, and S. E. Fraser, "Hyperspectral phasor analysis enables multiplexed 5d in vivo imaging," *Nature methods*, vol. 14, no. 2, p. 149, 2017.

[76] J. Livet, T. A. Weissman, H. Kang, R. W. Draft, J. Lu, R. A. Bennis, J. R. Sanes, and J. W. Lichtman, "Transgenic strategies for combinatorial expression of fluorescent proteins in the nervous system," *Nature*, vol. 450, no. 7166, p. 56, 2007.

[77] G. Feng, R. H. Mellor, M. Bernstein, C. Keller-Peck, Q. T. Nguyen, M. Wallace, J. M. Nerbonne, J. W. Lichtman, and J. R. Sanes, "Imaging neuronal subsets in transgenic mice expressing multiple spectral variants of gfp," *Neuron*, vol. 28, no. 1, pp. 41–51, 2000.

[78] C. S. Branda and S. M. Dymecki, "Talking about a revolution: The impact of site-specific recombinases on genetic analyses in mice," *Developmental cell*, vol. 6, no. 1, pp. 7–28, 2004.

[79] T. Saito and N. Nakatsuji, "Efficient gene transfer into the embryonic mouse brain using in vivo electroporation," *Developmental biology*, vol. 240, no. 1, pp. 237–246, 2001.

[80] H. Tabata and K. Nakajima, "Efficient in utero gene transfer system to the developing mouse brain using electroporation: visualization of neuronal migration in the developing cortex," *Neuroscience*, vol. 103, no. 4, pp. 865–872, 2001.

[81] H. Tabata and K. Nakajima, "Labeling embryonic mouse central nervous system cells by in utero electroporation," *Development, growth & differentiation*, vol. 50, no. 6, pp. 507–511, 2008.

[82] C. N. Bedbrook, B. E. Deverman, and V. Gradinaru, "Viral strategies for targeting the central and peripheral nervous systems," *Annual review of neuroscience*, no. 0, 2018.

[83] M. D. Weitzman and R. M. Linden, "Adeno-associated virus biology," in *Adeno-Associated Virus*, pp. 1–23, Springer, 2012.

[84] K. Y. Chan, M. J. Jang, B. B. Yoo, A. Greenbaum, N. Ravi, W.-L. Wu, L. Sánchez-Guardado, C. Lois, S. K. Mazmanian, B. E. Deverman, *et al.*, "Engineered aavs for efficient noninvasive gene delivery to the central and peripheral nervous systems," *Nature neuroscience*, vol. 20, no. 8, p. 1172, 2017.

[85] L. Luo, E. M. Callaway, and K. Svoboda, "Genetic dissection of neural circuits: a decade of progress," *Neuron*, vol. 98, no. 2, pp. 256–281, 2018.

[86] S. W. Oh, J. A. Harris, L. Ng, B. Winslow, N. Cain, S. Mihalas, Q. Wang, C. Lau, L. Kuan, A. M. Henry, *et al.*, "A mesoscale connectome of the mouse brain," *Nature*, vol. 508, no. 7495, p. 207, 2014.

[87] T. A. Weissman and Y. A. Pan, "Brainbow: new resources and emerging biological applications for multicolor genetic labeling and analysis," *Genetics*, vol. 199, no. 2, pp. 293–306, 2015.

[88] J. W. Lichtman, J. Livet, and J. R. Sanes, "A technicolour approach to the connectome," *Nature Reviews Neuroscience*, vol. 9, no. 6, p. 417, 2008.

[89] G. S. Jefferis and J. Livet, "Sparse and combinatorial neuron labelling," *Current opinion in neurobiology*, vol. 22, no. 1, pp. 101–110, 2012.

[90] B. Richier and I. Salecker, "Versatile genetic paintbrushes: Brainbow technologies," *Wiley Interdisciplinary Reviews: Developmental Biology*, vol. 4, no. 2, pp. 161–180, 2015.

[91] H. J. Snippert, L. G. Van Der Flier, T. Sato, J. H. Van Es, M. Van Den Born, C. Kroon-Veenboer, N. Barker, A. M. Klein, J. Van Rheenen, B. D. Simons, *et al.*, "Intestinal crypt homeostasis results from neutral competition between symmetrically dividing lgr5 stem cells," *Cell*, vol. 143, no. 1, pp. 134–144, 2010.

[92] V. Gupta and K. D. Poss, "Clonally dominant cardiomyocytes direct heart morphogenesis," *Nature*, vol. 484, no. 7395, p. 479, 2012.

[93] K. Weber, M. Thomaschewski, M. Warlich, T. Volz, K. Cornils, B. Niebuhr, M. Täger, M. Lütgehetmann, J.-M. Pollok, C. Stocking, *et al.*, "Rgb marking facilitates multicolor clonal cell tracking," *Nature medicine*, vol. 17, no. 4, p. 504, 2011.

[94] O. Kanca, E. Caussinus, A. S. Denes, A. Percival-Smith, and M. Affolter, "Raeppli: a whole-tissue labeling tool for live imaging of drosophila development," *Development*, pp. dev–102913, 2012.

[95] D. Hadjieconomou, S. Rotkopf, C. Alexandre, D. M. Bell, B. J. Dickson, and I. Salecker, "Flybow: genetic multicolor cell labeling for neural circuit analysis in drosophila melanogaster," *Nature methods*, vol. 8, no. 3, p. 260, 2011.

[96] S. Hampel, P. Chung, C. E. McKellar, D. Hall, L. L. Looger, and J. H. Simpson, "Drosophila brainbow: a recombinase-based fluorescence labeling technique to subdivide neural expression patterns," *Nature methods*, vol. 8, no. 3, p. 253, 2011.

[97] Y. A. Pan, T. Freundlich, T. A. Weissman, D. Schoppik, X. C. Wang, S. Zimmerman, B. Ciruna, J. R. Sanes, J. W. Lichtman, and A. F. Schier, "Zebrabow: multispectral cell labeling for cell tracing and lineage analysis in zebrafish," *Development*, vol. 140, no. 13, pp. 2835–2846, 2013.

[98] D. Cai, K. B. Cohen, T. Luo, J. W. Lichtman, and J. R. Sanes, "Improved tools for the brainbow toolbox," *Nature methods*, vol. 10, no. 6, p. 540, 2013.

[99] K. Loulier, R. Barry, P. Mahou, Y. Le Franc, W. Supatto, K. S. Matho, S. Ieng, S. Fouquet, E. Dupin, R. Benosman, *et al.*, "Multiplex cell and lineage tracking with combinatorial labels," *Neuron*, vol. 81, no. 3, pp. 505–520, 2014.

[100] I. Tabansky, A. Lenarcic, R. W. Draft, K. Loulier, D. B. Keskin, J. Rosains, J. Rivera-Feliciano, J. W. Lichtman, J. Livet, J. N. Stern, *et al.*, "Developmental bias in cleavage-stage mouse blastomeres," *Current Biology*, vol. 23, no. 1, pp. 21–31, 2013.

[101] J. Ma, Z. Shen, Y.-C. Yu, and S.-H. Shi, "Neural lineage tracing in the mammalian brain," *Current opinion in neurobiology*, vol. 50, pp. 7–16, 2018.

[102] K. Kretzschmar and F. M. Watt, "Lineage tracing," *Cell*, vol. 148, no. 1-2, pp. 33–45, 2012.

[103] J. Fink, A. Andersson-Rolf, and B.-K. Koo, "Adult stem cell lineage tracing and deep tissue imaging," *BMB reports*, vol. 48, no. 12, p. 655, 2015.

[104] A. Alemany, M. Florescu, C. S. Baron, J. Peterson-Maduro, and A. van Oudenaarden, "Whole-organism clone tracing using single-cell sequencing," *Nature*, vol. 556, no. 7699, p. 108, 2018.

[105] D. E. Wagner, C. Weinreb, Z. M. Collins, J. A. Briggs, S. G. Megason, and A. M. Klein, "Single-cell mapping of gene expression landscapes and lineage in the zebrafish embryo," *Science*, vol. 360, no. 6392, pp. 981–987, 2018.

[106] A. McKenna, G. M. Findlay, J. A. Gagnon, M. S. Horwitz, A. F. Schier, and J. Shendure, "Whole-organism lineage tracing by combinatorial and cumulative genome editing," *Science*, vol. 353, no. 6298, p. aaf7907, 2016.

[107] E. Shapiro, T. Biezuner, and S. Linnarsson, "Single-cell sequencing-based technologies will revolutionize whole-organism science," *Nature Reviews Genetics*, vol. 14, no. 9, p. 618, 2013.

[108] S. D. Perli, C. H. Cui, and T. K. Lu, "Continuous genetic recording with self-targeting crispr-cas in human cells," *Science*, vol. 353, no. 6304, p. aag0511, 2016.

[109] P. Pantazis and W. Supatto, "Advances in whole-embryo imaging: a quantitative transition is underway," *Nature Reviews Molecular Cell Biology*, vol. 15, no. 5, p. 327, 2014.

[110] Y. Rinkevich, P. Lindau, H. Ueno, M. T. Longaker, and I. L. Weissman, "Germ-layer and lineage-restricted stem/progenitors regenerate the mouse digit tip," *Nature*, vol. 476, no. 7361, p. 409, 2011.

[111] T. L. Tay, D. Mai, J. Dautzenberg, F. Fernández-Klett, G. Lin, M. Datta, A. Drougard, T. Stempfl, A. Ardura-Fabregat, O. Staszewski, *et al.*, "A new fate mapping system reveals context-dependent random or clonal expansion of microglia," *Nature neuroscience*, vol. 20, no. 6, p. 793, 2017.

[112] K. Weber, M. Thomaschewski, D. Benten, and B. Fehse, "Rgb marking with lentiviral vectors for multicolor clonal cell tracking," *nature protocols*, vol. 7, no. 5, p. 839, 2012.

[113] S. Lamprecht, E. M. Schmidt, C. Blaj, H. Hermeking, A. Jung, T. Kirchner, and D. Horst, "Multicolor lineage tracing reveals clonal architecture and dynamics in colon cancer," *Nature communications*, vol. 8, no. 1, p. 1406, 2017.

[114] F. García-Moreno, N. A. Vasistha, J. Begbie, and Z. Molnár, "Clone is a new method to target single progenitors and study their progeny in mouse and chick," *Development*, vol. 141, no. 7, pp. 1589–1598, 2014.

[115] J. García-Marqués and L. López-Mascaraque, "Clonal identity determines astrocyte cortical heterogeneity," *Cerebral cortex*, vol. 23, no. 6, pp. 1463–1472, 2013.

[116] M. I. Worley, L. Setiawan, and I. K. Hariharan, "Tie-dye: a combinatorial marking system to visualize and genetically manipulate clones during development in drosophila melanogaster," *Development*, pp. dev–096057, 2013.

[117] E. Roy, Z. Neufeld, J. Livet, and K. Khosrotehrani, "Concise review: understanding clonal dynamics in homeostasis and injury through multicolor lineage tracing," *Stem Cells*, vol. 32, no. 12, pp. 3046–3054, 2014.

[118] K. Cornils, L. Thielecke, S. Hüser, M. Forgber, M. Thomaschewski, N. Kleist, K. Hussein, K. Riecken, T. Volz, S. Gerdes, *et al.*, "Multiplexing clonality: combining rgb marking and genetic barcoding," *Nucleic acids research*, vol. 42, no. 7, pp. e56–e56, 2014.

[119] D. Gomez-Nicola, K. Riecken, B. Fehse, and V. H. Perry, "In-vivo rgb marking and multicolour single-cell tracking in the adult brain," *Scientific reports*, vol. 4, p. 7520, 2014.

[120] R. Cajal, *Histology of the Nervous System of Man and Vertebrates (History of Neuroscience, No 6)(2 Volume Set)*.
Oxford: Oxford University Press, 1995.

[121] J. Wang, M. L. O'sullivan, D. Mukherjee, V. M. Puñal, S. Farsiu, and J. N. Kay, "Anatomy and spatial organization of müller glia in mouse retina," *Journal of Comparative Neurology*, vol. 525, no. 8, pp. 1759–1777, 2017.

[122] E. Robles, A. Filosa, and H. Baier, "Precise lamination of retinal axons generates multiple parallel input pathways in the tectum," *Journal of Neuroscience*, vol. 33, no. 11, pp. 5027–5039, 2013.

[123] L. Dumas, C. Heitz-Marchaland, S. Fouquet, U. Suter, J. Livet, C. Moreau-Fauvarque, and A. Chédotal, "Multicolor analysis of oligodendrocyte morphology, interactions, and development with brainbow," *Glia*, vol. 63, no. 4, pp. 699–717, 2015.

[124] F. N. Zaidi, V. Cicchini, D. Kaufman, E. Ko, A. Ko, H. Van Tassel, and M. C. Whitehead, "Innervation of taste buds revealed with brainbow-labeling in mouse," *Journal of anatomy*, vol. 229, no. 6, pp. 778–790, 2016.

[125] S. Hammer, A. Monavarfeshani, T. Lemon, J. Su, and M. A. Fox, "Multiple retinal axons converge onto relay cells in the adult mouse thalamus," *Cell reports*, vol. 12, no. 10, pp. 1575–1583, 2015.

[126] Y. Hadas, A. Etlin, H. Falk, O. Avraham, O. Kobiler, A. Panet, A. Lev-Tov, and A. Klar, "A 'tool box'for deciphering neuronal circuits in the developing chick spinal cord," *Nucleic acids research*, vol. 42, no. 19, pp. e148–e148, 2014.

[127] P. Mahou, "These de doctorat de l'ecole polytechnique,"

[128] R. S. Pillai, C. Boudoux, G. Labroille, N. Olivier, I. Veilleux, E. Farge, M. Joffre, and E. Beaurepaire, "Multiplexed two-photon microscopy of dynamic biological samples with shaped broadband pulses," *Optics express*, vol. 17, no. 15, pp. 12741–12752, 2009.

[129] G. Labroille, R. S. Pillai, X. Solinas, C. Boudoux, N. Olivier, E. Beaurepaire, and M. Joffre, "Dispersion-based pulse shaping for multiplexed two-photon fluorescence microscopy," *Optics letters*, vol. 35, no. 20, pp. 3444–3446, 2010.

[130] J. P. Gordon, "Theory of the soliton self-frequency shift," *Optics letters*, vol. 11, no. 10, pp. 662–664, 1986.

[131] K. Wang, T.-M. Liu, J. Wu, N. G. Horton, C. P. Lin, and C. Xu, "Three-color femtosecond source for simultaneous excitation of three fluorescent proteins in two-photon fluorescence microscopy," *Biomedical optics express*, vol. 3, no. 9, pp. 1972–1977, 2012.

[132] K.-C. Li, L. L. Huang, J.-H. Liang, and M.-C. Chan, "Simple approach to three-color two-photon microscopy by a fiber-optic wavelength convertor," *Biomedical optics express*, vol. 7, no. 11, pp. 4803–4815, 2016.

[133] C. Zhang, V. Bucklew, P. Edwards, C. Janisch, and Z. Liu, "Divided pulse soliton self-frequency shift: a multi-color, dual-polarization, power-scalable, broadly tunable optical source," *Optics letters*, vol. 42, no. 3, pp. 502–505, 2017.

[134] P. Mahou, M. Zimmerley, K. Loulier, K. S. Matho, G. Labroille, X. Morin, W. Supatto, J. Livet, D. Débarre, and E. Beaurepaire, "Multicolor two-photon tissue imaging by wavelength mixing," *Nature methods*, vol. 9, no. 8, p. 815, 2012.

[135] C. Stringari, L. Abdeladim, G. Malkinson, P. Mahou, X. Solinas, I. Lamarre, S. Brizion, J.-B. Galey, W. Supatto, R. Legouis, *et al.*, "Multicolor two-photon imaging of endogenous fluorophores in living tissues by wavelength mixing," *Scientific Reports*, vol. 7, no. 1, p. 3792, 2017.

[136] P. Mahou, J. Vermot, E. Beaurepaire, and W. Supatto, "Multicolor two-photon light-sheet microscopy," *Nature methods*, vol. 11, no. 6, p. 600, 2014.

[137] N. Dray, S. Bedu, N. Vuillemin, A. Alunni, M. Coolen, M. Krecsmarik, W. Supatto, E. Beaurepaire, and L. Bally-Cuif, "Large-scale live imaging of adult neural stem cells in their endogenous niche," *Development*, pp. dev–123018, 2015.

[138] E. P. Perillo, J. W. Jarrett, Y.-L. Liu, A. Hassan, D. C. Fernée, J. R. Goldak, A. Bonteanu, D. J. Spence, H.-C. Yeh, and A. K. Dunn, "Two-color multiphoton in vivo imaging with a femtosecond diamond raman laser," *Light: Science & Applications*, vol. 6, no. 11, p. e17095, 2017.

[139] J. Trägårdh, M. Murtagh, G. Robb, M. Parsons, J. Lin, D. J. Spence, and G. McConnell, "Two-color, two-photon imaging at long excitation wavelengths using a diamond raman laser," *Microscopy and Microanalysis*, vol. 22, no. 4, pp. 803–807, 2016.

[140] H. Kennedy, D. Van Essen, Y. Christen, *et al.*, *Micro-, Meso-and Macro-connectomics of the Brain*.
Springer, 2016.

[141] D. C. Van Essen, S. M. Smith, D. M. Barch, T. E. Behrens, E. Yacoub, K. Ugurbil, W.-M. H. Consortium, *et al.*, "The wu-minn human connectome project: an overview," *Neuroimage*, vol. 80, pp. 62–79, 2013.

[142] M. Helmstaedter, K. L. Briggman, S. C. Turaga, V. Jain, H. S. Seung, and W. Denk, "Connectomic reconstruction of the inner plexiform layer in the mouse retina," *Nature*, vol. 500, no. 7461, p. 168, 2013.

[143] D. B. Chklovskii, S. Vitaladevuni, and L. K. Scheffer, "Semi-automated reconstruction of neural circuits using electron microscopy," *Current opinion in neurobiology*, vol. 20, no. 5, pp. 667–675, 2010.

[144] H. Hintiryan, N. N. Foster, I. Bowman, M. Bay, M. Y. Song, L. Gou, S. Yamashita, M. S. Bienkowski, B. Zingg, M. Zhu, *et al.*, "The mouse cortico-striatal projectome," *Nature neuroscience*, vol. 19, no. 8, p. 1100, 2016.

[145] B. J. Hunnicutt, B. C. Jongbloets, W. T. Birdsong, K. J. Gertz, H. Zhong, and T. Mao, "A comprehensive excitatory input map of the striatum reveals novel functional organization," *Elife*, vol. 5, p. e19103, 2016.

[146] X. Li, B. Yu, Q. Sun, Y. Zhang, M. Ren, X. Zhang, A. Li, J. Yuan, L. Madisen, Q. Luo, *et al.*, "Generation of a whole-brain atlas for the cholinergic system and mesoscopic projectome analysis of basal forebrain cholinergic neurons," *Proceedings of the National Academy of Sciences*, p. 201703601, 2017.

[147] A. Hoerder-Suabedissen, S. Hayashi, L. Upton, Z. Nolan, D. Casas-Torremocha, E. Grant, S. Viswanathan, P. O. Kanold, F. Clasca, Y. Kim, *et al.*, "Subset of cortical layer 6b neurons selectively innervates higher order thalamic nuclei in mice," *Cerebral Cortex*, vol. 28, no. 5, pp. 1882–1897, 2018.

[148] D. Kleinfeld, A. Bharioke, P. Blinder, D. D. Bock, K. L. Briggman, D. B. Chklovskii, W. Denk, M. Helmstaedter, J. P. Kaufhold, W.-C. A. Lee, *et al.*, "Large-scale automated histology in the pursuit of connectomes," *Journal of Neuroscience*, vol. 31, no. 45, pp. 16125–16138, 2011.

[149] J. Kornfeld and W. Denk, "Progress and remaining challenges in high-throughput volume electron microscopy," *Current opinion in neurobiology*, vol. 50, pp. 261–267, 2018.

[150] G. Paxinos and K. B. Franklin, *The mouse brain in stereotaxic coordinates*. Gulf professional publishing, 2004.

[151] G. Paxinos and K. W. Ashwell, *Atlas of the developing rat nervous system*. Academic Press, 2018.

[152] A. W. Toga, K. Ambach, B. Quinn, M. Hutchin, and J. S. Burton, "Postmortem anatomy from cryosectioned whole human brain," *Journal of neuroscience methods*, vol. 54, no. 2, pp. 239–252, 1994.

[153] P. S. Tsai, B. Friedman, A. I. Ifarraguerri, B. D. Thompson, V. Lev-Ram, C. B. Schaffer, Q. Xiong, R. Y. Tsien, J. A. Squier, and D. Kleinfeld, "All-optical histology using ultrashort laser pulses," *Neuron*, vol. 39, no. 1, pp. 27–41, 2003.

[154] T. Ragan, J. D. Sylvan, K. H. Kim, H. Huang, K. Bahlmann, R. T. Lee, and P. T. So, "High-resolution whole organ imaging using two-photon tissue cytometry," *Journal of biomedical optics*, vol. 12, no. 1, p. 014015, 2007.

[155] M. Oberlaender, V. J. Dercksen, R. Egger, M. Gensel, B. Sakmann, and H.-C. Hege, "Automated three-dimensional detection and counting of neuron somata," *Journal of neuroscience methods*, vol. 180, no. 1, pp. 147–160, 2009.

[156] M. Oberlaender, C. P. de Kock, R. M. Bruno, A. Ramirez, H. S. Meyer, V. J. Dercksen, M. Helmstaedter, and B. Sakmann, "Cell type–specific three-dimensional structure of thalamocortical circuits in a column of rat vibrissal cortex," *Cerebral cortex*, vol. 22, no. 10, pp. 2375–2391, 2011.

[157] K. S. Matho, *Connectomic analysis of the binaural circuit and investigation of mechanisms controlling its development*.
PhD thesis, Université Pierre et Marie Curie, 2013.

[158] A. Li, H. Gong, B. Zhang, Q. Wang, C. Yan, J. Wu, Q. Liu, S. Zeng, and Q. Luo, "Micro-optical sectioning tomography to obtain a high-resolution atlas of the mouse brain," *Science*, vol. 330, no. 6009, pp. 1404–1408, 2010.

[159] H. Gong, D. Xu, J. Yuan, X. Li, C. Guo, J. Peng, Y. Li, L. A. Schwarz, A. Li, B. Hu, *et al.*, "High-throughput dual-colour precision imaging for brain-wide connectome with cytoarchitectonic landmarks at the cellular level," *Nature communications*, vol. 7, p. 12142, 2016.

[160] H. Gong, S. Zeng, C. Yan, X. Lv, Z. Yang, T. Xu, Z. Feng, W. Ding, X. Qi, A. Li, *et al.*, "Continuously tracing brain-wide long-distance axonal projections in mice at a one-micron voxel resolution," *Neuroimage*, vol. 74, pp. 87–98, 2013.

[161] M. A. Neil, R. Juškaitis, and T. Wilson, "Method of obtaining optical sectioning by using structured light in a conventional microscope," *Optics letters*, vol. 22, no. 24, pp. 1905–1907, 1997.

[162] C. Guo, J. Peng, Y. Zhang, A. Li, Y. Li, J. Yuan, X. Xu, M. Ren, H. Gong, and S. Chen, "Single-axon level morphological analysis of corticofugal projection neurons in mouse barrel field," *Scientific reports*, vol. 7, no. 1, p. 2846, 2017.

[163] T. Ragan, "Systems and methods for imaging and processing tissue," July 8 2014. US Patent 8,771,978.

[164] S. P. Amato, F. Pan, J. Schwartz, and T. M. Ragan, "Whole brain imaging with serial two-photon tomography," *Frontiers in neuroanatomy*, vol. 10, p. 31, 2016.

[165] Y. Kim, G. R. Yang, K. Pradhan, K. U. Venkataraju, M. Bota, L. C. G. Del Molino, G. Fitzgerald, K. Ram, M. He, J. M. Levine, *et al.*, "Brain-wide maps reveal stereotyped cell-type-based cortical architecture and subcortical sexual dimorphism," *Cell*, vol. 171, no. 2, pp. 456–469, 2017.

[166] P. Delafontaine-Martel, J. Lefebvre, R. Damseh, A. Castonguay, P. Tardif, and F. Lesage, "Large scale serial two-photon microscopy to investigate local vascular changes in whole rodent brain models of alzheimer's disease," in *Multiphoton Microscopy in the Biomedical Sciences XVIII*, vol. 10498, p. 104982O, International Society for Optics and Photonics, 2018.

[167] J. A. Harris, S. Mihalas, K. E. Hirokawa, J. D. Whitesell, J. Knox, A. Bernard, P. Bohn, S. Caldejon, L. Casal, A. Cho, *et al.*, "The organization of intracortical connections by layer and cell class in the mouse brain," *bioRxiv*, p. 292961, 2018.

[168] K. Seiriki, A. Kasai, T. Hashimoto, W. Schulze, M. Niu, S. Yamaguchi, T. Nakazawa, K.-i. Inoue, S. Uezono, M. Takada, *et al.*, "High-speed and scalable whole-brain imaging in rodents and primates," *Neuron*, vol. 94, no. 6, pp. 1085–1100, 2017.

[169] A. Narasimhan, J. Mizrachi, K. U. Venkatraju, D. F. Albeanu, and P. Osten, "A high resolution whole brain imaging using oblique light sheet tomography," *bioRxiv*, p. 132423, 2017.

[170] J. Lefebvre, A. Castonguay, P. Pouliot, M. Descoteaux, and F. Lesage, "Whole mouse brain imaging using optical coherence tomography: reconstruction, normalization, segmentation, and comparison with diffusion mri," *Neurophotonics*, vol. 4, no. 4, p. 041501, 2017.

[171] T. T. Wong, R. Zhang, C. Zhang, H.-C. Hsu, K. I. Maslov, L. Wang, J. Shi, R. Chen, K. K. Shung, Q. Zhou, *et al.*, "Label-free automated three-dimensional imaging of whole organs by microtomy-assisted photoacoustic microscopy," *Nature communications*, vol. 8, no. 1, p. 1386, 2017.

[172] M. Jeong, Y. Kim, J. Kim, D. D. Ferrante, P. P. Mitra, P. Osten, and D. Kim, "Comparative three-dimensional connectome map of motor cortical projections in the mouse brain," *Scientific reports*, vol. 6, p. 20072, 2016.

[173] W. Guo, X. Liu, Y. Liu, Y. Gang, X. He, Y. Jia, F. Yin, P. Li, F. Huang, H. Zhou, *et al.*, "Chemical reactivation of resin-embedded phuji adds red for simultaneous two-color imaging with egfp," *Biomedical optics express*, vol. 8, no. 7, pp. 3281–3288, 2017.

[174] A. Negrean and H. D. Mansvelder, "Optimal lens design and use in laser-scanning microscopy," *Biomedical optics express*, vol. 5, no. 5, pp. 1588–1609, 2014.

[175] S.-C. Chen and M. L. Culpepper, "Oscillating microtome with flexure drive," Sept. 23 2014. US Patent 8,839,700.

[176] K. Chung and K. Deisseroth, "Clarity for mapping the nervous system," *Nature methods*, vol. 10, no. 6, p. 508, 2013.

[177] B. Hsueh, V. M. Burns, P. Pauerstein, K. Holzem, L. Ye, K. Engberg, A.-C. Wang, X. Gu, H. Chakravarthy, H. E. Arda, *et al.*, "Pathways to clinical clarity: volumetric analysis of irregular, soft, and heterogeneous tissues in development and disease," *Scientific reports*, vol. 7, no. 1, p. 5899, 2017.

[178] S. Preibisch, S. Saalfeld, and P. Tomancak, "Globally optimal stitching of tiled 3d microscopic image acquisitions," *Bioinformatics*, vol. 25, no. 11, pp. 1463–1465, 2009.

[179] D. Hörl, F. R. Rusak, F. Preusser, P. Tillberg, N. Randel, R. K. Chhetri, A. Cardona, P. J. Keller, H. Harz, H. Leonhardt, *et al.*, "Bigstitcher: Reconstructing high-resolution image datasets of cleared and expanded samples," *bioRxiv*, p. 343954, 2018.

[180] M. Ducros, L. Moreaux, J. Bradley, P. Tiret, O. Griesbeck, and S. Charpak, "Spectral unmixing: analysis of performance in the olfactory bulb in vivo," *PLoS One*, vol. 4, no. 2, p. e4418, 2009.

[181] Y. Barad, H. Eisenberg, M. Horowitz, and Y. Silberberg, "Nonlinear scanning laser microscopy by third harmonic generation," *Applied Physics Letters*, vol. 70, no. 8, pp. 922–924, 1997.

[182] A. Zumbusch, G. R. Holtom, and X. S. Xie, "Three-dimensional vibrational imaging by coherent anti-stokes raman scattering," *Physical review letters*, vol. 82, no. 20, p. 4142, 1999.

[183] B. Weigelin, G.-J. Bakker, and P. Friedl, "Third harmonic generation microscopy of cells and tissue organization," *J Cell Sci*, pp. jcs–152272, 2016.

[184] M. J. Farrar, F. W. Wise, J. R. Fetcho, and C. B. Schaffer, "In vivo imaging of myelin in the vertebrate central nervous system using third harmonic generation microscopy," *Biophysical journal*, vol. 100, no. 5, pp. 1362–1371, 2011.

[185] S. Witte, A. Negrean, J. C. Lodder, C. P. De Kock, G. T. Silva, H. D. Mansvelder, and M. L. Groot, "Label-free live brain imaging and targeted patching with third-harmonic generation microscopy," *Proceedings of the National Academy of Sciences*, vol. 108, no. 15, pp. 5970–5975, 2011.

[186] H. Lim, D. Sharoukhov, I. Kassim, Y. Zhang, J. L. Salzer, and C. V. Melendez-Vasquez, "Label-free imaging of schwann cell myelination by third harmonic generation microscopy," *Proceedings of the National Academy of Sciences*, vol. 111, no. 50, pp. 18025–18030, 2014.

[187] H. Wang, Y. Fu, P. Zickmund, R. Shi, and J.-X. Cheng, "Coherent anti-stokes raman scattering imaging of axonal myelin in live spinal tissues," *Biophysical journal*, vol. 89, no. 1, pp. 581–591, 2005.

[188] T. B. Huff and J.-X. Cheng, "In vivo coherent anti-stokes raman scattering imaging of sciatic nerve tissue," *Journal of microscopy*, vol. 225, no. 2, pp. 175–182, 2007.

[189] Y. Shi, R. Shi, J.-X. Cheng, D. Zhang, T. B. Huff, X. Wang, and X.-M. Xu, "Longitudinal in vivo coherent anti-stokes raman scattering imaging of demyelination and remyelination in injured spinal cord," *Journal of biomedical optics*, vol. 16, no. 10, p. 106012, 2011.

[190] Y. Fu, H. Wang, T. B. Huff, R. Shi, and J.-X. Cheng, "Coherent anti-stokes raman scattering imaging of myelin degradation reveals a calcium-dependent pathway in lyso-ptdcho-induced demyelination," *Journal of neuroscience research*, vol. 85, no. 13, pp. 2870–2881, 2007.

[191] P. Gasecka, A. Jaouen, F.-Z. Bioud, H. B. de Aguiar, J. Duboisset, P. Ferrand, H. Rigneault, N. K. Balla, F. Debarbieux, and S. Brasselet, "Lipid order degradation in autoimmune demyelination probed by polarized coherent raman microscopy," *Biophysical journal*, vol. 113, no. 7, pp. 1520–1530, 2017.

[192] Y. Fu, T. B. Huff, H.-W. Wang, H. Wang, and J.-X. Cheng, "Ex vivo and in vivo imaging of myelin fibers in mouse brain by coherent anti-stokes raman scattering microscopy," *Optics express*, vol. 16, no. 24, pp. 19396–19409, 2008.

[193] T. Hellerer, A. M. Enejder, and A. Zumbusch, "Spectral focusing: High spectral resolution spectroscopy with broad-bandwidth laser pulses," *Applied Physics Letters*, vol. 85, no. 1, pp. 25–27, 2004.

[194] J. P. Day, K. F. Domke, G. Rago, H. Kano, H.-o. Hamaguchi, E. M. Vartiainen, and M. Bonn, "Quantitative coherent anti-stokes raman scattering (cars) microscopy," *The Journal of Physical Chemistry B*, vol. 115, no. 24, pp. 7713–7725, 2011.

[195] S. Abeytunge, Y. Li, R. Toledo-Crow, B. A. Larson, and M. Rajadhyaksha, "Rapid confocal imaging of large areas of excised tissue with strip mosaicing," *Journal of biomedical optics*, vol. 16, no. 5, p. 050504, 2011.

[196] E. J. Botcherby, C. W. Smith, M. M. Kohl, D. Débarre, M. J. Booth, R. Juškaitis, O. Paulsen, and T. Wilson, "Aberration-free three-dimensional multiphoton imaging of neuronal activity at khz rates," *Proceedings of the National Academy of Sciences*, vol. 109, no. 8, pp. 2919–2924, 2012.

[197] L. Madisen, A. R. Garner, D. Shimaoka, A. S. Chuong, N. C. Klapoetke, L. Li, A. van der Bourg, Y. Niino, L. Egolf, C. Monetti, *et al.*, "Transgenic mice for intersectional targeting of neural sensors and effectors with high specificity and performance," *Neuron*, vol. 85, no. 5, pp. 942–958, 2015.

[198] S. Murphy, K. Rokicki, C. Bruns, Y. Yu, L. Foster, E. Trautman, D. Olbris, T. Wolff, A. Nern, Y. Aso, *et al.*, "The janelia workstation for neuroscience," *Keystone Big Data in Biology. San Francisco, CA*, 2014.

[199] M. M. Halassa, T. Fellin, H. Takano, J.-H. Dong, and P. G. Haydon, "Synaptic islands defined by the territory of a single astrocyte," *Journal of Neuroscience*, vol. 27, no. 24, pp. 6473–6477, 2007.

[200] D. D. Wang and A. Bordey, "The astrocyte odyssey," *Progress in neurobiology*, vol. 86, no. 4, pp. 342–367, 2008.

[201] N. J. Abbott, L. Rönnbäck, and E. Hansson, "Astrocyte–endothelial interactions at the blood–brain barrier," *Nature Reviews Neuroscience*, vol. 7, no. 1, p. 41, 2006.

[202] M. Bélanger, I. Allaman, and P. J. Magistretti, "Brain energy metabolism: focus on astrocyte-neuron metabolic cooperation," *Cell metabolism*, vol. 14, no. 6, pp. 724–738, 2011.

[203] L. E. Clarke and B. A. Barres, "Emerging roles of astrocytes in neural circuit development," *Nature Reviews Neuroscience*, vol. 14, no. 5, p. 311, 2013.

[204] N. J. Allen, "Astrocyte regulation of synaptic behavior," *Annual review of cell and developmental biology*, vol. 30, pp. 439–463, 2014.

[205] E. A. Newman, "New roles for astrocytes: regulation of synaptic transmission," *Trends in neurosciences*, vol. 26, no. 10, pp. 536–542, 2003.

[206] M. Pabst, O. Braganza, H. Dannenberg, W. Hu, L. Pothmann, J. Rosen, I. Mody, K. van Loo, K. Deisseroth, A. J. Becker, *et al.*, "Astrocyte intermediaries of septal cholinergic modulation in the hippocampus," *Neuron*, vol. 90, no. 4, pp. 853–865, 2016.

[207] C. M. Alberini, E. Cruz, G. Descalzi, B. Bessières, and V. Gao, "Astrocyte glycogen and lactate: New insights into learning and memory mechanisms," *Glia*, vol. 66, no. 6, pp. 1244–1262, 2018.

[208] L. E. Clarke, S. A. Liddelow, C. Chakraborty, A. E. Münch, M. Heiman, and B. A. Barres, "Normal aging induces a1-like astrocyte reactivity," *Proceedings of the National Academy of Sciences*, vol. 115, no. 8, pp. E1896–E1905, 2018.

[209] D. T. Lioy, S. K. Garg, C. E. Monaghan, J. Raber, K. D. Foust, B. K. Kaspar, P. G. Hirrlinger, F. Kirchhoff, J. M. Bissonnette, N. Ballas, *et al.*, "A role for glia in the progression of rett's syndrome," *Nature*, vol. 475, no. 7357, p. 497, 2011.

[210] Y. Koyama, "Functional alterations of astrocytes in mental disorders: pharmacological significance as a drug target," *Frontiers in cellular neuroscience*, vol. 9, p. 261, 2015.

[211] D. Lanjakornsiripan, B.-J. Pior, D. Kawaguchi, S. Furutachi, T. Tahara, Y. Katsuyama, Y. Suzuki, Y. Fukazawa, and Y. Gotoh, "Layer-specific morphological and molecular differences in neocortical astrocytes and their dependence on neuronal layers," *Nature communications*, vol. 9, no. 1, p. 1623, 2018.

[212] Y. Zhang and B. A. Barres, "Astrocyte heterogeneity: an underappreciated topic in neurobiology," *Current opinion in neurobiology*, vol. 20, no. 5, pp. 588–594, 2010.

[213] A. Kriegstein and A. Alvarez-Buylla, "The glial nature of embryonic and adult neural stem cells," *Annual review of neuroscience*, vol. 32, pp. 149–184, 2009.

[214] M. Torigoe, K. Yamauchi, Y. Zhu, H. Kobayashi, and F. Murakami, "Association of astrocytes with neurons and astrocytes derived from distinct progenitor domains in the subpallium," *Scientific reports*, vol. 5, p. 12258, 2015.

[215] W.-P. Ge, A. Miyawaki, F. H. Gage, Y. N. Jan, and L. Y. Jan, "Local generation of glia is a major astrocyte source in postnatal cortex," *Nature*, vol. 484, no. 7394, p. 376, 2012.

[216] C.-L. Wang, L. Zhang, Y. Zhou, J. Zhou, X.-J. Yang, S.-m. Duan, Z.-Q. Xiong, and Y.-Q. Ding, "Activity-dependent development of callosal projections in the somatosensory cortex," *Journal of Neuroscience*, vol. 27, no. 42, pp. 11334–11342, 2007.

[217] M. López-Hidalgo, W. B. Hoover, and J. Schummers, "Spatial organization of astrocytes in ferret visual cortex," *Journal of Comparative Neurology*, vol. 524, no. 17, pp. 3561–3576, 2016.

[218] E. A. Bushong, M. E. Martone, Y. Z. Jones, and M. H. Ellisman, "Protoplasmic astrocytes in ca1 stratum radiatum occupy separate anatomical domains," *Journal of Neuroscience*, vol. 22, no. 1, pp. 183–192, 2002.

[219] C. J. Niedworok, A. P. Brown, M. J. Cardoso, P. Osten, S. Ourselin, M. Modat, and T. W. Margrie, "amap is a validated pipeline for registration and segmentation of high-resolution mouse brain data," *Nature communications*, vol. 7, p. 11879, 2016.

[220] D. Fürth, T. Vaissière, O. Tzortzi, Y. Xuan, A. Märtin, I. Lazaridis, G. Spigolon, G. Fisone, R. Tomer, K. Deisseroth, *et al.*, "An interactive framework for whole-brain maps at cellular resolution," *Nature neuroscience*, vol. 21, no. 1, p. 139, 2018.

[221] P. Mailly, V. Aliane, H. J. Groenewegen, S. N. Haber, and J.-M. Deniau, "The rat prefrontostriatal system analyzed in 3d: evidence for multiple interacting functional units," *Journal of Neuroscience*, vol. 33, no. 13, pp. 5718–5727, 2013.

[222] S. Tsuriel, S. Gudes, R. W. Draft, A. M. Binshtok, and J. W. Lichtman, "Multispectral labeling technique to map many neighboring axonal projections in the same tissue," *nAture methods*, vol. 12, no. 6, p. 547, 2015.

[223] J. Zhou, Y. Wen, L. She, Y.-n. Sui, L. Liu, L. J. Richards, and M.-m. Poo, "Axon position within the corpus callosum determines contralateral cortical projection," *Proceedings of the National Academy of Sciences*, vol. 110, no. 29, pp. E2714–E2723, 2013.

[224] L. Pessoa, "Emotion and cognition and the amygdala: from "what is it?" to "what's to be done?"," *Neuropsychologia*, vol. 48, no. 12, pp. 3416–3429, 2010.

[225] M. Sarter and H. J. Markowitsch, "Involvement of the amygdala in learning and memory: a critical review, with emphasis on anatomical relations.," *Behavioral neuroscience*, vol. 99, no. 2, p. 342, 1985.

[226] N. Otsu, "A threshold selection method from gray-level histograms," *IEEE transactions on systems, man, and cybernetics*, vol. 9, no. 1, pp. 62–66, 1979.

[227] E. A. Susaki and H. R. Ueda, "Whole-body and whole-organ clearing and imaging techniques with single-cell resolution: toward organism-level systems biology in mammals," *Cell chemical biology*, vol. 23, no. 1, pp. 137–157, 2016.

[228] P. J. Keller and H.-U. Dodt, "Light sheet microscopy of living or cleared specimens," *Current opinion in neurobiology*, vol. 22, no. 1, pp. 138–143, 2012.

[229] R. Tomer, M. Lovett-Barron, I. Kauvar, A. Andalman, V. M. Burns, S. Sankaran, L. Grosenick, M. Broxton, S. Yang, and K. Deisseroth, "Sped light sheet microscopy: fast

mapping of biological system structure and function," *Cell*, vol. 163, no. 7, pp. 1796–1806, 2015.

[230] O. A. Bayraktar, L. C. Fuentealba, A. Alvarez-Buylla, and D. H. Rowitch, "Astrocyte development and heterogeneity," *Cold Spring Harbor perspectives in biology*, p. a020362, 2014.

[231] S. Pontes-Quero, L. Heredia, V. Casquero-García, M. Fernández-Chacón, W. Luo, A. Hermoso, M. Bansal, I. Garcia-Gonzalez, M. S. Sanchez-Muñoz, J. R. Perea, *et al.*, "Dual ifgmosaic: a versatile method for multispectral and combinatorial mosaic gene-function analysis," *Cell*, vol. 170, no. 4, pp. 800–814, 2017.

[232] E. Beaurepaire, M. Oheim, and J. Mertz, "Ultra-deep two-photon fluorescence excitation in turbid media," *Optics Communications*, vol. 188, no. 1-4, pp. 25–29, 2001.

[233] P. Theer, M. T. Hasan, and W. Denk, "Two-photon imaging to a depth of 1000 μm in living brains by use of a ti: Al 2 o 3 regenerative amplifier," *Optics letters*, vol. 28, no. 12, pp. 1022–1024, 2003.

[234] J. Ying, F. Liu, and R. Alfano, "Spatial distribution of two-photon-excited fluorescence in scattering media," *Applied optics*, vol. 38, no. 1, pp. 224–229, 1999.

[235] D. Kobat, M. E. Durst, N. Nishimura, A. W. Wong, C. B. Schaffer, and C. Xu, "Deep tissue multiphoton microscopy using longer wavelength excitation," *Optics express*, vol. 17, no. 16, pp. 13354–13364, 2009.

[236] D. Kobat, N. G. Horton, and C. Xu, "In vivo two-photon microscopy to 1.6-mm depth in mouse cortex," *Journal of biomedical optics*, vol. 16, no. 10, p. 106014, 2011.

[237] D. Shcherbo, C. S. Murphy, G. V. Ermakova, E. A. Solovieva, T. V. Chepurnykh, A. S. Shcheglov, V. V. Verkhusha, V. Z. Pletnev, K. L. Hazelwood, P. M. Roche, *et al.*, "Far-red fluorescent tags for protein imaging in living tissues," *Biochemical journal*, vol. 418, no. 3, pp. 567–574, 2009.

[238] C. Tischbirek, A. Birkner, H. Jia, B. Sakmann, and A. Konnerth, "Deep two-photon brain imaging with a red-shifted fluorometric ca2+ indicator," *Proceedings of the National Academy of Sciences*, vol. 112, no. 36, pp. 11377–11382, 2015.

[239] D. G. Ouzounov, T. Wang, M. Wang, D. D. Feng, N. G. Horton, J. C. Cruz-Hernández, Y.-T. Cheng, J. Reimer, A. S. Tolias, N. Nishimura, *et al.*, "In vivo three-photon imaging of activity of gcamp6-labeled neurons deep in intact mouse brain," *Nature methods*, vol. 14, no. 4, p. 388, 2017.

[240] C. Xu, W. Zipfel, J. B. Shear, R. M. Williams, and W. W. Webb, "Multiphoton fluorescence excitation: new spectral windows for biological nonlinear microscopy," *Proceedings of the National Academy of Sciences*, vol. 93, no. 20, pp. 10763–10768, 1996.

[241] S. W. Hell, K. Bahlmann, M. Schrader, A. Soini, H. M. Malak, I. Gryczynski, and J. R. Lakowicz, "Three-photon excitation in fluorescence microscopy," *Journal of Biomedical Optics*, vol. 1, no. 1, pp. 71–75, 1996.

[242] D. L. Wokosin, V. E. Centonze, S. Crittenden, and J. White, "Three-photon excitation fluorescence imaging of biological specimens using an all-solid-state laser," *Bioimaging*, vol. 4, no. 3, pp. 208–214, 1996.

[243] I. Gryczynski, H. Malak, and J. R. Lakowicz, "Three-photon excitation of a tryptophan derivative using a fs-ti: Sapphire laser," *Biospectroscopy*, vol. 2, no. 1, pp. 9–15, 1996.

[244] S. Maiti, J. B. Shear, R. Williams, W. Zipfel, and W. W. Webb, "Measuring serotonin distribution in live cells with three-photon excitation," *Science*, vol. 275, no. 5299, pp. 530–532, 1997.

[245] L. Shi, L. A. Sordillo, A. Rodríguez-Contreras, and R. Alfano, "Transmission in near-infrared optical windows for deep brain imaging," *Journal of biophotonics*, vol. 9, no. 1-2, pp. 38–43, 2016.

[246] J. Binding, J. B. Arous, J.-F. Léger, S. Gigan, C. Boccara, and L. Bourdieu, "Brain refractive index measured in vivo with high-na defocus-corrected full-field oct and consequences for two-photon microscopy," *Optics express*, vol. 19, no. 6, pp. 4833–4847, 2011.

[247] C. Xu and W. W. Webb, "Measurement of two-photon excitation cross sections of molecular fluorophores with data from 690 to 1050 nm," *JOSA B*, vol. 13, no. 3, pp. 481–491, 1996.

[248] N. G. Horton and C. Xu, "Dispersion compensation in three-photon fluorescence microscopy at 1,700 nm," *Biomedical optics express*, vol. 6, no. 4, pp. 1392–1397, 2014.

[249] C. J. Rowlands, D. Park, O. T. Bruns, K. D. Piatkevich, D. Fukumura, R. K. Jain, M. G. Bawendi, E. S. Boyden, and P. T. So, "Wide-field three-photon excitation in biological samples," *Light: Science & Applications*, vol. 6, no. 5, p. e16255, 2017.

[250] C. Rodriguez, Y. Liang, R. Lu, and N. Ji, "Three-photon fluorescence microscopy with an axially elongated bessel focus," *Optics letters*, vol. 43, no. 8, pp. 1914–1917, 2018.

[251] B. Chen, X. Huang, D. Gou, J. Zeng, G. Chen, M. Pang, Y. Hu, Z. Zhao, Y. Zhang, Z. Zhou, *et al.*, "Rapid volumetric imaging with bessel-beam three-photon microscopy," *Biomedical optics express*, vol. 9, no. 4, pp. 1992–2000, 2018.

[252] X. Tao, H.-H. Lin, T. Lam, R. Rodriguez, J. W. Wang, and J. Kubby, "Transcutical three-photon fluorescence imaging of drosophila brain at subcellular resolution with adaptive optics," in *CLEO: Applications and Technology*, pp. ATu1B–2, Optical Society of America, 2017.

[253] M. Yildirim, N. Durr, and A. Ben-Yakar, "Tripling the maximum imaging depth with third-harmonic generation microscopy," *Journal of biomedical optics*, vol. 20, no. 9, p. 096013, 2015.

[254] L.-C. Cheng, N. G. Horton, K. Wang, S.-J. Chen, and C. Xu, "Measurements of multiphoton action cross sections for multiphoton microscopy," *Biomedical optics express*, vol. 5, no. 10, pp. 3427–3433, 2014.

[255] K. Wang, N. G. Horton, K. Charan, and C. Xu, "Advanced fiber soliton sources for nonlinear deep tissue imaging in biophotonics," *IEEE J. Sel. Top. Quantum Electron.*, vol. 20, no. 2, p. 6800311, 2014.

[256] T. Noronen, S. Firstov, E. Dianov, and O. G. Okhotnikov, "1700 nm dispersion managed mode-locked bismuth fiber laser," *Scientific reports*, vol. 6, p. 24876, 2016.

[257] A. Khegai, M. Melkumov, K. Riumkin, V. Khopin, S. Firstov, and E. Dianov, "Nalm-based bismuth-doped fiber laser at 1.7 μm," *Optics letters*, vol. 43, no. 5, pp. 1127–1130, 2018.

[258] T. Noronen, O. Okhotnikov, and R. Gumenyuk, "Electronically tunable thulium-holmium mode-locked fiber laser for the 1700-1800 nm wavelength band," *Optics Express*, vol. 24, no. 13, pp. 14703–14708, 2016.

[259] F. M. Mitschke and L. F. Mollenauer, "Discovery of the soliton self-frequency shift," *Optics letters*, vol. 11, no. 10, pp. 659–661, 1986.

[260] P. Cadroas, L. Abdeladim, L. Kotov, M. Likhachev, D. Lipatov, D. Gaponov, A. Hideur, M. Tang, J. Livet, W. Supatto, *et al.*, "All-fiber femtosecond laser providing 9 nj, 50 mhz pulses at 1650 nm for three-photon microscopy," *Journal of Optics*, vol. 19, no. 6, p. 065506, 2017.

[261] J. H. Lee, J. van Howe, C. Xu, and X. Liu, "Soliton self-frequency shift: experimental demonstrations and applications," *IEEE Journal of Selected Topics in Quantum Electronics*, vol. 14, no. 3, pp. 713–723, 2008.

[262] L. Rishøj, G. Prabhakar, J. Demas, and S. Ramachandran, "30 nj, 50 fs all-fiber source at 1300 nm using soliton shifting in lma hom fiber," in *Lasers and Electro-Optics (CLEO), 2016 Conference on*, pp. 1–2, IEEE, 2016.

[263] H.-Y. Chung, W. Liu, Q. Cao, F. X. Kärtner, and G. Chang, "Er-fiber laser enabled, energy scalable femtosecond source tunable from 1.3 to 1.7 μm," *Optics Express*, vol. 25, no. 14, pp. 15760–15771, 2017.

[264] W. Supatto, *Imagerie multiphoton quantitative et ablation laser par impulsions femtosecondes pour l'étude de l'expression génétique mécano-sensible chez l'embryon de drosophile sauvage*.
PhD thesis, Paris 7, 2005.

[265] S. Adachi, H. Ishii, T. Kanai, N. Ishii, A. Kosuge, and S. Watanabe, "1.5 mj, 6.4 fs parametric chirped-pulse amplification system at 1 khz," *Optics letters*, vol. 32, no. 17, pp. 2487–2489, 2007.

[266] H. Ishizuki and T. Taira, "Improvement of laser-beam distortion in large-aperture pp-mgln device by using x-axis czochralski-grown crystal," *Optics express*, vol. 22, no. 16, pp. 19668–19673, 2014.

[267] Z. Wang, C. Liu, Z. Shen, Q. Zhang, H. Teng, and Z. Wei, "High-contrast 1.16 pw ti: sapphire laser system combined with a doubled chirped-pulse amplification scheme and a femtosecond optical-parametric amplifier," *Optics letters*, vol. 36, no. 16, pp. 3194–3196, 2011.

[268] N. Kuzmin, P. Wesseling, P. de Witt Hamer, D. Noske, G. Galgano, H. Mansvelder, J. Baayen, and M. Groot, "Third harmonic generation imaging for fast, label-free pathology of human brain tumors," *Biomedical optics express*, vol. 7, no. 5, pp. 1889–1904, 2016.

[269] X. Morin, F. Jaouen, and P. Durbec, "Control of planar divisions by the g-protein regulator lgn maintains progenitors in the chick neuroepithelium," *Nature neuroscience*, vol. 10, no. 11, p. 1440, 2007.

[270] J. S. Barbosa, R. Sanchez-Gonzalez, R. Di Giaimo, E. V. Baumgart, F. J. Theis, M. Götz, and J. Ninkovic, "Live imaging of adult neural stem cell behavior in the intact and injured zebrafish brain," *Science*, vol. 348, no. 6236, pp. 789–793, 2015.

[271] A. Alunni and L. Bally-Cuif, "A comparative view of regenerative neurogenesis in vertebrates," *Development*, vol. 143, no. 5, pp. 741–753, 2016.

[272] C. Satou, Y. Kimura, and S.-i. Higashijima, "Generation of multiple classes of v0 neurons in zebrafish spinal cord: progenitor heterogeneity and temporal control of neuronal diversity," *Journal of Neuroscience*, vol. 32, no. 5, pp. 1771–1783, 2012.

[273] R. Madelaine and P. Blader, "A cluster of non-redundant ngn1 binding sites is required for regulation of deltaa expression in zebrafish," *Developmental biology*, vol. 350, no. 1, pp. 198–207, 2011.

[274] R. M. White, A. Sessa, C. Burke, T. Bowman, J. LeBlanc, C. Ceol, C. Bourque, M. Dovey, W. Goessling, C. E. Burns, *et al.*, "Transparent adult zebrafish as a tool for in vivo transplantation analysis," *Cell stem cell*, vol. 2, no. 2, pp. 183–189, 2008.

[275] A. Schönle and S. W. Hell, "Heating by absorption in the focus of an objective lens," *Optics letters*, vol. 23, no. 5, pp. 325–327, 1998.

[276] P. Qiu, R. Liang, J. He, and K. Wang, "Estimation of temperature rise at the focus of objective lens at the 1700 nm window," *Journal of Innovative Optical Health Sciences*, vol. 10, no. 02, p. 1650048, 2017.

[277] K. König, T. Becker, P. Fischer, I. Riemann, and K.-J. Halbhuber, "Pulse-length dependence of cellular response to intense near-infrared laser pulses in multiphoton microscopes," *Optics letters*, vol. 24, no. 2, pp. 113–115, 1999.

[278] K. König, "Intracellular nanosurgery with near infrared femtosecond laser pulses k. könig ", i. riemann, p. fischer and k.-j. halbhuber," *Cellular and molecular biology*, vol. 45, no. 2, pp. 195–201, 1999.

[279] A. Facomprez, E. Beaurepaire, and D. Débarre, "Accuracy of correction in modal sensorless adaptive optics," *Optics express*, vol. 20, no. 3, pp. 2598–2612, 2012.

[280] K. Wang, W. Sun, C. T. Richie, B. K. Harvey, E. Betzig, and N. Ji, "Direct wavefront sensing for high-resolution in vivo imaging in scattering tissue," *Nature communications*, vol. 6, p. 7276, 2015.

[281] L. Kong and M. Cui, "In vivo neuroimaging through the highly scattering tissue via iterative multi-photon adaptive compensation technique," *Optics Express*, vol. 23, no. 5, pp. 6145–6150, 2015.

[282] N. Ji, "Adaptive optical fluorescence microscopy," *Nature methods*, vol. 14, no. 4, p. 374, 2017.

[283] J.-H. Park, W. Sun, and M. Cui, "High-resolution in vivo imaging of mouse brain through the intact skull," *Proceedings of the National Academy of Sciences*, vol. 112, no. 30, pp. 9236–9241, 2015.

[284] N. Olivier, D. Débarre, and E. Beaurepaire, "Dynamic aberration correction for multiharmonic microscopy," *Optics letters*, vol. 34, no. 20, pp. 3145–3147, 2009.

[285] D. Sinefeld, H. P. Paudel, D. G. Ouzounov, T. G. Bifano, and C. Xu, "Adaptive optics in multiphoton microscopy: comparison of two, three and four photon fluorescence," *Optics express*, vol. 23, no. 24, pp. 31472–31483, 2015.

[286] O. Katz, E. Small, Y. Guan, and Y. Silberberg, "Noninvasive nonlinear focusing and imaging through strongly scattering turbid layers," *Optica*, vol. 1, no. 3, pp. 170–174, 2014.

[287] R. Lu, W. Sun, Y. Liang, A. Kerlin, J. Bierfeld, J. D. Seelig, D. E. Wilson, B. Scholl, B. Mohar, M. Tanimoto, *et al.*, "Video-rate volumetric functional imaging of the brain at synaptic resolution," *Nature neuroscience*, vol. 20, no. 4, p. 620, 2017.

université PARIS-SACLAY
ÉCOLE DOCTORALE
INTERFACES
Approches Interdisciplinaires : Fondements, Applications et Innovation

Titre : Microscopie non linéaire multicolore de grands volumes de tissu cérébral

Mots clés : Microscopie multiphoton, marquage Brainbow, mélange de fréquences, microscopie à découpe sériée, microscopie à 3 photons

Résumé : La microscopie non linéaire a transformé le domaine de la neurobiologie depuis les années 1990, en permettant d'acquérir des images tridimensionnelles de tissus épais avec une résolution subcellulaire. Cependant, les profondeurs d'imagerie accessibles sont limitées à quelques centaines de micromètres dans des tissus diffusants tels que le tissu cérébral. Au cours des dernières années, plusieurs stratégies ont été développées pour dépasser cette limitation de profondeur et accéder à de plus grands volumes de tissu. Ces avancées récentes ont jusqu'à présent été limitées en terme de modes de contrastes accessibles, et ont souvent été réduites à des approches monochromes. Ce travail de thèse vise à développer des techniques d'imagerie non linéaires de grands volumes et de grande profondeur dotées de diverses possibilités de contrastes, indispensables pour l'étude de tissus complexes tels que le tissu cérébral. Dans un premier chapitre, nous présentons les difficultés associées à l'imagerie de grand volume de tissu cérébral, avec une emphase particulière sur les puissantes stratégies de marquages génétiques dont l'usage à jusqu'à présent été limité à des faibles étendues. Ensuite, nous introduisons la microscopie Chrom-SMP (chromatic serial multiphoton), une méthode développée au cours de cette thèse et consistant à combiner l'excitation deux-photon multicouleurs par mélange de fréquences avec une technique d'histologie automatisée (i.e découpe sériée) pour accéder à plusieurs contrastes non linéaires à travers de grands volumes de tissus ex vivo, allant de plusieurs mm^3 à des cerveaux entiers, avec une résolution micrométrique et un coalignement intrinsèque des canaux spectraux. Dans un troisième chapitre, nous explorons le potentiel de cette nouvelle approche pour la neurobiologie. En particulier, nous démontrons l'histologie multicouleur de plusieurs mm^3 de tissu "Brainbow" avec une résolution constante dans l'ensemble du volume imagé. Nous illustrons le potentiel de notre approche à travers l'analyse de la morphologie, des interactions et du lignage des astrocytes du cortex cérébral de souris. Nous explorons également l'apport du Chrom-SMP pour le suivi multiplexé de projections neuronales marquées par des traceurs de couleurs distinctes sur de grandes distances. Enfin, nous présentons dans un quatrième chapitre le développement de la microscopie à trois photons multimodale, approche permettant d'augmenter la profondeur d'imagerie sur tissus vivants.

Title : Large volume multicolor nonlinear microscopy of neural tissues

Keywords : Multiphoton microscopy, Brainbow labeling, wavelength-mixing, block-face imaging, three-photon microscopy

Abstract : Multiphoton microscopy has transformed neurobiology during the two last decades by enabling 3D imaging of thick tissues at subcellular resolution. However the depths provided by multiphoton microscopy are limited to few hundreds of micrometers inside scattering tissues such as the brain. In the recent years, several strategies have emerged to overcome this depth limitation and to access larger volumes of tissue. Although these novel approaches are transforming brain imaging, they currently lack efficient multicolor and multicontrast modalities. This work aims to develop large-scale and deep-tissue multiphoton imaging modalities with augmented contrast capabilities. In a first chapter, we present the challenges of high-content large-volume brain imaging, with a particular emphasis on powerful multicolor labeling strategies which have so far been restricted to limited scales. We then introduce chromatic serial multiphoton tomography, a method which combines automated histology with wavelength-mixing to access multiple nonlinear contrasts across large volumes, from several mm^3 to whole brains, with submicron resolution and intrinsic channel registration. In a third chapter, we demonstrate the potential of this novel approach to open novel experimental paradigms in neurobiological studies. In particular, we demonstrate multicolor volumetric histology of several mm^3 of Brainbow-labeled tissues with preserved diffraction-limited resolution and illustrate the strengths of this method through color-based tridimensional analysis of astrocyte morphology, interactions and lineage in the mouse cerebral cortex. We further illustrate the potential of the method through multiplexed whole-brain mapping of axonal projections labeled with distinct tracers. Finally, we develop multimodal three-photon microscopy as a method to access larger depths in live settings.

Université Paris-Saclay
Espace Technologique / Immeuble Discovery
Route de l'Orme aux Merisiers RD 128 / 91190 Saint-Aubin, France